Cloud Condensation Nuclei in the Amazon Basin: Their Role in a Tropical Rainforest

Thesis by

Gregory C. Roberts

In Partial Fulfillment of the Requirements

for the Degree of

Doctor of Philosophy

California Institute of Technology

Pasadena, California

2001

(Defended December 12, 2000)

Acknowledgements

"Success is in the journey, not in the destination." — *Anonymous*

Many people have touched my life during this journey through graduate school and I owe many thanks to those who have helped make this degree possible. The roads have not always been straight; and sometimes, there were no roads to follow in the rainforests of Africa and South America.

I was fortunate to have two advisors that gave me the flexibility and support to develop into an independent and self-motivated researcher. Few graduate students have two advisors looking out for them. Andi inspired me to push the limits in my own work and explore beyond the traditional approach within our discipline. Michael provided invaluable support during my presence at Caltech.

I wish to thank Gar Lala for his insight and helping build the CCN counters, and Paulo Artaxo for his enthusiasm and support during the LBA projects. I would also like to thank Chris Sorensen being a mentor and supporting me throughout graduate school. I enjoyed the runs we had together in Scotland.

Thanks to my classmates who helped me get through those first years (I'm glad they are over!). Thanks to my friends who helped me maintain a saner side of life – my running buddies (Rob and Marc), my climbing buddies (Kirk, Tyler, and Paco), and my sailing buddies (Ben and Grant). Ein Hefe, bitte – Prost, Marc und an das ganze MPIC! *Thanks Grant* and Udo for providing the occasional shelter from the beschissenes German weather.

I thank Linda Scott who kept me in touch with the events at Caltech, her smile, and for sending my mail to all four corners of the globe. Thanks Fran and Laurel for helping me rectify the administrative mess every time I came back to Caltech and Pat Draper who understood.

My journey through graduate school has been full of international adventures where I have met special people that have had a lasting impact. Thanks David (Absolute) for the survival coarse at Max Planck Institute. Your guidance to conducting field experiments and packing Zargekisten was so helpful for the later campaigns. Dominique Nganga, Prudence and Louis ont fait possible le voyage dans le coeur d' Afrique. Je vous remercie pour toutes les memoires. Thanks to Alex and the NCAR group for their teamwork during the EXPRESSO campaign. Surviving Brazilian bureaucracy would not have been possible without the free spirits of Beatrice and João Luis, Brandão and the LBA scientific team. I extend a special thanks to Jens and Pascal for their friendship and unmatched perseverance during LBA – Jens kept us organized and Pascal kicked it in the microcircuits where it hurt the most. Agradeço Marco Antônio e Juscelino por terem me ajudado a descobrir a Amazônia. Thanks Earle for the many enlightening (pun intended) discussions.

And last but not least, thanks to my family, whose never-ending support and care packages (cookies and jelly beans, included) provided invaluable motivation to keep trekking through the journey.

Abstract

Cloud condensation nuclei (CCN) are closely linked to cloud structure and precipitation; yet, their role in tropical climates remains largely unknown. CCN measurements were performed during several field campaigns during 1998 and 1999 as part of the Large Scale Biosphere-Atmosphere Experiment in Amazonia (LBA) in the states of Amazonas and Rondônia. An airborne experiment transected the Amazon Basin and allowed for sampling of different airmasses ranging from clean maritime aerosol along the eastern coast to the smoke plumes and regional haze of the biomass burning. CCN concentrations between 0.15% and 1.5% supersaturation were measured using static thermal-gradient CCN chambers.

The wet-season CCN concentrations measured in the unpolluted Amazon Basin were surprisingly low and resembled conditions more typical of marine locations than of other continental sites. It is remarkable that very similar CCN concentrations prevail in pristine marine and continental regions, in spite of the different aerosol production mechanisms and particle compositions. Physical and chemical properties responsible for CCN activation were estimated using a number and mass size distribution closure. In spite of the large organic fraction in Amazonian aerosol, the results suggest that the soluble, inorganic component accounts for most of the CCN activity during the wet season.

Biomass burning smoke aerosol dramatically increased CCN concentrations during the dry season, which likely increases colloidal stability and cloud lifetime, resulting in the observed non-precipitating clouds. Because of the low natural CCN

abundance in Amazonia, climatic effects related to the enhanced aerosol emissions due to human activity may have a stronger impact on climate change than in other continental regions.

An early part of my research also included measuring the air-to-sea flux of biogenic trace gases on the Black Sea and the characterization of aerosol composition and their sources in the central African rainforest.

Table of Contents

List of Figures

List of Tables

Chapter 1

Introduction

1.1. Research Objectives

The main objective of the research is to characterize the properties of cloud condensation nuclei (CCN) in humid equatorial regions where convective cloud processes are an important regulator of the tropical climate. Although the importance of CCN on cloud formation and the subsequent effects on climate has long been recognized, no published data exists for CCN measurements in the Amazon Basin or other humid tropical rain forests. *Twomey and Wojciechowski* [1969] measured CCN aboard an aircraft over various regions in Africa, mostly in the dry tropics. *Désalmand* [1985] suggested a seasonal variation of CCN spectra based on experiments in Ivory Coast, Africa.

Some of the specific questions concerning the properties of CCN and their role in regulating tropical climates, which will be addressed in the research, are as follows:

How do the characteristics of CCN in tropical regions compare to other measurements?

No CCN measurements in tropical rain forests have been made and background concentrations in clean continental environments are not well quantified. CCN concentrations were determined during the wet and dry seasons to quantify the annual variation over the Amazon Basin. The seasonal changes in CCN spectra are presented in Chapters 3, 5 and 6.

What properties of CCN are responsible for their activation?

The principal factors in reducing the critical supersaturation of an aerosol primarily depend on the amount of soluble material and surface-active species. The aerosol size distribution also effects CCN activity and droplet growth kinetics. The contribution of water-soluble inorganic and organic species to increasing the CCN activity will be evaluated in Chapters 4 and 6.

What are the origins of CCN?

Chapter 4 presents the results of multi-stage cascade impactors, which were used to quantify the relative amounts of inorganic and organic constituents. The factors associated with reducing the critical supersaturation of CCN depend on the physical and chemical properties of the fine fraction aerosol. Chapter 7 discusses the aerosol cycle in the Amazon Basin, and specifically, the processes that influence CCN activity.

What are the effects of anthropogenic activity on CCN characteristics and potential consequences in regional climate?

A convective cloud parcel model illustrates the modifications to cloud properties between the wet and dry season in Chapter 6. Identifying natural CCN levels will provide insight to the anthropogenic effects on cloud properties (i.e., albedo and precipitation).

1.2. Implementation of Research

The measurements were performed during the Large Scale Biosphere-Atmosphere Experiment in Amazonia (LBA) in 1998 and 1999 during wet and dry seasons (Figure 1.1). The LBA project is an international research initiative lead by Brazil and is designed to study the interactions between Amazonia and the earth system. The field experiments enabled a thorough characterization of CCN in a humid equatorial rain forest during the wet and dry seasons and provide useful data to address the points outlined in the research objectives.

The Cooperative LBA Airborne Regional Experiment (CLAIRE) occurred from March 28 to April 15, 1998, at a ground site located 125 km northeast of Manaus, in the state of Amazonas, Brazil. The CLAIRE experiment took place in the wet season and the anthropogenic contribution to the ambient aerosol was negligible. The purpose of these measurements was to characterize the clean air masses originating over the rain forest.

The European Studies on Trace gases and Atmospheric Chemistry experiment (EUSTACH) expanded operations to include wet and dry season experiments at both forest and pasture sites in the state of Rondônia in 1999. The wet season measurements (April 7 to May 21, 1999) extended into the beginning of the burning season when fires began in the neighboring state of Mato Grosso. The dry season experiment occurred from September 15 to November 1, 1999 from the peak of fire activity (beginning to middle of September) to the onset of the wet season (end of October). The forest site was located in the Jaru Biological Reserve about 90 km north of Ji-Paraná along the Machado River. During the wet season, anthropogenic contribution to the ambient aerosol was

negligible. The pasture site was located on the Fazenda Nossa Senhora about 50 km east of Ji-Paraná. The deforested region extends for at least 60 km surrounding the pasture site. As a consequence, anthropogenic contributions from local traffic and nearby cities (e.g., Ouro Preto d'Oueste and Ji-Paraná) influence aerosol properties. An airborne experiment transected the Amazon Basin and allowed for sampling of different airmasses ranging from clean maritime aerosol along the eastern coast to the smoke plumes and regional haze of the biomass burning.

1.3. Cloud Condensation Nuclei

Cloud condensation nuclei (CCN) play an essential role in cloud formation, which is determined by heterogeneous water nucleation on aerosol particles [*Köhler*, 1936; *Seinfeld and Pandis*, 1998]. The equilibrium saturation ratio (S_v^{eq}) of a droplet of a given diameter (D_p) and temperature (T) is described by a modified Köhler equation as

$$\frac{p_A}{p_A^o} = S_v^{eq} = \exp\left(\frac{4\sigma' M_w}{kT\rho_w D_p} - \frac{\Phi M_w}{\frac{\pi\rho' D_p^{\,3}}{6} - \sum_i m_i}\left[\sum_i \frac{\nu_i m_i}{M_i}\right] \right) \tag{1.1}$$

where k is the Boltzmann constant, σ' is the surface tension of the solution, M_w and M_i are the respective molecular weights of water and solute, m_i is the dissolved solute mass, ρ_w and ρ' are the densities of water and aqueous solution, respectively, ν_i is the number of ions into which a solute molecule dissociates (van't Hoff factor), and Φ is the osmotic

coefficient of the aqueous solution. For a pure water droplet, the vapor pressure at the curved surface p_A always exceeds the vapor pressure over a flat interface $p_A°$. However, depending on the magnitude of the curvature term, relative to the solute-effect term, the equilibrium saturation ratio may be greater than or less than one.

The Kelvin effect (i.e., the surface tension term; A/D_p) accounts for enhanced vapor pressure due to droplet curvature. The Raoult effect (i.e., solute mass term; B/D_p^3) depresses the vapor pressure due to dissolved mass. Supersaturation ratios are often expressed in percent (e.g., S_v (%) = (S_v (ratio) – 1) x 100%) throughout this text. Figure 1.2 illustrates the relative importance of the competing Kelvin (i.e., curvature) and Raoult (i.e., solute-effect) terms and shows the resulting Köhler curve.

The Köhler curve represents the equilibrium saturation ratio of water vapor for an aqueous solution droplet of a given diameter and amount of solute. The presence of surface-active substances also has a significant influence on the equilibrium vapor pressure by affecting the droplet's surface tension [*Shulman et al.*, 1996]. The maximum S_v^{eq} of the resulting Köhler curve defines the critical supersaturation (S_c) and occurs at the critical droplet diameter (D_{pc}). The droplet is in stable equilibrium with its environment when its diameter is less than D_{pc}. However, once the particle has activated (i.e., $D_p > D_{pc}$), the particle will continue to grow as long as the surrounding vapor pressure of water in the air is greater than the equilibrium vapor pressure of the solution droplet. The supersaturation ratio varies spatially and temporally during natural cloud formation and only particles with S_c smaller than the maximum attained supersaturation grow into cloud droplets.

The critical supersaturation of a particle implicitly contains all chemical and dry particle size information required to predict cloud droplet formation [*Hudson*, 1993]. The physical and chemical properties of the aerosol influence the relationship between CCN concentration and the supersaturation at which the particles will activate. CCN concentrations can vary over several orders of magnitude – from several thousand per cubic centimeter [*Herrerra and Castro*, 1988] to fewer than 10 cm^{-3} [*Radke and Hobbs*, 1969]. The magnitude and shape of the CCN spectra is important, since it determines how droplet number and maximum supersaturation vary with updraft [*Twomey*, 1959].

1.4. Additional Research

In addition to the current research, a significant portion of the thesis research involved two field projects that were not directly related to the main thesis topic. The results are included as appendices at the end of the thesis.

Appendix B presents the results from the Experiment for Regional Sources and Sinks of Oxidants (EXPRESSO). The fieldwork for EXPRESSO-96 took place during the dry season in November and December 1996 to assess the role of biomass burning on atmospheric chemistry, climate and ecology in equatorial regions of Africa. The purpose of the aerosol portion of this experiment was to quantify the composition and the concentrations of aerosol particles in a tropical rain forest, to identify the major regional sources, and to evaluate the relative contribution from these sources, and in particular from biomass burning.

Appendix C presents the results from the European River – Ocean System 21 project (EROS 21). The cruise track of the R/V Professor Vodyanitskiy allowed us to sample different representative water masses of the Black Sea from estuarine to shelf waters along the Danube front, and from shelf waters to open seawaters above the slope and the main deep basin. Our research intends to extend the global inventories of CH_4, N_2O and DMS fluxes to the atmosphere from marine environments and to indicate potential interactions between these fluxes and the biogeochemical changes on the northwestern shelf of the Black Sea. We investigated the distribution of CH_4, N_2O and DMS in surface waters of the northwestern Black Sea, mainly influenced by the Danube River inflow. CH_4 and N_2O mixing ratios in the atmosphere above the sea were also measured, in order to estimate the flux of these gases from the surface shelf waters.

1.5. References

Désalmand, F., An attempt to characterize a relationship between supersaturation spectrum, size spectrum and solubiliity of CCN observed over a tropical rain forest, *J. Atmos. Sci.*, *42* (5), 472, 1985.

Herrerra, J.R., and J.J. Castro, Production of cloud condensation nuclei in Mexico City, *J. Appl. Meteor.*, *27*, 1189-1192, 1988.

Hudson, J.G., Cloud condensation nuclei, *Journal of Applied Meteorology*, *32*, 596-607, 1993.

Köhler, H., The nucleus in and the growth of hygroscopic droplets, *Trans. Faraday Soc.*, *32*, 1152-1161, 1936.

Radke, L.F., and P.V. Hobbs, Measurement of cloud condensation nuclei, light scattering coefficient, sodium-containing particles, and Aitken nuclei in the Olympic Mountains of Washington, *J. Atmos. Sci.*, *26*, 281, 1969.

Seinfeld, J.H., and S.N. Pandis, *Atmospheric chemistry and physics: From air pollution to climate change*, 1326 pp., John Wiley, New York, 1998.

Shulman, M.L., M.C. Jacobson, R.J. Charlson, R.E. Synovec, and T.E. Young, Dissolution behavior and surface tension effects of organic compounds in nucleating cloud droplets, *Geophys. Res. Lett.*, *23*, 277-280, 1996.

Twomey, S., The influence of cloud nucleus population on the microstructure and stability of convective clouds, *Tellus*, *11*, 408-411, 1959.

Twomey, S., and T.A. Wojciechowski, Observations of the geographical variations of cloud nuclei, *J. Atmos. Sci.*, *25*, 333-334, 1969.

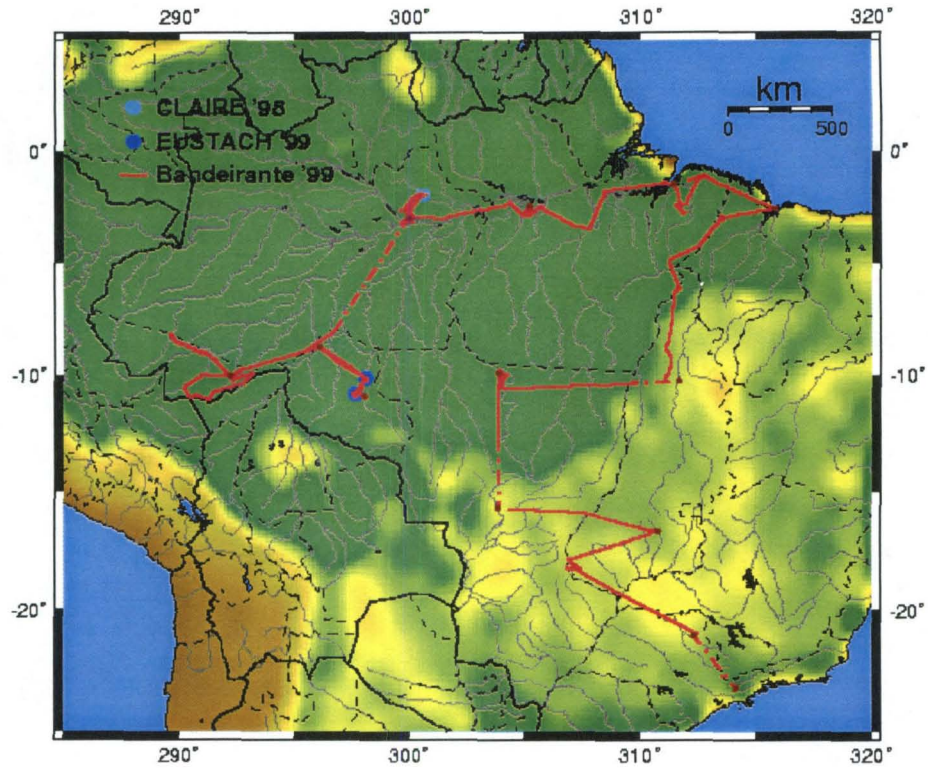

Figure 1.1. Field sites during the Large Scale Biosphere-Atmosphere Experiment in Amazonia (LBA).

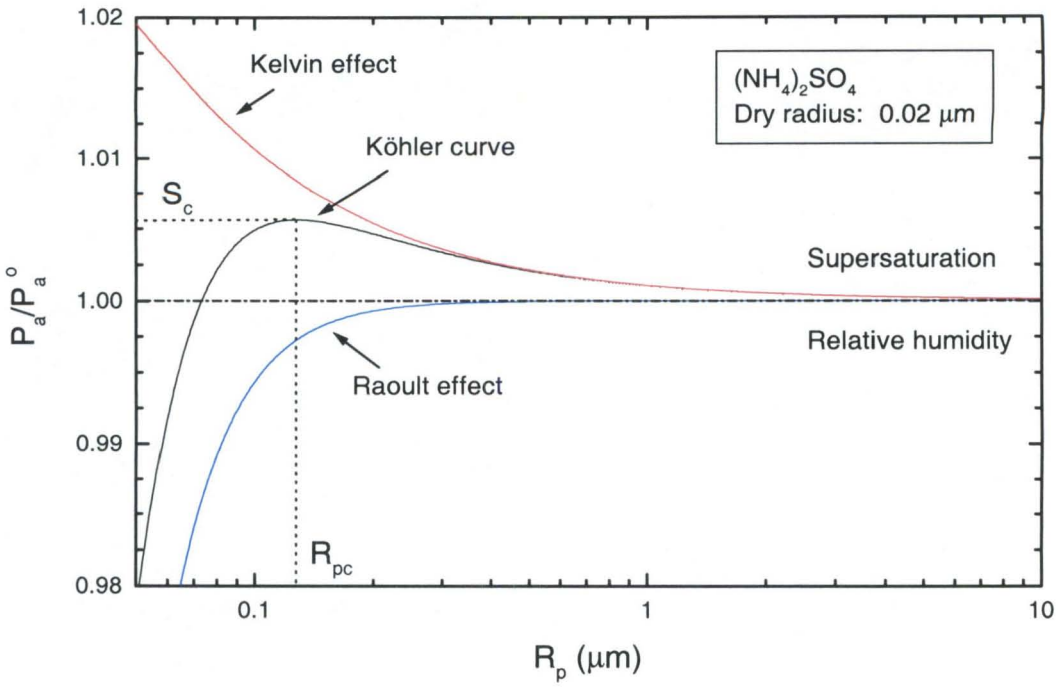

Figure 1.2. Köhler curve for an aqueous $(NH_4)_2SO_4$ droplet at 20°C and a dry radius of 0.02 μm.

Chapter 2

Calibration of thermal-gradient cloud condensation nucleus counter

Abstract

The importance of atmospheric aerosols in understanding global climate change has renewed interest in measurements of cloud condensation nuclei (CCN). To obtain CCN number concentrations, a thermal-gradient CCN chamber was developed. The instrument deduces the CCN concentration from measurements of laser light scattered by water droplets. A correlation between the absolute aerosol concentration and the number of droplets within the sample volume provides the instrument's calibration. Measuring the cross section of the laser beam is uncertain due to the blooming of the laser beam at its edges. Hence we rely on an empirical calibration of the CCN counter. The calibration was performed by sampling a monodisperse aerosol larger than the critical activation size at several supersaturations. The photographic method of calibrating the CCN counter is independent of supersaturation. An error analysis indicates that the measurement error ranges from 45% to 15% for CCN concentrations between 50 and 500 cm^{-3}. For CCN concentrations greater than 500 cm^{-3}, the measurement error is approximately ±15%.

2.1. Introduction

Cloud condensation nuclei (CCN) have a fundamental role in determining the global climate. The size, concentration, and affinity to water vapor of CCN directly influence the size and concentration of cloud droplets, which determines the radiative properties of clouds [*Twomey*, 1977]. Measurements of CCN concentrations can be determined by direct activation in a chamber of controlled supersaturations or deduced in a continuous flow chamber from particle size information. The static thermal-gradient chamber is perhaps the most widely used since its introduction by *Twomey* [1963]. A known supersaturation profile develops in the chamber between two wet parallel plates. Once activated, aerosol particles will grow and gravitationally settle out of the illuminated sample volume.

Two methods are commonly used to determine CCN concentrations in static thermal-gradient CCN instruments by comparing direct and indirect counting procedures of an ambient aerosol to obtain the empirical calibration for the CCN counter. The traditional approach of measuring the amount of light scattered in the chamber is appealing as it leads to simple automated method in determining CCN number concentrations. The calibration is obtained empirically and has been investigated by several groups [*Bartlett and Ayers*, 1981; *Lala and Jiusto*, 1977; *Oliveira and Vali*, 1995]. However, growth kinetics of activated aerosol depend on the particle size distribution, which may influence the interpretation of CCN number concentrations in various ambient conditions (see Appendix A).

Since CCN measurements were desired at a wide range of supersaturations and number concentrations, the photographic detection method was chosen. Directly counting particles through photographic methods has the advantage of being size independent. In the past, this method required sophisticated image processing to yield viable results; however, the advent of faster computers allows for efficient and automated processing of the sample images. This chapter describes a calibration procedure for determining CCN concentrations using a photographic method and digital image processing.

2.2. Experimental Methods

2.2.1. Static Thermal-gradient Chamber

CCN measurements were made using a static thermal-gradient diffusion instrument, which operated similarly to the chamber described by *Lala and Jiusto* [1977]. The CCN counter, shown in Figure 2.1, was fitted with a photodiode laser and digital camera to measure droplet concentrations. Activated CCN particles quickly grow to several micrometers in diameter and gravitationally settle out of the chamber. A 670 nm photodiode laser illuminates the activated droplets while the digital camera, normal to the laser beam, registers digital images every second during the supersaturation cycle. The CCN concentration at a particular supersaturation is calculated by imaging software, which automatically determines the number of activated droplets in each picture.

A CCN cycle begins with a 10 second flush at 3 liters min^{-1} to remove the previous sample and draw in air for a new sample. The instrument's inlet valve closes

and isolates the chamber, which allows the supersaturation profile to develop between two parallel horizontal wetted plates. The CCN counter operates at a desired supersaturation (e.g., between 0.15 and 1.5% supersaturation) by controlling the temperature difference between the wetted plates. Supersaturations between 0.3 and 1.0% were used for these calibrations. The diameter of the chamber is 100 mm and the top and bottom plates are separated by 10 mm. The dimensions allow for air in the chamber to reach an equilibrium supersaturation profile in several seconds [*Alofs and Carstens*, 1976]. Whatman filter papers on the top and bottom plates are kept wetted by an external capillary system. The top plate temperature is allowed to float with the ambient temperature and the bottom plate is cooled as necessary to achieve the prescribed supersaturation. Temperature fluctuations between plates during measurements are within 0.1 $^{\circ}$C, so the supersaturation is constant within $\pm 0.05\%$ S_c.

2.2.2. *Calibration System*

Calibration of the CCN counter is accomplished using the setup shown in Figure 2.2. Aerosol was created by a nebulizer using a 0.3 g liter^{-1} $(NH_4)_2SO_4$ solution and passed through a diffusion dryer and neutralizer before being introduced into the differential mobility analyzer (DMA) (TSI 3071). The flow rates through the DMA were controlled to 20 liters per minute (lpm) for sheath and excess air and 2.0 lpm for inlet and monodisperse aerosol flow. The voltage potential in the DMA was maintained constant throughout a sampling period to yield monodisperse aerosol. Particle diameters between 0.02 and 0.2 μm were chosen to observe various degrees of activation at different

supersaturations. The monodisperse aerosol passed through another neutralizer before entering an initially aerosol free vessel from which the particles were sampled. The vessel allows the aerosol concentrations to vary without changing the system parameters during the sampling. When the aerosol concentration within the vessel reaches a desired value, aerosol generation is stopped. The aerosol was simultaneously sampled from the vessel by the condensation particle counter (CPC) and CCN counters. To allow for continuous monitoring of particle concentrations during the batch sampling of the CCN counter, an aerosol free dilution air of 4 lpm was required so that outside aerosol did not contaminate the sample stream. The CCN chamber was purged 10 seconds before each sample to ensure a clean chamber. Number concentrations were recorded every 3 seconds using a CPC counter and ranged between zero and 10^4 particles cm^{-3}. The CPC counter has a detection efficiency near 100% for particles with diameters larger than 0.018 μm.

2.3. Calibration Procedure

2.3.1. Optical Alignment

Correctly setting the video camera's focal length is critical for accurate calibrations. Because of the narrow depth of field in which objects are focused, the width of the laser beam is constrained to less than 2 mm. A sharp focus of the illuminated volume is accomplished by focusing on an object (e.g., lettering of a box-shaped capacitor or electrical relay) on the near and far side of the laser beam. Before beginning

the calibrations, the focus is verified by examining the video camera's output of cloud droplets. Large droplets with dim centers indicate out-of-focus droplets.

The alignment of the video camera with the center of the CCN chamber is also important for accurate calibrations. The image area used for the measurements is placed in the center of the chamber between the upper and lower plates. Because the supersaturation profile is parabolic, only the center 2.5 mm of the chamber is used, where the maximum difference in supersaturation is less than 10% of the desired supersaturation. The dimensions of the video image are 560×38 pixels which corresponds to an image size of 30.9×2.5 mm. The width of the laser beam is ~ 1 mm, which yields a sample volume of ~ 0.077 cm^{-3}. The image must also be aligned such that it is parallel to the upper and lower plates in the chamber. Measuring the cross section of the laser beam is uncertain due to the blooming of the laser beam at its edges. Hence, we rely on an empirical calibration of the CCN counter.

2.3.2. Image Processing

The CCN concentration is determined by counting the number of water droplets in an illuminated portion of the laser beam using a video camera and personal computer (PC) video capture card. When the CCN cycle begins, digital images of the illuminated volume are captured and analyzed at 1 Hz for 10 seconds. Image processing software (e.g., Matlab) automatically determines the number of objects and the total number of pixels above a threshold value (i.e., 100, 150, and 200). Thresholding converts the grayscale image to a binary image, where pixels above and below the threshold are white

and black, respectively. The number of objects and pixel count are used to determine the particle concentration for a given image. Of the 11 images in the cycle, the image with the highest particle concentration establishes the CCN concentration.

2.3.3. Deriving CCN Number Concentrations

The empirical calibration of the CCN counter consists of comparing the number of objects and pixel count to CPC measurements. Figure 2.3 presents a typical calibration series and the evolution of the calibration parameters. Below a concentration of ~ 1700 cm^{-3}, the number of objects counted in the image exhibits a linear relationship with the aerosol concentration (Figure 2.4a). Above 1700 cm^{-3}, the expected object count diminishes due to coincidence errors. Droplet coincidence results from one or more droplets being partially obscured by other droplets and the cluster being counted as a single droplet. Hence the photographic calibration is performed for linear (e.g., < 1700 cm^{-3}) and non-linear (e.g., > 1700 cm^{-3}) regions individually.

Figure 2.4a illustrates the linear relationship between the number of objects counted by the imaging software, N_{obj}, and the aerosol concentration, N_{CPC}. The slope, m, of this relationship is

$$m = V^{-1} = \frac{\Delta N_{obj}}{\Delta N_{CPC}} \tag{2.1}$$

where V is the illuminated sample volume of the CCN chamber. For the calibration of this CCN counter, an illuminated volume of 0.076 cm^{-3} and 0.093 cm^{-3} was determined for threshold values of 200 and 100, respectively; these value agrees well with the value calculated by directly measuring the sample volume.

Therefore, the CCN concentration, N_{CCN}, is simply

$$N_{CCN} = \frac{N_{obj} + N_{coinc}}{V} \tag{2.2}$$

where N_{coinc} is the additional number of objects to adjust for coincidence errors. By correcting for coincidence errors, CCN concentrations up to 10^4 cm^{-3} can be determined (Figure 2.4b). N_{coinc} is calculated as

$$N_{coinc} = P_{tot} \cdot \phi - N_{obj} \tag{2.3}$$

where P_{tot} is the total number of pixels above the threshold intensity value and ϕ is the ratio of N_{obj} and P_{tot} in the linear regime (i.e., $N_{obj} < 120$; $N_{CPC} < 1700$ cm^{-3}). N_{coinc} is zero for $N_{obj} < 120$ (i.e., $P_{tot} < 1800$ pixels). At higher concentrations, however, N_{coinc} is determined by polynomial fit to P_{tot} (Figure 2.5) due to the non-linearity between N_{obj} and P_{tot}.

2.3.4. Error Analysis

The counting error can be significant at low supersaturations and low aerosol concentrations since there are few illuminated particles in the sample volume. An error analysis indicates that the means of the measurements are nearly normal and the standard deviation equals the square root of the total number of objects in the image (i.e., $\sigma = \sqrt{N_{obj} + N_{coinc}}$) for low concentrations. The relative error, *RE*, of the CCN measurements is

$$RE(\%) = \begin{cases} \dfrac{1}{\sqrt{N_{obj} + N_{coinc}}} & \text{for } \left(N_{obj} + N_{coinc}\right) \leq 44 \\ 0.15 & \text{for } (N_{obj} + N_{coinc}) > 44 \end{cases} \tag{2.4}$$

The measurement threshold is approximately 40 cm^{-3}, which corresponds to 3 droplets in the sample volume.

2.4. Conclusions

A CCN counter was calibrated using a digital camera and video capture card to directly determine the CCN concentration from image processing and the calibrated, illuminated volume. The photographic method of calibrating the CCN counter is independent of supersaturation. Random errors in measured CCN concentrations are calculated using Poisson counting statistics and range from 45% to 15% for CCN concentrations between 50 and 500 cm^{-3}. For CCN concentrations greater than 500 cm^{-3}, the overall measurement error is approximately ±15%.

2.5. References

Alofs, D.J., and J.C. Carstens, Numerical simulations of a widely used cloud nucleus counter, *J. Appl. Meteorol.*, *15*, 350, 1976.

Bartlett, B.M., and G.P. Ayers, Static diffusion cloud chamber, *J. Rech. Atmos.*, *15*, 231-233, 1981.

Lala, G.G., and J.E. Jiusto, An automatic light scattering CCN counter, *J. Appl. Meteor.*, *16* (4), 413-418, 1977.

Oliveira, J.C.P., and G. Vali, Calibration of a photoelectric cloud condensation nucleus chamber, *Atmos. Res.*, *38*, 237, 1995.

Twomey, S., Measurements of natural cloud nuclei, *J. Rech. Atmos.*, *1*, 101-105, 1963.

Twomey, S., The influence of pollution on the short-wave albedo of clouds, *J. Atmos. Sci.*, *34*, 1149-1152, 1977.

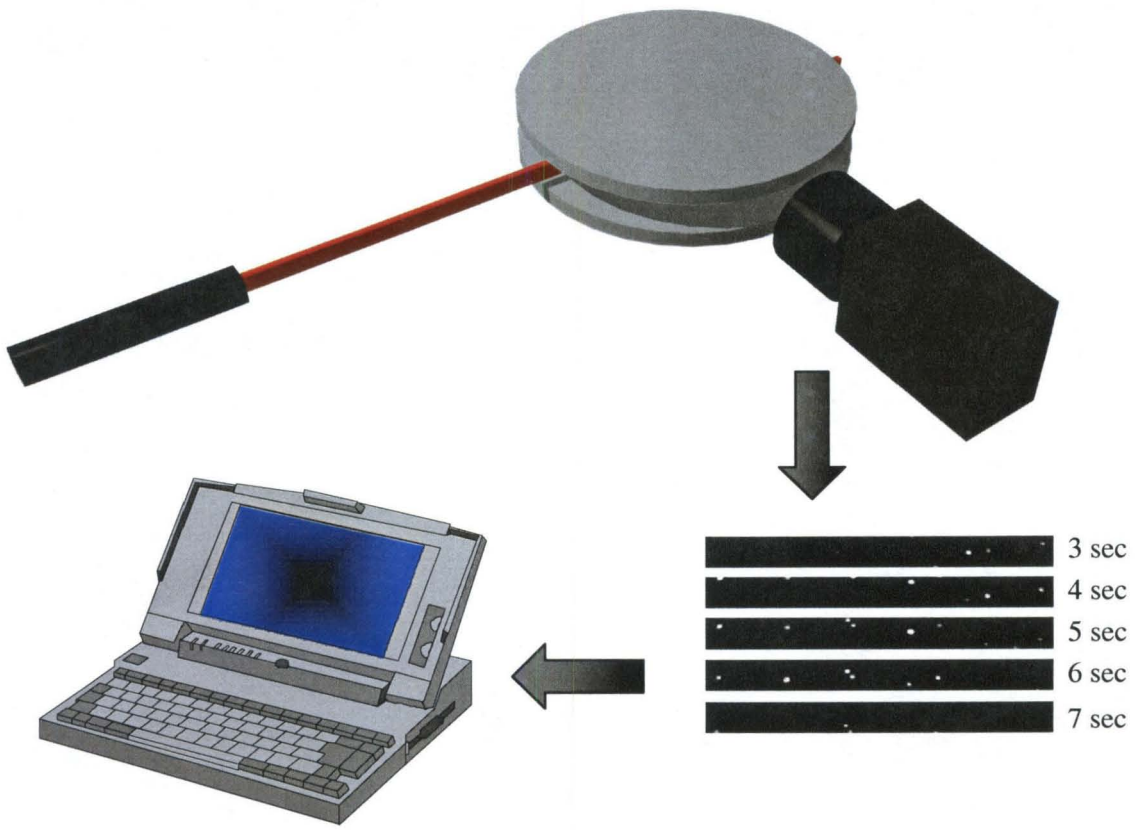

Figure 2.1. Operational schematic of the thermal-gradient CCN chamber. A laser beam illuminates droplets between two wetted plates. A digital camera records the images, which are processed by a computer.

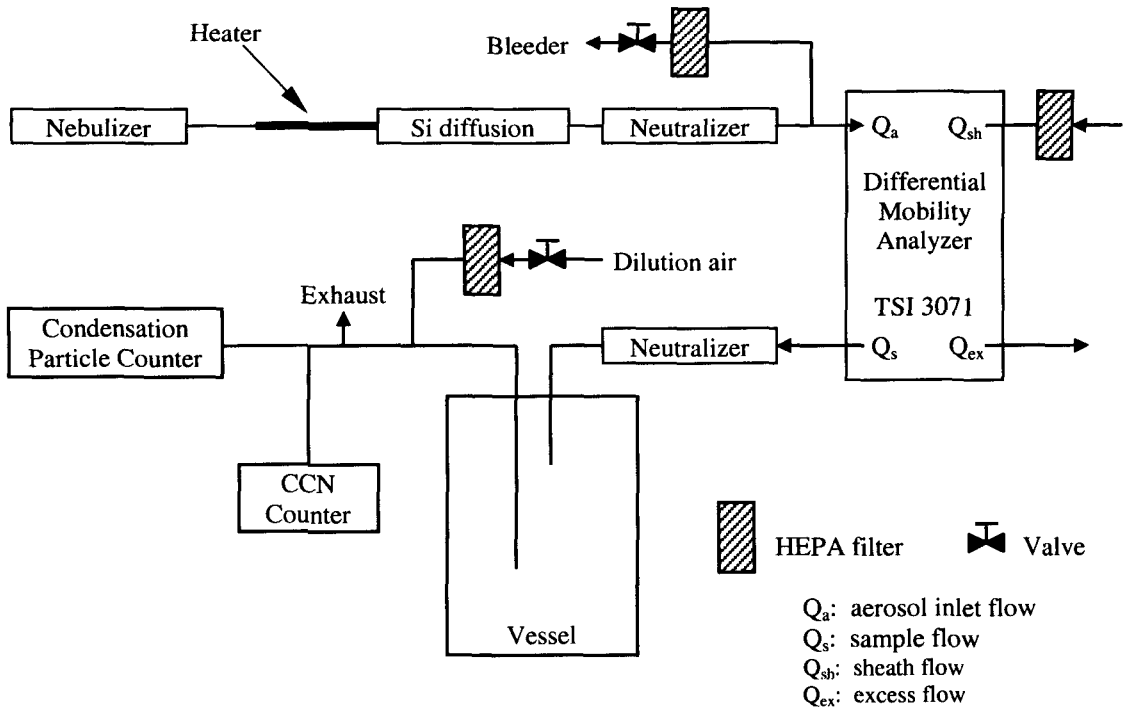

Figure 2.2. The experimental setup for the calibrations of the CCN chamber.

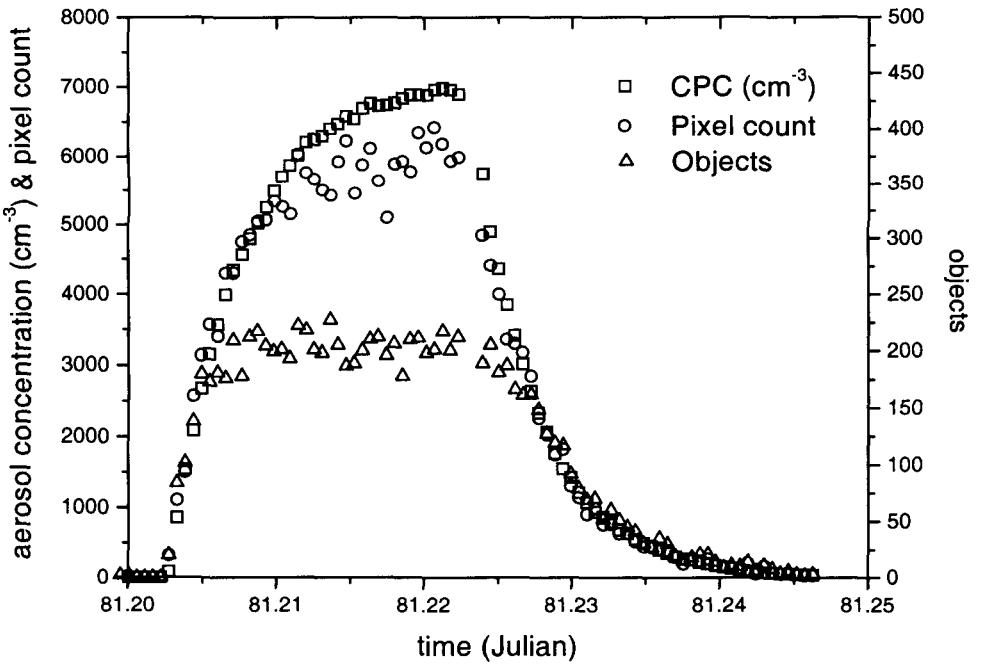

Figure 2.3. Time series of calibration experiment.

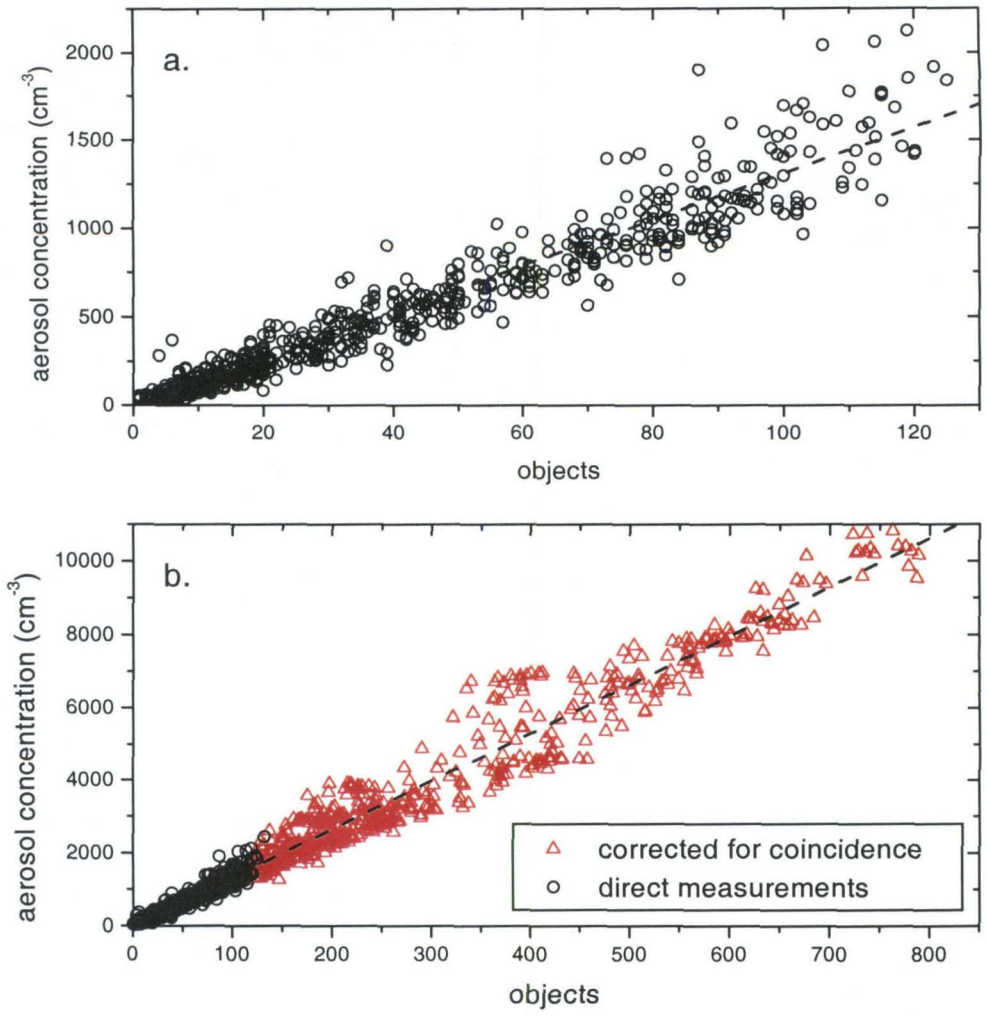

Figure 2.4. Relationship between number of illuminated objects in the sample volume and total aerosol concentration. a) No coincidence correction is necessary for aerosol concentrations < 1700 cm^{-3}. b) Coincidence corrections are applied at higher concentrations.

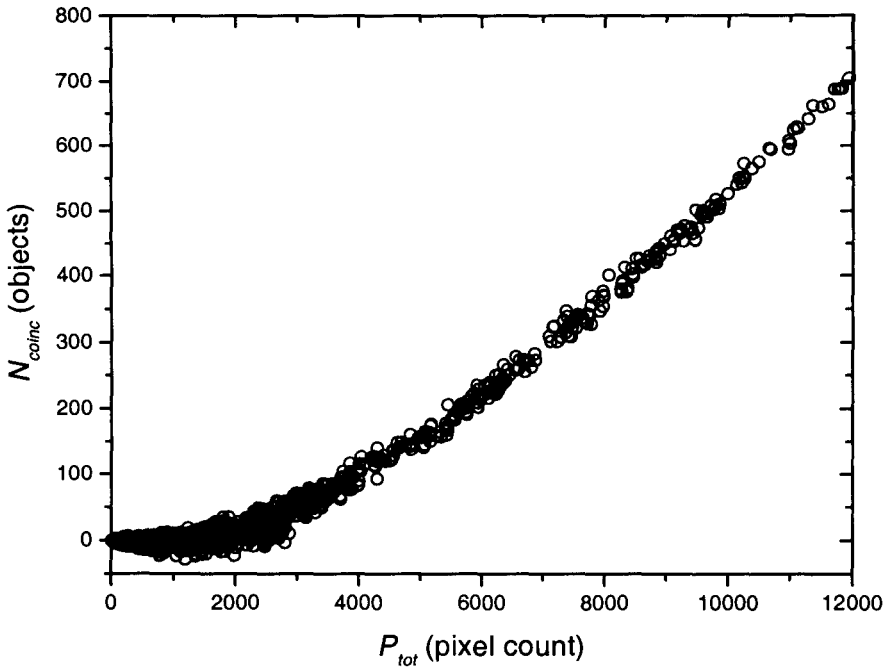

Figure 2.5. Relationship of coincidence correction to the number of pixels above the threshold value in the image.

Chapter 3

Cloud condensation nuclei in the Amazon Basin: "Marine" conditions over a continent?

Abstract

Cloud condensation nuclei (CCN) are linked to radiative forcing, precipitation, and cloud structure; yet, their role in tropical climates remains largely unknown. CCN concentrations (N_{CCN}) measured during the wet season in the Amazon Basin were surprisingly low (mean N_{CCN} at 1% supersaturation: 267 ± 132 cm^{-3}) and resembled concentrations more typical of marine locations than most continental sites. At low background CCN concentrations, cloud properties are more sensitive to an increase in N_{CCN}. Therefore, enhanced aerosol emissions due to human activity in the Amazon Basin may have a stronger impact on climate than emissions in other continental regions. In spite of the large organic fraction in the Amazonian aerosol, a detailed analysis of number distributions and size-dependent chemical composition indicates that sulfate plays an important role in CCN activity.

3.1. Introduction

Cloud condensation nuclei (CCN) are a subset of the atmospheric aerosol population, which undergo rapid growth into cloud droplets at a specified supersaturation. Although the importance of CCN for cloud properties and the subsequent effects on hydrology and climate has long been recognized, measurements of CCN in the tropics, where this vital subset of aerosol may exert its greatest impact, have largely been neglected. Aerosol/CCN/cloud interactions are understudied in the tropics relative to mid-latitudes, especially considering the importance of the tropics to global climate. Anthropogenically-induced changes in tropical regions could potentially lead to a number of climatically important processes in ways that are different from other regions [*Gedney and Valdes*, 2000]. Recent modeling studies suggest that increased CCN concentrations in the tropics change the altitude and mechanism of rain production [*Graf et al.*, 2000]. Because of large-scale atmospheric circulation in the tropics (i.e., International Tropical Convergence Zone and Hadley Circulation), the resulting dynamic effects propagate worldwide, including to higher latitudes, and have a much greater impact on global climate than previously thought [*Graf et al.*, 2000; *Oort and Yienger*, 1996].

Conventionally, a distinction has been made in CCN studies between "marine" and "continental" environments, which are characterized by low and high CCN concentrations (N_{CCN}), respectively [*Squires*, 1956]. Most "continental" measurements have been made in extratropical and usually moderately to heavily polluted regions [*Pruppacher and Klett*, 1997; Tables 9.1-9.4]. In spite of their vast extent, and their key

role in climate dynamics, no measurements are available from other humid tropical regions. Because of the large emissions of biogenic hydrocarbons and the intense photochemical activity in the tropics, some authors had predicted a high rate of organic aerosol formation in this region [*Andreae and Crutzen*, 1997]. A strong aerosol source could result in fairly high CCN concentrations in the remote wet tropics, even during the wet season, when frequent rain events provide a strong sink for CCN.

Here, we will discuss results of the first measurements of CCN in the Amazon Basin, and provide insight to their fundamental role in the tropical continental climate, as well as the chemical and physical properties that enable activation and subsequent growth into cloud droplets. We will use these results to examine the validity of the distinction between "marine" and "continental" CCN population types.

3.2. The LBA-CLAIRE Observations

The measurements were performed during the Cooperative LBA Airborne Regional Experiment (CLAIRE), a part of the Large Scale Biosphere-Atmosphere Experiment in Amazonia (LBA). Sampling occurred from March 28 to April 15, 1998, at a ground site (1°55.5' S, 59°24.8' W; 160 m above sea level) located 125 km northeast of Manaus, in the state of Amazonas, Brazil. Backward airmass trajectories indicate that our site was not adversely affected by anthropogenic sources, as surface air masses originated from the northeast to east; hence had traveled a thousand kilometers over the most remote regions of the Amazon rain forest for almost a week before being sampled.

CCN measurements between 0.15% and 1.5% supersaturation (S) were performed using a static thermal-gradient CCN chamber similar to the system described by *Lala and Jiusto* [1977]. Instead of the original light-scattering design, the CCN instrument was equipped with a photodiode laser and digital camera to directly determine the CCN concentration from image processing and the calibrated, illuminated volume (see Chapter 2). An error analysis indicates that for typical aerosol spectra, the overall measurement error is approximately ±10% at 1.5% S and ±30% at 0.15% S. Temperature fluctuations during measurements are usually within 0.1 °C, so the supersaturation is constant within ±0.05% S. Total aerosol concentrations (N_{CN}) were measured using a TSI 3010 Condensation Particle Counter.

Number concentrations of CCN and CN from the LBA-CLAIRE field experiment were low (mean N_{CCN} at 1% S: 267 ± 132 cm^{-3}; mean N_{CN}: 390 ± 250 cm^{-3}; Table 3.1). The observed variations of N_{CCN} and N_{CN} were primarily related to rainfall and temperature fluctuations (Plate1). The values of N_{CCN} and N_{CN} are in the range typically considered as "marine". Measurements in North America have also shown instances of low CCN concentrations in the absence of strong anthropogenic sources [*Hobbs et al.*, 1985; *Hudson and Frisbie*, 1991]. Since the transition from "marine" to "continental" is rapid [*Hudson*, 1991], local anthropogenic sources could restore "continental" CCN concentrations soon after precipitation/scavenging events. Such a "restoration" of "continental" CCN, however, is not observed at our site.

Furthermore, we find that the average CCN/CN ratio ($f_{CCN/CN}$) is strikingly high compared to most other "continental" measurements, and resembles much more what is conventionally regarded as "marine" values [*Pruppacher and Klett*, 1997; Tables 9.3-

9.4]. The high $f_{CCN/CN}$ ratio observed in Amazonia also implies that there are few particles present in the size range smaller than $CCN_{1.5}$ (at 1.5% *S*; i.e., diameter < 0.04 μm for Amazonian aerosols of mixed composition). Since these smaller particles are indicative of recent particle formation, our data also suggest a low rate of new particle formation, in contrast to what had been suggested by *Andreae and Crutzen* [1997]. Our measurements of low N_{CCN} are consistent with observations of warm-precipitating clouds in the Amazon Basin [*Mohr et al.*, 1999]. Observations in the field suggest that these cloud systems exhibit the less-developed convective structure that is normally associated with oceanic CCN distributions.

In spite of the "marine" character of our CCN spectra, the long distance of our site from the ocean (5-7 days of airmass travel) and the high frequency of rainfall under wet season conditions makes it unlikely that marine aerosol made a major contribution to the CCN population at our site. This is supported by our chemical measurements during CLAIRE, which show an average aerosol mass composition for the fine fraction (diameter < 1 μm) of approximately 15% sulfate, 5% other inorganic and 80% organic material. The fine-mode organic material probably originates from a combination of primary biogenic aerosol and the condensation of low and semi-volatile oxidation products of volatile organic carbon species (VOCs; i.e., terpenes) emitted from forest vegetation. Biogenic emissions from the forest vegetation also include a significant sulfur component [*Andreae et al.*, 1990], which could provide a source for the fine-mode sulfate.

A particle's critical supersaturation (S_c) implicitly contains all chemical and dry particle size information pertinent to cloud formation and can be calculated for a multi-

component aerosol by separating the mass distribution into soluble and insoluble components. The critical supersaturation is described by Köhler theory [*Köhler*, 1936; *Pruppacher and Klett*, 1997] and depends primarily on the dissolved solute mass and surface tension. The physical and chemical characteristics of the fine-mode aerosol determine N_{CCN} and the properties responsible for CCN activation. Number and mass distributions were measured using a Differential Mobility Particle Sizer (DMPS) (*J. Zhou et al.*, Sub-micrometer aerosol particle size distribution and hygroscopic growth measurements in the Amazonian rain forest during the wet season, submitted to *J. Geophys. Res.*, 2001) and a multiple-stage cascade impactor (MOUDI, MSP Corp.), respectively. The composition and mass data from the MOUDI impactor samples (e.g., particle-induced X-ray emission and gravimetric analysis) were transformed into a continuous distribution of composition versus size. These measurements allow an independent prediction of CCN activity by using Köhler theory to derive a distribution of S_c versus size. Although no direct measurements of sulfur speciation have been performed on our samples, a stoichiometric balance of anions and cations [*Gerab et al.*, 1998] indicates that fine-particulate sulfate has been partially neutralized by ammonium in nearly a 1:1 molar ratio. Therefore, the model divides the aerosol mass into soluble inorganic (NH_4HSO_4), and insoluble (inorganic and organic) components. The resulting relationship between S_c and particle size is combined with the number distribution to yield an independent prediction of N_{CCN}. Furthermore, $f_{CCN/CN}$ can be determined by the ratio of the calculated N_{CCN} to N_{CN} and compared to measured values. *Novakov and Penner* [1993] performed a similar calculation of CCN activity that was based on an

externally mixed aerosol; yet, they also noted that internally mixed estimations of CCN concentrations, as we have done here, were within 10%.

The resulting modeled CCN spectra, from the number and mass distribution closure, are shown in Figure 3.2. The CCN spectrum based upon a simple model of sulfate and insoluble constituents agrees well with the measured CCN spectrum (Table 3.1; solid circles in Figure 3.2). It must be noted, however, that this model does not represent a unique solution; this issue will be explored in detail in a future paper (*G. Roberts et al.*, Sensitivity of CCN spectra on chemical and physical properties of aerosol, submitted to *J. Geophys. Res.*, 2001; Chapter 4).

Organic aerosol components affect CCN activity both by providing soluble material and by changing the surface tension of the droplet solution [*Facchini et al.*, 1999]. We applied the relationship between organic carbon concentration and surface tension, used by *Facchini et al.* [1999], to estimate potential influences of surfactants on the CCN spectra in the Amazon Basin. Comparison of our model calculation with the measurements (Figure 3.2) suggests that a 15% decrease in surface tension at 10^{-2} molarity of dissolved organic carbon is probably the upper limit of the surface tension effects consistent with our results from the Amazon Basin.

3.3. Significance of the Results

Our results show that low CCN concentrations and high CCN/CN ratios over the unpolluted Amazon Basin resemble conditions previously reported from marine environments, and that they are different from what has been previously thought of as

"continental" conditions. This calls into question the conventional distinction between these regimes, and suggests that a more relevant distinction would be between pristine and polluted conditions. Furthermore, it may be necessary to introduce subcategories, such as tropical, temperate, arctic, etc., as climatic conditions and natural aerosol sources of the Amazon Basin do not apply to other regions. It is remarkable that similar CCN and CN concentrations prevail in marine and continental regions, in spite of the different aerosol production mechanisms and particle compositions. A positive feedback cycle has been proposed for the marine atmosphere where drizzle removes CCN from the boundary layer and maintains the low CCN concentrations favorable for precipitation [*Albrecht*, 1989]; a similar feedback cycle may also apply to the rain forest environment. While drizzle removes CCN without significantly effecting smaller particles, atmospheric lifetimes of small particles (i.e., diameter < 0.06 μm) range from hours to a couple of days due to coagulation, scavenging of interstitial aerosol and growth by condensation [*Hoppel et al.*, 1990]. Hence interstitial aerosol grow to become CCN, and cloud processing/scavenging provide a sink to maintain a quasi-steady state number distribution [*Kaufman and Tanré*, 1994].

Studies have shown that modification of cloud properties, such as cloud thickness [*Pincus and Baker*, 1994], albedo, cloud fraction and lifetime [*Albrecht*, 1989], is most sensitive at low initial N_{CCN}. Because of the large thickness typical of convective clouds over the humid tropics, substantial modification of cloud albedo due to increased CCN is not expected. However, because of the low natural CCN abundance in Amazonia, climatic effects related to the impact of CCN on rainfall production could have a greater impact here than in other continental regimes [*Graf et al.*, 2000; *Twomey*, 1991]. CCN

measurements have shown that biomass burning smoke aerosol dramatically increases CCN concentrations [*Novakov and Corrigan*, 1996]. This should increase colloidal stability and cloud lifetime, resulting in the well-developed, non-precipitating clouds observed during the burning season, with droplet radii below the threshold required for warm precipitation [*Kaufman and Fraser*, 1997; *Reid et al.*, 1999]. The influence of smoke on rain formation was shown more directly by the analysis of data from the Tropical Rainfall Measuring Mission (TRMM) taken near Kalimantan, where a distinct difference in cloud structure and radar reflectance was seen between clouds influenced by biomass burning and those in cleaner areas. Although Rosenfeld did not perform CCN measurements, it can be inferred from the known CCN-activity of biomass smoke that the smoke-laden air also contained higher CCN concentrations. *Rosenfeld* [1999] showed that the clouds affected by smoke had significantly smaller droplet size and were less likely to precipitate than clouds in adjacent unpolluted areas.

The response of cloud droplet concentration and radius to changes in N_{CCN} is the basis for the modification of precipitation, cloud fraction and indirect forcing. The interaction of these factors controls the heat flux into the rain forest, which is, in return, the primary driver of convective cloud formation. Human activity, such as fossil fuel and biomass burning, modifies physical and chemical properties of the aerosol population – components that dictate CCN activity – and could lead to imbalances in the meteorological cycle within the Amazon Basin and translate to changes in global climate as well.

3.4. References

Albrecht, B.A., Aerosols, cloud microphysics, and fractional cloudiness, *Science, 245*, 1227-1230, 1989.

Andreae, M.O., H. Berresheim, H. Bingemer, D.J. Jacob, B.L. Lewis, S.-M. Li, and R.W. Talbot, The atmospheric sulfur cycle over the Amazon Basin, 2, Wet season, *J. Geophys. Res.*, *95*, 16,813-16,824, 1990.

Andreae, M.O., and P.J. Crutzen, Atmospheric aerosols: Biogeochemical sources and role in atmospheric chemistry, *Science*, *276* (5315), 1052-1056, 1997.

Facchini, M.C., M. Mircea, S. Fuzzi, and R.J. Charlson, Cloud albedo enhancement by surface-active organic solutes in growing droplets, *Nature*, *401* (6750), 257-259, 1999.

Gedney, N., and P. Valdes, The effect of Amazonian deforestation on the northern hemisphere circulation and climate, *Geophys. Res. Lett.*, *27* (19), 3053-3056, 2000.

Gerab, F., P. Artaxo, R. Gillet, and G. Ayers, PIXE, PIGE and ion chromatography of aerosol particles from northeast Amazon Basin, *Nucl. Instrum. Methods Phys. Res. B.*, *138*, 955-960, 1998.

Graf, H.-F., F.J. Nober, and D. Rosenfeld, The possible effect of biomass burning on local precipitation and global climate, in *13th International Conference on Clouds and Precipitation*, pp. 882-885, Reno, Nevada USA, 2000.

Hobbs, P.V., D.A. Bowdle, and L.F. Radke, Particles in the lower troposphere over the high plains of the United States, 2, Cloud condensation nuclei, *J. Climate and Appl. Meteor.*, *24*, 1358-1369, 1985.

Hoppel, W.A., J.W. Fitzgerald, G.M. Frick, R.E. Larson, and E.J. Mack, Aerosol size distributions and optical properties found in the marine boundary layer over the Atlantic Ocean, *J. Geophys. Res.*, *95*, 3659-3686, 1990.

Hudson, J.G., Observations of anthropogenic cloud condensation nuclei, *Atmos. Environ.*, *25*, 2449-2455, 1991.

Hudson, J.G., and P.R. Frisbie, Surface cloud condensation nuclei and condensation nuclei measurements at Reno, Nevada, *Atmos. Environ.*, *25*, 2285-2299, 1991.

Kaufman, Y.J., and R.S. Fraser, The effect of smoke particles on clouds and climate forcing, *Science*, *277* (5332), 1636-1639, 1997.

Kaufman, Y.J., and D. Tanré, Effect of variations in supersaturation on the formation of cloud condensation nuclei, *Nature*, *369*, 45-48, 1994.

Köhler, H., The nucleus in and the growth of hygroscopic droplets, *Trans. Faraday Soc.*, *32*, 1152-1161, 1936.

Lala, G.G., and J.E. Jiusto, An automatic light scattering CCN counter, *J. Appl. Meteor.*, *16* (4), 413-418, 1977.

Mohr, K., J. Famiglietti, and E. Zipser, The contribution to tropical rainfall with respect to convective system type, size, and intensity estimated from the 85-GHz ice-scattering signature, *J. Appl. Meteorol.*, *38*, 596-606, 1999.

Novakov, T., and C.E. Corrigan, Cloud condensation nucleus activity of the organic component of biomass smoke particles, *Geophys. Res. Lett.*, *23* (16), 2141-2144, 1996.

Novakov, T., and J.E. Penner, Large contribution of organic aerosols to cloud-condensation-nuclei concentrations, *Nature*, *365*, 823-826, 1993.

Oort, A., and J. Yienger, Observed interannual variability in the Hadley circulation and its connection to ENSO, *J. Cli.*, *9*, 2751-2767, 1996.

Pincus, R., and M.B. Baker, Effect of precipitation on the albedo susceptibility of clouds in the marine boundary layer, *Nature*, *372*, 250-252, 1994.

Pruppacher, H.R., and J.D. Klett, *Microphysics of Clouds and Precipitation*, Kluwer Academic Publishers, Boston, 1997.

Reid, J.S., P.V. Hobbs, A.L. Rangno, and D.A. Hegg, Relationships between cloud droplet effective radius, liquid water content, and droplet concentration for warm clouds in Brazil embedded in biomass smoke, *J. Geophys. Res.*, *104* (D6), 6145-6153, 1999.

Rosenfeld, D., TRMM observed first direct evidence of smoke from forest fires inhibiting rainfall, *Geophys. Res. Lett.*, *26*, 3105-3108, 1999.

Squires, P., The microstructure of cumuli in maritime and continental air, *Tellus*, *8*, 443-444, 1956.

Twomey, S., Aerosols, clouds, and radiation, *Atmos. Environ.*, *25* (11), 2435-2442, 1991.

Table 3.1. Average measured CCN spectrum during LBA-CLAIRE .

S[a], %	$N_{CCN\ or\ CN}$, cm^{-3}
0.15	33 ± 24
0.30	101 ± 60
0.60	182 ± 92
1.00	267 ± 132
1.50	320 ± 164
CN[b]	390 ± 250

[a] S is the supersaturation of the CCN measurements.

[b] The average N_{CN} shown in the table is for corresponding CCN measurements. The average N_{CN} from Figure 3.1 (over the CLAIRE experiment) is 460 ± 320 cm^{-3}.

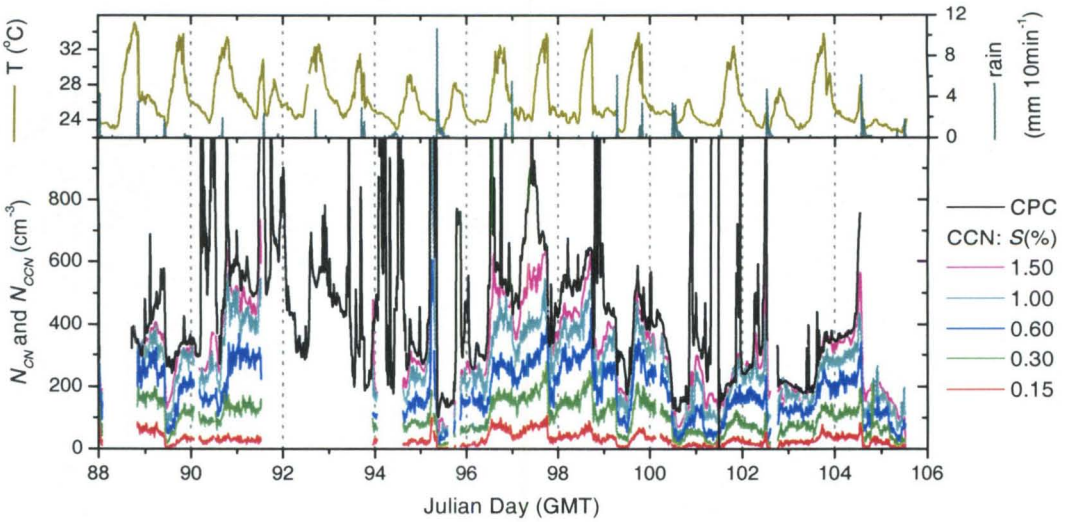

Figure 3.1. Time series of N_{CCN} and N_{CN}. Ambient temperature and rainfall are shown in the upper graph.

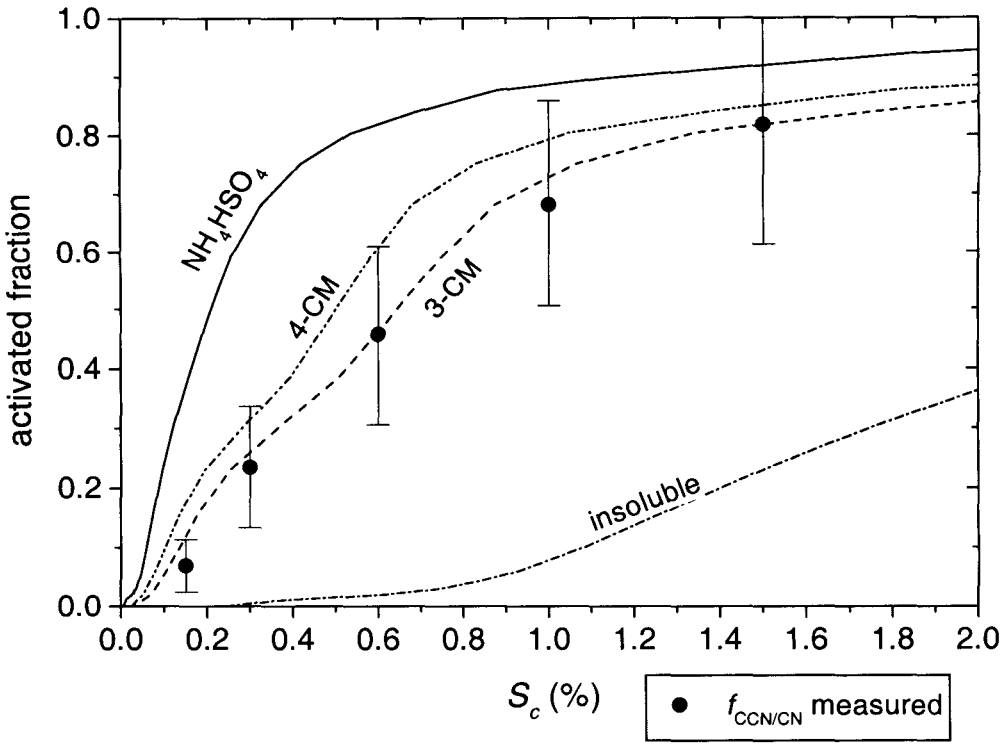

Figure 3.2. Fraction of aerosol expected to activate as CCN. The three-component (3-CM) example divides the aerosol mass into soluble inorganic (NH_4HSO_4) and insoluble (inorganic and organic) components. The four-component model (4-CM) introduces the effect of 0.01 M dissolved organic carbon and the reduction of surface tension by 15%. Examples of NH_4HSO_4 and insoluble aerosol illustrate the limits of CCN activity based on measured number distributions.

Chapter 4

Sensitivity of CCN spectra on chemical and physical properties of aerosol: A case study from the Amazon Basin

Abstract

Organic material, about half of which is water-soluble, constitutes nearly 80% of the wet-season aerosol mass in the Amazon Basin, while soluble inorganic salts (predominantly ammonium bisulfate) represent about 15%. A detailed analysis of number distributions and the size-dependent chemical composition of the aerosol indicates that, in principle, the sulfate fraction could account for most of the cloud condensation nuclei (CCN) activity. Uncertainty about the chemical speciation of the water-soluble organic component precludes a rigorous analysis of its contribution to nucleation activity. Within reasonable assumptions we can, however, predict a similar contribution of the organic component to CCN activity as that from sulfate. Because of the nonlinear dependence of droplet nucleation behavior on solute amount, the nucleation activity cannot be attributed uniquely to the inorganic or organic fractions. The role of water-soluble organic compounds as surfactants, however, may be significant (especially in the case of biomass-burning aerosol) and more field measurements are needed to quantify their effects on the surface tension of ambient aerosols. The parametric dependence of the CCN spectra on the physical and chemical properties of the aerosol show that the number distribution, soluble content of the aerosol, and surface tension effects all play an important role in determining CCN spectra.

4.1. Introduction

The role of organic material on the nucleating activity of atmospheric aerosols has received much attention in recent years [*Cruz and Pandis*, 1998; *Facchini et al.*, 1999; *Liu et al.*, 1996; *Rivera-Carpio et al.*, 1996]. Measurements of fine aerosol composition have indicated that water-soluble organic species can comprise more than half of the total aerosol mass [*Saxena and Hildemann*, 1996]. Particles smaller than 0.5 μm dry diameter (d_p) account for most of the number concentration; therefore, identifying the physical and chemical properties of aerosol in the CCN-size range (i.e., $0.05 < d_p < 0.5$ μm) is important for characterizing CCN spectra.

Novakov and Penner [1993] considered their calculations of CCN concentration (N_{CCN}) based on an externally mixed aerosol; yet, they also noted that internally mixed estimations were within 10%. Although the derivation of N_{CCN} does not critically depend on the assumed mixed state, atmospheric processes do effect the aerosol composition. As an air parcel is likely to be processed through 10 or more non-precipitating cloud cycles [*Hoppel et al.*, 1990], cloud droplet growth and evaporation modifies the CCN spectrum. A statistical model of CCN growth into cloud droplets suggests that even a low natural variation of supersaturations in cloud processes ($0.3 \pm 0.2\%$ S_v) maintains quasi-steady state aerosol number distributions [*Kaufman and Tanré*, 1994] that are similar to those observed over the ocean and Amazon rain forest [*Zhou et al.*, 2001].

Earlier measurements of mass distributions in the Amazon Basin show that wet-season aerosols in this size range are primarily composed of sulfates and organics [*Artaxo and Hansson*, 1995; *Talbot et al.*, 1990; *Wouters et al.*, 1993]. A large organic

component and some sulfate is an inherent part of individual particles, $d_p < 0.5$ μm [*Wouters et al.*, 1993], which supports the observations of significant cloud processing and organic deposition. Biogenic emissions from rain forest vegetation provide a potentially strong source for aerosol formation and growth. The sulfate fraction, which constitutes 5 to 25% of the mass loading in the fine size fraction of Amazonian aerosols, may originate from the biogenic emissions of reduced sulfur compounds, such as hydrogen sulfide (H_2S) and dimethyl sulfide (DMS) from forest vegetation [*Andreae and Andreae*, 1988; *Andreae et al.*, 1990a]. The fine-mode organic material, which constitutes up to 80% of the aerosol mass [*Artaxo and Hansson*, 1995; *Wouters et al.*, 1993], probably originates from a combination of primary biogenic aerosol and biogenic emissions of volatile organic carbon species (VOCs; i.e., monoterpenes) emitted from forest vegetation. The oxidation products of VOCs yield low and semi-volatile compounds that can partition to the aerosol phase. Hence, there may exist a "cooperative" relationship between organics and sulfates for aerosol formation, which ultimately influences cloud properties in the Amazon Basin. The sulfate fraction influences CCN properties through addition of soluble material while the organic fraction enhances CCN activity by contributing soluble material and/or lowering the surface tension of a deliquesced aerosol [*Facchini et al.*, 1999; *Shulman et al.*, 1996].

Here, we will discuss results of CCN measurements, in light of the chemical and physical properties of wet-season rain forest aerosol that enable activation and subsequent growth into cloud droplets. Variables that describe the size distribution, soluble content, and surface tension are studied independently to explore the parametric dependence of CCN spectra (see Appendix 4.B for a description of the variables).

Identifying the principal chemical and physical components that define wet-season CCN spectra in the Amazon Basin provides a reference to assess the potential influences of anthropogenic activity, such as biomass burning, on the rain forest climate.

4.2. Experimental Method

The measurements were performed during the Cooperative LBA Airborne Regional Experiment 1998 (CLAIRE-98), a part of the Large Scale Biosphere-Atmosphere Experiment in Amazônia (LBA). Sampling occurred from March 28 to April 15, 1998, at a ground site (1° 55.5' S, 59° 24.8' W; 160 m above sea level) located 125 km northeast of Manaus, in the state of Amazonas, Brazil. Isentropic backward airmass trajectories indicate that our site was not affected by anthropogenic sources. Surface air masses originated from the northeast to east; hence had traveled a thousand kilometers over the most remote regions of the Amazon rain forest for almost a week before being sampled. A total of 185 mm of rain fell during the 19 days of the experiment, which is about normal for the month of April.

A static thermal-gradient chamber measured N_{CCN} at supersaturations (S_v) between 0.15 and 1.5% S_v. Additional aerosol instrumentation, which identified physical and chemical properties and permitted an independent assessment of CCN activity, included a multi-stage cascade impactor to measure mass distribution ($n_M(D_p)$), a differential mobility particle sizer to measure number distributions ($n_N(d_p)$), and a condensation particle counter to measure total aerosol concentrations (N). Sampling for each instrument took place 6 m above the ground via individual inlets that were extended

2 m above the roof of the laboratory. The details of each instrument are discussed in the following sections.

4.2.1. Static Thermal-gradient Chamber

CCN measurements were made using a static thermal-gradient diffusion instrument, which operated similarly to the chamber described by *Lala and Jiusto* [1977]. Instead of the original light scattering design, our CCN counter was fitted with a photodiode laser and digital camera to measure droplet concentrations (see Chapter 2). Activated CCN particles quickly grow to several micrometers in diameter and gravitationally settle out of the chamber. A 670 nm photodiode laser illuminates the activated droplets while the digital camera, normal to the laser beam, registers images every second during the supersaturation cycle. The CCN concentration at a particular supersaturation is determined during post processing. Imaging software (e.g., Matlab) automatically determines the number of activated CCN in each picture. The CCN concentration is calculated based on the picture with the highest number of particles and the calibrated illuminated volume. The calibration procedure involved generating a quasi-monodisperse aerosol of a known concentration and counting the number of activated droplets in the digital image. An error analysis indicates that for typical aerosol spectra, the overall measurement error is approximately ±10% at 1.5% S_v and ±30% at 0.15% S_v. These measured analytical errors agree well with theoretical estimates by *Nenes et al.* [2001].

CCN number concentrations were determined every 25 seconds at a supersaturation between 0.15 and 1.5% S_v (i.e., 0.15, 0.30, 0.60, 1.0 and 1.5% S_v). CCN spectra were measured every six to seven minutes. A CCN cycle begins with a seven-second flush at 3 liters min^{-1} to remove the previous sample and draw in air for a new sample. The instrument's inlet valve closes and isolates the chamber, which allows the supersaturation profile to develop between two horizontal parallel wetted plates. The CCN counter operates at a desired supersaturation by controlling the temperature difference between the wetted plates. The diameter of the chamber is 100 mm and the top and bottom plates are separated by 10 mm. The dimensions allow for air in the chamber to reach an equilibrium supersaturation profile in several seconds. Whatman filter papers on the top and bottom plates are kept wetted by an external capillary system. The top plate temperature is allowed to float with the ambient temperature, which ranged from 20 to 35 °C, and the bottom plate is cooled as necessary to achieve the prescribed supersaturation. Temperature fluctuations during measurements are usually within 0.1 °C, so the supersaturation is constant within ±0.05% S_c.

4.2.2. Multi-stage Cascade Impactor

Mass distributions were resolved with a rotating micro-orifice uniform deposit cascade impactor (MOUDI, MSP Corp.) with 50% cutoff aerodynamic diameters (D_{50}) of 0.093, 0.175, 0.330, 0.560, 1.00, 1.80 and 3.20 μm. The MOUDI impactor uses circular jets on seven impactor stages, plus an eighth inlet stage to remove particles larger than 18 μm. Aerosols were collected on 47 mm diameter Teflon substrates and a quartz-fiber

after-filter, which collects particles smaller than 0.093 μm; the inlet stage and quartz fiber after-filters were not analyzed. The MOUDI impactor operated for 48 or 72 hours at an airflow rate of 25 to 30 liters min^{-1} to collect sufficient particulate mass for analysis. The flow rate was regulated using differential pressure gauges and the volume was measured using a calibrated dry gas meter. The gravimetric analysis was done by weighing each filter before and after sampling with a microbalance (1 μg sensitivity) in a room with stabilized temperature (20 °C) and relative humidity (40%). The filters were pre-equilibrated in this room for at least 24 hours.

Elemental concentrations on each stage of the impactor were analyzed for up to 26 elements using particle-induced X-ray emission analysis (PIXE) at the University of São Paulo, Brazil. Precise experimental details of the PIXE analysis are given elsewhere [*Artaxo and Orsini*, 1987; *Johansson and Campbell*, 1988]. The following 21 elements were detected in the samples: Mg, Al, Si, P, S, Cl, K, Ca, Sc, Ti, V, Cr, Mn, Fe, Ni, Cu, Zn, Br, Sr, Zr, Pb. The detection limit was typically 10 ng m^{-3} for elements with $Z \leq 20$, and around 1 ng m^{-3} for $21 \leq Z < 40$. The precision of the PIXE analysis varied from a few percent for the major elements to about 30% for elements with concentrations near the analytical detection limit.

4.2.3. Differential Mobility Analysis

The DMPS (Differential Mobility Particle Sizer) has been used to measure the number distribution of aerosol particles with diameters from 0.003 to 0.85 μm [*Zhou et al.*, 2001]. The diameter of the DMPS measurements was accurately determined to

within 2%. An ultrafine differential mobility analyzer (UDMA) and a differential mobility analyzer (DMA) covered particle sizes from 0.003 to 0.022 μm and 0.022 to 0.85 μm, respectively. The integration of the measured number distribution yields the total aerosol concentration between 0.003 and 0.85 μm. The sheath flow was treated with dryers and the particle size was measured in the dry condition. Individual condensation particle counters (CPC) were used for particle detection after each DMA: ultrafine CPC Model 3025 and CPC Model 7610 (TSI Incorporated, Shoreview, Minnesota, USA). Both CPCs were calibrated for counting efficiency as a function of the particle size. During the measurements, the two DMAs operated in a stepwise scanning mode starting from 0.022 μm diameter, and stepping downwards or upwards, respectively. Equal logarithmic diameter steps were used in the scans for a total of 36 mobility channels. A single scan over the whole size range took 15 minutes.

The hygroscopic properties of aerosol particles were measured with a H-TDMA (Hygroscopic Tandem Differential Mobility Analyzer) [*Zhou et al.*, 2001]. The H-TDMA determines, *in-situ*, the hygroscopic diameter growth of individual aerosol particles when taken from a dry state (RH < 10%) to a controlled humidified state. The H-TDMA consists mainly of three parts: (1) a DMA which selects a narrow, quasi-monodisperse size range of the atmospheric aerosol at low RH; (2) humidifiers which condition the air to a well defined RH; (3) and a second DMA which determines the change in diameter caused by the humidification. During the CLAIRE-98 campaign, the H-TDMA measurements were performed for six particle dry diameters (0.035, 0.050, 0.073, 0.109, 0.166 and 0.264 μm) at 90% RH and three dry diameters (0.050, 0.073 and 0.166 μm) at 70% RH. Since CCN activity is estimated from initial dry composition,

these growth factors are used to correct the aerodynamic diameters from the MOUDI impactor to equivalent dry aerosol size (Section 4.3.1.1).

4.2.4. Condensation Particle Counter

An additional CPC Model 3010 (CPC_{3010}; TSI Incorporated, Shoreview, Minnesota, USA) measured total ambient aerosol concentrations (N_{3010}) every 30 seconds and was directly compared to the CCN concentrations to estimate the efficiency of aerosol to serve as CCN. The ratio of the total aerosol concentration (e.g., N_{3010}) to N_{CCN} determines $f_{CCN/CN}$. The CPC_{3010} has a 50% detection efficiency at 0.01 μm and varies from 0 to nearly 100% particle detection from 0.006 to 0.018 μm, respectively. This efficiency curve will be applied in Section 4.3 to compare the measurements of the CPC_{3010} to the aerosol concentration derived from the measured number distribution (N_{DMPS}).

4.3. Results

CCN number concentrations from the LBA-CLAIRE-98 field experiment were low and resulted in a spectrum resembling those typical of oceanic environments [*Roberts et al.*, 2001] (see Chapter 3). Table 4.1 summarizes the mean CCN spectra for the four MOUDI impactor sampling periods. The fractional contribution of N_{CCN} at each supersaturation was normalized to $N_{1.5}$ (at 1.5% S_v) for each supersaturation cycle (e.g., for a given cycle, $N_{0.3}$ was divided by $N_{1.5}$) to exclude bias from variable absolute

concentrations in investigating the shape of CCN spectra. Hence, the standard deviation of $f_{CCN/CN}$, in Table 4.1, presents the variability of the mean CCN spectrum and not the variability of N_{CCN}. $N_{1.0}$ and the relative time fraction of continuous CCN measurements to the MOUDI sampling period are also reported in Table 4.1.

Total aerosol concentrations were typically between 300 and 700 cm^{-3} with a mean value of 460 cm^{-3}. Consequently, we find that the average CCN/CN ratio ($f_{CCN/CN}$) also is strikingly high compared to other "continental" measurements, and resembles much more what is conventionally regarded as "marine" values [*Pruppacher and Klett*, 1997]. The high $f_{CCN/CN}$ ratio observed in Amazonia also implies that there are few particles present in the size range below that typical of CCN (i.e., $d_p < 0.05$ μm (at 0.3% S) to 0.10 μm (at 1.0% S) for Amazonian aerosols of mixed composition). The low abundance of aerosol smaller than $d_p = 0.05$ μm has also been confirmed by *Zhou et al.* [2001]. Since small interstitial aerosol are representative of recent particle formation, our data also suggest a low rate of new particle formation.

4.3.1. Physical and Chemical Properties of CCN

A particle's critical supersaturation (S_c) implicitly contains all chemical and dry particle size information and can be calculated for a multi-component aerosol by separating the dry mass distribution ($n_M(d_p)$) into soluble (i.e., sulfate and/or organic) and insoluble components. The equilibrium saturation ratio (S_v^{eq}) of a droplet of a given diameter (D_p) and temperature (T) is described by a modified Köhler equation as

$$S_v^{eq} = \exp\left(\frac{4\sigma' M_w}{kT\rho_w D_p} - \frac{\Phi M_w}{\frac{\pi\rho' D_p^3}{6} - \sum_i m_i} \left[\sum_i \frac{\nu_i m_i}{M_i} \right] \right) \tag{4.1}$$

where k is the Boltzmann constant, σ' is the surface tension of the solution, M_w and M_i are the respective molecular weights of water and solute, m_i is the dissolved solute mass, ρ_w and ρ' are the densities of water and aqueous solution, respectively, ν_i is the number of ions into which a solute molecule dissociates (van't Hoff factor), and Φ is the osmotic coefficient of the aqueous solution. The maximum S_v^{eq} of the resulting Köhler curve defines S_c and occurs at the critical droplet diameter (D_{pc}) [*Seinfeld and Pandis*, 1998]. The Kelvin effect (i.e., the surface tension term) accounts for enhanced vapor pressure due to droplet curvature. The Raoult effect (i.e., solute mass term) depresses the vapor pressure due to dissolved mass. Supersaturation ratios are expressed in percent (e.g., S_v (%) = (S_v (ratio) – 1) × 100%) throughout this text.

The following sections apply a closure technique to estimate the CCN activity of rain forest aerosol based on measured $n_M(D_p)$ and $n_N(d_p)$. The independent calculations are compared to the measured results in Section 4.3.2.

4.3.1.1. Mass distributions

Four MOUDI-impactor samples (e.g., MD_4, MD_6, MD_9 and MD_10), which coincided with CCN measurements, were used for the closure analysis described here. PIXE analysis detected 21 elements and, after converting element concentrations to oxide

form, accounted for only 10% of the fine aerosol mass. Table 4.2 presents the size fractionated chemical composition from PIXE analysis for the ensemble average of the four MOUDI impactor samples. Sulfur was the single most abundant element in the fine fraction. Important elements, such as carbon, oxygen and nitrogen, are not detected by PIXE, yet constitute a large fraction of the aerosol mass and will be incorporated into our analysis using approximation from current literature values. Oxide calculations are estimated based on average crustal composition from the following molar ratios: Al_2O_3, CaO, Fe_3O_4, K_2O, MgO, P_2O_5, SiO_2, TiO_2 [*Mason*, 1966]. These oxides and all other elements except sulfur are considered as the insoluble inorganic component and exhibit a uni-modal mass distribution with a median diameter in the coarse size fraction (ca. 3 μm). The gravimetric mass distribution is bimodal with median diameters in the fine and coarse fraction of 0.3 and 4 μm, respectively. Sulfur is also slightly bimodal with the main contribution in the fine aerosol mass fraction and a "tail" that extends into the coarse size fraction. Although no direct measurements of the sulfur speciation have been performed on our samples, earlier aerosol measurements in the Amazon Basin during the wet season show that sulfur is predominantly found as sulfate, SO_4^{2-} [*Gerab et al.*, 1998; *Reid and Hobbs*, 1998]. A stoichiometric balance of the anions and cations [*Gerab et al.*, 1998; *Talbot et al.*, 1990] further indicates that fine particulate SO_4^{2-} has been partially neutralized by ammonium at nearly a 1:1 molar ratio. Therefore, the mass distribution for ammonium bisulfate (NH_4HSO_4) has been estimated using sulfur concentrations from PIXE analysis. The soluble inorganic (e.g., NH_4HSO_4) and insoluble inorganic (e.g., oxides) contribution to the total aerosol mass collected on each impactor stage is shown in Table 4.3.

Köhler theory (Equation 4.1) calculates CCN activity based on the soluble content, which lowers a droplet's S_v^{eq} (i.e., Raoult effect). Some of the elements determined by PIXE analysis, such as sulfur (S), chlorine (Cl), potassium (K), and calcium (Ca) could exist as water-soluble anions and cations (i.e., SO_4^{2-}, Cl^-, K^+, Ca^{2+}). Figure 4.1, however, shows that SO_4^{2-} dominates the inorganic water-soluble fraction for fine aerosol particles. Cl^-, K^+, and Ca^{2+} combined make up less than 5% of the SO_4^{2-} mass and are consequently neglected for the calculation of CCN activity (see Section 4.4). Slightly acidic cloud droplets in the Amazon Basin [*Talbot et al.*, 1990] also inhibit the dissolution of CO_2 to form carbonate anions (CO_3^{2-} and HCO^{3-}).

The sampling of nitrates (NO_3^-) in aerosols has long presented experimental challenges; however, several experimental and theoretical analyses indicate that, in Amazonia, NO_3^- is predominantly found in the coarse fraction ($d_p > 1$ μm). Single particle analysis of size fractionated aerosol in the Amazon Basin showed NO_3^- is negligible for aerosol diameters less than 0.5 μm [*Wouters et al.*, 1993]. *Talbot et al.* [1988] and *Artaxo et al.* [1988] found that a maximum of 25% of the total aerosol NO_3^- was contained in the fine fraction and the NO_3^-/SO_4^{-2}- fine-mode mass ratio was less than 20%. In addition, theoretical estimations by *Basset and Seinfeld* [1984] have also led to similar conclusions. While SO_4^{2-} and NO_3^- are primarily found in the fine- and coarse-modes, respectively, the combined fine and coarse fraction molar concentrations show that particulate SO_4^{2-} mass tends to be slightly higher than NO_3^- [*Talbot et al.*, 1988; *Talbot et al.*, 1990]. Although the variability is large, precipitation chemistry shows similar SO_4^{2-}/NO_3^- mass ratios [*Andreae et al.*, 1990b; *Williams et al.*, 1997]. The authors believe that NO_3^- in the fine-mode is small compared to SO_4^{2-} (less than 20%

SO_4^{2-} mass) and can be neglected for CCN activity estimations. Section 4.4 looks at the errors induced to the mean CCN spectrum by changing the soluble mass – a 20% change in soluble material yields the least significant modification to the mean CCN spectrum of all variables that were studied.

Water-soluble organic carbon compounds (WSOC), such as sugars, sugar-derivates, and/or dicarboxylic acids, contribute an undetermined amount of water-soluble species and could induce changes in the droplet's surface tension. Hence, the WSOC component may affect the CCN activity and is analyzed in closer detail in Section 4.3.2.2. The unknown material not detected by PIXE analysis constitutes about 80% of the mass, which is approximately the amount of organic material present in the fine aerosol [*Artaxo and Hansson*, 1995; *Mayol-Bracero et al.*, 2001a; *Wouters et al.*, 1993]. The organic material is estimated from the difference between the total dry mass and the sum of the oxides and NH_4HSO_4 (i.e., the white area below the $n_M(d_p)$ (MOUDI) in Figure 4.2). The average aerosol mass composition for the fine fraction was ca. 15% NH_4HSO_4, 5% insoluble inorganic, and the other 80% is assumed to be organic material.

The simplest method of reporting MOUDI impactor data is to generate a discrete size distribution from each stage's D_{50}. The aerosol size distribution between stages is assumed to be constant and the result looks like a histogram. This method has the advantage of simply and unambiguously representing the raw data. However, the histogram representation is inappropriate for the calculation of CCN activity. A continuous mass distribution of important constituents (i.e., soluble and insoluble material) is necessary to compute CCN spectra. The mass collected on each stage (Table 4.3) was used to derive the continuous mass distributions (Figure 4.2) for each of the

MOUDI impactor sample periods. The basis of our inversion technique used an adaptation to the Twomey non-linear iterative algorithm that is described by *Winklmayr et al. [1990]*, referred to as WWJ90 hereafter. Several important modifications have been made to the WWJ90 inversion technique and are outlined in Appendix 4.A. Extrapolating the composition to aerosol sizes smaller than the D_{50} of the lowest MOUDI impactor stage (i.e., $D_p < 0.093$ μm) introduces significant error for estimations at supersaturations > 0.6% S_v.

The mass distributions in Figure 4.2 have been calculated to dry aerosol diameters based on hygroscopic growth factor measurements. The MOUDI impactor separates the aerosol according to their moist aerodynamic diameter, which is influenced by the diel changes in relative humidity (RH). The DMPS, however, measures number distributions by dry electrical mobility diameters. Therefore, to determine the chemical composition at a dry diameter, the aerodynamic diameter in the inverted distribution needs to be corrected to account for hygroscopic growth. H-TDMA growth factor measurements (Table 4.4) were obtained at 90% RH and may not necessarily reflect the actual growth factor for the MOUDI impactor, because of the wide range of relative humidity throughout the sampling period. Hence, a hygroscopic growth model [*Swietlicki et al.*, 1999] was used to estimate mean growth factors, which were weighted by ambient relative humidity to account for non-linearity in hygroscopic growth. These weighted growth factors are also summarized in Table 4.4. Hygroscopic growth is less for smaller particles because of the increased influence of the Kelvin effect. A power law relationship between dry particle diameter and weighted hygroscopic growth converts the mass distribution from aerodynamic wet diameters to dry diameters.

The MOUDI impactor provides the necessary chemical information to determine a particle's critical supersaturation (S_c) at given diameter using Köhler theory. However, deriving the number concentration from the mass distribution can yield unreliable results due to the r-cubed dependence and the variation in growth factors from changing relative humidity. The DMPS measurements accurately determined the aerosol concentrations as a function of size. A dry particle density of 1.5 g cm^{-3} was used in deriving the mass distribution from the DMPS measurements (Figure 4.2). Hence, the measured number distribution of the DMPS, combined with the relative chemical information of the MOUDI, provides a reliable estimate of CCN spectra.

4.3.1.2. Number distributions

The number distributions measured by the DMPS were averaged to determine the mean distribution for the corresponding MOUDI impactor sampling period (Figure 4.3). Both Aitken ($0.02 < d_p < 0.1$ μm) and accumulation ($0.1 < d_p < 1$ μm) modes were present with the median diameters 0.068 and 0.15 μm, respectively. The nucleation mode ($d_p < 0.02$ μm) was rarely observed and there is a strong indication that ultrafine particles were not formed close to the ground, but most likely aloft [*Zhou et al.*, 2001]. Airborne measurements in the Amazon Basin have found evidence that new particle formation may occur near cloud boundaries (Chapter 5). The accumulation mode particles may have been formed via in-cloud processing of Aitken mode particles through the uptake of SO_2 in heterogeneous reactions in cloud droplets [*Bower and Choularton*, 1993; *O'Dowd et al.*, 1999].

The total aerosol concentrations estimated by integrating the 36 DMPS measuring channels ($0.003 < d_p < 0.85$ μm) were compared to CPC_{3010} measurements. Since the number distribution includes particles below the detection limit of the CPC_{3010}, the efficiency curve of the CPC_{3010} (Section 4.2.4) was utilized when calculating the DMPS-derived aerosol concentration, N_{DMPS}. The CCN spectra closure (Section 4.3.2) uses N_{DMPS} to determine the theoretical fraction of CCN to total aerosol concentration. N_{DMPS} were slightly higher than N_{3010} with a regression slope of 1.10 ($r^2 \approx 0.6$). The discrepancy is likely due to different sampling inlets and/or inlet losses from the low sample flow of the CPC_{3010}.

4.3.2. CCN Spectra Closure

The results of the mass (Figure 4.2) and number (Figure 4.3) distributions, which have been described in Section 4.3.1 enable independent calculations of CCN spectra and will be compared to the measured CCN spectra reported in Table 4.1. A multiple-component approach allows for a closer approximation of CCN activity as the water soluble and insoluble components are comprised of both inorganic and organic material and can be treated as such in the Köhler equation (Equation 4.1). The ratio of each component (i.e., soluble/insoluble inorganic/organic material) is estimated using the mass distributions from Figure 4.2 to determine the relative contribution of soluble and insoluble components. Chemical and physical properties of each component that dictate a particle's S_c are shown in Table 4.5. Integrating the number distribution above a given diameter, which exhibits a particular S_c, yields N_{CCN} at that supersaturation. Furthermore,

$f_{CCN/CN}$ can be determined by the ratio of the calculated N_{CCN} to N_{DMPS} and compared to measured values shown in Table 4.1.

4.3.2.1. Three-component CCN spectra

Using the measurements presented in Section 4.3.1, the simplest case for estimating CCN spectra divides the aerosol mass into three components – soluble inorganic (NH_4HSO_4), insoluble inorganic (oxides), and insoluble organic (the unknown mass) as shown in Figure 4.2. The critical supersaturation, calculated by Equation 4.1 and the aerosol properties in Table 4.5, varies with composition, but generally decreases with increasing diameter. The resulting relationships between S_c and D_p are shown in Figure 4.3. Figure 4.3 also shows limiting cases for pure NH_4HSO_4 and insoluble aerosol to illustrate the maximum range of S_c. The relationships between a particle's S_c and d_p are combined with the number distribution, also shown in Figure 4.3, to yield the independent calculations of CCN spectra (Figure 4.4). Integration of $n_N(d_p)$ until a dry particle's S_c equals S_v of the CCN instrument, results in a theoretical N_{CCN}. For example, a particle of d_p = 0.054 μm has a critical supersaturation of 1.0% S_v based on the three-component model (Figure 4.2a). Therefore, the area under $n_N(d_p)$ in Figure 4.3a from $0.054 < d_p < 0.850$ μm is the concentration of aerosol expected to activate at 1.0% S_v in the CCN counter. The computed N_{CCN} is divided by the total aerosol concentration, N_{DMPS}, to calculate $f_{CCN/CN}$. The resulting CCN spectra (Figure 4.4), which utilize a simplified three-component model of NH_4HSO_4 and insoluble constituents, agree particularly well with the measured results reported in Table 4.1.

Estimates for the H-TDMA-derived soluble mass fraction in Table 4.4 [*Zhou et al.*, 2001] provide a third independent method of calculating CCN spectra (Section 4.3.2.1). *Zhou et al.* [2001] concluded that ca. 20% of the aerosol mass fraction from $0.03 < d_p < 0.26$ μm was soluble (Table 4.4) based on calculations of a bi-component aerosol (i.e., NH_4HSO_4 and an insoluble core). The density of the insoluble core was 1.5 g cm^{-3}. A CCN spectrum, generated from the H-TDMA results, is shown in Figure 4.5, along with the CCN spectrum based on the MOUDI composition for comparison. The CCN spectra were generated from the average number distribution (Figure 4.2a). As the soluble component from the H-TDMA measurements is similar to that determined by the MOUDI impactor, the resulting CCN spectra agree quite well.

4.3.2.2. Organic component

4.3.2.2.1. Solute effect

Aerosol in the Amazon Basin has a large organic component, and about half of which is water-soluble. However, uncertainty about the chemical speciation and the solubility of WSOC precludes a rigorous analysis of its contribution to nucleation activity. Within reasonable assumptions about molecular weight, density and van't Hoff factor, we can predict a similar contribution to CCN activity as that from the soluble inorganic component. Figure 4.6 shows the potential contribution of 40% aerosol mass of completely soluble WSOC to the CCN spectra. To illustrate the differences in CCN activity based on molecular weight, WSOC are divided into smaller compounds (e.g.,

dicarboxylic acids (DCA); 140 g mol^{-1}) and humics (1400 g mol^{-1}). The contributions of 40% mass of completely soluble DCA and humics are separately shown in Figure 4.6. An increase in molecular weight reduces the solute effect term (i.e., Raoult term) and, subsequently, reduces CCN activity. Surface tension effects are not included in Figure 4.6 and will be discussed in the next section.

The combined contribution of 15% NH_4HSO_4 and 40% completely soluble WSOC (i.e., DCA), shown in Figure 4.6, overestimates the solubility effects consistent with our measurements. Completely soluble WSOC probably exaggerates the solubility of ambient aerosol WSOC, but serves to illustrate the maximum contribution of WSOC to CCN activity. Presumably, ambient aerosol would contain a mix of sulfate, DCA and humics – at mass ratios and solubility that provide a good match to the observations. Because of the nonlinear dependence of droplet nucleation behavior on solute amount (Sections 4.4 and 4.5; Figure 4.10), the nucleation activity cannot be attributed uniquely to the inorganic or organic fractions. For example, an initially organic aerosol could readily activate into a cloud droplet due to a relatively small amount of WSOC. The subsequent acquisition of sulfate from cloud processing [*Bower and Choularton*, 1993; *O'Dowd et al.*, 1999] would then enhance CCN activity. However, the addition of sulfate will not increase CCN activity in a linear fashion. The opposite scenario would also be true for particles that initially contain inorganic salts and accumulate WSOC by partitioning of semi-volatile organic compounds [*Kavouras et al.*, 1998].

4.3.2.2.2. Surface tension effect

Non-idealities, such as the interactions of alkaline ions on WSOC and the subsequent effects on σ', are difficult to determine. *Shulman et al.* [1996] and *Facchini et al.* [1999] determined the relationship between dissolved WSOC concentrations and the reduction in surface tension for specific WSOC and bulk atmospheric cloud water samples, respectively. Both studies show similar changes in surface tension. However, as detailed chemical analysis of the organic fraction has not been performed, Facchini's relationship was applied here to estimate potential influences of surfactants on wet-season CCN spectra in the Amazon Basin. *Facchini et al.* [1999] determined the relationship of σ' as a function of dissolved organic carbon (DOC) concentration for fog and cloud water samples. DOC concentrations (10^{-4} – 10^{-2} M) that exist for droplet sizes near D_{pc} were recreated by evaporating the fog or cloud liquid sample volumes up to several orders of magnitude. The change in surface tension ($\Delta\sigma'/\sigma'$) was measured revealing a –30% $\Delta\sigma'/\sigma'$ at the highest concentration (i.e., 10^{-1} M DOC). DOC concentrations less than 0.001 M exert minor changes to the droplet surface tension and the soluble effect is negligible. A range of WSOC from 0.001 to 0.1 M DOC will be applied here to estimate potential influences of surfactants on wet-season CCN spectra in the Amazon Basin by adding a fourth component to the multi-component model.

The organic component, which constitutes nearly 80% of the aerosol mass, can be separated into soluble and insoluble terms. As in the earlier section, the WSOC content is estimated as 50% of the total organic composition. Changes in surface tension are

estimated based on the relationship described by *Facchini et al.* [1999] for 0.001, 0.01 and 0.1 M DOC and corresponds to $\Delta\sigma'/\sigma'$ of -3.8, -15 and -30%, respectively. The modifications to the CCN spectra in Figure 4.7 result from the combined effects of surface tension and DOC solubility on CCN spectra. Changes in σ' influence CCN activity more than WSOC solubility (see Section 4.4) and -15% $\Delta\sigma'/\sigma'$ is probably the upper limit of the surface tension effects consistent with our measurements in the Amazon Basin (Figure 4.7).

4.4. Quantifying the Sensitivity of CCN Spectra

The number distribution, soluble content of the aerosol, and surface tension effects all play an important role in determining CCN spectra and each of these factors were incorporated in the analysis in Section 4.3. However, their individual contribution in regulating CCN spectra is not known and will be quantified in this section. Studying the effects of the individual components that influence CCN spectra allows us to identify the most important aerosol properties that determine CCN activity.

4.4.1. Key Parameters

Idealized size distributions with prescribed $n_N(d_p)$ and chemical composition are used to clearly sort out the physics involved. Number distributions are of the single mode lognormal form

$$\frac{dN}{d\log d_p} = \frac{N}{\sqrt{2\pi}\ln\sigma_g}\exp\left[\frac{-\left(\ln d_p - \ln d_{pg}\right)^2}{2\ln^2\sigma_g}\right] \tag{4.2}$$

where N is the aerosol number concentration, d_{pg} is the number mode diameter, and σ_g is the geometric standard deviation. Values for N, d_{pg} and σ_g that best represent the average wet-season number distribution are 459 cm^{-3}, 0.0823 μm, and 1.83, respectively. A particle's S_c is determined for a three-component aerosol using the measured averages (e.g., 15% NH_4HSO_4, 5% insoluble inorganic, 80% insoluble organic; Section 4.3.2.1) and is uniform for all d_p. These physical and chemical properties establish a size distribution that yields a reference CCN spectrum.

4.4.2. Parametric Dependence

To explore the parametric dependence of CCN spectra, variables that describe the size distribution, soluble content, and surface tension were independently studied (Figure 4.8). The modifications to the reference CCN spectrum were quantified for a given supersaturation from the following expression:

$$\delta_S = |N_\Delta - N_S| \tag{4.3}$$

where N_S and N_Δ are the CCN number concentrations for the reference and modified CCN spectra, respectively, and δ_S describes the absolute difference at a given supersaturation. Table 4.6 summarizes the change in CCN spectra for $S_v < 1.5\%$ for a 20% change in physical and chemical parameters that influence CCN activity. Figure 4.9 presents δ_s as a function of S_c to easily compare the parametric modifications, which are discussed in more detail below.

The number distribution, approximated by a lognormal function (Equation 4.2), depends on three parameters (i.e., N, D_{pg} and σ_g), that are individually investigated.

1. An increase or decrease in N directly affects the number of CCN available for activation and shifts CCN spectra accordingly (Figure 4.8a).
2. The geometric median diameter (d_{pg}) affects CCN spectra (Figure 4.8b) by dictating the fraction of aerosol larger than a critical dry diameter (d_{pc}), which is the smallest diameter that will activate at a given supersaturation. Increasing or decreasing d_{pg} results in respective changes to the activated aerosol fraction, $f_{CCN/CN}$. When $d_{pg} > d_{pc}$, a 20% decrease in d_{pg} has a greater effect on CCN spectra because the higher "shoulder" of the number distribution extends to sizes smaller than d_{pc}. Note: the opposite would be true when $d_{pg} < d_{pc}$.
3. The geometric standard deviation (σ_g) affects the shape of the number distribution. Increasing σ_g flattens $n_N(d_p)$ by reducing the peak height and extending $n_N(d_p)$ over a larger size range. Since larger aerosol sizes correspond to smaller S_c, particles initially activate at lower S_c and increase N_{CCN} (i.e., raise

the CCN spectrum; Figure 4.8c). The CCN concentrations for the reference and modified CCN spectra are equal when $d_p = d_{pg}$. This occurs at the critical supersaturation of d_{pg}. At larger critical supersaturations (i.e., $d_p < d_{pg}$), fewer CCN activate because particles extend to smaller sizes when σ_g increases. Conversely, reducing σ_g sharpens $n_N(d_p)$ and reduces the number of CCN available for activation at low supersaturations, resulting in an initial reduction in CCN spectra. Furthermore, the CCN concentration increases when $d_p < d_{pg}$ because of the narrower number distribution. A 20% decrease in σ_g has a larger effect on CCN spectra than a similar increase in σ_g and 20% changes in the water-soluble content.

The effects of water-soluble content on CCN spectra have been used throughout this paper to illustrate the limiting cases of completely soluble and insoluble particles. In this discussion, we consider a 20% change to the NH_4HSO_4 mass fraction to quantify the effects of the soluble fraction (Figure 4.8d). The interpretation of these modifications is not restricted to NH_4HSO_4 and may be applied to any water-soluble species, including WSOCs. A particle's S_c is inversely proportional to its water-soluble content. Hence, increasing or decreasing the water-soluble content enhances or reduces CCN spectra, respectively. A 20% change in NH_4HSO_4 (i.e., soluble material) yields the least change to CCN spectra (Table 4.6). The changes, however, are not linear and Figure 4.10 illustrates that modifications to CCN spectra are most sensitive at lower S_c. Therefore, a reduction in the soluble fraction exerts a greater impact on resulting CCN spectra than an

increase. Furthermore, a 20% change of soluble material is more important for aerosols that initially contain less soluble material.

Lowering a droplet's σ' changes droplet growth characteristics and is another parameter that needs to be explored. A 20% decrease in σ' yields a reduction in CCN spectra (Figure 4.8d) that is similar to modifications in parameters that describe the number distribution (e.g., D_{pg}, σ_g and N). An increase in surface tension is not physically relevant and is not included in our analysis.

Quantifying the average modification in CCN spectra depends on the range of supersaturation; however, the general trends remain the same. The average absolute difference $<\delta_S>$, reported in Table 4.6, were calculated for $< 1.5\%$ S_v. Parameters that dictate the number distribution and surface tension effects are relatively more important than varying the soluble content. The role of WSOCs as surfactants may be significant, especially for biomass burning aerosol, and more field measurements are needed to quantify the effects of surface tension on ambient aerosols.

4.5. Discussion

As the time scales of our closure estimation are determined by the sampling time of the MOUDI impactor, the natural variability of CCN spectra over a two-day period limits the resolution at which the chemical influences can be discerned. Nevertheless, these results suggest that, while the soluble inorganic component contributes relatively little to the total aerosol mass, ca. 15% NH_4HSO_4 is sufficient to account for the observed CCN activity during the wet season in the Amazon Basin. However, the change in CCN

spectra is not linear with soluble fraction. Figure 4.10 illustrates the changes in CCN spectra based on the three-component model for various amounts of NH_4HSO_4. We use NH_4HSO_4 for comparison to our measured results; yet, the same trend would be observed for any water-soluble compound. The average number distribution (Figure 4.3a) was used to derive CCN concentrations for Figure 4.10. CCN spectra are most sensitive at the low solute amount case where even a 5% contribution of water-soluble material is enough to raise the CCN spectrum by an amount detectable within the measurement errors. The difference between CCN spectra of 50% and 100% water-soluble matter material, however, is significantly less than the change for the low solute amount case. This apparent insensitivity to a notable increase in soluble material was highlighted in Figure 4.6 by combining solute effects of NH_4HSO_4 and WSOC. Although the results from the earlier section indicate that varying the soluble content induces relatively small changes to the reference CCN spectrum, the difference between the reference CCN spectrum and the insoluble CCN spectrum is much greater than any other modification (Figure 4.9). Therefore, the existing presence of soluble compounds in the aerosol reduces the sensitivity of CCN spectra to the contribution of moderate additional amounts of other water-soluble species.

Although organic material constitutes nearly 80% of the aerosol mass in the Amazon Basin [*Artaxo and Maenhaut*, 1990; *Wouters et al.*, 1993], its effect on CCN activity of wet-season aerosol cannot be readily determined from our CCN measurements. Since the water-soluble inorganic fraction of the fine-mode aerosol is primarily sulfate, we hypothesize that even a small mass fraction of sulfate present on a particle plays a significant role in dictating CCN activity. This hypothesis, however, does

not suggest that organic compounds cannot serve as CCN. Organic compounds cover a very wide range of molecular forms, solubilities, and physical properties, which makes a complete characterization extremely difficult. Since a large fraction of the biomass-burning aerosol consists of humic-like substances [*Mayol-Bracero et al.*, 2001b], the solubility and surface tension effects of biomass burning aerosol may play an important role in increasing the CCN activity during the dry season. *Novakov and Corrigan* [1996] report that pure organic smoke from cellulose is able to form CCN without being associated to sulfates or other inorganic compounds. Based on their reported size distribution and activated CCN fractions, a ca. 5-10% soluble mass fraction can account for their measured CCN activity. Levoglucosan, a highly soluble sugar present in biomass burning smoke [*Graham et al.*, 2001], or soluble humic-like compounds [*Mayol-Bracero et al.*, 2001b] could exist in sufficient quantities to account for CCN activity in the absence of soluble inorganic salts. Less than ca. 5% soluble mass fraction may also be possible when considering surface tension effects. However, surface tension effects alone probably do not account for CCN activity as $\Delta\sigma'/\sigma'$ would need to be at least -50% to reproduce the observed CCN activity reported by *Novakov and Corrigan* [1996]. Such a reduction in σ' is tenuous based on the measurements by *Facchini et al.* [1999; 2000].

These results present challenges for both the experimental and modeling communities. In order to measure the effects of organic material in ambient aerosols, the precision of CCN measurements will have to be improved. The required precision of CCN measurements depends largely on the sensitivity of cloud properties to variations in the CCN spectrum from modeling studies. *Facchini et al.* [1999] estimated a 6% decrease in effective cloud droplet diameter for a 30% change in surface tension (e.g., 0.1

M DOC), resulting in a ca. 1% change in top-of-atmosphere albedo locally. However, a 15% decrease in surface tension for a 0.01 M DOC is probably the upper limit of the surface tension effects consistent with our measurements in the Amazon Basin. The intensive appearance of small organic fragments (i.e., C_xH_y-; $x < 3$, $y < 7$) and the lack of phosphate-containing compounds (i.e., phospholipids) in the fine-mode wet-season Amazonian aerosols [*Wouters et al.*, 1993] suggests a secondary biogenic origin. Organic compounds associated with secondary aerosol, such as mono- and dicarboxylic acids, show less surface tension effects than polyacidic substances [*Facchini et al.*, 2000].

4.6. Conclusions

Based on the measured physical and chemical properties of wet season aerosol in the Amazon Basin, the sulfate mass fraction could account for most of the CCN activity. However, uncertainty about the chemical speciation and the solubility of the large organic component precludes a rigorous analysis of its contribution to nucleation activity. Within reasonable characterization of the organic component, we can predict a similar contribution to CCN activity as that from the soluble inorganic component. A parameterization of the aerosol properties that dictate CCN activity shows that measuring the number distribution and surface tension effects are relatively more important than precisely determining the soluble content. The additional dissolution of water-soluble compounds will not dramatically affect resulting wet-season CCN spectra and a 15% decrease in surface tension is probably the upper limit of surface tension effects consistent with our wet-season measurements in the Amazon Basin.

4.8. References

Andreae, M.O., and T.W. Andreae, The cycle of biogenic sulfur compounds over the Amazon Basin. I. Dry season, *J. Geophys. Res.*, *93*, 1487-1497, 1988.

Andreae, M.O., H. Berresheim, H. Bingemer, D.J. Jacob, B.L. Lewis, S.-M. Li, and R.W. Talbot, The atmospheric sulfur cycle over the Amazon Basin, 2, Wet season, *J. Geophys. Res.*, *95*, 16,813-16,824, 1990a.

Andreae, M.O., R.W. Talbot, H. Berresheim, and K.M. Beecher, Precipitation chemistry in central Amazonia, *J. Geophys. Res.*, *95*, 16,987-16,999, 1990b.

Artaxo, P., and H.C. Hansson, Size distribution of biogenic aerosol particles from the Amazon basin, *Atmos. Environ.*, *29* (3), 393, 1995.

Artaxo, P., and W. Maenhaut, Trace element concentrations and size distributions of biogenic aerosols from the Amazon Basin during the wet season, *Nucl. Instrum. Methods Phys. Res.*, *49* (Sect. B), 366-371, 1990.

Artaxo, P., and C. Orsini, PIXE and receptor models applied to remote aerosol source apportionment in Brazil., *Nucl. Instrum. Methods Phys. Res.*, *22* (Sec. B), 259-263, 1987.

Artaxo, P., H. Storms, F. Bruynseels, R. Van Grieken, and W. Maenhaut, Composition and sources of aerosols from the Amazon basin, *J. Geophys. Res.*, *93*, 1605-1615, 1988.

Basset, M.E., and J.H. Seinfeld, Atmospheric equilibrium model of sulfate and nitrate aerosols -- II. Particle size analysis, *Atmos. Environ.*, *18*, 1163-1170, 1984.

Bower, K.N., and T.W. Choularton, Cloud processing of the cloud condensation nucleus spectrum and its climatological consequences, *Q. J. R. Meteorol. Soc.*, *119*, 655, 1993.

Cruz, C., and S. Pandis, The effect of organic coatings on the cloud condensation nuclei activation of inorganic atmospheric aerosol, *J. Geophys. Res.*, *103*, 13111-13123, 1998.

Facchini, M., S. Decesari, M. Mircea, S. Fuzzi, and G. Loglio, Surface tension of atmospheric wet aerosol and cloud/fog droplets in relation to their organic carbon content and chemical composition, *Atmos. Environ.*, *34*, 4853-4857, 2000.

Facchini, M.C., M. Mircea, S. Fuzzi, and R.J. Charlson, Cloud albedo enhancement by surface-active organic solutes in growing droplets, *Nature*, *401* (6750), 257-259, 1999.

Gerab, F., P. Artaxo, R. Gillet, and G. Ayers, PIXE, PIGE and ion chromatography of aerosol particles from northeast Amazon Basin, *Nucl. Instrum. Methods Phys. Res. B.*, *138*, 955-960, 1998.

Graham, B., O. Mayol-Bracero, P. Guyon, G. Roberts, S. Decesari, M. Facchini, P. Artaxo, W. Maenhaut, P. Köll, and M. Andreae, Water-soluble organic compounds in biomass burning aerosols over Amazonia, *Submitted to J. Geophys. Res.*, 2001.

Hoppel, W.A., J.W. Fitzgerald, G.M. Frick, R.E. Larson, and E.J. Mack, Aerosol size distributions and optical properties found in the marine boundary layer over the Atlantic Ocean, *J. Geophys. Res.*, *95*, 3659-3686, 1990.

Johansson, S., and J. Campbell, *PIXE - a Novel Technique for Elemental Analysis*, Wiley, New York, 1988.

Kaufman, Y.J., and D. Tanré, Effect of variations in supersaturation on the formation of cloud condensation nuclei, *Nature*, *369*, 45-48, 1994.

Kavouras, I.G., N. Mihalopoulos, and E.G. Stephanou, Formation of atmospheric particles from organic acids produced by forests, *Nature*, *395* (6703), 683-686, 1998.

Lala, G.G., and J.E. Jiusto, An automatic light scattering CCN counter, *J. Appl. Meteor.*, *16* (4), 413-418, 1977.

Lide, D., *CRC Handbook of Chemistry and Physics*, CRC Press, Cleveland, Ohio, 2000.

Liu, P.S.K., W.R. Leaitch, C.M. Banic, and S.-M. Li, Aerosol observations at Chebogue Point during the 1993 North Atlantic Regional Experiment: Relationships among cloud condensation nuclei, size distribution, and chemistry, *J. Geophys. Res.*, *101*, 28,971-28,990, 1996.

Marple, V., K. Rubow, and S. Behm, A micro-orifice uniform deposit impactor (MOUDI) - Description, calibration, and use, *Aerosol Sci. Technol.*, *14*, 434-446, 1991.

Mason, B., *Principles of Geochemistry*, John Wiley, New York, 1966.

Mayol-Bracero, O.L., P. Guyon, B. Graham, G. Roberts, M.O. Andreae, S. Decesari, M.C. Facchini, S. Fuzzi, and P. Artaxo, Water-Soluble Organic Compounds in Biomass Burning Aerosols over Amazonia: 2. Apportionment of the Chemical Composition and Importance of the Polyacidic Fraction, *Submitted to J. Geophys. Res.*, 2001a.

Mayol-Bracero, O.L., P. Guyon, B. Graham, G. Roberts, M.O. Andreae, S. Decesari, M.C. Facchini, S. Fuzzi, P. Artaxo, and W. Maenhaut, Black Carbon, Organic Carbon and Water-Soluble Organic Compounds in Biomass Smoke Particles over the Amazon Basin, *Submitted to J. Geophys. Res.*, 2001b.

Nenes, A., P. Chuang, R. Flagan, and J. Seinfeld, A theoretical analysis of cloud condensation nucleus (CCN) instruments, *J. Geophys. Res.*, *106*, 3449-3474, 2001.

Novakov, T., and C.E. Corrigan, Cloud condensation nucleus activity of the organic component of biomass smoke particles, *Geophys. Res. Lett.*, *23* (16), 2141-2144, 1996.

Novakov, T., and J.E. Penner, Large contribution of organic aerosols to cloud-condensation-nuclei concentrations, *Nature*, *365*, 823-826, 1993.

O'Dowd, C., J. Lowe, and M. Smith, Observations and modelling of aerosol growth in marine stratocumulus - case study, *Atmos. Environ.*, *33*, 3053-3062, 1999.

Pruppacher, H.R., and J.D. Klett, *Microphysics of Clouds and Precipitation*, Kluwer Academic Publishers, Boston, 1997.

Reid, J.S., and P.V. Hobbs, Physical and optical properties of young smoke from individual biomass fires in Brazil, *J. Geophys. Res.*, *103*, 32,013-32,030, 1998.

Rivera-Carpio, C.A., C.E. Corrigan, T. Novakov, J.E. Penner, C.F. Rogers, and J.C. Chow, Derivation of contributions of sulfate and carbonaceous aerosols to cloud condensation nuclei from mass size distributions, *J. Geophys. Res.*, *101*, 19,483-19,493, 1996.

Roberts, G., J. Zhou, P. Artaxo, and M. Andreae, Cloud condensation nuclei in the Amazon Basin: "Marine" conditions over a continent?, *in press, Geophys. Res. Lett.*, 2001.

Saxena, P., and L.M. Hildemann, Water soluble organics in atmospheric particles: A critical review of the literature and application of thermodynamics to identify candidate compounds, *J. Atmos. Chem.*, *24* (1), 57-109, 1996.

Seinfeld, J.H., and S.N. Pandis, *Atmospheric chemistry and physics: From air pollution to climate change*, 1326 pp., John Wiley, New York, 1998.

Shulman, M.L., M.C. Jacobson, R.J. Charlson, R.E. Synovec, and T.E. Young, Dissolution behavior and surface tension effects of organic compounds in nucleating cloud droplets, *Geophys. Res. Lett.*, *23*, 277-280, 1996.

Swietlicki, E., J. Zhou, O. Berg, B. Martinsson, G. Frank, S.-I. Cederfelt, U. Dusek, A. Berner, W. Birmili, A. Wiedensohler, B. Yuskiewicz, and K. Bower, A closure study of sub-micrometer aerosol particle hygroscopic behaviour, *Atmos. Res.*, *50*, 205-240, 1999.

Talbot, R.W., M.O. Andreae, T.W. Andreae, and R.C. Harriss, Regional aerosol chemistry of the Amazon Basin during the dry season, *J. Geophys. Res.*, *93*, 1499-1508, 1988.

Talbot, R.W., M.O. Andreae, H. Berresheim, P. Artaxo, M. Garstang, R.C. Harriss, K.M. Beecher, and S.M. Li, Aerosol chemistry during the wet season in Central Amazonia: The influence of long-range transport, *J. Geophys. Res.*, *95* (D10), 16955, 1990.

Williams, M.R., T.R. Fisher, and J.M. Melack, Chemical composition and deposition of rain in the Central Amazon, Brazil, *Atmos. Environ.*, *31* (2), 207, 1997.

Winklmayr, W., H.-C. Wang, and W. John, Adaptation of the Twomey Algorithm to the Inversion of Cascade Impactor Data, *Aerosol Sci. Technol.*, *13*, 322-331, 1990.

Wouters, L., S. Hagedoren, I. Dierck, P. Artaxo, and R.V. Grieken, Laser microprobe mass analysis of Amazon Basin aerosols, *Atmos. Environ.*, *27A* (5), 661-668, 1993.

Zhou, J., E. Swietlicki, H. Hansson, and P. Artaxo, Sub-micrometer aerosol particle size distribution and hygroscopic growth measurements in the Amazonian rain forest during the wet season, *Submitted to J. Geophys. Res.*, 2001.

Table 4.1. Average normalized CCN spectrum during LBA-CLAIRE-98.

	$f_{CCN/CN}$				
S_v (%)	Average	MD_4	MD_6	MD_9	MD_10
0.15	0.070 ± 0.044	0.059 ± 0.033	0.056 ± 0.040	0.063 ± 0.045	0.100 ± 0.060
0.30	0.235 ± 0.101	0.228 ± 0.075	0.190 ± 0.085	0.225 ± 0.118	0.297 ± 0.128
0.60	0.458 ± 0.152	0.458 ± 0.135	0.396 ± 0.142	0.414 ± 0.154	0.563 ± 0.176
1.00	0.682 ± 0.177	0.705 ± 0.153	0.615 ± 0.180	0.618 ± 0.182	0.790 ± 0.194
1.50	0.818 ± 0.205	0.824 ± 0.188	0.762 ± 0.201	0.752 ± 0.231	0.935 ± 0.199
$N_{1.0}$ (cm^{-3})	265 ± 132	402 ± 102	233 ± 239	206 ± 99	224 ± 89
data	0.86	0.56	0.91	1.0	0.98

S_v is the supersaturation of the CCN measurements. $f_{CCN/CN}$ represents the ratio of N_{CCN} to N_{3010} and is determined from a normalized CCN spectrum and $N_{1.5}$ (N_{CCN} at 1.5% S_v). Concentrations of CCN at 1% S (i.e., $N_{1.0}$) are reported in the table. The values in the row titled "data" are the relative time fractions of continuous CCN measurements during the MOUDI sampling. The standard deviations in this paper are reported as one sigma.

Table 4.2. Ensemble average and standard deviation (one sigma) of the four MOUDI samples during LBA-CLAIRE-98.

	Aerodynamic 50% cutoff diameter (D_{50})						
Element	0.093 μm	0.175 μm	0.33 μm	0.56 μm	1.0 μm	1.8 μm	3.2 μm
Mg	-	-	-	-	2.83 ± 0.91	2.31 ± 0.56	5 ± 1.34
Al	-	-	2.78 ± 0.73	6.72 ± 1.21	17.3 ± 1.8	16.7 ± 1.8	28.3 ± 2.0
Si	2.51 ± 0.66	2.32 ± 0.67	5.98 ± 0.71	12.1 ± 0.8	28.7 ± 1.3	27.1 ± 1.2	30.9 ± 1.3
P	-	-	-	-	1.26 ± 0.2	7.66 ± 0.32	23.4 ± 0.8
S	3.94 ± 0.38	20.6 ± 0.8	20.0 ± 0.8	6.13 ± 0.43	5.64 ± 0.43	7.41 ± 0.47	16.9 ± 0.7
Cl	0.50 ± 0.17	-	-	0.57 ± 0.09	3.37 ± 0.28	11.6 ± 0.5	27.9 ± 1.0
K	-	1.19 ± 0.06	2.18 ± 0.13	1.12 ± 0.09	5.73 ± 0.22	18.3 ± 0.57	53.0 ± 1.6
Ca	-	0.53 ± 0.18	0.17 ± 0.08	0.37 ± 0.08	2.85 ± 0.3	4.17 ± 0.42	6.55 ± 0.46
Sc	-	-	0.05 ± 0.02	0.05 ± 0.01	0.06 ± 0.03	-	-
Ti	-	-	0.18 ± 0.05	0.33 ± 0.06	1.22 ± 0.13	1.5 ± 0.15	3.76 ± 0.25
V	0.04 ± 0.02	-	-	-	-	-	0.06 ± 0.02
Cr	-	-	0.28 ± 0.03	-	-	-	-
Mn	-	-	0.05 ± 0.01	0.03 ± 0.01	0.09 ± 0.01	0.12 ± 0.02	0.21 ± 0.03
Fe	0.19 ± 0.02	0.26 ± 0.05	2.18 ± 0.15	2.87 ± 0.18	7.69 ± 0.42	8.15 ± 0.44	15.2 ± 0.8
Ni	-	-	0.04 ± 0	-	-	-	-
Cu	0.02 ± 0.01	0.03 ± 0.01	0.05 ± 0.01	0.06 ± 0.01	0.07 ± 0.01	0.08 ± 0.01	0.12 ± 0.02
Zn	0.03 ± 0.01	0.04 ± 0.01	0.08 ± 0.01	0.05 ± 0.01	0.09 ± 0.01	0.18 ± 0.02	0.51 ± 0.05
Br	-	-	-	-	-	-	0.2 ± 0.08
Sr	0.02 ± 0.01	0.01 ± 0.00	-	-	0.04 ± 0.01	0.04 ± 0.02	0.07 ± 0.03
Zr	-	0.01 ± 0.00	-	-	0.04 ± 0.01	-	0.05 ± 0.02
Pb	0.01 ± 0.00	0.01 ± 0.00	0.02 ± 0.01	0.01 ± 0.01	0.01 ± 0.01	-	0.02 ± 0.01
mass	96.4 ± 9.6	328.0 ± 32.8	341.5 ± 34.2	262.1 ± 26.2	636.7 ± 63.7	1611 ± 161	4892 ± 489

PIXE and gravimetric analysis determined the elemental and mass concentrations, respectively. Mean elemental aerosol concentrations are reported in ng m^{-3}.

Table 4.3. The soluble (NH_4HSO_4) and insoluble inorganic (oxides) contribution to the total aerosol mass collected on each MOUDI impactor stage.

	Component	Aerodynamic 50% cutoff diameter (D_{50}) 0.093 μm	0.175 μm	0.33 μm	0.56 μm	1.0 μm	1.8 μm	3.2 μm
Average (ng m^{-3})	mass	96.4 ± 9.6	327 ± 32	341 ± 34	262 ± 26	636 ± 63	1611 ± 161	4891 ± 489
	NH_4HSO_4	14.1 ± 1.4	73.8 ± 2.9	71.8 ± 2.9	22.0 ± 1.6	20.3 ± 1.5	26.6 ± 1.7	60.5 ± 2.6
	oxides	6.2 ± 1.7	7.6 ± 1.8	24.8 ± 3.5	45.8 ± 4.9	128 ± 10	164 ± 10	310 ± 15
MD_4 (ng m^{-3})	mass	179 ± 18	432 ± 43	331 ± 33	280 ± 28	601 ± 60	1209 ± 121	2965 ± 297
	NH_4HSO_4	20.6 ± 1.5	72.7 ± 3.0	63.3 ± 2.6	18.5 ± 1.6	22.0 ± 1.7	25.0 ± 1.7	51.9 ± 2.4
	oxides	4.4 ± 1.5	6.3 ± 1.7	12.7 ± 1.9	36.0 ± 5.6	95.6 ± 10.9	126 ± 10	245 ± 14
MD_6 (ng m^{-3})	mass	57.7 ± 5.8	330 ± 33	314 ± 31	256 ± 26	490 ± 49	1483 ± 148	5232 ± 523
	NH_4HSO_4	9.0 ± 1.4	43.3 ± 2.2	46.7 ± 2.2	8.9 ± 1.2	9.2 ± 1.4	18.5 ± 1.6	52.1 ± 2.4
	oxides	5.6 ± 2.0	3.5 ± 1.5	6.8 ± 1.6	12.2 ± 1.7	44.1 ± 6.1	88.2 ± 7.8	267 ± 15
MD_9 (ng m^{-3})	mass	*66.9 ± 24.8***	245 ± 25	354 ± 35	245 ± 25	605 ± 61	1687 ± 169	4978 ± 498
	NH_4HSO_4	13.4 ± 1.3	73.2 ± 2.9	61.8 ± 2.6	17.3 ± 1.5	19.7 ± 1.6	26.8 ± 1.7	55.7 ± 2.5
	oxides	8.6 ± 1.9	9.1 ± 2.1	27.9 ± 5.1	52.9 ± 6.3	136 ± 11	158 ± 9.1	269 ± 14
MD_10 (ng m^{-3})	mass	81.8 ± 8.2	305 ± 31	367 ± 37	268 ± 27	850 ± 85	2065 ± 207	6391 ± 639
	NH_4HSO_4	13.6 ± 1.2	106 ± 4	116 ± 4	43.3 ± 1.9	30.2 ± 1.6	36.2 ± 1.7	82.3 ± 3.0
	oxides	6.4 ± 1.3	11.5 ± 1.7	51.8 ± 5.2	82.2 ± 6.0	240 ± 13	287 ± 14	462 ± 19

Table 4.3 (continued). These values are used as the mass loading $m_i(D_p)$ for the non-linear inversion routine discussed in Appendix 4.A.

**Mass and standard deviation (one sigma) for this stage was estimated based on the average ratio of the first and second impactor stages of the other samples.

Table 4.4. Summary of aerosol hygroscopic properties during the LBA-CLAIRE 1998 experiment.

	d_p					
	0.035 μm	0.050 μm	0.073 μm	0.109 μm	0.166 μm	0.264 μm
Growth factor[+]	1.17 ± 0.05	1.16 ± 0.04	1.17 ± 0.04	1.22 ± 0.06	1.26 ± 0.07	1.32 ± 0.07
Soluble fraction[*]	0.20 ± 0.06	0.17 ± 0.05	0.16 ± 0.05	0.21 ± 0.07	0.24 ± 0.08	0.31 ± 0.09
MD_04[‡]	1.18 ± 0.09	1.18 ± 0.10	1.19 ± 0.12	1.26 ± 0.17	1.32 ± 0.22	1.40 ± 0.29
MD_06[‡]	1.23 ± 0.08	1.24 ± 0.10	1.26 ± 0.13	1.36 ± 0.19	1.45 ± 0.25	1.57 ± 0.33
MD_09[‡]	1.24 ± 0.07	1.25 ± 0.09	1.27 ± 0.1	1.37 ± 0.15	1.45 ± 0.19	1.57 ± 0.25
MD_10[‡]	1.19 ± 0.08	1.19 ± 0.09	1.2 ± 0.1	1.27 ± 0.15	1.33 ± 0.19	1.42 ± 0.24

[+] growth factor measured at 90% RH [*Zhou et al.*, 2001]

[*] soluble mass fraction based on a NH_4HSO_4 and inactive core aerosol [*Zhou et al.*, 2001]

[‡] growth factor weighted by diel changes in RH [*Swietlicki et al.*, 1999]

Table 4.5. Properties of important components used in Köhler Theory to estimate CCN activity.

Material	Density ($g\ cm^{-3}$)	Molecular weight ($g\ mol^{-1}$)	Solubility (mole $liter^{-1}$ H_2O)	Van't Hoff factor
NH_4HSO_4	1.780[-]	115.11[-]	6.55[-]	2.0
WSOC	1.3[‡]	140[‡]	0.1 – 0.001 (carbon)[+]	1.0
Insoluble inorganic	2.5[*]	NA	0.0	0.0
Insoluble organic	1.3[‡]	NA	0.0	0.0

[-] *CRC Handbook* [*Lide*, 2000]

[‡] values are similar to WSOC such as glutaric and adipic acid

[+] *Facchini et al.* [1999]

[*] average crustal material [*Mason*, 1966]

Table 4.6. Parametric changes that effect the CCN spectra.

Parameter	$<\delta_S>$
20% mass increase of NH_4HSO_4 (12% NH_4HSO_4, 5% insoluble inorganic, 83% insoluble organic)	13.4
20% mass decrease of NH_4HSO_4 (18% NH_4HSO_4, 5% insoluble inorganic, 77% insoluble organic)	16.4
20% increase in lognormal standard deviation ($\sigma = 2.20$)	19.0
20% decrease in lognormal standard deviation ($\sigma = 1.46$)	35.2
20% increase in median diameter ($D_{pg} = 0.0999$ μm)	39.1
20% decrease in surface tension ($\sigma = 57.07$ dyne cm^{-1})	47.3
20% increase/decrease in number concentration ($N = 367$ and 550 cm^{-3})	48.6
20% decrease in median diameter ($D_{pg} = 0.0666$ μm)	50.8
insoluble CCN spectra compared to reference CCN spectra – measures the effect of 15% addition of NH_4HSO_4	235.8

$<\delta_S>$ shows the average absolute change in the CCN wspectrum for $S_v < 1.5\%$.

The parameters that effect the CCN spectra are listed from least important to most important factors.

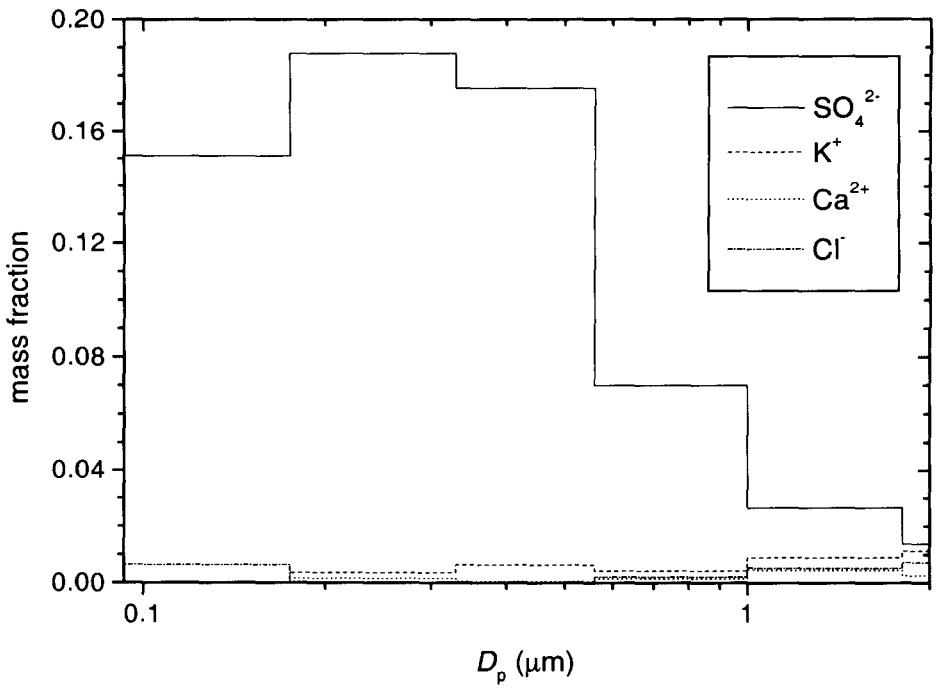

Figure 4.1. Potential water-soluble anions and cations inferred from elemental concentrations detected in PIXE analysis.

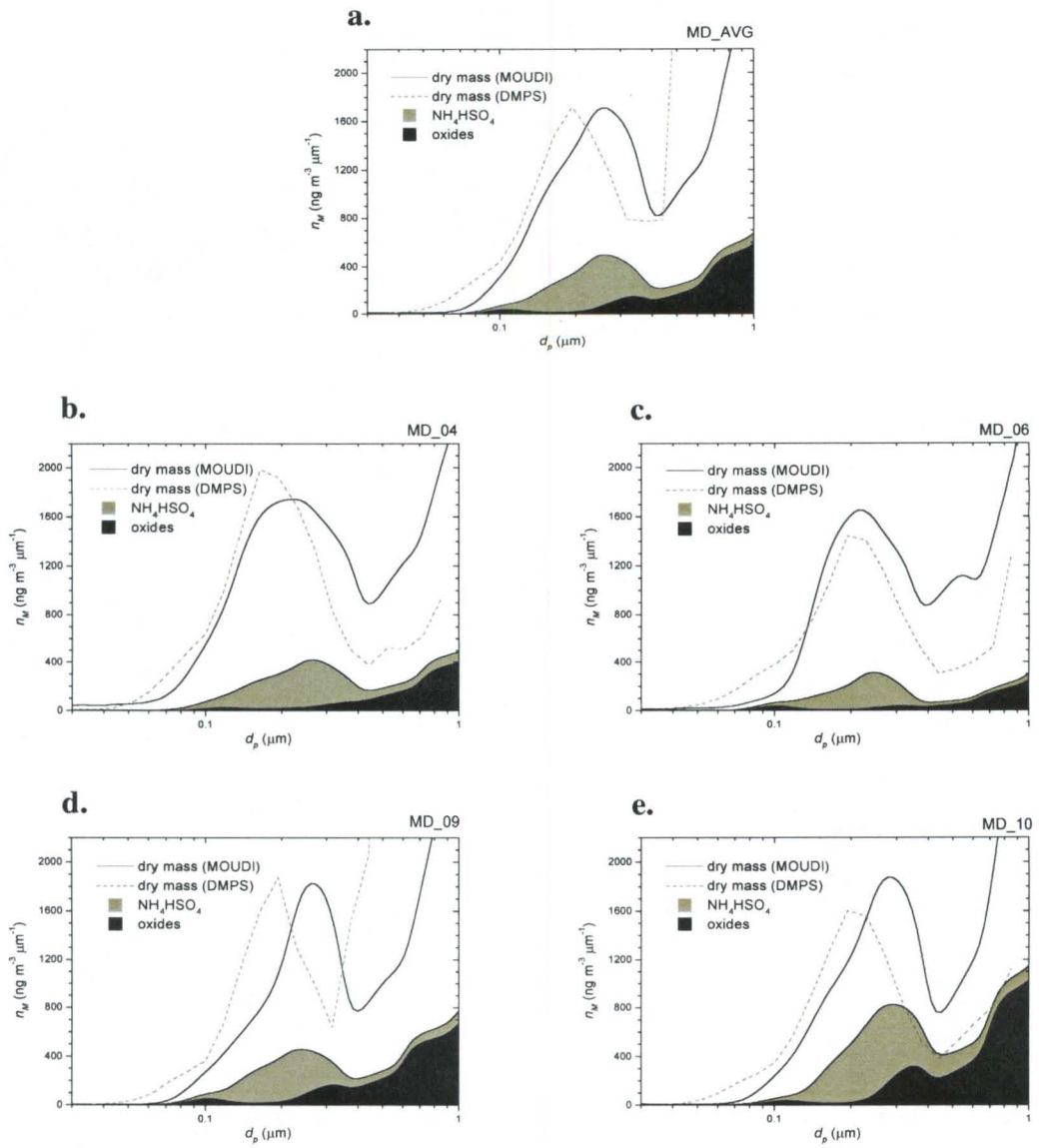

Figure 4.2. Inverted $n_M(d_p)$ (dM dlog^{-1} d_p) of MOUDI impactor data. Total dry aerosol mass was determined gravimetrically. NH_4HSO_4 and oxides were calculated based on PIXE analysis for S and average crustal composition (i.e., Al_2O_3, SiO_2, etc…), respectively. The remaining material (white area under $n_M(d_p$, dry mass)) has not been identified and is probably organic matter. RH growth factors from Table 4.4. Mass distributions derived from DMPS measurements (ρ = 1.5 g cm^{-3}) are shown for comparison.

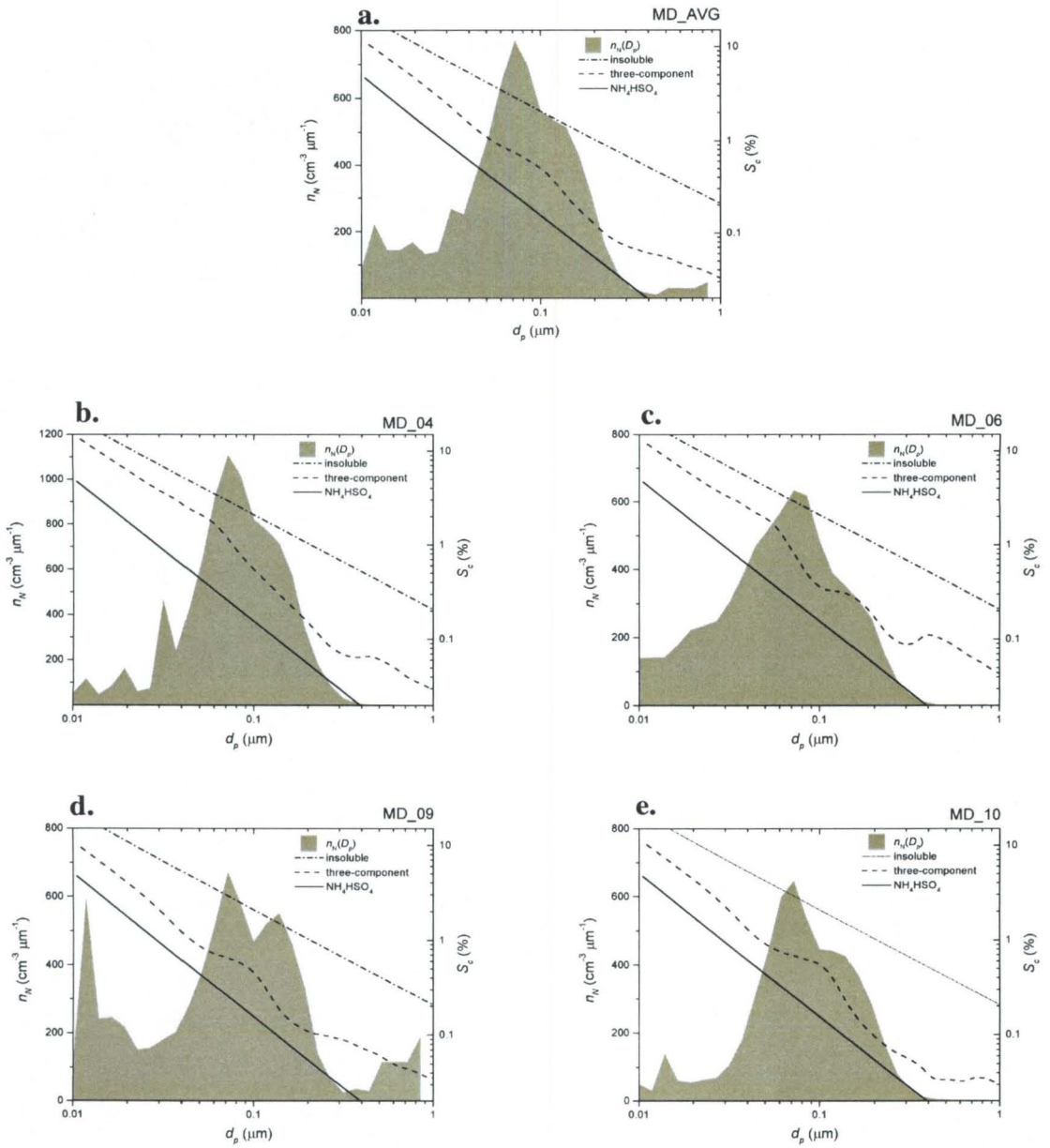

Figure 4.3. Number distributions (dN dlog^{-1} d_p), averaged for the respective MOUDI sample, are shown in gray. S_c was calculated for the three-component model using the chemical composition shown in Figure 4.2. Limiting cases for S_c are represented by pure NH_4HSO_4 and insoluble aerosol.

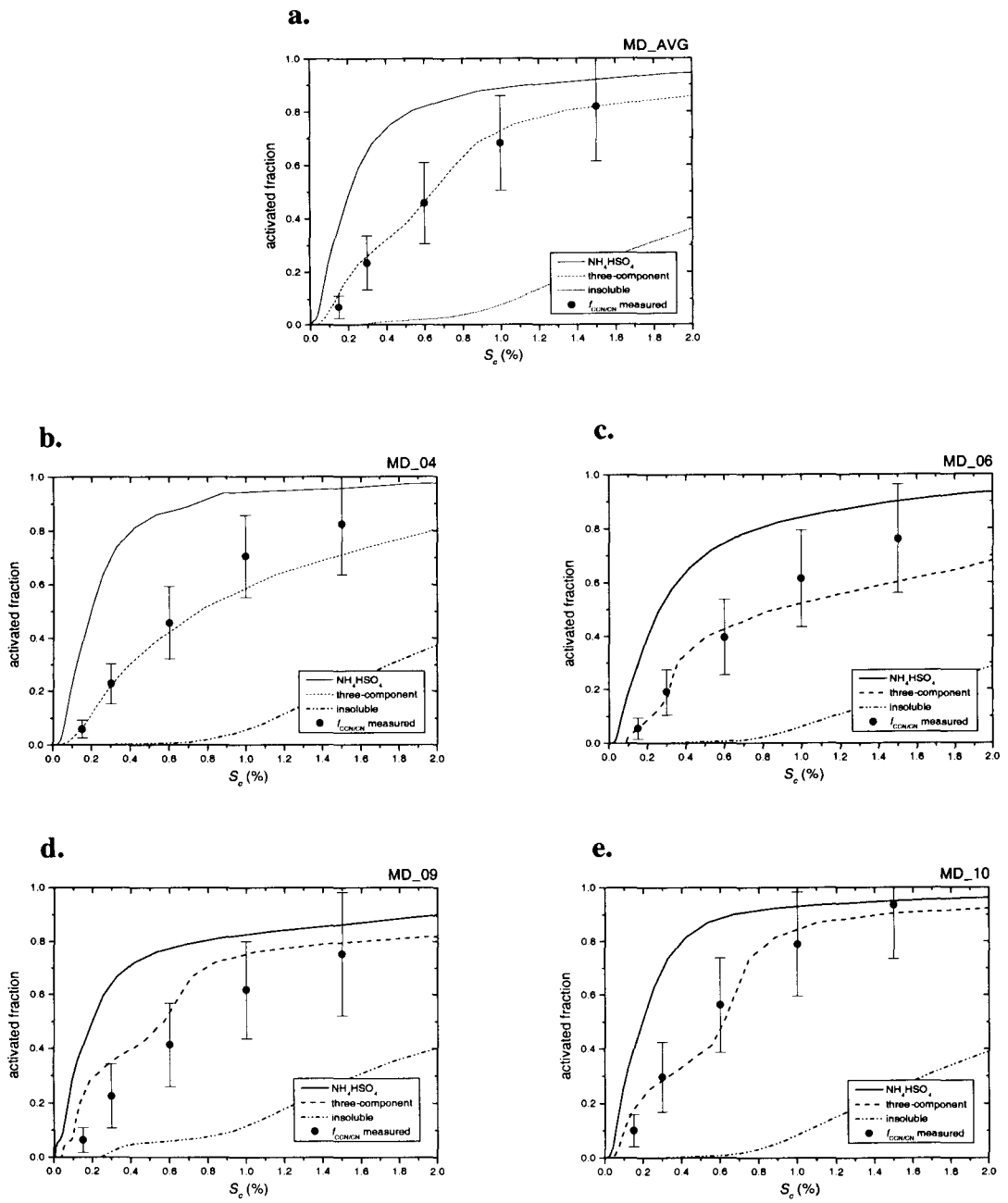

Figure 4.4. Fraction of aerosol expected to activate as CCN for a three-component model. The spectra were calculated using the relationship between $n_M(d_p)$ and S_c shown in Figure 4.3. Examples of pure NH_4HSO_4 and insoluble aerosol illustrate the limiting CCN spectra.

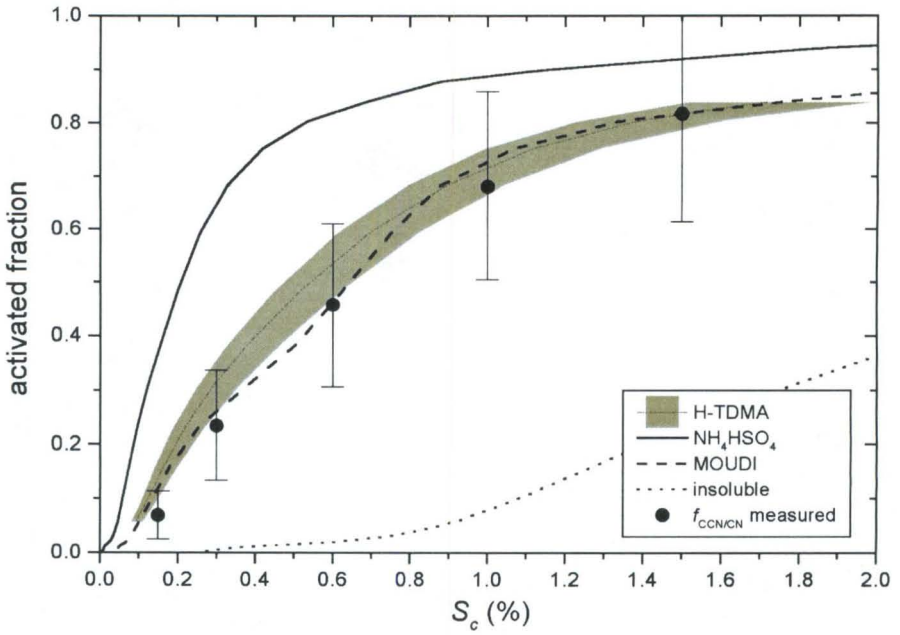

Figure 4.5. Average CCN spectra for MOUDI and H-TDMA soluble fractions of NH_4HSO_4. The gray area indicates the error in the spectra for the DMPS calculations.

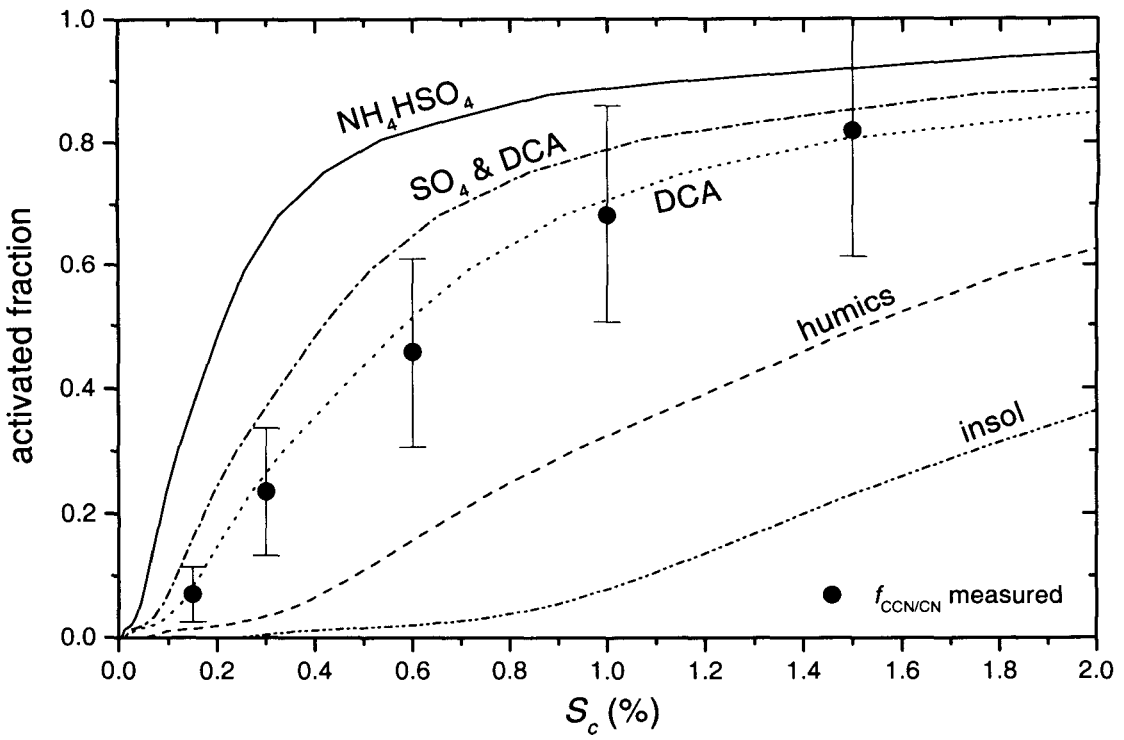

Figure 4.6. Potential effect of completely soluble WSOC on CCN spectra. The CCN spectra for a 40% soluble mass are labeled separately for DCA (140 g mol^{-1}) and humic substances (1400 g mol^{-1}). 'SO_4 & DCA' shows the combined contribution of NH_4HSO_4 and DCA. Pure NH_4HSO_4 and insoluble aerosol represent the limiting cases.

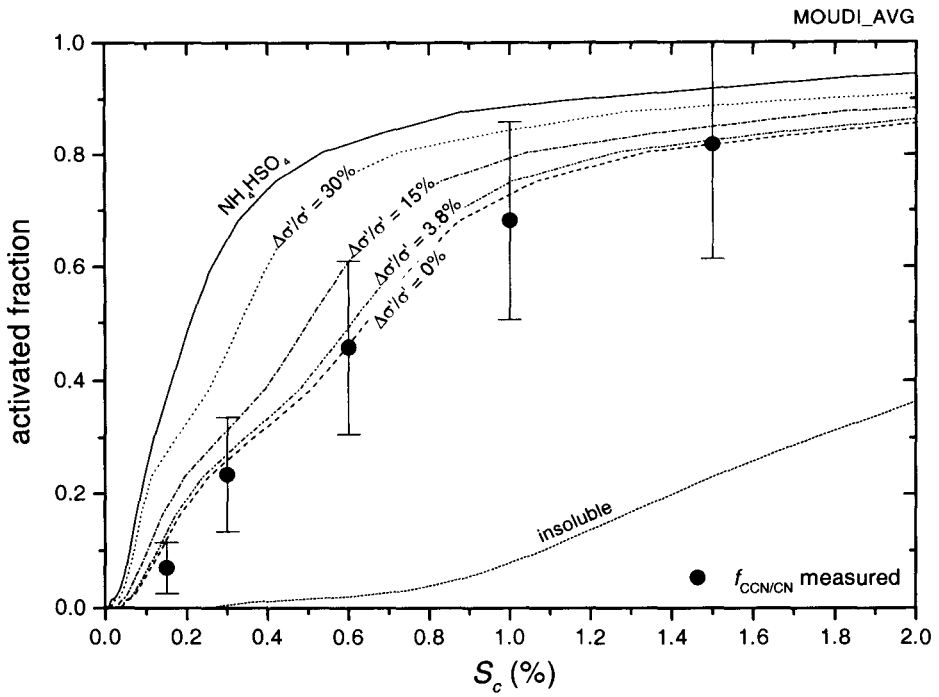

Figure 4.7. Effect of surface tension on CCN spectra. The change in surface tension $\Delta\sigma'/\sigma'$ was estimated using the relationship described by *Facchini et al.* [1999]. WSOC concentration of 0.1, 0.01, and 0.001 M DOC corresponded to $\Delta\sigma'/\sigma'$ of -3.8, -15 and -30%, respectively. Pure NH_4HSO_4 and insoluble aerosol represent the limiting cases.

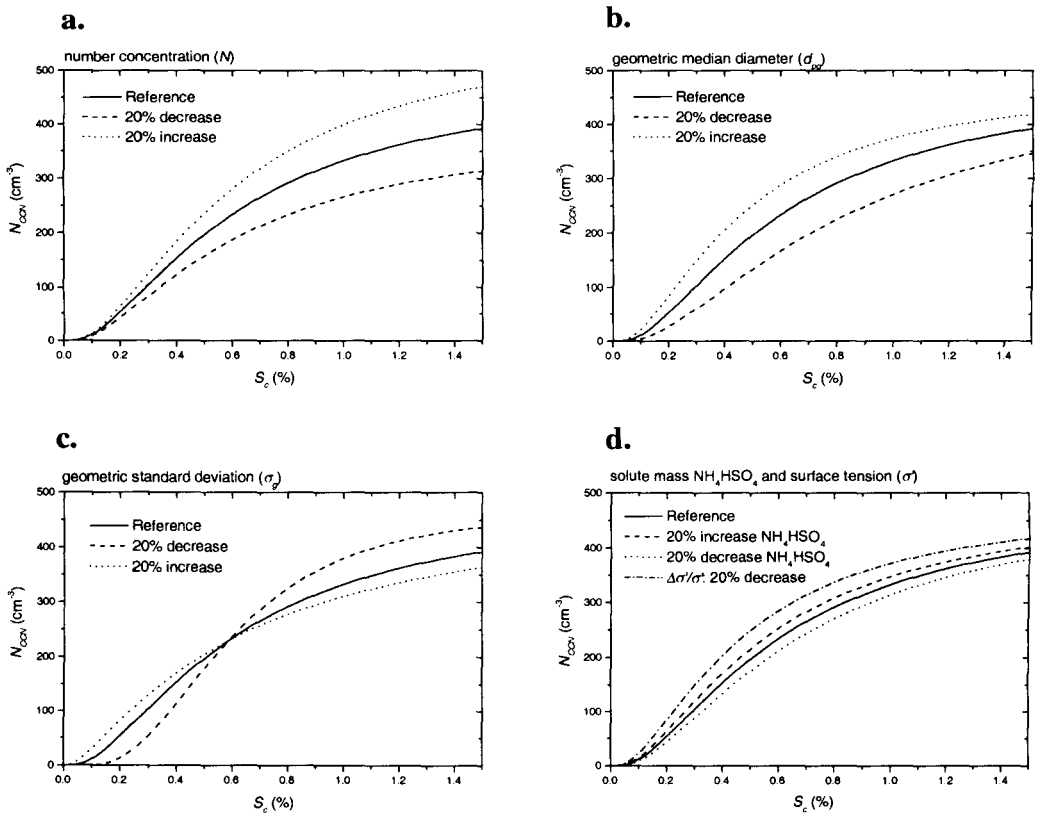

Figure 4.8. Modification in the reference CCN spectra due to changes in physical and chemical properties that affect CCN activity.

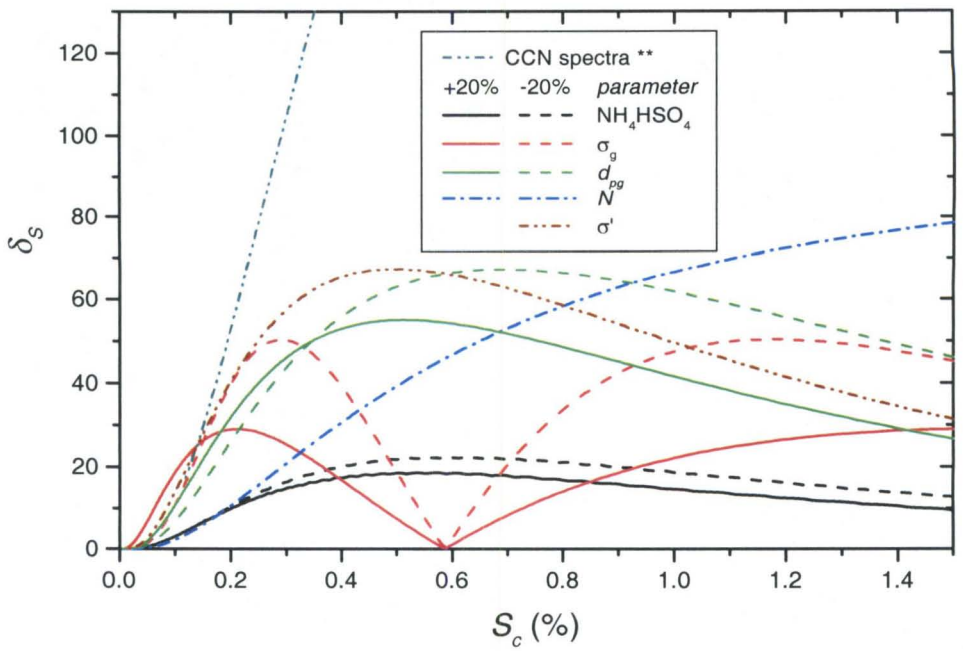

Figure 4.9. Sensitivity of CCN spectra on parameters that influence a particle's S_c.

** Reference CCN spectra compared to insoluble CCN spectra measures the effect of 15% addition of NH_4HSO_4

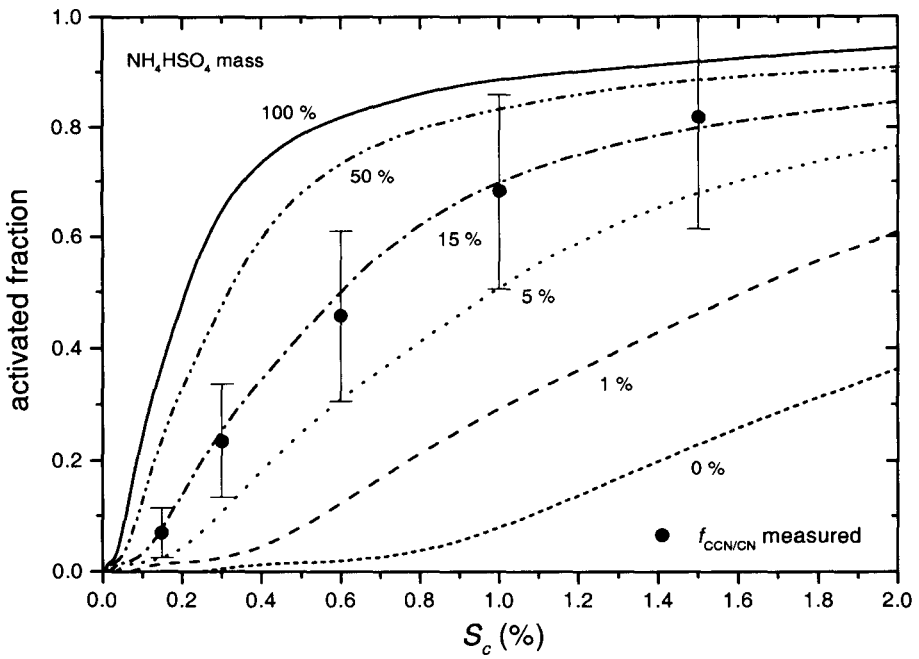

Figure 4.10. CCN spectra for a three-component model of various amounts of NH_4HSO_4. The spectra were calculated using the average number distribution (Figure 4.4a). The insoluble inorganic mass contribution was 5%; while the insoluble organic contribution depended on the NH_4HSO_4 mass fraction.

Appendix 4.A.

Recovering the mass distribution, $f(D_p)$, involves solving the Fredholm equation of the first kind for each impactor stage. The measured mass on an impactor stage i, m_i, is approximated by integrating the product of the i^{th} stage's kernel function, $k_i(D_p)$, and the j^{th} iteration of the mass distribution, $f_j(D_p)$,

$$m_{ij}(D_p) = \sum_{p=1}^{x} k_i(D_p) f_j(D_p) \delta \log D_p \qquad (4.A.1)$$

where $m_{ij}(D_p)$ is the calculated mass for stage i and iteration step j, D_p is the particle diameter at array number p, and x is the resolution at which the size distribution is evaluated, typically $x = 200$. The mass distribution, $f_{j+1}(D_p)$,

$$f_{j+1}(D_p) = f_j(D_p)\left[1 + a_i(D_p)\left(\frac{m_i}{m_{ij}} - 1\right)\right] \qquad (4.A.2)$$

is solved iteratively by multiplying the previous iteration's mass distribution, $f_j(D_p)$ to the product of a weighting function, $a_i(D_p)$, and an expression containing the ratio of the actual mass to the calculated mass.

Since the MOUDI impactor has narrow kernel functions, direct weighting of the correction factor with these functions tends to introduce the structure of the kernel functions in the resulting distribution. Hence, a weighting function proposed by *Winklmayr et al.* [1990] was defined as

$$a_i(D_p) = \left\{ \frac{k_i(D_p)}{\max[k_i(D_p)]} \right\}^r \tag{4.A.3}$$

The exponent r ranged between 0.3 and 0.7; a value of 0.7 produced the best results and was used for our inversions.

Smooth kernel curves for the MOUDI are derived by fitting a s-shaped function to the calibrated stage collection efficiency (Figure 4.A.1) reported by *Marple et al.* [1991]. The efficiency curves for each stage were estimated using

$$E(D_p) = \left[1 + \left(\frac{D_{50}}{D_p} \right)^{2s} \right]^{-1} \tag{4.A.4}$$

where D_p is the particle diameter, D_{50} is the 50% cutpoint, and s is the steepness factor; the values of these parameters are reported in Table 4.A.1. The kernel functions, shown in Figure 4.A.2, are derived from the efficiency curves in the order of the largest to smallest stage using the following expressions:

$$k_n(D_p) = E_n(D_p) \tag{4.A.5}$$

$$k_i(D_p) = E_i(D_p)\left[1 - E_{i+1}(D_p)\right] \times \ldots \times \left[1 - E_n(D_p)\right] \tag{4.A.6}$$

where $i = n - 1, n - 2, \ldots, 1$; n = number of stages

There is a lack of information at the endpoints, which makes it difficult to extrapolate the distribution beyond the D_{50}'s of the first and last stages. Therefore, artificial stages (stages 0, 1, 9, 10, 11) were introduced with the characteristics of the real stages. For the MOUDI impactor, stage 9 is the inlet stage, which we did not analyze, but the steepness factor for this stage is known. The steepness values for the other fictitious stages were estimated by a power log extrapolation from the previous stages. The only purpose of this method is to provide a continuation of the first-guess distribution.

Estimates for the fictitious stage loadings were calculated using multi-modal lognormal distributions that best represent the measured mass distribution of each component. This lognormal estimation procedure for the first-guess distribution is the primary difference between this inversion technique and that of *Winklmayr et al.* [1990]. A multi-modal mass distribution is described by the following expression:

$$\frac{\delta M}{\delta \log D_p} = \sum_{a=1}^{b} \frac{M_a}{\sqrt{2\pi}\ln\sigma_a} \exp\left[\frac{-\left(\ln D_p - \ln D_{pg,a}\right)^2}{2\ln^2 \sigma_a}\right] \qquad (4.A.7)$$

where M_a is the mass of a component, $D_{pg,a}$ is the median diameter, σ_a is the geometric standard deviation for a given mode a, and b is the number of modes. A maximum of two modes were used to describe the mass distributions and the parameters of the lognormal approximations are shown in Table 4.A.2.

Integration between the D_{50}'s of the artificial stages yields the estimated mass for the first-guess distribution. Stages were not allowed to be less than 10% of the adjacent stages in order to provide some continuity to the inversion routine. This constraint did

not effect the measured size distribution, but often increased the estimated loading for the fictitious stages at the tail of the lognormal distribution. A three-term moving average was used to smooth the first-guess distribution, $f_0(D_p)$:

$$f_0(D_p) = 0.25f_0(D_{p-1}) + 0.5f_0(D_p) + 0.25f_0(D_{p+1}) \quad (4.A.8)$$

$$f_0(D_1) = 0.75f_0(D_1) + 0.25f_0(D_2) \quad (4.A.9)$$

$$f_0(D_x) = 0.75f_0(D_x) + 0.25f_0(D_{x-1}) \quad (4.A.10)$$

where p are array numbers along the size distribution up to the x values in the array.

The size distribution is calculated between one half D_{50} of stage 0 and two times D_{50} of stage 11, but the results are used between one half the D_{50} of the smallest MOUDI stage (2) and two times that of the largest stage. The stages 1 through 9 were included in the iteration process. The iteration was complete when the error parameter (ζ) was less than five percent. The error parameter used by *Winklmayr et al.* [1990] was defined as

$$\xi^2 = \frac{1}{n}\sum_{i=1}^{n}\left[\frac{m_i - m_{ij}}{\delta m_i}\right]^2 \quad (4.A.11)$$

where δm_i is the absolute uncertainty for the mass on stage i, and n is the number of stages. m_i and m_{ij} are the measured and calculated mass loadings on stage i, respectively. Only the measured stages (2-8) determined the stopping criteria.

Table 4.A.1. Calibrated MOUDI impactor parameters for non-linear inversion routine.

Stage number	D_{50}[a] (St_{50})	D_{50}[b] (manufactured)	s
11[c]	-	*72*	*1.6*
10[c]	-	*36*	*2.7*
9[c]	-	18	4.6
8	3.62	3.20	17.3
7	2.03	1.80	10.0
6	1.13	1.00	10.9
5	0.633	0.560	10.4
4	0.373	0.330	5.3
3	0.198	0.175	4.9
2	0.105	0.093	3.8
1[c]	-	*0.047*	*2.9*
0[c]	-	*0.023*	*2.2*

[a] calculated from theory (St_{50} = Stokes number for D_{50})

[b] values given for manufactured version of our impactor

[c] fictitious stages used for extrapolation

abbreviation: s, steepness parameter

Table 4.A.2. Parameter for multi-modal lognormal distributions (4.A.7) that represent the data presented in Table 4.3.

		first mode			second mode		
Component		M_1 (ng m^{-3})	$D_{pg,1}$ (μm)	$\sigma_{g,1}$	M_2 (ng m^{-3})	$D_{pg,2}$ (μm)	$\sigma_{g,2}$
Average	mass	2151	0.35	1.77	16066	4.29	2.04
	sulfate	399	0.33	1.57	266	3.43	2.43
	oxides	1581	2.99	2.48	-	-	-
MD_4	mass	2514	0.29	1.84	11254	3.85	2.16
	sulfate	389	0.31	1.64	241	3.20	2.36
	oxides	1218	3.06	2.50	-	-	-
MD_6	mass	2158	0.37	1.80	15717	4.55	1.96
	sulfate	240	0.34	1.51	181	4.11	2.07
	oxides	950	4.30	2.35	-	-	-
MD_9	mass	1872	0.39	1.64	16325	4.24	1.97
	sulfate	364	0.32	1.56	254	3.30	2.36
	oxides	1535	2.70	2.56	-	-	-
MD_10	mass	1888	0.35	1.60	21043	4.33	2.10
	sulfate	585	0.35	1.55	415	3.16	3.01
	oxides	2669	2.70	2.46	-	-	-

M_i is the mass for mode i, D_{pg} is the geometric median diameter, and $\sigma_{g,i}$ is the geometric standard deviation for mode i.

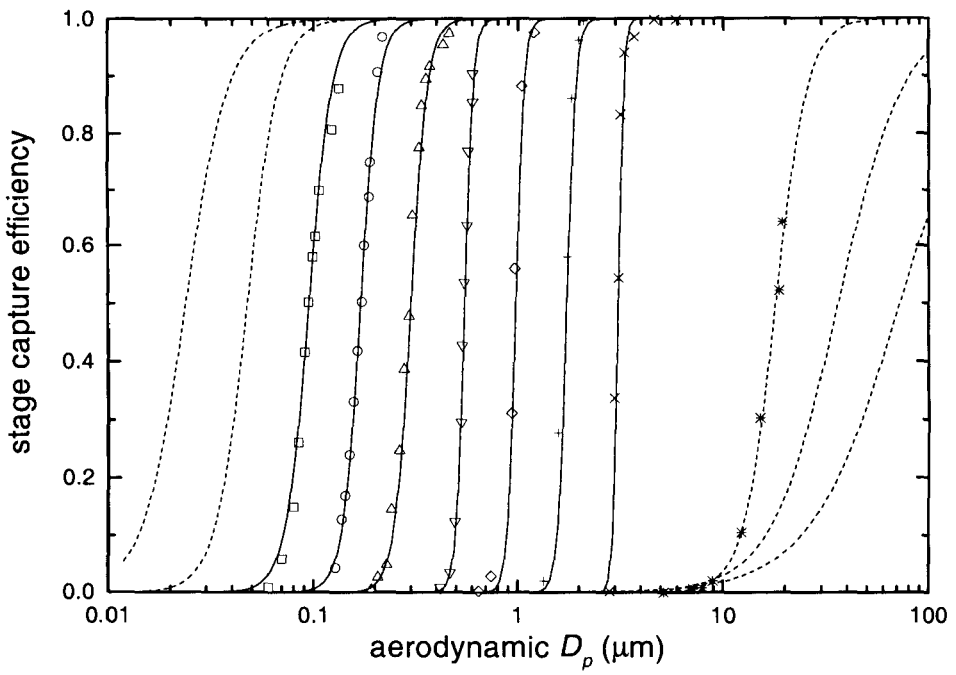

Figure 4.A.1. Calibrated efficiency functions for the symetric curve (4.A.4). The dotted curves correspond to the artificial stages.

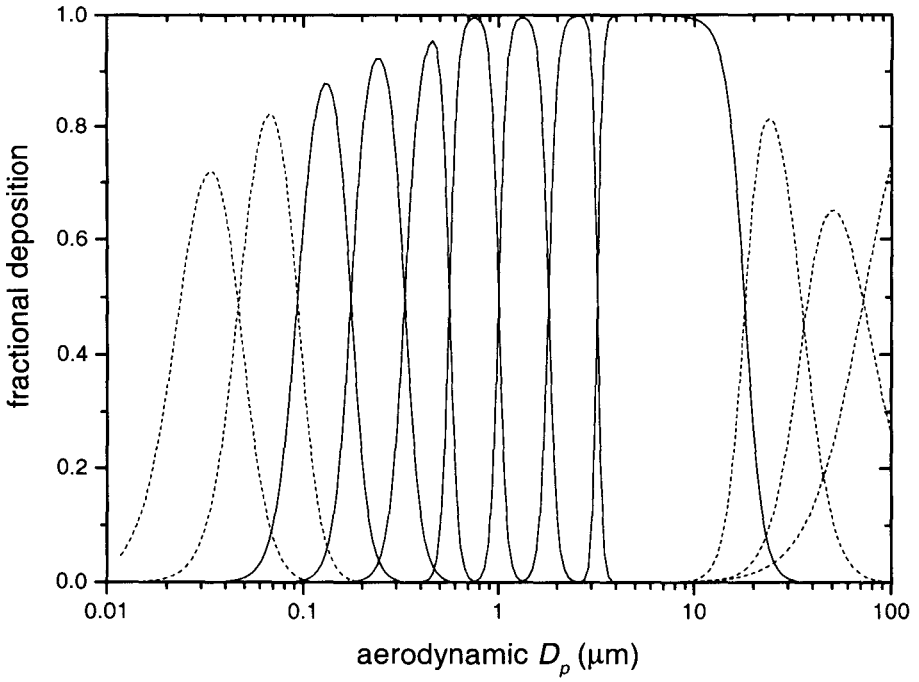

Figure 4.A.2. Kernel functions for the manufactured version of the MOUDI impactor. The dotted curves correspond to the artificial stages.

Appendix 4.B.

Definition of variables:

$a_i(D_p)$	kernel weighting function for stage i
D_{50}	50% cutoff wet diameter
d_{50}	50% cutoff dry diameter
D_p	wet particle diameter
d_p	dry particle diameter
D_{pc}	critical droplet diameter
d_{pg}	geometric median particle diameter
$E_i(D_p)$	efficiency function for MOUDI stage i
$f_{CCN/CN}$	fraction of aerosol that serve as CCN
$f_j(D_p)$	inverted mass distribution for iteration j
k	Boltzmann constant
$k_i(D_p)$	kernel function for stage I
M	aerosol mass concentration
M_i	molecular weight of species i
m_i	mass of species i
M_w	molecular weight of water
N	aerosol number concentration
n	number of MOUDI stages
N_{3010}	measured N from the CPC_{3010}
N_{CCN}	CCN concentration
N_{DMPS}	integrated N from DMPS measurements of $n_N(d_p)$

$n_M(D_p)$	mass distribution (wet diameter)
$n_M(d_p)$	mass distribution (dry diameter)
$n_N(d_p)$	number distribution (dry diameter)
N_R	Reference N_{CCN}
N_X	N_{CCN} at X% S_c
N_Δ	N_{CCN} for parameter change
RH	relative humidity
s	steepness factor
S_c	critical supersaturation
St_{50}	Stokes number for D_{50}
S_v	supersaturation
S_v^{eq}	equilibrium supersaturation
T	temperature
$\Delta\,\sigma'/\,\sigma'$	change in surface tension
Φ	osmotic coefficient
δ_S	relative change in CCN spectra
ν_i	van't Hoff factor
ρ'	density of aqueous solution
ρ_i	density of species i
ρ_w	density of water
σ'	surface tension of solution
σ_g	geometric standard deviation
ζ	stopping error parameter

Chapter 5

Airborne measurements of cloud condensation nuclei in the Amazon Basin

Abstract

Airborne cloud condensation nuclei (CCN) concentrations were measured during Coorperative Large Scale Biosphere-Atmosphere Experiment over Amazonas (LBA) in September 1999. The experiment followed a flight plan that transected the Amazon Basin and allowed for sampling of different air masses ranging from regional haze and smoke plumes of biomass burning to relatively clean environments along the northeastern coast and remote sections of the rain forest. Biomass burning aerosol does serve as CCN and differences in CCN activity were found between young and aged smoke. Vertical profiles of CCN up to 5 km above sea level were also obtained. New particle formation at cloud tops was observed and could be an important source of aerosol in the Amazon Basin.

5.1. Introduction

The process of deforestation and agricultural clearing in tropical regions including the Amazon Basin and the African savanna involves large-scale dry-season burning, which is an important source of gaseous and particulate emissions [*Andreae et al.*, 1998; *Andreae et al.*, 1988; *Cachier et al.*, 1996; *Lacaux et al.*, 1993]. Most fires in the Brazilian Amazon are the reburning of forests cleared in previous years and to the conversion to pastures for cattle grazing or agricultural purposes. There are few direct measurements of the activity of biomass burning smoke as CCN. *Warner and Twomey* [1967] observed elevated CCN concentrations in the plumes of sugar cane fires in Australia and in laboratory burns of sugar cane leaves. Elevated concentrations of cloud droplets associated with these plumes were also observed in marine cumuli off the west coast of Australia. Their data did not include measurements of the total number concentrations of aerosol particles (N_{CN}), so the fraction of the smoke particles active as CCN cannot be calculated. Data were also taken during brushfire events in the Ivory Coast [*Désalmand*, 1985]. These measurements were limited to two events on different days and showed that from 25% to 100% of submicron particles are active as CCN. *Radke et al.* [1988; 1978] have observed high levels of CCN activity in field observations of Northern Hemisphere biomass fires. High CCN concentrations were measured in Kuwait fire plumes [*Hudson and Clarke*, 1992]. *Novakov and Corrigan* [1996] reported that pure organic smoke from cellulose is able to form CCN without being associated to sulfates or other inorganic compounds.

Airborne CCN measurements [*Delene et al.*, 1998; *Hegg*, 1995; *Hudson and Svensson*, 1995; *Raga and Jonas*, 1995] have provided information on the spatial distribution of CCN. The reported data contribute to the knowledge of large-scale distributions of aerosol emitted from vegetation fires and their contribution to CCN activity. Parametrization of cloud cover and its associated variability and uncertainty constitutes a major obstacle to the development of global climate models. Variations in CCN may cause the most notable effects when superimposed in relatively clear environments, such as is the case of biomass burning emissions in the Amazon Basin [*Ackerman et al.*, 1994; *Albrecht*, 1989; *Roberts et al.*, 2001] (see Chapter 6). This paper presents the results of the first airborne CCN measurements in the troposphere related to biomass burning in the Amazon Basin.

5.2. Aircraft Experiment

Cloud condensation nuclei (CCN) concentrations were measured aboard INPE's (Instituto Nacional de Pesquisas Espacias) EMB110 Bandeirante twin-engine plane during the Coorperative Large Scale Biosphere-Atmosphere Experiment over Amazonas (LBA). Sampling occurred from September 2 to 14, 1999 during the peak fire activity for most of the Brazilian Amazon. Table 5.1 provides supplementary information on the 18 flights. The flight missions (Figure 5.1) included transects and profiles to characterize the horizontal and vertical structure of the atmosphere. Transect flights were often at low altitude (1000 m) in conjunction with digital land/vegetation classification experiments. The aircraft was not pressurized, and thus imposed a maximum limit of 4,500 m in flight

altitude. Vertical profiles were obtained at selected sites and followed a spiral formation that lasted 20 to 30 minutes.

The first half of the flight plan transected the Amazon Basin along the band of deforestation, which is the southeastern edge of the rain forest where land-use change is most intense. The flights from Cuiabá to São Luís along the band of deforestation allowed for sampling of regional haze and smoke plumes of biomass burning. Measurements during the second half of the experiment took place in relatively clean environments along the northeastern coast and remote sections of the rain forest. Figure 5.1 shows the flight plan coupled with Geostationary Operational Environmental Satellite Automated Biomass Burning Algorithm (*GOES-8 ABBA)* fire data to illustrate the extent of the biomass burning during this campaign.

5.3. Instrumentation

CCN measurements were made using a static thermal-gradient diffusion instrument, which operated similarly to the chamber described by *Lala and Jiusto* [1977]. CCN number concentrations (N_{CCN}) were determined every 25 seconds at a supersaturation between 0.2% and 1.0% S_v. The CCN counter operated at a single supersaturation (0.6% or 1.0% S_v) during profiles to optimize vertical resolution. Supersaturation cycles between 0.2% and 1.0% S_v were periodically taken during transit flights and transects to obtain CCN spectra of the regional smoke haze.

The CCN counter in this study was fitted with a photodiode laser and digital camera to measure droplet concentrations (see Chapter 2). Activated CCN particles

quickly grow to several micrometers in diameter and gravitationally settle out of the chamber. A 670 nm photodiode laser illuminates the activated droplets while the digital camera, normal to the laser beam, registers images every second during the supersaturation cycle. The CCN concentration at a particular supersaturation is determined during by data processing. Imaging software (e.g., Matlab) is used to automatically determine the number of activated CCN in each picture. The actual CCN concentration is based on the picture with the highest number of particles and on the calibrated illuminated volume. The calibration procedure involved generating a quasi-monodisperse aerosol of a known concentration and counting the number of activated droplets in the in the digital image. An error analysis indicates, that for typical aerosol spectra, the overall measurement error is approximately ±15% at 1.5% S_v and ±30% at 0.15% S_v. These measured analytical errors agree will with theoretical estimates by *Nenes et al.* [2001].

The airborne experiment included other real-time aerosol instrumentation, which complimented the CCN measurements. A condensation particle counter (TSI CPC 3010) measured aerosol concentrations (N_{CN}) of particles with a diameter larger than 10 nm. N_{CN} serves as a reference aerosol concentration and assesses the activation efficiency of CCN. A three-wavelength integrating nephelometer (TSI Model 3563) measured hemispherical aerosol scattering ratios every second. A seven-wavelength Aethalometer (Magee Scientific) measured black carbon (BC) concentrations based on the optical attenuation of a beam of light transmitted through the sample when collected on quartz-fiber filters.

The aethalometer and nephelometer sampled directly from individual isokinetic aerosol inlets. The CCN and CPC counters shared a common inlet and were separated by a reduced-angle Y-tee to minimize biasing the aerosol size distribution. The CCN inlet was attached downstream of the CPC inlet and a bypass was added to minimize the effects of the discrete sampling by the CCN counter. Conical isokinetic aerosol inlets were located below the aircraft and as close as possible (< 1.5 m) from the instrumentation to minimize particle losses and prevent contamination. Reported measurements have not been corrected for standard temperature-pressure (STP) conditions and are expressed as ambient concentrations.

Ancillary measurements included geographical position and altitude of the aircraft from a Global Positioning System (GPS), and a radiosonde unit (VAISALA) to measure pressure, temperature and relative humidity; an additional temperature measurement was obtained by a fast-response thermo-couple. The pressure and relative humidity sensors were calibrated using control tower information obtained shortly before take off of each flight. The relative humidity data was adjusted to reflect the relative humidity at the temperature of the thermo-couple temperature sensor. Water vapor concentrations were determined from the relative humidity and used to correct for wet-adiabatic effects in the potential temperature calculations.

5.4. Results and Discussion

The flight trajectories can be roughly separated into biomass burning (Cuiabá to São Luís) and rain forest (São Luís to Porto Velho) transects. Although biomass burning

was observed during the latter part of the rain forest transect, the section from São Luís to Manaus showed little influence of biomass burning aerosol as indicated by GOES-8 fire data and backward wind trajectories. Smoke aerosol may produce CCN, although the ratio of N_{CCN} to N_{CN} ($f_{CCN/CN}$) decreases for biomass burning aerosol compared to the wet season. The following sections take a closer look at selected flight missions and discuss important results of CCN properties in the Amazon Basin.

5.4.1. Profile: near Santarém, Pará – September 9, 18:43 - 19:07 GMT (2.71 °S 54.80 °W)

The profile near Santarém, Para was characterized by convective activity as indicated by the surrounding non-precipitating *cumulus mediocris* and *congestus* clouds (Figure 5.2). The atmosphere exhibited conditional stability as most clouds were low-lying *mediocris*, cottonball-like structures, but a few scattered *congestus* cloud columns extended to nearly 600 mbar (4200 m). The cloud base, which occurred at 920 mbar (1000 m; point A in Figures 5.2 and 5.3), was characterized by the sudden decrease in the atmospheric water vapor content. The tops of the mediocris clouds, at 800 mbar (2000 m; point B in Figures 5.2 and 5.3), coincided with the reduction in aerosol concentrations and mark the top of the well-developed boundary layer (BL). The nearby congestus columns reached 4200 m and probably did not contain ice nuclei as their tops were under the freezing level. The profile occurred during the mid-afternoon (local time = GMT – 3) and the aircraft avoided flying through clouds during the measurements.

Aerosol concentrations in the BL were relatively low ($N_{CN} \approx 1500$ cm^{-3}) due to the proximity to the Atlantic coast and a recent precipitation event. Uniform aerosol concentrations within the BL indicate that ground-level CCN concentrations are representative of concentrations at the cloud base and throughout the mixed layer. Similar measurements have been reported [*Delene et al.*, 1998; *Hudson*, 1982]. These results suggest that ground-based measurements can be used for modeling the BL during periods of convective activity. The particle enhancement at the BL top shows a significant increase in $f_{CCN/CN}$, which indicates a modification of the CCN by cloud processing [*Bower and Choularton*, 1993; *Hegg et al.*, 1993; *Hobbs*, 1971; *Hoppel et al.*, 1990; *Odowd et al.*, 1997]. Maximum aerosol concentrations were observed below the boundary layer and small peaks were often located between small temperature inversions or above a slight increase in the gradient in temperature profiles. Such stable layers are expected in the dry season when stable anti-cyclone tropospheric circulation prevails in the region.

The ratio of $CCN_{1.0}$ (at 1% S_v) to CN number concentrations ($f_{CCN/CN}$) gives useful insight to cloud processes and notable differences are observed throughout the profile. There is a slight increase in $f_{CCN/CN}$ within the BL as values increase near ground level to the top of the BL and mediocris clouds. The latter ratio is nearly constant in the neighboring congestus cloud columns until CCN concentrations drop to nearly zero at their tops. The absence of an increase of N_{CCN} at the two peaks in N_{CN} (720 and 780 mbar; points C and D in Figures 5.2 and 5.3) is consistent with new particle formation. This relationship has been observed by others [*Hegg*, 1991; *Hegg et al.*, 1993; *Hegg et al.*, 1990; *Schäfer and Georgii*, 1994]. The reduction in N_{CCN} is consistent with new

particle formation, since these ultrafine particles are too small to serve as CCN. Particle diameters for $CCN_{1.0}$ are in the range of 45 to 60 nm diameter depending on their specific chemical composition. The TSI CPC 3010 counter measures aerosols with diameters larger than 10 nm, which is on the large end of the ultrafine particles. Thus, the measurements obtained with the TSI 3010 are most likely capturing the tailing edge of the lognormal distribution of the ultrafine aerosol number distribution. Simultaneous measurements by an instrument with a smaller size detection limit (i.e., TSI CPC 3025; $D_{p,50}$ = 3 nm) would have been necessary to completely characterize these peaks. Previous studies have noted that a favorable situation for new particle nucleation arises when the preexisting surface area is low [*Hegg et al.*, 1993]. Cloud scavenging in this region appears to have removed accumulation mode aerosol as CCN. New particle formation near cloud borders may be the primary natural aerosol generation mechanism that maintains N_{CCN} and N_{CN} as cloud processes scavenge aerosols.

5.4.2. Transect: Alta Floresta, Mato Grosso to Palmas, Tocantins; September 6, 14:06 to 18:22 GMT (9.872 °S 56.105 °W - 10.205 °S 48.343 °W)

The transect from Alta Floresta to Palmas (Figure 5.4) characterized biomass burning activity in the region of intense deforestation along southeastern perimeter of the rain forest. Sampling occurred within the boundary layer at ca. 900 mbar. Intense fire activity is clearly evident during the first half of the transect by the high and variable aerosol concentrations. Total aerosol concentrations often exceeded 10^4 cm^{-3} during the plume events and averaged around 4500 cm^{-3} in the regional haze.

The smoke aerosol in Mato Grosso (i.e., during the first half of the transect) was younger than the regional haze in Tocantins (i.e., second half of the transect). Significant differences in the ratio of CCN to total aerosol ($f_{CCN/CN}$) are observed between young and aged smoke. Smoke particles evolve rapidly after emission and their physical and chemical properties indicate their age. Aged smoke is larger and contains more water-soluble species than younger smoke [*Reid and Hobbs*, 1998]; and, as a consequence, serves more readily as CCN. The change in $f_{CCN/CN}$ is especially visible during the large plume in the second half of the transect (time = 249.715). In the regional smoke haze, $f_{CCN/CN}$ is around 0.5 and becomes smaller during the plume event as $N_{CN} > 15000$ cm^{-3} and $N_{CCN} \approx 4000$ cm^{-3}.

5.5. Conclusions

Biomass burning is a strong source of CCN, although the ratio of CCN to total aerosol concentration is less than during the wet season. Aged smoke is larger and contains more water-soluble species than younger smoke; hence, serves more readily as CCN. Verticle profiles also indicate that the boundary layer is well mixed and ground-level aerosol concentrations are representative of concentrations at the cloud base. The boundary layer is clearly marked by the decrease in aerosol concentrations and the free troposphere exhibits uniform aerosol concentrations with height except during convective activity. New particle formation at the cloud tops was observed, which could be an important source of aerosol in the Amazon Basin.

5.6. References

Ackerman, A.S., O.B. Toon, and P.V. Hobbs, Reassessing the dependence of cloud condensation nucleus concentration on formation rate, *Nature*, *367*, 445-447, 1994.

Albrecht, B.A., Aerosols, cloud microphysics, and fractional cloudiness, *Science*, *245*, 1227-1230, 1989.

Andreae, M.O., T.W. Andreae, H. Annegarn, F. Beer, H. Cachier, P. Le Canut, W. Elbert, W. Maenhaut, I. Salma, F.G. Wienhold, and T. Zenker, Airborne studies of aerosol emissions from savanna fires in southern Africa, 2, Aerosol chemical composition, *J. Geophys. Res.*, *103*, 32,119-32,128, 1998.

Andreae, M.O., E.V. Browell, M. Garstang, G.L. Gregory, R.C. Harriss, G.F. Hill, D.J. Jacob, M.C. Pereira, G.W. Sachse, A.W. Setzer, P.L.S. Dias, R.W. Talbot, A.L. Torres, and S.C. Wofsy, Biomass burning emissions and associated haze layer over Amazonia, *J. Geophys. Res.*, *93* (D2), 1509, 1988.

Bower, K.N., and T.W. Choularton, Cloud processing of the cloud condensation nucleus spectrum and its climatological consequences, *Q. J. R. Meteorol. Soc.*, *119*, 655, 1993.

Cachier, H., C. Liousse, M.-H. Pertuisot, A. Gaudichet, F. Echalar, and J.-P. Lacaux, African fire particulate emission and atmospheric influence, in *Biomass Burning and Global Change*, edited by J.S. Levine, pp. 428-440, MIT Press, Cambridge, Mass., 1996.

Delene, D.J., T. Deshler, P. Wechsler, and G.A. Vali, A balloon-borne cloud condensation nuclei counter, *J. Geophys. Res.*, *103* (D8), 8927, 1998.

Désalmand, F., An attempt to characterize a relationship between supersaturation spectrum, size spectrum and solubiliity of CCN observed over a tropical rain forest, *J. Atmos. Sci.*, *42* (5), 472, 1985.

Hegg, D.A., Particle production in clouds, *Geophys. Res. Lett.*, *18*, 995-998, 1991.

Hegg, D.A., The cloud condensation nucleus-sulfate mass relationship and cloud albedo, *J. Geophys. Res.*, 1995.

Hegg, D.A., R.J. Ferek, and P.V. Hobbs, Aerosol size distributions in the cloudy atmospheric boundary layer of the North Atlantic Ocean, *J. Geophys. Res.*, *98*, 8841-8846, 1993.

Hegg, D.A., L.F. Radke, and P.V. Hobbs, Particle production associated with marine clouds, *J. Geophys. Res.*, *95*, 13917-13926, 1990.

Hobbs, P.V., Simultaneous airborne measurements of cloud condensation nuclei and sodium- containing particles over the ocean, *Q. J. R. met. Soc.*, *97*, 263-271, 1971.

Hoppel, W.A., J.W. Fitzgerald, G.M. Frick, R.E. Larson, and E.J. Mack, Aerosol size distributions and optical properties found in the marine boundary layer over the Atlantic Ocean, *J. Geophys. Res.*, *95*, 3659-3686, 1990.

Hudson, J., and G. Svensson, Cloud microphysical relationships in California marine stratus, *J. Appl. Meteorol.*, *34*, 2655-2666, 1995.

Hudson, J.G., Correlation between surface and cloud base CCN spectra in Montana, *J. Appl. Meteorol.*, *21*, 1427, 1982.

Hudson, J.G., and A.D. Clarke, Aerosol and cloud condensation nuclei measurements in the Kuwait plume, *J. Geophys. Res.*, *97*, 14,533-14,536, 1992.

Lacaux, J.-P., H. Cachier, and R. Delmas, Biomass burning in Africa: An overview of its impact on atmospheric chemistry, in *Fire in the Environment: The Ecological, Atmospheric, and Climatic Importance of Vegetation Fires*, edited by P.J. Crutzen, and J.G. Goldammer, pp. 159-191, J. Wiley & Sons, Chichester, England, 1993.

Lala, G.G., and J.E. Jiusto, An automatic light scattering CCN counter, *J. Appl. Meteor.*, *16* (4), 413-418, 1977.

Nenes, A., P. Chuang, R. Flagan, and J. Seinfeld, A theoretical analysis of cloud condensation nucleus (CCN) instruments, *J. Geophys. Res.*, *106*, 3449-3474, 2001.

Novakov, T., and C.E. Corrigan, Cloud condensation nucleus activity of the organic component of biomass smoke particles, *Geophys. Res. Lett.*, *23* (16), 2141-2144, 1996.

Odowd, C.D., J.A. Lowe, M.H. Smith, B. Davison, N. Hewitt, and R.M. Harrison, Biogenic sulphur emissions and inferred non-sea-salt-sulphate cloud condensation nuclei in and around Antarctica, *J. Geophys. Res.*, *102* (11D), 12839-12854, 1997.

Radke, L.F., D.A. Hegg, J.H. Lyons, C.A. Brock, P.V. Hobbs, R. Weiss, and R. Rasmussen, Airborne measurements on smokes from biomass burning, in *Aerosols and Climate*, edited by P.V. Hobbs, and M.P. McCormick, pp. 411-422, A. Deepak Publishing, Hampton, VA, 1988.

Radke, L.F., J.L. Stith, D.A. Hegg, and P.V. Hobbs, Airborne studies of particles and gases from forest fires, *Journal of Air Pollution Control Association*, *28*, 30-34, 1978.

Raga, G., and P. Jonas, Vertical distribution of aerosol particles and CCN in clear air around the British Isles, *Atmos. Environ.*, *29*, 673-684, 1995.

Reid, J.S., and P.V. Hobbs, Physical and optical properties of young smoke from individual biomass fires in Brazil, *J. Geophys. Res.*, *103*, 32,013-32,030, 1998.

Roberts, G., J. Zhou, P. Artaxo, and M. Andreae, Cloud condensation nuclei in the Amazon Basin: "Marine" conditions over a continent?, *in press, Geophys. Res. Lett.*, 2001.

Schäfer, B., and H.-W. Georgii, Airborne measurements of condensation nuclei and cloud condensation nuclei above the alpine foothills, *Beitr. Phys. Atmosph.*, *67* (4), 335, 1994.

Warner, J., and S. Twomey, The production of cloud nuclei by cane fires and the effect on cloud drop concentrations, *J. Atmos. Sci.*, *24*, 1967.

Table 5.1. Mission flights data for the Banderante during the 1999 LBA dry season experiment.

		Itinerary	
No.	Date	Start	End
1	2 Sept. Fl. 1	SJ dos Campos, SP	Ribeirão Preto, SP
2	2 Sept. Fl. 2	Ribeirão Preto, SP	Goiânia, GO
3	3 Sept.	Goiânia, GO	Cuiabá, MT
4	4 Sept.	Cuiabá, MT	Alta Floresta, MT
5	5 Sept.	Alta Floresta, MT	Alta Floresta, MT
6	6 Sept.	Alta Floresta, MT	Palmas, TO
7	7 Sept.	Palmas, TO	São Luís, MA
8	8 Sept.	São Luís, MA	Belém, PA
9	9 Sept. Fl. 1	Belém, PA	Santarém, PA
10	9 Sept. Fl. 2	Santarém, PA	Santarém, PA
11	10 Sept.	Santarém, PA	Manaus, AM
12	11 Sept. Fl. 1	Manaus, AM	Manaus, AM
13	11 Sept. Fl. 2	Manaus, AM	Rio Branco, AC
14	12 Sept. Fl. 1	Rio Branco, AC	Rio Branco, AC
15	12 Sept. Fl. 2	Rio Branco, AC	Rio Branco, AC
16	13 Sept. Fl. 1	Rio Branco, AC	Porto Velho, RO
17	13 Sept. Fl. 2	Porto Velho, RO	Porto Velho, RO
18	14 Sept.	Porto Velho, RO	Ji-Paraná, RO

Typical vertical profile altitude range is 500 to 4000 m.

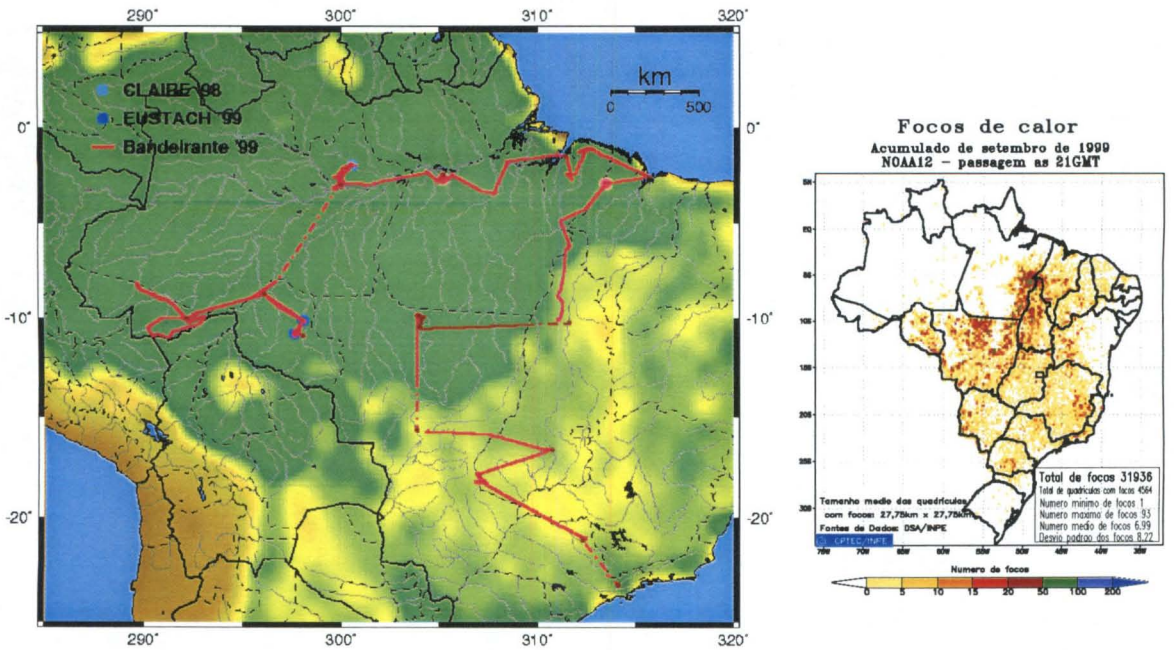

Figure 5.1. Flight missions for the Bandeirante aircraft during LBA from September 2 to 14, 1999. Solid lines indicate the transit flights.

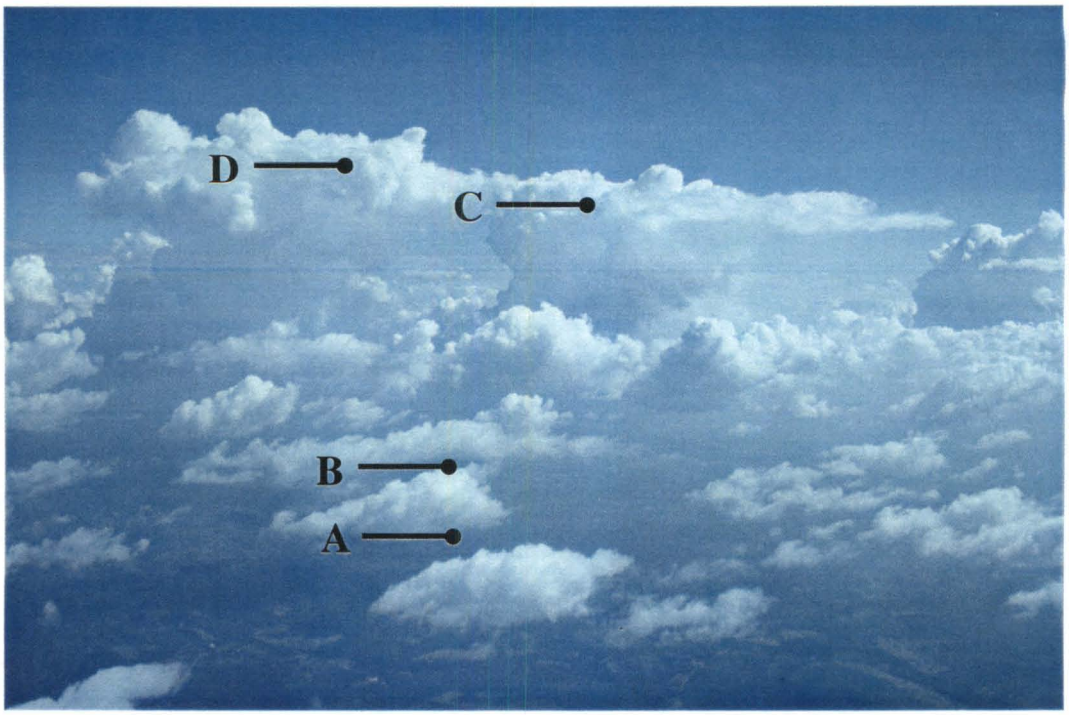

Figure 5.2. Picture of profile near Santarém. A, B, C and D correspond to the levels in Figure 5.3.

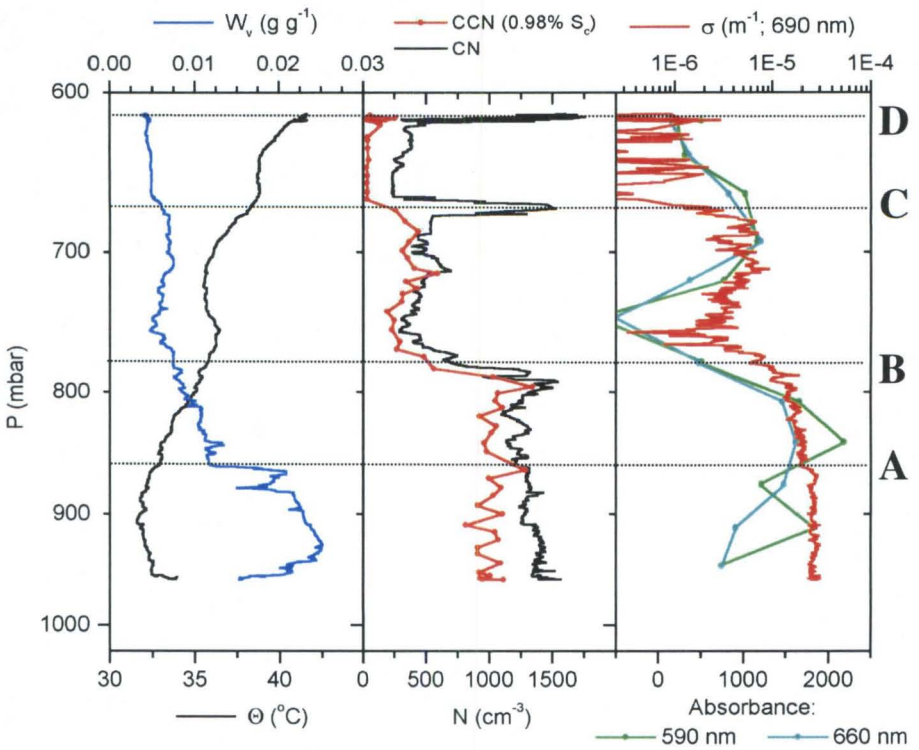

Figure 5.3. Profile: near Santarém, Pará – September 9, 18:43 - 19:07 GMT (2.708 °S 54.803 °W). The letters (A, B, C and D) correspond to regions of the picture in Figure 5.2.

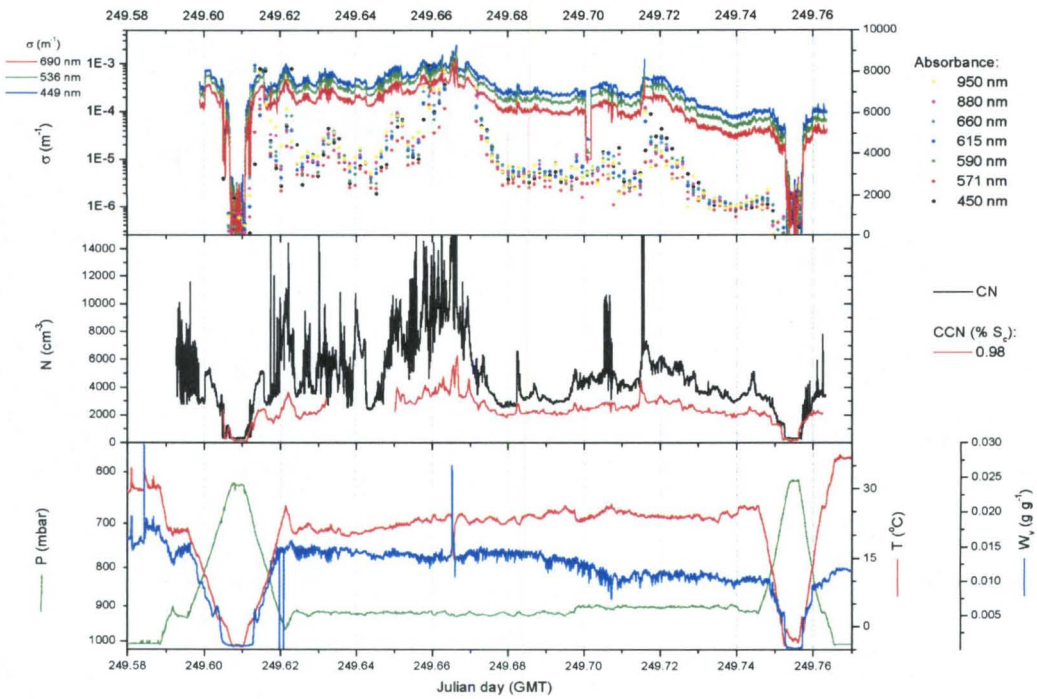

Figure 5.4. Time series: Alta Floresta, Mato Grosso to Palmas, Tocantins; September 6, 14:06 to 18:22 GMT (9.872 °S 56.105 °W - 10.205 °S 48.343 °W).

Chapter 6

Assessing the impact of biomass burning on cloud properties in the Amazon Basin

Abstract

Cloud condensation nuclei (CCN) measurements were performed during several field campaigns during 1998 and 1999 as part of the Large Scale Biosphere-Atmosphere Experiment in Amazonia (LBA). Sampling occurred at ground-based sites in the states of Amazonas and Rondônia, Brazil. CCN concentrations measured during the wet season were low and resembled concentrations more typical of marine conditions than most continental sites. During the dry season, biomass burning smoke aerosol dramatically increased CCN concentrations.

A 1-D cloud parcel model has been used to assess the impact of biomass burning aerosol on cloud properties in the Amazon Basin and identify the physical and chemical properties of aerosol that influence droplet growth. Sensitivity tests show that complete characterization of the aerosol is necessary when kinetic growth limitations are important. The modification of cloud properties, such as cloud effective radius and maximum supersaturation, is most sensitive at low CCN concentrations. The change in wet-season CCN spectra from forested and deforested regions does not seem to exert significant modifications in cloud properties. Hence the differences in surface albedo between the forested and deforested regions may have a greater impact on the hydrological cycle and convective activity during the wet season. Cloud droplet concentrations could increase by up to seven times during the dry season, which leads to a decrease in cloud effective radius by a factor of two; this can imply a maximum indirect radiative forcing due to aerosol as high as ca. -27 W m^{-2}. Kinetic limitations are important, especially during the dry season, and enhance the dependence of cloud properties on aerosol chemistry. Cloud

droplet concentrations may be overestimated by 20 to 35% compared to models based on equilibrium calculations of droplet activation.

6.1. Introduction

Biomass burning in the Amazon Basin [*Setzer and Pereira*, 1991] generates smoke of variable density across millions of square kilometers during the dry season between June and October. A complex interaction between water vapor, light absorption by "black carbon", and atmospheric stability affects the strength of convection and subsequent cloud development and cloud albedo. Measurements during the dry season reveal a stable spatial distribution of water vapor in contrast to the variability of aerosol concentrations [*Kaufman et al.*, 1992]. Hence, the cloud optical properties in the Amazon dry season may be less dependent on variations of the meteorological conditions.

Biomass burning smoke aerosol dramatically increases cloud condensation nuclei (CCN) concentrations, which could increase colloidal stability and cloud lifetime. The influence of smoke on rain formation was directly shown by the analysis of data from the Tropical Rainfall Measuring Mission (TRMM) taken near Kalimantan, where a distinct difference in cloud structure and radar reflectance was seen between clouds influenced by biomass burning and those in cleaner areas. The clouds in cleaner areas had warmer and larger drops than the non-precipitating clouds affected by smoke [*Rosenfeld*, 1999]. Effective cloud radii have decreased by 10 to 15% in the Amazon Basin from 1985 to 1995 (Advanced Very High Resolution Radiometer (AVHRR) analysis by T. Nakajima). The reduction in effective cloud radii has been more significant during the wet season (i.e., 13.6 to 11.8 μm) compared to the dry season (i.e., 9.7 to 9.0 μm) and may be related to the rapid demographic changes in the Amazon Basin during this period.

The motivation of our work is to assess the potential impact of human development in the Amazon Basin and biomass burning aerosol on cloud properties. In the following sections, we explore cloud droplet formation for measured CCN spectra in the Amazon Basin using a 1-D cloud parcel model with detailed aerosol microphysics. This model incorporates water vapor growth kinetics and is discussed in much greater detail by *Nenes et al.* [2001b]. The wet-season CCN spectra differ dramatically from dry season CCN spectra due to the presence of biomass burning aerosol. We also examine the appropriateness of assuming equilibrium activation, an assumption usually taken in general circulation model assessments of indirect forcing.

6.2. Experimental Description

6.2.1. Site Description

The measurements were performed during the Large Scale Biosphere-Atmosphere Experiment in Amazônia (LBA) in 1998 and 1999 during wet and dry seasons (Figure 6.1). The LBA project is an international research initiative lead by Brazil and is designed to study the interactions between Amazonia and the earth system. The Cooperative LBA Airborne Regional Experiment (CLAIRE) occurred from March 28 to April 15, 1998, at a ground site (1°55.5' S, 59°24.8' W; 160 m above sea level) located 125 km northeast of Manaus, in the state of Amazonas, Brazil. The CLAIRE experiment took place during the wet season. Backward airmass trajectory calculations indicate that our site was not adversely affected by anthropogenic sources, as surface air masses

originated from the northeast to east; hence had traveled a thousand kilometers over the most remote regions of the Amazon rain forest for almost a week before being sampled. Sampling for each instrument took place 6 m above the ground via individual inlets that were extended 2 m above the roof of the laboratory.

In 1999, the European Studies on Trace gases and Atmospheric Chemistry experiment (EUSTACH) expanded operations to include wet- and dry-season measurements. Forest and pasture sites in the state of Rondônia were selected to characterize the influence of human settlement and deforestation in the Amazon Basin. The wet season measurements extended into the beginning of the burning season when fires began in the neighboring state of Mato Grosso. The dry-season experiment occurred from September 15 to November 1, 1999, which corresponded to the peak of fire activity (beginning to middle of September) to the onset of the wet season (end of October). The forest site was located in the Jaru Biological Reserve (10°05.07' S, 61°55.92'; 130 m above sea level) about 90 km north of Ji-Paraná along the Machado River. Measurements took place at 50 m height on a meteorological tower to characterize the contribution from the mixed boundary layer. The surrounding forest canopy is approximately 30 m high. During the wet season, anthropogenic contribution to the ambient aerosol was negligible, since the prevailing wind direction was mostly from forested regions to the east. The pasture site was located on the Fazenda Nossa Senhora (10°45.78' S, 62°21.45' W; 270 m above sea level) about 50 km to the east of Ji-Paraná. Sampling for each instrument took place 5 m above the ground via individual inlets that were extended 1.5 m above the roof of the laboratory. The deforested region extends for at least 60 km surrounding the pasture site. As a consequence, anthropogenic

contributions from local traffic, factories and nearby cities (i.e., Ouro Preto d'Oueste and Ji-Paraná) influence aerosol properties.

6.2.2. Instrumentation

A static thermal-gradient chamber measured CCN concentrations, N_{CCN}, at supersaturations, S_v, between 0.15 and 1.5% S_v. The operation of the instrument is similar to the chamber described by *Lala and Jiusto* [1977]. Instead of the traditional light scattering design, our CCN counter was fitted with a photodiode laser and digital camera to measure droplet concentrations (see Chapter 2). A 670 nm wavelength photodiode laser illuminates the activated droplets while the digital camera, normal to the laser beam, registers images every second during the supersaturation cycle. The CCN concentration at a particular supersaturation is determined during post processing. Imaging software automatically determines the number of activated CCN in each image. The CCN concentration is calculated based on the image with the highest number of particles and on the calibrated illuminated volume. The calibration procedure involved generating a quasi-monodisperse aerosol of a known concentration and counting the number of activated droplets in the digital image. An error analysis for calibration measurements indicates that for typical aerosol spectra, the overall measurement error in number concentrations is approximately ±15% at 1.5% S_v and ±30% at 0.15% S_v. These uncertainties are in agreement with the theoretical predictions by *Nenes et al.* [2001a].

CCN number concentrations were determined every 25 seconds at a supersaturation between 0.15 and 1.5 % S_v, yielding a complete CCN spectrum in six to

seven minutes. A CCN cycle begins with a seven-second flush at 3 liters min^{-1} to remove the previous sample and draw in air for a new sample. The instrument's inlet valve closes and isolates the chamber, which allows the supersaturation profile to develop between two horizontal parallel wetted plates. The CCN counter operates at a desired supersaturation by controlling the temperature difference between the wetted plates. The diameter of the chamber is 100 mm and the top and bottom plates are separated by 10 mm. The dimensions allow for air in the chamber to reach an equilibrium supersaturation profile in several seconds. Whatman filter papers on the top and bottom plates are kept wetted by an external capillary system. The top plate temperature is allowed to float with the ambient temperature, which ranged from 20 to 35 °C, and the bottom plate is cooled as necessary to achieve the prescribed supersaturation. Temperature fluctuations during measurements are usually within 0.1 °C, so the supersaturation is constant within ±0.05% S_v. Activated CCN particles quickly grow to several micrometers in diameter and gravitationally settle out of the chamber.

6.3. Model Description

6.3.1. Cloud Parcel Model

A cloud parcel model [*Pruppacher and Klett*, 1997; *Seinfeld and Pandis*, 1998] is the simplest tool that can be used to simulate the evolution of droplet distributions throughout a non-precipitating cloud column. It also predicts the maximum influence of aerosol on cloud properties because it focuses on the early stages of cloud formation,

where droplets are produced through diffusional growth. The cloud parcel model used for this study has explicit aerosol microphysics and can account for the presence of slightly soluble and surfactant substances. During the initial stages of cloud development, water vapor transport to the growing droplets may not be sufficiently rapid for small particles near their critical size to activate. Consequently, they can re-evaporate and become interstitial aerosol, which exert a negligible effect on the cloud optical properties and precipitation processes. For this study, the parcel is assumed to be adiabatic. A further description of the 1-D cloud parcel model is described by *Nenes et al.* [2001b].

6.3.2. Cloud Optical Properties

Cloud albedo, R_c, is calculated based on the two-stream approximation of a non-absorbing, horizontally homogeneous cloud [*Lacis and Hansen*, 1974].

$$R_c(z) = \frac{\tau}{7.7 + \tau} \tag{6.1}$$

where τ is the cloud optical depth,

$$\tau = \int_0^H \frac{3\rho_a w_L(z)}{2\rho_w r_{eff}(z)} dz \tag{6.2}$$

where $w_L(z)$ is the liquid water mixing ratio profile along the cloud column. ρ_w is the water density, ρ_a is the air density and $r_{eff}(z)$ is the cloud droplet distribution effective radius. The difference in cloud albedo at height z is used to assess modifications in cloud properties between the different simulations. Assuming that the droplet population is

monodisperse and has an overwhelming amount of liquid water, the expression for $r_{eff}(z)$ is given by

$$r_{eff}(z) = \left(\frac{3w_L(z)}{4\pi N_i(z)\rho_w} \right)^{\frac{1}{3}} \tag{6.3}$$

where $N(z)$ is the droplet concentration and is equal to the number of particles that are larger than the activated particle with the smallest dry diameter. Critical parameters are calculated from Köhler theory [*Köhler*, 1936; *Seinfeld and Pandis*, 1998].

6.3.3. Kinetic Limitations

To be able to estimate anthropogenic aerosol indirect forcing, analytical approximations for particle activation to form cloud droplets have been implemented in general circulation models (GCMs). These expressions generally assume that particles are at equilibrium with the ambient water vapor concentration and that they respond instantaneously to changes thereof. Droplets, however, need a finite time to grow. As a result, the assumption of equilibrium can lead to an overestimation in droplet number as a result of mass transfer limitations, which would insert a bias in any indirect forcing calculation [*Nenes et al.*, 2001b].

The importance of kinetic growth limitations on droplet formation will be measured in terms of both droplet number and cloud albedo. For this purpose, the number concentrations of droplets, N_{eq} and N_{kn}, based on equilibrium and kinetic approaches, respectively, are required. N_{eq} is based on the assumption that particles activate instantaneously and is the upper limit to the number of droplets that can be

formed. N_{kn} is the droplet concentration from the particle growth equations [*Nenes et al.*, 2001b]. Based on the variation of N_{kn} and N_{eq} with cloud depth, z, one can define another useful quantity, the total droplet ratio, $\alpha(z)$:

$$\alpha(z) = \frac{N_{kn}(z)}{N_{eq}(z)} \tag{6.4}$$

which expresses the ratio of actual droplets to the maximum droplets attainable at a certain cloud depth. Vertical profiles of the activation ratios can provide insight regarding the kinetic limitation mechanisms [*Nenes et al.*, 2001b].

6.4. CCN Spectra Measurements

CCN spectra measurements for all the field campaigns are summarized in Figure 6.2. CCN number concentrations during wet-season field campaigns were low and resulted in a spectrum typical of oceanic environments [*Roberts et al.*, 2001a] (see Chapter 3). The CLAIRE and EUSTACH experiments took place in 1998 and 1999, respectively, at sites nearly 1000 km apart; yet, the wet-season CCN spectra were nearly identical regardless of the sampling location and the year. The uniformity of physical and chemical aerosol properties suggests a common biogenic source of the aerosol throughout the Amazon Basin. Hence, we consider the forest site wet-season CCN spectrum as the natural background Amazonian CCN spectrum and a reference to which the change in cloud properties may be compared.

The pasture site wet-season CCN spectrum (EUSTACH) was similar to the wet-season forest site. However, there is a slight shift to higher CCN concentrations at larger

supersaturations due to local anthropogenic aerosol sources. The significance of this enhancement in the CCN spectra will be characterized in later sections and yields useful information to the potential changes due to the human development in the Amazon Basin.

At the end of the wet season (e.g., middle of May 1999), biomass burning began in the neighboring state of Mato Grosso. Isentropic backward airmass trajectories [*NOAA Air Resources Laboratory*, 1997] indicate that surface air mass originated from the east; hence had traveled several hundred kilometers over the Amazon rain forest for a couple of days before being sampled. A strong diel cycle in CCN concentrations was observed, which suggests evidence of coupling aerosol transport to the development of the boundary layer. Obvious changes to the CCN spectra were observed as the fire activity increased during the transition period. CCN concentrations increase and the shape of the spectra changed, as well. The enhanced "curvature" of the transition period CCN spectrum probably occurs because of a shift to a larger median diameter of the number distribution [*Reid et al.*, 1998; *Roberts et al.*, 2001b] (see Chapter 4).

During the dry season, N_{CCN} were highly variable depending on the proximity of the burning and averaged about an order of magnitude higher than during the wet season. The spectra were similar to measurements at mid-latitudes near urban centers [*Hobbs et al.*, 1985; *Hudson and Frisbie*, 1991] and fire plumes [*Hudson and Clarke*, 1992]. The sources of the biomass-burning aerosol included local fires and aged smoke that had been transported from other regions in Brazil.

6.5. Simulation Parameters

To explore the parametric dependence of the development of the boundary layer convective cloud formation on the CCN spectra, the parcel model was used to explore the sensitivity of effective cloud radius, albedo, and maximum parcel supersaturation on physical and chemical properties of the aerosol population. Size distributions of lognormal form were used to represent the aerosol for which CCN spectra were measured

$$\frac{dN_i}{d\log d_p} = \frac{N_i}{\sqrt{2\pi}\ln\sigma_{g,i}}\exp\left[\frac{-\left(\ln d_p - \ln d_{pg,i}\right)^2}{2\ln^2\sigma_{g,i}}\right] \tag{6.5}$$

where N_i is the aerosol number concentration, $d_{pg,i}$ is the geometric median diameter, and $\sigma_{g,i}$ is the geometric standard deviation for mode i. Values for N, d_{pg}, and σ_g that best represent the measured CCN spectra are shown in Table 6.1. A particle's critical supersaturation, S_c, is determined for a two-component aerosol based on measured literature values for the amount of NH_4HSO_4 [*Reid et al.*, 1998; *Roberts et al.*, 2001b] and water-soluble organic compounds (WSOCs) [*Mayol-Bracero et al.*, 2001]. WSOCs enhance CCN activity by adding soluble material and reducing the surface tension of liquid cloud droplets. A relationship of dissolved organic carbon to surface tension effects [*Facchini et al.*, 1999] was used here to estimate potential influences of surfactants on CCN spectra and subsequent cloud properties.

The properties of the components in our model are shown in Table 6.2. The size distribution and relative mass fraction of each component (Table 6.1) were chosen to accurately describe measured CCN spectra (Figures 6.2 and 6.3). Parameters were either

measured or constrained based on previous experiments. The number distribution was first determined and chemical composition was adjusted to yield a CCN spectrum that matched the measured spectrum.

The wet-season number distribution was directly measured during the CLAIRE experiment [*Zhou et al.*, 2001] and fitted to a single or tri-modal lognormal distribution (Table 6.1). Varying the chemical properties of the single mode distributions assessed the effect of WSOCs. A tri-modal distribution with a composition similar to the average chemical composition reported in *Roberts et al.* [2001b] (Chapter 4) serves as a "realistic" wet-season aerosol distribution. The principal difference is the addition of a large mode at 900 μm, which illustrates the effects of the "giant" CCN (GCCN).

Wet-season pasture site CCN spectra were nearly identical to the forest data except for a slight increase in N_{CCN} at higher supersatuations, which can be accounted for by increasing N and/or D_{pg} of the wet-season number distribution. Anthropogenic inputs, such as exhaust from diesel automobiles or nearby factories, increase aerosol concentrations and may contribute to a larger median diameter in the size distribution [*Kleeman et al.*, 2000]. Two number distributions were investigated for the pasture site CCN spectrum by varying D_{pg} and N of the wet-season forest size aerosol distribution (Table 6.1).

Number distribution measurements for the transition and dry-season spectra were not available; as a result, approximations were made based on literature values. Since both the transition and dry-season CCN spectra involved biomass smoke aerosol, D_{pg} and σ_g were constrained by a linear relationship reported by *Reid et al.* [1998]

$$\sigma_g = -3.16\, D_{pg} + 2.18 \tag{6.6}$$

where $0.09 < D_{pg} < 0.28$ μm is the maximum range allowed based on measurements during the SCAR-B (Smoke, Clouds and Radiation-Brazil experiment) [*Kaufman et al.*, 1998]. These constraints on the geometric median diameter limit the range of the geometric standard deviation to $1.3 < \sigma_g < 1.9$. Smoke particles evolve rapidly after emission and their physical and chemical properties are related to their age. Young smoke exhibits a smaller median diameter than aged smoke and could be reflected by the difference in CCN spectra between the dry and transition periods. The more pronounced "curvature" in the transition period CCN spectra is indicative of aged, larger smoke aerosol, which was transported for several days over the rain forest.

Since a large fraction of the biomass-burning aerosol consists of humic-like substances [*Mayol-Bracero et al.*, 2001], the solubility and surface tension effects of biomass burning aerosol may play an important role in increasing the CCN activity during the dry season. *Reid et al.* [1998] also report average sulfate composition for biomass burning smoke aerosol to be several percent of the total aerosol mass (i.e., 1-2% for young aerosol and < 7.6% for aged aerosol). Hence, the physical and chemical properties of the dry-season aerosol were selected based on literature values and constrained to fit the measured CCN spectra between 0.15 and 1.5% S_v. As the mode diameter or surface tension effects increase, the amount of soluble material (i.e., NH_4HSO_4) must be reduced (see Table 6.1). Such chemical and physical differences in aerosol properties will affect cloud droplet growth and result in a range of cloud properties. The effect of GCCN was not studied for the biomass burning aerosol;

however, the presence of GCCN enhances the development of precipitation in mixed-phase convective clouds in regions with high aerosol concentrations [*Yin et al.*, 2000].

The sensitivity of cloud properties was also calculated as a function of increasing aerosol number concentration using the wet-season forest site approximations of the size distribution (Table 6.1). The median diameter, median standard deviation, and chemical composition remained constant, while the number concentration varied from 10^2 to 10^4 cm^{-3}. The wet-season forest site spectrum provides a reference to assess the effects of anthropogenic aerosol input on cloud properties in the Amazon Basin.

6.6. Model Results

The effects of biomass burning and the sensitivity of wet-season cloud properties are considered for the measured CCN spectra in the Amazon Basin (Figure 6.2). Wet-season CCN spectra allowed for maximum supersaturations that were nearly two times higher than for the dry-season spectra (Table 6.3). Maximum parcel supersaturation attained in the cloud parcels increased with updraft velocity due to the higher rates of adiabatic cooling and decreased with increasing N because of the competition of water vapor by more particles. The reduction in maximum parcel supersaturation is a non-linear function of N_{CCN} and is most sensitive at low concentrations (Figure 6.4), which are observed during the wet season.

6.6.1. Sensitivity of Cloud Properties on Aerosol Distribution

As the physical and chemical characteristics of an aerosol population influence CCN activity and subsequent growth into cloud droplets, sensitivity tests using the wet- and dry-season CCN spectra have been performed to determine the influence of various parameters on droplet growth.

6.6.1.1. Wet-season CCN spectra

The resulting CCN spectra from the modeled size distributions presented in Table 6.1 closely resemble the measured wet-season spectra between 0.15 and 1.5 % S_v (Figure 6.3). The activation and growth of the cloud droplets were similar between the single mode distributions in spite of the differences in chemical composition. Hence, differences in cloud albedo and maximum in-cloud supersaturation are suspected to be less influenced by aerosol chemistry during the wet season. The largest difference in wet-season simulations is observed between the single and tri-modal distributions at low updraft velocities (Table 6.3), when the difference in activated cloud droplets is the greatest. This difference become insignificant as updraft velocity increases (i.e., higher supersaturations).

The tri-modal distribution exhibited larger droplets due to the activation of the 900 μm mode. This large mode is a source of GCCN, which can play an important role in initiating precipitation [*Yin et al.*, 2000]. Although collision and coalescence were not included in our model, strong kinetic limitations may further enhance the precipitation

efficiency. The driving force for droplet growth (i.e., the difference between the saturation ratio at the droplet surface and that of the surrounding air) is greater for larger droplets; hence the larger droplets could effectively draw water vapor away from the smaller droplets.

6.6.1.2. Dry-season CCN spectra

Variations in number distribution and chemical composition can yield different cloud properties in spite of similarities to the measured CCN spectrum. The importance of chemical composition and the influence of kinetic effects for the dry-season CCN are highlighted by cases DA and DDST in Table 6.1. The size distribution is identical for both cases; however, surface tension effects have been incorporated into the latter. A close inspection of the CCN spectra of DA and DDST illustrates the enhanced CCN activity of larger particles (i.e., smaller critical supersaturation) due to surface tension effects (not shown). Hence the smaller rate of droplet activation allows a few particles to activate and grow into droplets before kinetic effects dominate at larger droplet concentrations. The surface tension effect essentially serves as the same role as GCCN, but on a smaller scale; and the kinetic growth limitations at high droplet concentrations amplify this effect. At stronger updraft velocities (i.e., 1 and 3 m s^{-1}), the relative differences in droplet growth, maximum in-cloud supersaturation, and albedo decrease among the dry-season simulations.

6.6.2. Cloud Droplet Number

The cloud droplet number is a key parameter in regulating cloud properties. As evapotranspiration maintains a relatively uniform spatial distribution of water vapor above the forest canopy, cloud droplet number is primarily dependent on updraft velocity and the CCN spectra. The fraction of aerosol that serves as CCN, $f_{CCN/CN}$, for each of the simulated size distributions is shown in Figure 6.5. In spite of the lower parcel supersaturations for the transition period (Table 6.3), the larger mode diameter allows for higher $f_{CCN/CN}$ than the wet season. $f_{CCN/CN}$ for the dry-season spectra are less than for the wet season due to the order of magnitude increase in number concentrations and the enhanced kinetic growth effects.

The fractional increase in cloud droplet number concentration compared to the wet-season reference spectra is shown in Figure 6.6 for each of the measured CCN spectra. Due to the low aerosol concentrations and the similarities in CCN spectra between the wet-season forest and pasture sites, the differences in droplet concentrations are minimal. This similarity in droplet concentration is expected since 1) the maximum parcel supersaturation during the wet season is 0.82% (at 3.0 m s^{-1} updraft velocity; Table 6.3) the CCN spectra for the forest and pasture sites are nearly identical for $S_c < 0.82\%$. It is necessary to point out that the initial conditions for these model runs were identical to isolate the effect of the aerosol properties on clouds. Significant differences in the water vapor content and surface heating rates could induce dramatic changes in convective activity.

Biomass burning yields up to a seven-fold increase in droplet concentrations (Figure 6.6) even though the maximum parcel supersaturation decreased (Table 6.3). The largest increase in droplet number occurred for the dry season because of the order of magnitude increase in aerosol concentration. In spite of a 40% increase in N from the wet season to the transition period, the cloud droplet concentration increased by at least a factor of two. The large mode diameter in the transition period size distribution allows for more particles to activate at lower supersaturations. This increase in droplet concentration also induces a significant reduction in maximum parcel supersaturation (Table 6.3). Small changes in parcel supersaturation while activating aerosol near the mode diameter (i.e., transition period) have a greater effect than activating aerosol at the shoulder of the distribution (i.e., dry season). The resulting changes in cloud properties are discussed in the following sections.

These simulations reveal that kinetic limitations are important regardless of updraft velocity and cloud height for all measured Amazonian CCN spectra. These results are expected since kinetic effects have been shown to be present for number concentrations greater than 100 cm^{-3} [*Nenes et al.*, 2001b]. In our simulations, we calculate asymptotic values for $\alpha(z)$ and the results are summarized in Table 6.4. Kinetic effects become more apparent as updraft velocity decreases (e.g., smaller water vapor flux) and droplet concentrations increase (e.g., dry season). This could lead to an overprediction of cloud droplet number to 20 and 35% for low updraft velocities of 0.1 m s^{-1} during the wet and dry seasons, respectively (Table 6.4).

6.6.3. Cloud Effective Radius

Cloud optical properties and precipitation processes are influenced by the droplet effective radius. The higher aerosol number concentrations and larger mode diameters during the transition period and dry season reduce the effective radius by nearly a factor of two compared to the wet season (Figure 6.7). These results are expected since $r_{eff} \propto N^{1/3}$ for the same amount of liquid water content [*Twomey*, 1977]; an increase in N by a factor of 2.5 and 5.5 for the transition period and dry season result in ca. 30% and 45% reduction in effective cloud radii, respectively. These results are supported by satellite images taken over the Amazon Basin that show the presence of dense smoke can reduce the remotely sensed drop radius of continental cloud drops from 15 to 9 μm [*Kaufman and Nakajima*, 1993].

Although collision and coalescence is not included in the model, the large reduction in r_{eff} reduces the probability for collision with other droplets [*Pruppacher and Klett*, 1997]. Sensitivity of r_{eff} is independent on cloud vertical extent and is most sensitive at low aerosol concentrations found during the wet season (Figure 6.8).

6.6.4. Cloud Albedo

A climatically important effect would be considered for a change in albedo larger than ca. 0.005; this albedo change can potentially exert a radiative forcing of nearly –1 W m^{-2} [*Eltahir and Humphries*, 1998]. Albedo difference is a function of cloud depth and becomes maximum within the first 300 m of the cloud. Figure 6.9 shows the maximum

difference in cloud albedo for simulations using the measured Amazonian CCN spectra. The differences are positive due to the increasing droplet concentrations of the pasture site, transition period and dry season. The wet-season forest site provides a reference to assessing the change in albedo.

The change in albedo between the forest and pasture site (Figure 6.9) does not appear to be significant because the difference in activated droplets (Figure 6.4) is neglible. This implies that during the wet season, the driving force in climate change may result from the change in surface albedo. The albedo of the Amazon rain forest is between 0.11 and 0.13 [*Gash and Shuttleworth*, 1991]. Following deforestation, there will almost always be an increase in surface albedo. In Rondônia, the forest is often replaced by short grass for cattle grazing, which can result in surface albedos up to 0.25 [*Gash and Shuttleworth*, 1991]. Deforestation will result in a reduction in the amount of radiative energy that is absorbed by the earth's surface, resulting in less evaporation and a smaller driving force for convective activity [*Gash and Shuttleworth*, 1991]. A reduction in convective activity could inhibit precipitation; however, an inhomogeneous region of forest and pastures generates areas of local instability, which could actually increase the driving force for convective activity [*Baidya and Avissar*, 2001].

Significant enhancements in cloud albedo are calculated for biomass burning aerosol (Figure 6.9). The maximum change in albedo between the wet and dry seasons is 0.20, which corresponds to an inter-seasonal indirect aerosol forcing up to ca. -27 W m^{-2}. These simulated values for indirect forcing are comparable to the direct forcing from biomass burning aerosol reported by *Ross et al.* [1998]. Albedo is primarily dependent

on droplet concentration; hence, changes in albedo (Figure 6.9) follow similar trends as droplet concentration (Figure 6.6)

The quantity used for assessing the importance of kinetic effects, in terms of cloud albedo is the difference between thermodynamic and kinetic albedo. The discrepancy in albedo comes from the difference in cloud droplet number concentration between the thermodynamic and kinetic approximations. The thermodynamic albedo tends to be higher than the kinetic albedo, because the same amount of liquid cloud water is shared among a larger number of cloud droplets. The height, at which the maximum difference occurs, decreases with increasing updraft velocity and number concentration. The dry-season distribution exhibits the largest albedo difference, shown in Figure 6.10, due to enhanced kinetic effects. Wet season (i.e., pasture and forest sites) and transitition period result in comparable differences (Figure 6.10). The differences in albedo from kinetic effects, however, are small compared to the increase albedo due to enhanced aerosol concentrations during biomass burning.

6.7. Conclusions

We have investigated the change in cloud properties based on measured CCN spectra during the wet and dry seasons in the Amazon Basin. CCN concentrations rise by nearly an order of magnitude from wet to dry seasons, which increase droplet concentrations up to a factor of seven at high updraft velocities. The resulting modifications in cloud properties are most sensitive at low number concentrations that are found in wet-season conditions. Variations in the size distribution and chemical

composition induce subtle changes in the CCN spectra that can affect droplet growth when kinetic limitations are important. Kinetic limitations reduce droplet concentrations up to 20% in the wet season and 35% in the dry season. Kinetic effects are, however, small compared to the changed in cloud properties induced by biomass burning aerosol.

Anthropogenic activity, such as industrial emissions and biomass burning, modifies physical and chemical properties of the aerosol population – components that dictate CCN activity – and could lead to important changes in cloud properties that govern the energy cycle within the Amazon Basin. The response of cloud droplet concentration to changes in CCN concentrations is the basis for the modification of precipitation, cloud fraction and indirect forcing. However, changes in surface albedo have not been included in this study and are an important driving force in the hydrological cycle and convective activity. An increase in aerosol concentrations during the wet season will likely have a greater effect on the rain forest climate than intensification of biomass burning during the dry season due to the higher sensitivity at the low ambient aerosol concentrations.

6.8. References

Baidya, R., and R. Avissar, Impact of land use/land cover change on regional hydrometeorology in the Amazon., *submitted to J. Geophys. Res.*, 2001.

Eltahir, E., and E.J. Humphries, The role of clouds in the surface energy balance over the Amazon forest, *Int. J. Climatol.*, *18*, 1575-1591, 1998.

Facchini, M.C., M. Mircea, S. Fuzzi, and R.J. Charlson, Cloud albedo enhancement by surface-active organic solutes in growing droplets, *Nature*, *401* (6750), 257-259, 1999.

Gash, J.H.C., and W.J. Shuttleworth, Tropical deforestation: Albedo and the surface-energy balance, *Climatic Change*, *19*, 123-133, 1991.

Hobbs, P.V., D.A. Bowdle, and L.F. Radke, Particles in the lower troposphere over the high plains of the United States, 2, Cloud condensation nuclei, *J. Climate and Appl. Meteor.*, *24*, 1358-1369, 1985.

Hudson, J.G., and A.D. Clarke, Aerosol and cloud condensation nuclei measurements in the Kuwait plume, *J. Geophys. Res.*, *97*, 14,533-14,536, 1992.

Hudson, J.G., and P.R. Frisbie, Surface cloud condensation nuclei and condensation nuclei measurements at Reno, Nevada, *Atmos. Environ.*, *25*, 2285-2299, 1991.

Kaufman, Y.J., P.V. Hobbs, V.W.J.H. Kirchhoff, P. Artaxo, L.A. Remer, B.N. Holben, M.D. King, D.E. Ward, E.M. Prins, K.M. Longo, L.F. Mattos, C.A. Nobre, J.D. Spinhirne, Q. Ji, A.M. Thompson, J.F. Gleason, S.A. Christopher, and S.C. Tsay, Smoke, Clouds, and Radiation - Brazil (SCAR-B) experiment, *J. Geophys. Res.*, *103*, 31,783-31,808, 1998.

Kaufman, Y.J., and T. Nakajima, Effect of Amazon smoke on cloud microphysics and albedo - Analysis from satellite imagery, *J. Appl. Meteorology*, *32*, 729-744, 1993.

Kaufman, Y.J., A. Setzer, D. Ward, D. Tanré, B.N. Holben, P. Menzel, M.C. Pereira, and R. Rasmussen, Biomass Burning Airborne and Spaceborne Experiment in the Amazonas (BASE-A), *J. Geophys. Res.*, *97*, 14,581-14,599, 1992.

Kleeman, M., J. Schauer, and G. Cass, Size and composition distribution of fine particulate matter emitted from motor vehicles, *Environ. Sci. Tech.*, *34*, 1132-1142, 2000.

Köhler, H., The nucleus in and the growth of hygroscopic droplets, *Trans. Faraday Soc.*, *32*, 1152-1161, 1936.

Lacis, A., and J. Hansen, A parameterization of the absorption of solar radiation in the Earth's atmosphere, *J. Atmos. Sci.*, *31*, 118-133, 1974.

Lala, G.G., and J.E. Jiusto, An automatic light scattering CCN counter, *J. Appl. Meteor.*, *16* (4), 413-418, 1977.

Lide, D., *CRC Handbook of Chemistry and Physics*, CRC Press, Cleveland, Ohio, 2000.

Mason, B., *Principles of Geochemistry*, John Wiley, New York, 1966.

Mayol-Bracero, O.L., P. Guyon, B. Graham, G. Roberts, M.O. Andreae, S. Decesari, M.C. Facchini, S. Fuzzi, P. Artaxo, and W. Maenhaut, Black Carbon, Organic Carbon and Water-Soluble Organic Compounds in Biomass Smoke Particles over the Amazon Basin, *Submitted to J. Geophys. Res.*, 2001.

Nenes, A., P. Chuang, R. Flagan, and J. Seinfeld, A theoretical analysis of cloud condensation nucleus (CCN) instruments, *J. Geophys. Res.*, *106*, 3449-3474, 2001a.

Nenes, A., S. Ghan, H. Abdul-Razzak, P.Y. Chuang, and J.H. Seinfeld, Kinetic limitations on cloud droplet formation and impact on cloud albedo, *Tellus*, *53*, 133-149, 2001b.

NOAA Air Resources Laboratory, HYSPLIT 4, Hybrid Single-Particle Lagrangian Integrated Trajectory Model, Silver Spring, Md., 1997.

Pruppacher, H.R., and J.D. Klett, *Microphysics of Clouds and Precipitation*, Kluwer Academic Publishers, Boston, 1997.

Reid, J.S., P.V. Hobbs, R.J. Ferek, D.R. Blake, J.V. Martins, M.R. Dunlap, and C. Liousse, Physical, chemical, and optical properties of regional hazes dominated by smoke in Brazil, *J. Geophys. Res.*, *103*, 32,059-32,080, 1998.

Roberts, G., J. Zhou, P. Artaxo, and M. Andreae, Cloud condensation nuclei in the Amazon Basin: "Marine" conditions over a continent?, *in press, Geophys. Res. Lett.*, 2001a.

Roberts, G., J. Zhou, E. Swietlicki, P. Artaxo, and M. Andreae, Sensitivity of CCN spectra on chemical and physical properties of aerosol, *Submitted to J. Geophys. Res.*, 2001b.

Rosenfeld, D., TRMM observed first direct evidence of smoke from forest fires inhibiting rainfall, *Geophys. Res. Lett.*, *26*, 3105-3108, 1999.

Ross, J.L., P.V. Hobbs, and B. Holben, Radiative characteristics of regional hazes dominated by smoke from biomass burning in Brazil: Closure tests and direct radiative forcing, *J. Geophys. Res.*, *103*, 31,925-31,941, 1998.

Seinfeld, J.H., and S.N. Pandis, *Atmospheric chemistry and physics: From air pollution to climate change*, 1326 pp., John Wiley, New York, 1998.

Setzer, A.W., and M.C. Pereira, Amazon biomass burnings in 1987 and their tropospheric emissions, *Ambio*, *20*, 19-22, 1991.

Twomey, S., The influence of pollution on the short-wave albedo of clouds, *J. Atmos. Sci.*, *34*, 1149-1152, 1977.

Yin, Y., Z. Levin, T. Reisin, and S. Tzivion, The effects of giant cloud condensation nuclei on the development of precipitation in convective clouds - a numerical study, *Atmos. Res.*, *53*, 91-116, 2000.

Zhou, J., E. Swietlicki, H. Hansson, and P. Artaxo, Sub-micrometer aerosol particle size distribution and hygroscopic growth measurements in the Amazonian rain forest during the wet season, *Submitted to J. Geophys. Res.*, 2001.

Table 6.1. *Size* distribution parameters for CCN spectra.

season	ID	number distribution			NH_4HSO_4	OC
		N	D_{pg}	σ_g	mass fraction	mol C liter^{-1}
Wet season	WA	458.7	83.23	1.83	0.055	0
(forest)	WB	458.7	83.23	1.83	0.0611	0
	WCST	458.7	83.23	1.83	0.035	0.01
	WMST *	338.8	72.27	1.541	0.055	0
		92.37	162.8	1.307	0.15	0
		19.05	900	1.419	0.02	0.01
Pasture site	PA	550	86	1.83	0.055	0
	PB	500	100	1.83	0.055	0
Transition	TA	770	150	1.706	0.055	0
	TB	830	140	1.738	0.055	0
Dry season	DA	5200	90	1.896	0.056	0
	DB	5200	120	1.801	0.019	0
	DC	5200	150	1.706	0.007	0
	DDST	5200	90	1.896	0.02	0.035
	DEST	6000	90	1.896	0.02	0.01

Each case was run at constant updraft velocities of 0.1, 0.3, 1.0 and 3.0 m s^{-1}. For all cases except WMST, the insoluble core density was 1.55 g cm^{-3}.

**WMST is a tri-modal distribution that also contained an insoluble core of 2.5 g cm^{-3} in the 900 μm mode (mass fraction = 0.13). The remainder of the mass fraction was organic carbon (OC).

Table 6.2. Properties of important components used in Köhler theory to estimate CCN activity.

Material	Density ($g\ cm^{-3}$)	Molecular weight ($g\ mol^{-1}$)	Solubility (mole $liter^{-1}$ H_2O)	Van't Hoff factor
NH_4HSO_4	1.780[-]	115.11[-]	6.55[-]	2.0
WSOC	1.55[‡]	194.3[‡]	0.01 (carbon)[+]	2.79
Insoluble inorganic	2.5[*]	NA	0.0	0.0
Insoluble organic	1.55[‡]	NA	0.0	0.0

[-] *CRC Handbook* [*Lide*, 2000]

[‡] Facchini (person communication)

[+] *Facchini et al.* [1999]

[*] average crustal material [*Mason*, 1966]

Table 6.3. Maximum supersaturations as a function of updraft velocity attained in the cloud parcel model for different periods in the Amazon Basin.

	Maximum supersaturation, $S_{v,max}$ (%)			
Updraft vel. (m s^{-1})	Wet season * (forest)	Wet season (pasture)	Transition period	Dry season
0.1	0.270 ± 0.007	0.253 ± 0.013	0.191 ± 0.001	0.179 ± 0.027
0.3	0.399 ± 0.007	0.375 ± 0.016	0.285 ± 0.002	0.262 ± 0.027
1.0	0.639 ± 0.008	0.569 ± 0.067	0.462 ± 0.003	0.404 ± 0.028
3.0	1.034 ± 0.012	0.972 ± 0.023	0.756 ± 0.003	0.619 ± 0.027

* The averages in the table do not include the tri-modal wet-season simulation. The maximum supersaturation values for the tri-modal run are as follows: 0.199, 0.325, 0.578, and 1.007 for updraft velocities of 0.1, 0.3, 1.0, and 3.0 m s^{-1}, respectively.

Table 6.4. Asymptotic alpha ratios as a function of updraft velocity attained in the cloud parcel model for different periods in the Amazon Basin.

	Maximum droplet ratio, α (z) (N_{kn} N_{th}^{-1})			
Updraft vel. (m s^{-1})	Wet season (forest)	Wet season (pasture)	Transition period	Dry season
0.1	0.800 ± 0.033	0.825 ± 0.019	0.765 ± 0.011	0.674 ± 0.033
0.3	0.869 ± 0.014	0.859 ± 0.008	0.853 ± 0.002	0.736 ± 0.019
1.0	0.890 ± 0.018	0.910 ± 0.023	0.913 ± 0.010	0.824 ± 0.017
3.0	0.936 ± 0.020	0.945 ± 0.007	0.958 ± 0.001	0.886 ± 0.010

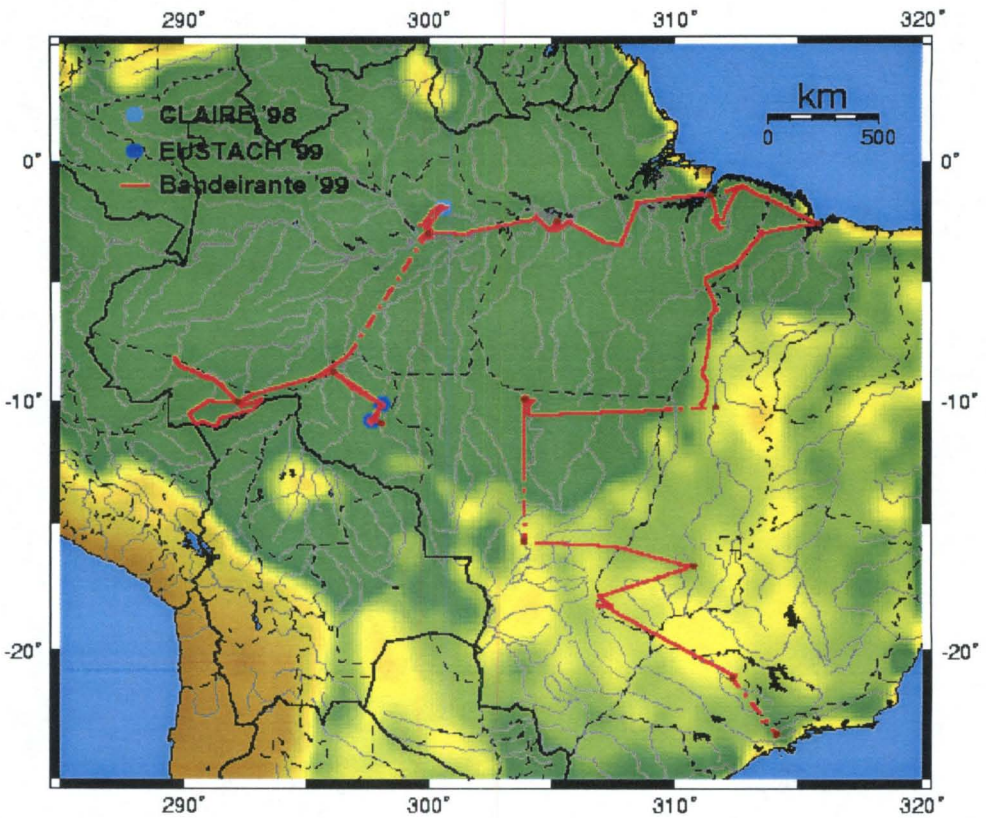

Figure 6.1. Overview of experimental sites during the Large Scale Biosphere-Atmosphere Experiment in Amazonia (LBA).

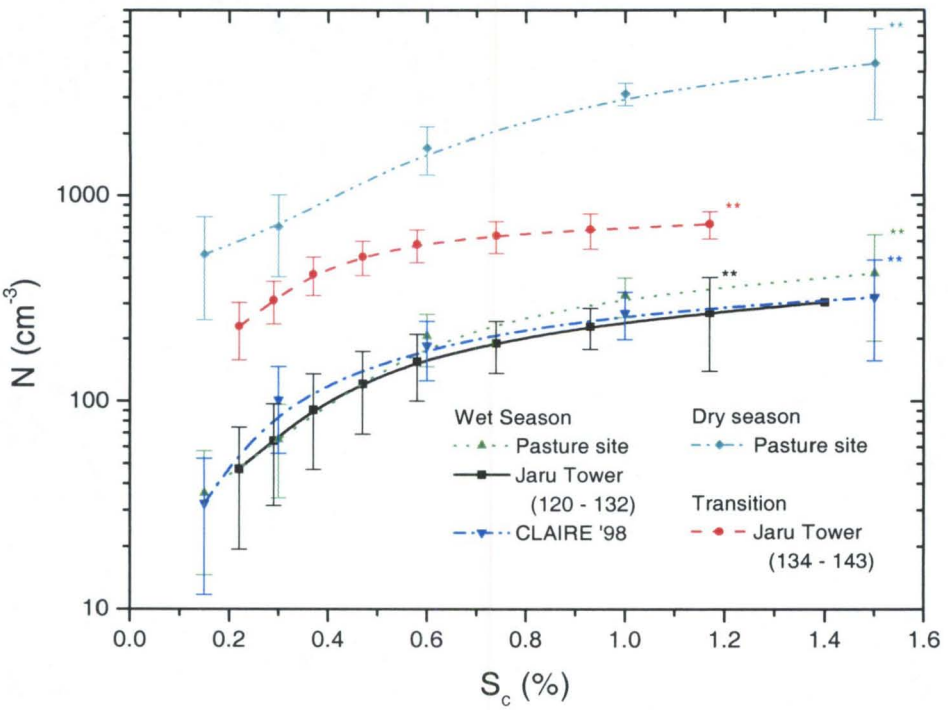

Figure 6.2. Summary of cumulative CCN spectra for wet, transition and dry seasons in the Amazon Basin.

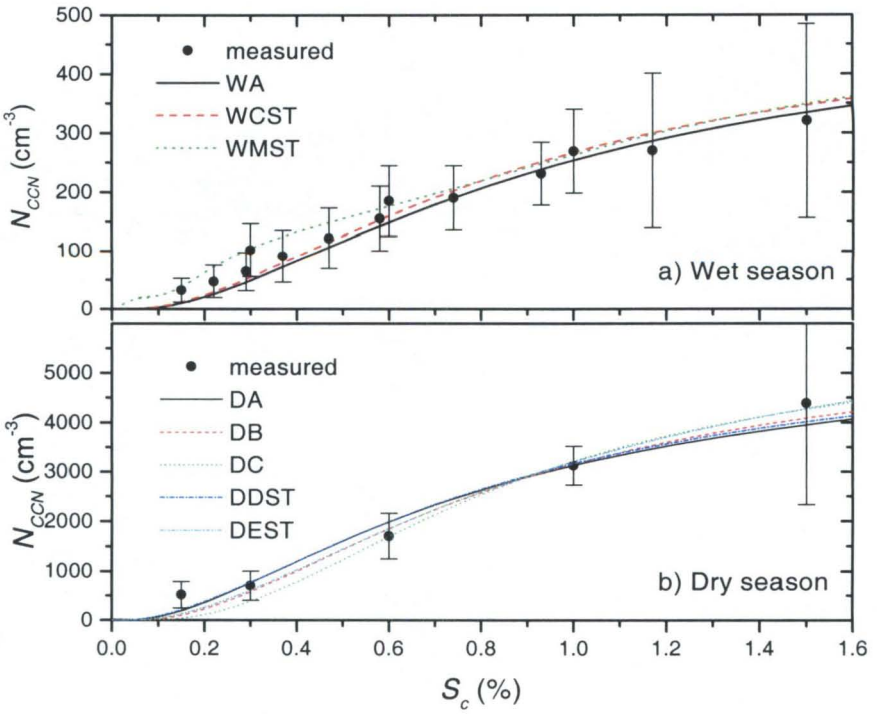

Figure 6.3. Modelled and measured CCN spectra for the wet and dry season.

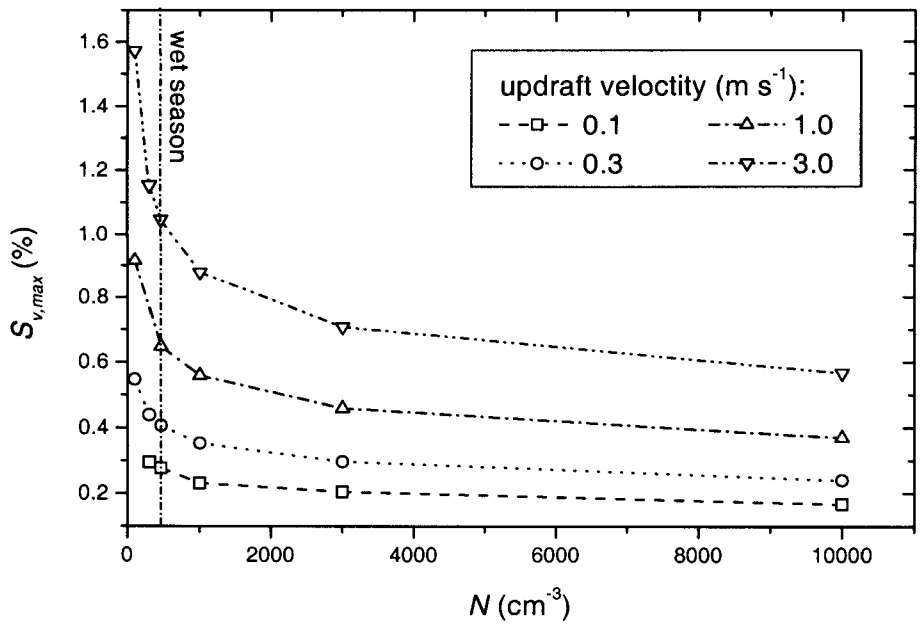

Figure 6.4. Cloud parcel maximum superaturation as a function of increasing aerosol concentrations using the wet-season forest site CCN number distribution (WA). Each curve represents a different updraft velocity.

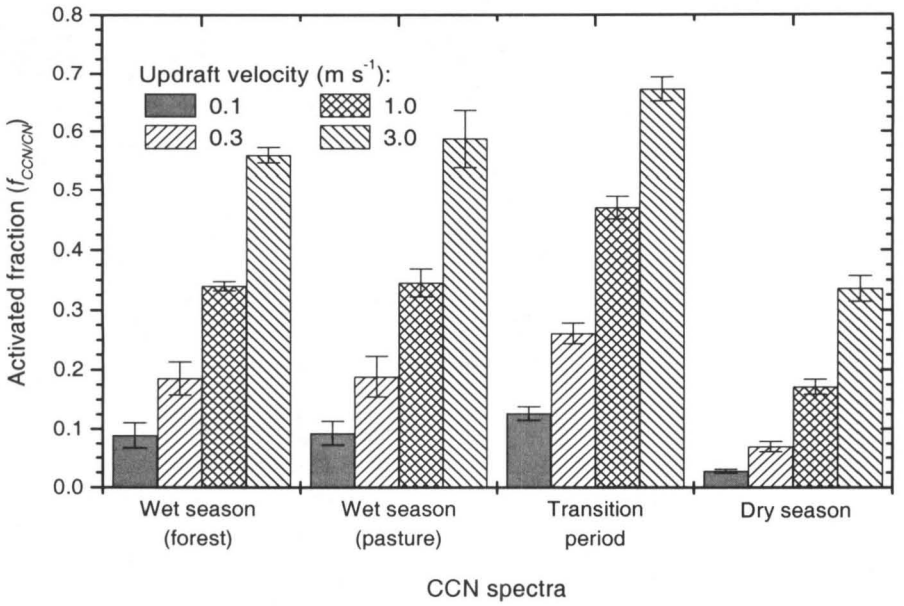

Figure 6.5. The fraction of aerosol that serve as CCN, $f_{CCN/CN}$, for the measured CCN spectra in the Amazon Basin.

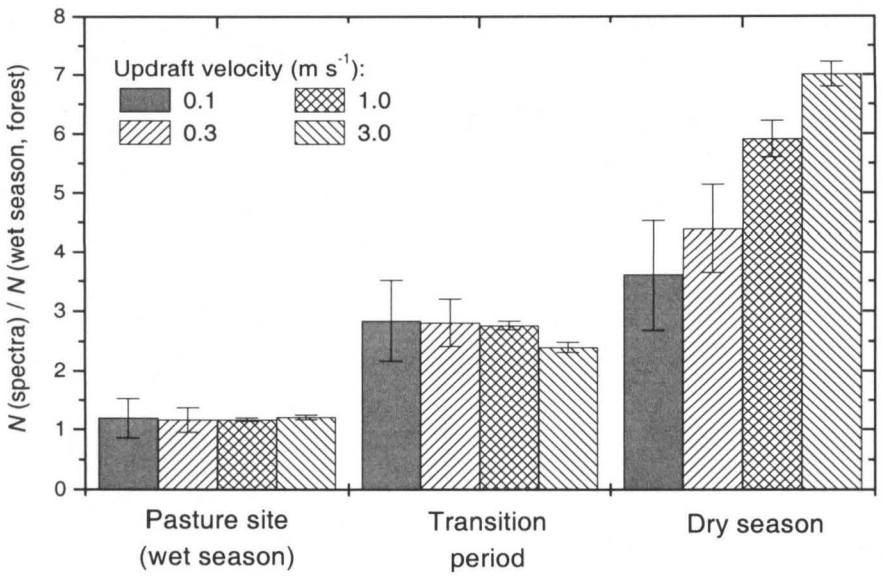

Figure 6.6. The ratio of cloud droplet concentration between the measured CCN spectra in the Amazon Basin and the wet season. The wet-season forest site CCN spectrum was used as a reference.

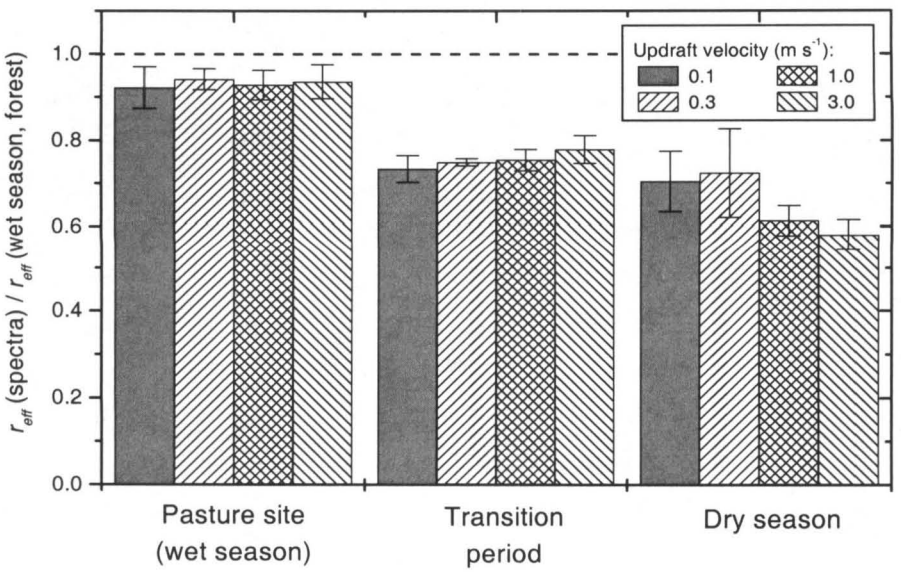

Figure 6.7. The ratio of effective cloud radius between the measured CCN spectra in the Amazon Basin and the wet season. The wet-season forest site CCN spectrum was used as a reference.

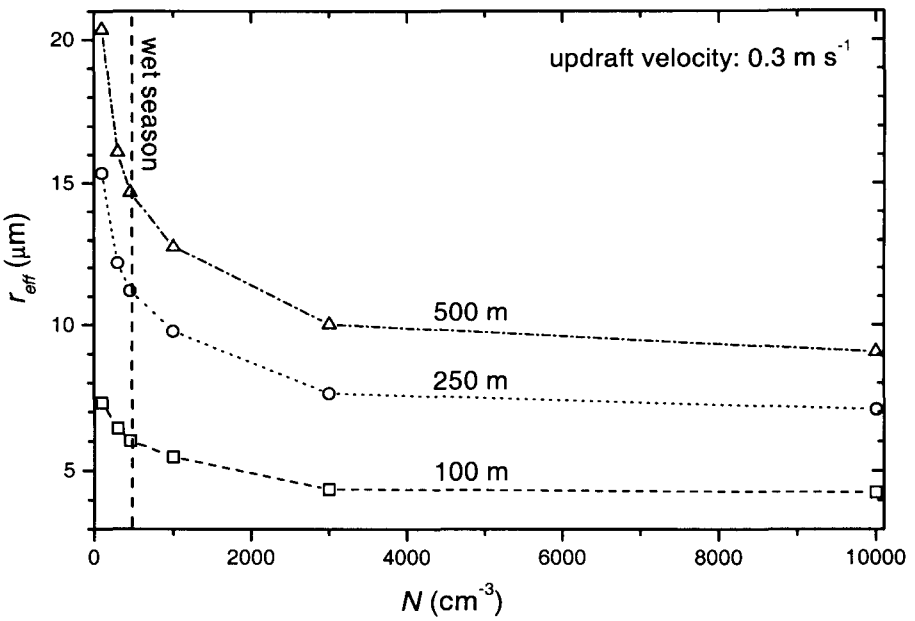

Figure 6.8. Effective cloud radius as a function of increasing aerosol concentrations for a variety of cloud depths. The wet-season forest site CCN spectrum was used with an updraft velocity of 0.3 m s^{-1}. The cloud depth is indicated on each line.

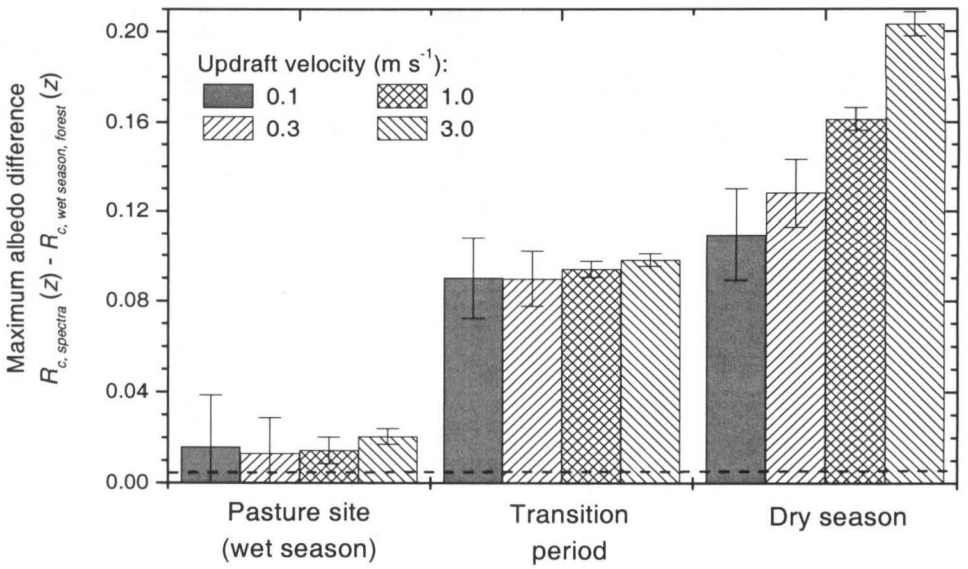

Figure 6.9. Maximum albedo differences between measured CCN spectra in the Amazon Basin for different updraft velocities. The aerosol distributions in Table 6.1 are used.

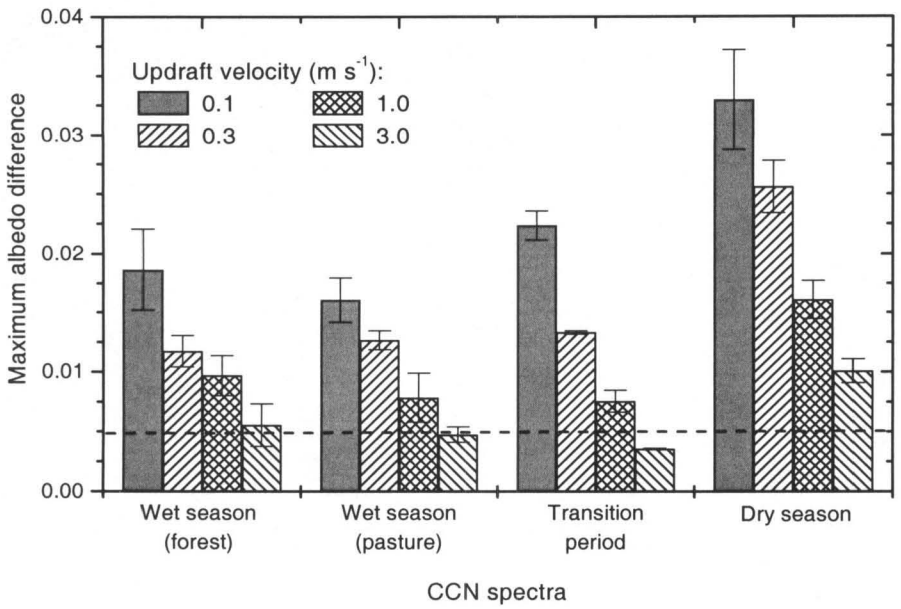

Figure 6.10. Maximum differences between thermodynamic and kinetic cloud albedo for different updraft velocities. The aerosol distributions in Table 6.1 are used.

Chapter 7

Origins and sources of cloud condensation nuclei in the Amazon Basin

Abstract

Recent data obtained during the Large Scale Biosphere-Atmosphere Experiment in Amazônia (LBA) have advanced our understanding of cloud condensation nuclei (CCN) and their role as an important regulator of precipitation and the energy cycle. Because CCN are coupled to the dynamic meteorological activity, they serve as an integral part of biosphere-atmosphere interactions. Aerosols in the Amazon Basin act efficiently as CCN, which raises important questions about their development during their transport over the rainforest. Natural variation of in-cloud supersaturations, scavenging of interstitial aerosol, and growth by condensation/partitioning of low-volatile species maintains the quasi-steady state aerosol size distribution that has been observed in the Amazon Basin.

7.1. Introduction

Clouds are an integral part of tropical climates by regulating the energy budget, evaporation, and large-scale atmospheric circulation. *Eltahir and Humphries* [1998] reported that a 1% change in cloudiness in the Amazon Basin exerts a radiative forcing of ca. -1 W m^{-2}, which would induce significant changes in net radiation into the rainforest. Such changes in radiation are likely to play important roles in large-scale land-atmosphere interactions that induce vertical motion and enhance cloud formation over rainforests and other continental regions [*Gedney and Valdes*, 2000; *Graf et al.*, 2000].

Cloud condensation nuclei (CCN) measurements were performed during several field campaigns in 1998 and 1999 as part of the Large Scale Biosphere-Atmosphere Experiment in Amazonia (LBA). Sampling occurred at ground-based sites in the states of Amazonas and Rondonia, Brazil (Chapter 3 and 6), as well as aircraft measurements throughout the Amazon Basin (Chapter 5). CCN concentrations between 0.15% and 1.5% supersaturation (S_v) were measured using static thermal-gradient CCN chambers that operated similarly to those described by *Lala and Jiusto* [1977]. The description and calibration of the CCN counter used for these experiments is discussed in Chapter 2.

As CCN are coupled to dynamic meteorological activity, understanding the chemical and physical properties that govern CCN activation advances our knowledge of many atmospheric processes in the Amazon Basin including heterogeneous chemistry, new particle formation, and cloud processing. Recent field measurements have provided new insight to the evolution of aerosols in the rainforest and at the processes that make up the natural components of the cycle of CCN in the rainforest (Figure 7.1): origin biogenic of CCN aerosol, cloud processing, aerosol scavenging, and new particle formation.

7.2. The CCN Cycle

CCN concentrations measured during the wet season in the Amazon Basin were surprisingly low and resembled conditions more typical of marine locations than of other continental sites (Chapter 3). Yet, the high efficiency of aerosols to serve as CCN raises important questions about conditioning processes during their transport over the rainforest. Coagulation, condensational growth and atmospheric processes have profound effects on size distribution and chemical composition.

7.2.1. The Origin of CCN

Possible natural sources for aerosol in the Amazon Basin include oxidation of natural biogenic emissions, emission of primary particles, entrainment from the free troposphere, and homogeneous nucleation of new particles. Depending on the meteorological conditions, the initial aerosol input into the rainforest originates from the Atlantic Ocean and/or anthropogenic sources from cities along Brazil's eastern coast. However, as CCN aerosol exhibit relatively short lifetimes, much of the original input will have been scavenged after several days (Section 7.2.3). A significant tropospheric source is unlikely because aerosols in the free troposphere are remarkably well distributed and exhibit lower concentrations of aerosol than in the boundary layer [*Gregory et al.*, 1986; *Pereira et al.*, 1996; *Talbot et al.*, 1990] (see Chapter 5). Long-range transport of Saharan dust depends on the position of the Inter-Tropical

Convergence Zone (ITCZ) and contributes to an important periodic source of aerosol mass [*Swap et al.*, 1996; *Talbot et al.*, 1990], but does not significantly increase number concentrations over the Amazon Basin *(Paulo Artaxo, personal communication*). During these dust events, the coarse mode ($D_p > 1$ μm) mass increases from 5-10 μg m^{-3} to 25-40 μg m^{-3} while the fine mode ($D_p < 1$ μm) mass increases by only 10-30%, mostly due to the tail of the coarse mode particle size distribution. When air masses from the Sahara Desert cross tropical Africa with active biomass burning, the black carbon concentration also increases slightly, but even in this situation, there is no significant increase in total aerosol number concentration.

Local primary biogenic sources, such as leaf fragments, pollen grains, fungi, algae, spores, bacteria, excrement and fragments of insects are closely associated to coarse mode K, P, and S [*Artaxo and Hansson*, 1995; *Simoneit et al.*, 1990]. In addition, single particle analysis of Amazonian aerosol also shows that phosphate is found mostly in the coarse mode. Hence, based on the measured number distribution, the contribution of coarse mode aerosol – and primary sources – to the total aerosol or CCN concentration is probably not significant.

Particles smaller than 0.3 μm diameter account for most of the number concentration; therefore, identifying the sources of aerosol in the CCN-size range (ca. $0.05 < D_p < 0.3$ μm) is important to tracing the origins of CCN. Previous measurements of mass distributions in the Amazon Basin show that aerosols in this size range are primarily composed of sulfates and organics [*Artaxo and Hansson*, 1995; *Wouters et al.*, 1993]. The sulfate fraction influences CCN properties by contributing soluble material while the organic fraction could enhance CCN activity two-fold; by contributing soluble

material and/or by lowering the surface tension of a deliquesced aerosol [*Facchini et al.*, 2000; *Shulman et al.*, 1996].

7.2.1.1. Sources of sulfate

The sulfate fraction, which constitutes 5 to 25% of the mass loading in the CCN-critical size fraction of Amazonian aerosols, may originate from the biogenic emissions of reduced sulfur compounds. Hydrogen sulfide (H_2S) and dimethyl sulfide (DMS) are the most important biogenic sulfur species emitted from the forest vegetation with respective fluxes of 1.5 and 0.5 nmol S m^{-2} min^{-1} in the Amazon Basin [*Andreae and Andreae*, 1988; *Andreae et al.*, 1990]. The total sulfur flux from the rainforest vegetation has been estimated to be 3 – 8 nmol S m^{-2} min^{-1}. Sulfur dioxide (SO_2) produced by the oxidation of DMS and H_2S is readily available for heterogeneous uptake on cloud droplets (Section *7.2*) or for new particle formation (Section *7.4*).

If the combined flux of H_2S and DMS is 2 nmol S m^{-2} min^{-1} and is converted uniformly to a strong acid within a 1-km-thick planetary boundary layer, then the volume production rate would be 2.9 nmol S m^{-3} day^{-1} (92 ng S m^{-3} day^{-1}). If half of the sulfur is lost to dry deposition [*Langner et al.*, 1992] and the rest were converted to particulate matter, this would replenish 46 ng S m^{-3} per day. Since the sulfur loading in coarse mode aerosol is about half of the fine mode and local primary biogenic aerosol is a major source of the coarse mode sulfur, the removal of H_2S and DMS-derived sulfur is not a large sink in the coarse fraction aerosol. Hence, we concentrate on the removal of fine fraction aerosol, where measurements taken in the Amazon rainforest indicate that the

mass loading of sulfur in the fine fraction is typically 50 ng m^{-3} (Chapter 4). Thus, the biogenic emissions of reduced sulfur compounds injected into the atmosphere could be sufficient to sustain the observed aerosol load of small particles against removal.

Recent models have suggested that SO_2 oxidation reactions are not rapid enough to make small nuclei grow to CCN size within the particle lifetime in the lower troposphere [*Kerminen et al.*, 2000]. Measured mass distributions also confirm that the fine mode aerosol constitutes a relatively small fraction of sulfates compared to the organic content [*Artaxo and Hansson*, 1995; *Wouters et al.*, 1993]. Hence, there may exist a "cooperative" relationship between organics and sulfates for CCN formation.

7.2.1.2. Sources of organic aerosol

The rainforest vegetation is an important emitter of VOCs such as monoterpenes [*Helmig et al.*, 1998; *Kesselmeier et al.*, 2000]. The flux of monoterpenes ($C_{10}H_x$) from the Amazon Basin has been estimated to be 0.55 mol C m^{-2} day^{-1} [*Guenther et al.*, 1995] and provides sufficient organic material for the predominantly "less-hygroscopic" organic Amazonian aerosols. The intensive appearance of small organic fragments (i.e., C_xH_y-; $x < 3$, $y < 7$) and the lack of phosphate containing compounds (i.e., phospholipids) in the fine mode Amazonian aerosols [*Wouters et al.*, 1993] suggest a secondary biogenic origin of the fine mode organic fraction. Multi-stage cascade impactor measurements have found that organic material constitutes up to 80% of the aerosol mass in the CCN size range [*Artaxo and Hansson*, 1995; *Wouters et al.*, 1993].

The photo-oxidation of monoterpenes yields low-volatile products that partition between the gas and particulate phases, accumulate in the condensed phase, and thus contribute to the ambient particulate mass [*Griffin et al.*, 1999; *Hoffmann et al.*, 1997]. Total monoterpene concentrations are ca. 0.6 ppb, where the primary species are α-pinene, β-pinene, p-cymene, and limonene [*Kesselmeier et al.*, 2000]. α-pinene and limonene have significant aerosol producing potential at realistic atmospheric oxidant concentrations [*Jacobson et al.*, 2000] and their mixing ratios in the Amazon Basin were ca. 0.3 and 0.05 ppb, respectively [*Kesselmeier et al.*, 2000]. The ozone and monoterpene mixing ratios in the Amazon Basin are rather low during the wet season (less than 20 and 0.6 ppb, respectively). Consequently, the aggregate formation rate for terpenoid products may not be sufficient for binary nucleation of secondary organic aerosol formation. Several field experiments have shown that monoterpene oxidation products are more likely to partition upon pre-existing particles than participate in homogeneous new particle formation [*Kavouras et al.*, 1999; *Marti et al.*, 1997].

7.2.2. Cloud Processing

The delicate balance of CCN over the Amazon may be maintained by convective mechanisms, as each volume of air cycles through a convective cloud about twice a day [*Miller et al.*, 1985]. A statistical model of CCN growth into cloud droplets suggests that even a low natural variation of supersaturations in cloud processes ($0.3 \pm 0.2\%$ S_v) maintains a quasi-steady state aerosol size distribution [*Kaufman and Tanré*, 1994] that is similar to those observed over the ocean and Amazon rainforest. As an air parcel is

likely to be processed through 10 or more non-precipitating cloud cycles [*Hoppel et al.*, 1990], cloud droplet growth and evaporation modifies the CCN spectrum. A large organic component and some sulfate is an inherent part of individual particles with diameters less than 0.5 μm [*Wouters et al.*, 1993]. These findings support the observations of significant cloud processing and organic deposition.

Cloud microphysics and heterogeneous chemistry depend strongly upon the reactive surface area of cloud droplets, which is dictated more by aerosol number concentrations than bulk aerosol mass. During the cloud phase, the droplets absorb trace gases and convert some of the gaseous material to particulate matter. Each cloud droplet will convert approximately the same amount of material regardless of the initial CCN size. Hence, small CCN will show a larger fractional increase in mass than larger CCN. Once an aerosol grows into a cloud droplet during any of the cloud cycles, it will be transformed into relatively efficient CCN for the remaining cloud interactions [*Bower and Choularton*, 1993; *Hegg et al.*, 1993; *Hobbs*, 1971; *Hoppel et al.*, 1990; *O'Dowd et al.*, 1999]. In addition to chemical conversion of trace gases, the smaller unactivated interstitial particles transfer their mass to the cloud droplets through Brownian diffusion. When the cloud droplets later evaporate, the resulting residue is larger than the original cloud nucleus.

The double-peaked number distributions observed in the Amazonian rainforest [*Zhou et al.*, 2001] are probably a result of cycling boundary layer air through clouds. Case studies showed that the double-peaked characteristics were associated with air that had passed through regions containing boundary layer clouds [*Hoppel et al.*, 1990]. In the Amazon Basin, both Aitken ($0.02 < d_p < 0.1$ μm) and accumulation ($0.1 < d_p < 1$ μm)

modes were present with the mean diameters 0.068 and 0.15 μm, respectively [*Zhou et al.*, 2001]. A minimum or a discontinuity in the number distribution occurred at $d_p = 0.1$ μm, which would correspond to a critical supersaturation of 0.5% and is in good agreement with expected cloud supersaturations. Such supersaturation would activate about 130 particles cm^{-3}, which is a reasonable number for cloud droplet concentrations. Mass distributions show a significant enhancement of sulfate from $0.1 < d_p < 0.3$ μm (Chapter 4). This size range has the longest residence time in the atmosphere [*Hoppel et al.*, 1990].

7.2.3. Aerosol Scavenging

Observed variations of CCN concentrations were primarily related to rainfall and temperature fluctuations. Collision and coalescence processes, which initiate precipitation, also effectively scavenge aerosol that served as seeds for cloud droplets. A reduction of aerosol concentrations was observed during rain events in the Amazon Basin (Figure 7.2) and the magnitude was typically related to the amount of rainfall and a decrease in surface air temperature (Figure 7.3). Such changes of surface meteorological conditions indicate a replacement of ground-level air parcels by air masses already processed by the storm front and support evidence for scavenging of the CCN aerosol fraction in cloud processes [*Harrison*, 1985; *Hobbs et al.*, 1985].

As the aerosol moves across the Amazon Basin, convective cloud processes enhance CCN activity (Section *7.2.2*) and CCN that readily activate at lower supersaturations are more likely to be scavenged. CCN lifetimes are quite short and have

been estimated to be 1-3 days [*Hoppel et al.*, 1990; *Jaenicke*, 1988]. Even newly formed aerosol (Section *7.2.4*) that are initially too small to serve as CCN, are removed primarily by condensational growth, interstitial cloud scavenging, and coagulation with a time constant of a day or less [*Hoppel et al.*, 1990]. These processes enable pre-CCN to eventually activate at higher supersaturations, which transforms them into readily available CCN. Hence, in the five to seven days required for an air mass to travel 1000 km into the Amazon Basin (i.e., from the Atlantic Ocean to Manaus), only about 20% of the aerosol number concentration has a likely coastal or oceanic origin.

7.2.4. New Particle Formation

Temporal measurements of number distributions show that homogeneous secondary particle formation over the rainforest rarely occurs at the ground level [*Zhou et al.*, 2001]. On the few occasions ultrafine particles ($D_p < 0.02$ μm) were observed, they had already grown to sizes larger than primary particles at the time of homogeneous nucleation ($0.003 < D_p < 0.01$ μm) and suggested that the ultrafine particles might have originated aloft. Marti *et al.* [1997] found that new particle formation was more highly associated with elevated production of gas phase sulfuric acid than oxidized organic products even in a boreal pine forest when reactive monoterpene emissions are considerably higher than those in the Amazon Basin.

Airborne measurements have found evidence that new particle formation in the Amazon Basin may occur in cloud outflow (Chapter 5). New particle production near cloud boundaries has been observed above the ocean and was attributed to homogeneous

heteromolecular nucleation of H_2SO_4– H_2O droplet conversion [*Hegg*, 1991; *Hegg et al.*, 1993; *Hegg et al.*, 1990; *Schäfer and Georgii*, 1994]. In remote marine regions, at altitudes greater than ca. 4 km above sea level, observations of nucleation near cloud perimeters are in fair agreement with current classical binary nucleation models [*Weber et al.*, 1998]. In tropical regions, the measured H_2SO_4 concentrations may be insufficient for binary nucleation in the warm climate near the earth's surface. The low temperatures, high water vapor content, and lack of preexisting particle surface area associated with high altitudes over the tropics may allow H_2SO_4 to become sufficiently saturated for the production of new H_2SO_4– H_2O particles.

At lower altitudes, the measurements substantially differ from H_2SO_4–H_2O predictions, possibly due to the closer proximity to surface sources of potential precursor species like NH_3. The rainforest provides an abundant supply of NH_3 and the nucleation threshold for H_2SO_4 is even less when NH_3 is present. A ternary mechanism has been suggested as a viable alternative pathway [*Korhonen et al.*, 1999] and ion-ion recombination of tropospheric aerosols may also explain the presence of a stable boundary layer aerosol population of several hundred particles per cm^3 [*Turco et al.*, 1998].

7.3. Conclusions

Since CCN are coupled to the dynamic meteorological activity, coagulation, condensational growth and atmospheric processes have profound impacts on the aerosol properties. Detailed analysis of number distributions and the size-dependent chemical

composition of the aerosol in the Amazon Basin indicate that sulfate and organics are the principal components of the aerosol that account for the CCN activity (Chapter 4). The sulfate and organic fraction of the CCN-size aerosol probably originate from the condensation/partitioning of the oxidation products of reduced sulfur and VOC emissions from the forest vegetation. Cloud processes modify the CCN spectrum and enable the smallest CCN to later activate at lower supersaturations. As particles are removed from the atmosphere by wet deposition, new particle formation (i.e., ternary mechanisms or ion-ion recombination) replenishes the aerosol number concentration. Natural variation of in-cloud supersaturations, scavenging of interstitial aerosol, and growth by condensation/partitioning of low-volatile species probably maintains the quasi-steady state aerosol size distribution that has been observed in the Amazon Basin.

7.4. References

Andreae, M.O., and T.W. Andreae, The cycle of biogenic sulfur compounds over the Amazon Basin: 1. Dry season, *J. Geophys. Res.*, *93* (D2), 1487, 1988.

Andreae, M.O., H. Berresheim, H. Bingemer, D.J. Jacob, B.L. Lewis, S.-M. Li, and R.W. Talbot, The atmospheric sulfur cycle over the Amazon Basin, 2, Wet season, *J. Geophys. Res.*, *95*, 16,813-16,824, 1990.

Artaxo, P., and H.C. Hansson, Size distribution of biogenic aerosol particles from the Amazon basin, *Atmos. Environ.*, *29* (3), 393, 1995.

Bower, K.N., and T.W. Choularton, Cloud processing of the cloud condensation nucleus spectrum and its climatological consequences, *Q. J. R. Meteorol. Soc.*, *119*, 655, 1993.

Eltahir, E., and E.J. Humphries, The role of clouds in the surface energy balance over the Amazon forest, *Int. J. Climatol.*, *18*, 1575-1591, 1998.

Facchini, M., S. Decesari, M. Mircea, S. Fuzzi, and G. Loglio, Surface tension of atmospheric wet aerosol and cloud/fog droplets in relation to their organic carbon content and chemical composition, *Atmos. Environ.*, *34*, 4853-4857, 2000.

Gedney, N., and P. Valdes, The effect of Amazonian deforestation on the northern hemisphere circulation and climate, *Geophys. Res. Lett.*, *27* (19), 3053-3056, 2000.

Graf, H.F., F.J. Nober, and D. Rosenfeld, Sensitivity of global climate to the detrimental impacts of smoke on rain clouds, 2000.

Gregory, G.L., R.C. Harriss, R.W. Talbot, R.A. Rasmussen, M. Garstang, M.O. Andreae, R.R. Hinton, E.V. Browell, S.M. Beck, D.I. Sebacher, M.A.K. Khalil, R.J. Ferek, and S.V. Harriss, Air chemistry over the tropical forest of Guyana, *J. Geophys. Res.*, *91*, 8603-8612, 1986.

Griffin, R.J., D.R. Cocker, III, R.C. Flagan, and J.H. Seinfeld, Organic aerosol formation from the oxidation of biogenic hydrocarbons, *J. Geophys. Res.*, *104*, 3555-3567, 1999.

Guenther, A., C.N. Hewitt, D. Erickson, R. Fall, C. Geron, T. Graedel, P. Harley, L. Klinger, M. Lerdau, W.A. McKay, T. Pierce, B. Scholes, R. Steinbrecher, R.

Tallamraju, J. Taylor, and P. Zimmerman, A global model of natural volatile organic compound emissions, *J. Geophys. Res.*, *100*, 8873-8892, 1995.

Harrison, L., The segregation of aerosols by cloud-nucleating activity. Part II: Observation of an urban aerosol, *J. Climate Appl. Meteorol.*, *24*, 312, 1985.

Hegg, D.A., Particle production in clouds, *Geophys. Res. Lett.*, *18*, 995-998, 1991.

Hegg, D.A., R.J. Ferek, and P.V. Hobbs, Aerosol size distributions in the cloudy atmospheric boundary layer of the North Atlantic Ocean, *J. Geophys. Res.*, *98*, 8841-8846, 1993.

Hegg, D.A., L.F. Radke, and P.V. Hobbs, Particle production associated with marine clouds, *J. Geophys. Res.*, *95*, 13917-13926, 1990.

Helmig, D., B. Balsley, K. Davis, L. Kuck, M. Jensen, J. Bognar, T. Smith, R. Arrieta, R. Rodriguez, and J. Birks, Vertical profiling and determination of landscape fluxes of biogenic nonmethane hydrocarbons within the planetary boundary layer in the Peruvian Amazon, *J. Geophys. Res.*, *103* (D19), 25519-25532, 1998.

Hobbs, P.V., Simultaneous airborne measurements of cloud condensation nuclei and sodium- containing particles over the ocean, *Q. J. R. met. Soc.*, *97*, 263-271, 1971.

Hobbs, P.V., D.A. Bowdle, and L.F. Radke, Particles in the lower troposphere over the high plains of the United States, 2, Cloud condensation nuclei, *J. Climate and Appl. Meteor.*, *24*, 1358-1369, 1985.

Hoffmann, T., J.R. Odum, F. Bowman, D. Collins, D. Klockow, R.C. Flagan, and J.H. Seinfeld, Formation of organic aerosols from the oxidation of biogenic hydrocarbons, *J. Atmos. Chem.*, *26*, 189-222, 1997.

Hoppel, W.A., J.W. Fitzgerald, G.M. Frick, R.E. Larson, and E.J. Mack, Aerosol size distributions and optical properties found in the marine boundary layer over the Atlantic Ocean, *J. Geophys. Res.*, *95*, 3659-3686, 1990.

Jacobson, M.C., H.-C. Hansson, K.J. Noone, and R.J. Charlson, Organic atmospheric aerosols: Review and state of the science, *Reviews of Geophysics and Space Physics*, 2000.

Jaenicke, R., Aerosol physics and chemistry, in *Meterology. Landolt-Börnstein, New Series, V/4b*, edited by G. Fischer, pp. 391-457, Springer, Berlin, 1988.

Kaufman, Y.J., and D. Tanré, Effect of variations in supersaturation on the formation of cloud condensation nuclei, *Nature*, *369*, 45-48, 1994.

Kavouras, I.G., N. Mihalopoulos, and E.G. Stephanou, Formation and gas/particle partitioning of monoterpenes photo-oxidation products over forests, *Geophys. Res. Lett.*, *26* (1), 55-58, 1999.

Kerminen, V., A. Virkkula, R. Hillamo, A. Wexler, and M. Kulmala, Secondary organics and atmospheric cloud condensation nuclei production, *J. Geophys. Res.*, *105* (D7), 9255-9264, 2000.

Kesselmeier, J., U. Kuhn, A. Wolf, M.O. Andreae, P. Ciccioli, E. Brancaleoni, M. Frattoni, L. Ganzeveld, A. Guenther, J. Greenberg, P. de Castro Casconcellos, S. Oliva, T. Tavares, and P. Artaxo, Atmospheric volatile organic compounds (VOC) at a remote tropical forest site in central Amazonia, *Atmos. Environ.*, 2000.

Korhonen, P., M. Kulmala, A. Laaksonen, Y. Viisanen, R. McGraw, and J. Seinfeld, Ternary nucleation of H_2SO_4, NH_3, and H_2O in the atmosphere, *J. Geophys. Res.*, *104*, 26349-26353, 1999.

Lala, G.G., and J.E. Jiusto, An automatic light scattering CCN counter, *J. Appl. Meteor.*, *16* (4), 413-418, 1977.

Langner, J., H. Rodhe, P.J. Crutzen, and P. Zimmermann, Anthropogenic influence on the distribution of tropospheric sulphate aerosol, *Nature*, *359*, 712-716, 1992.

Marti, J.J., R.J. Weber, P.H. McMurry, F. Eisele, D. Tanner, and A. Jefferson, New particle formation at a remote continental site: Assessing the contributions of SO_2 and organic precursors, *J .Geophys. Res.*, *102* (D5), 6331-6339, 1997.

Miller, J.M., D.M. Whelpdale, L.A. Barrie, I.S.A. Isaksen, H. Rodhe, and F.B. Smith, The transport of sulfur and nitrogen through the remote atmosphere, in *The Biogeochemical Cycling of Sulfur and Nitrogen in the Remote Atmosphere*, edited by J.N. Galloway, R.J. Charlson, M.O. Andreae, H. Rodhe, and D. Reidel, pp. 127-139, Hingham, Mass., 1985.

O'Dowd, C., J. Lowe, and M. Smith, Observations and modelling of aerosol growth in marine stratocumulus - case study, *Atmos. Environ.*, *33*, 3053-3062, 1999.

Pereira, E., A. Setzer, F. Gerab, P. Artaxo, M. Pereira, and G. Monroe, Airborne measurements of aerosols from burning biomass in Brazil related to the TRACE A experiment, *J. Geophys. Res.*, *101* (D19), 23983-23992, 1996.

Schäfer, B., and H.-W. Georgii, Airborne measurements of condensation nuclei and cloud condensation nuclei above the alpine foothills, *Beitr. Phys. Atmosph.*, *67* (4), 335, 1994.

Shulman, M.L., M.C. Jacobson, R.J. Charlson, R.E. Synovec, and T.E. Young, Dissolution behavior and surface tension effects of organic compounds in nucleating cloud droplets, *Geophys. Res. Lett.*, *23*, 277-280, 1996.

Simoneit, B.R.T., J.N. Cardoso, and N. Robinson, An assessment of the origin and composition of higher molecular weight organic matter in aerosols over Amazonia, *Chemosphere*, *21* (10-1), 1285-1301, 1990.

Swap, R., M. Garstang, S.A. Macko, P.D. Tyson, W. Maenhaut, P. Artaxo, P. Kållberg, and R. Talbot, The long-range transport of southern African aerosols to the tropical South Atlantic, *J. Geophys. Res.*, *101*, 23,777-23,792, 1996.

Talbot, R.W., M.O. Andreae, H. Berresheim, P. Artaxo, M. Garstang, R.C. Harriss, K.M. Beecher, and S.M. Li, Aerosol chemistry during the wet season in Central Amazonia: The influence of long-range transport, *J. Geophys. Res.*, *95*, 16,955-16,969, 1990.

Turco, R., J. Zhao, and F. Yu, A new source of tropospheric aerosols: Ion-ion recombination, *Geophys. Res. Lett.*, *26*, 55-58, 1998.

Weber, R.J., P.H. McMurry, L. Mauldin, D.J. Tanner, F.L. Eisele, F.J. Brechtel, S.M. Kreidenweis, G.L. Kok, R.D. Schillawski, and D. Baumgardner, A study of new particle formation and growth involving biogenic and trace gas species measured during ACE 1, *J. Geophys. Res.*, *103* (D13), 16385-16396, 1998.

Wouters, L., S. Hagedoren, I. Dierck, P. Artaxo, and R.V. Grieken, Laser microprobe mass analysis of Amazon Basin aerosols, *Atmos. Environ.*, *27A* (5), 661-668, 1993.

Zhou, J., E. Swietlicki, H. Hansson, and P. Artaxo, Sub-micrometer aerosol particle size distribution and hygroscopic growth measurements in the Amazonian rain forest during the wet season, *Submitted to J. Geophys. Res.*, 2001.

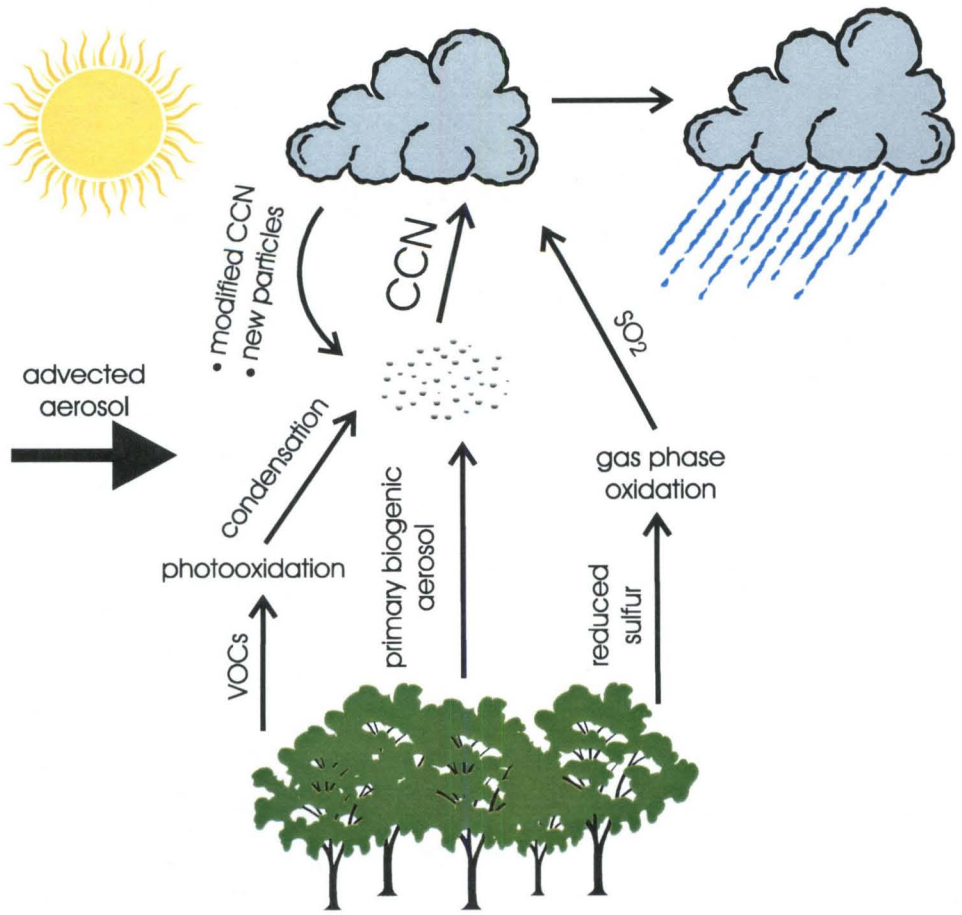

Figure 7.1. Cycle of CCN in the Amazon Basin.

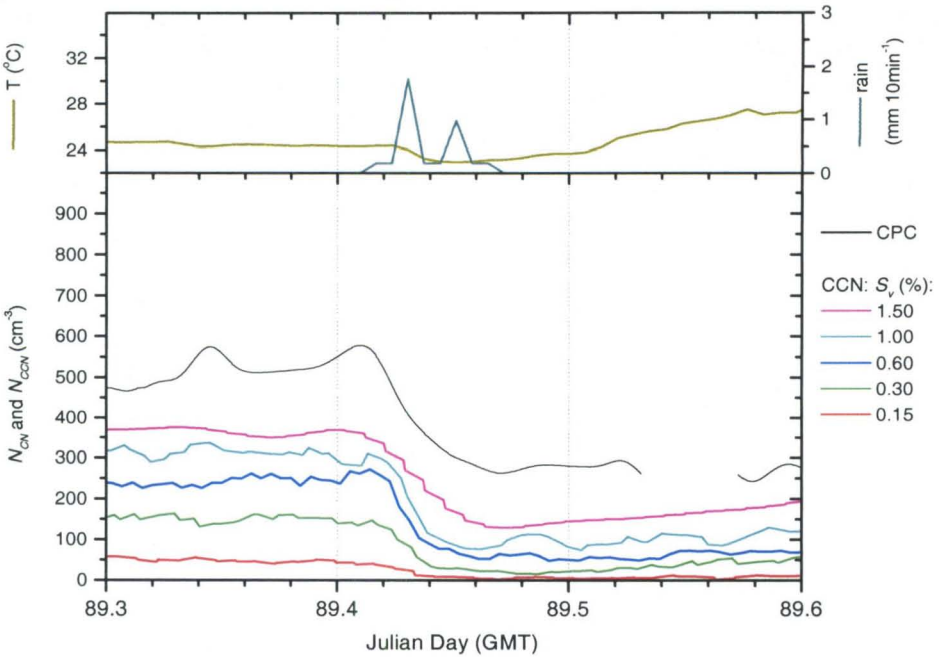

Figure 7.2. Temporal evolution of precipitation scavenging during rain event. The upper graph shows the rate of rainfall and the lower graph shows the decrease in aerosol concentrations.

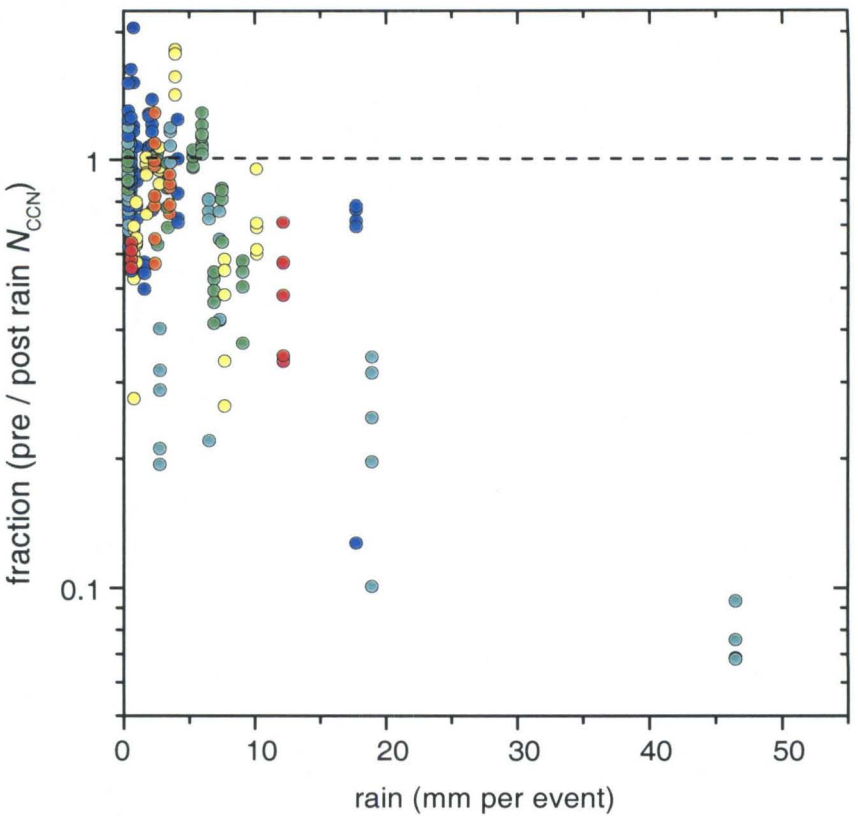

Figure 7.3. Precipitation scavenging of CCN aerosol as a function of the total amount of rainfall in the event.

Chapter 8

Conclusions

8.1. CCN in the Amazon Basin

The measurements, performed during the Large Scale Biosphere-Atmosphere Experiment in Amazonia (LBA), have enhanced our understanding of CCN and its role in tropical and global climate. Our results show that low CCN concentrations and high CCN/CN ratios over the unpolluted Amazon Basin resemble conditions previously reported from marine environments. It is remarkable that similar CCN concentrations prevail in pristine marine and continental regions, in spite of the different aerosol production mechanisms and particle compositions.

Although organic material constitutes nearly 80% of the aerosol mass in the Amazon Basin, a detailed analysis of number distributions and the size-dependent chemical composition of the aerosol indicates that sulfates can account for most of the CCN activity during the wet season. The potential effects of water-soluble organic carbon compounds (WSOCs) on CCN activity cannot be readily determined from our CCN measurements. The role of WSOCs as surfactants, however, may be significant and more field measurements are needed to quantify their effects on surface tension of ambient aerosols especially during the biomass burning season.

Measurements during the dry season have shown that biomass burning smoke aerosol increases CCN concentrations by an order or magnitude over Amazonia. This increases colloidal stability and cloud lifetime, resulting in the non-precipitating clouds observed in the dry season. Our model studies have confirmed that modification of cloud properties is most sensitive at low initial CCN concentrations. The effective cloud radius

decreased by a factor of two during the biomass burning season, which inhibits precipitation processes. Potential changes of albedo in stratiform clouds may also be significant.

The response of cloud droplet concentration and radius to changes in CCN concentrations is the basis for the modification of precipitation, cloud fraction and indirect forcing. The interaction of these factors controls the heat flux into the rainforest, which is, in return, the primary driver of convective cloud formation. Because of the low natural CCN abundance in Amazonia, climatic effects related to the enhanced aerosol emissions due to human activity may have a stronger impact on climate change than in other continental regions.

8.2. Future Research

The aerosol cycle in the Amazon Basin is based upon recent field experiments as part of the LBA project where measurements have provided new insight to the evolution of aerosols in the rainforest. The atmospheric processes that enable the development of CCN unify many disciplines of atmospheric chemistry and physics. An understanding of the natural aerosol cycle in the Amazon Basin provides a reference to assess the potential influences of anthropogenic activity in a perturbed environment. However, various segments of this research that need further exploration and present challenges for future experiments are as follows:

- Detailed inorganic and organic compositions of aerosol with diameters less than 0.5 μm are needed to better understand the origins and properties of the CCN size aerosol.
- Surface tension effects from water-soluble organic aerosols have not been well quantified. These effects are expected to be higher in biomass burning aerosol, which is largely comprised of humic substances.
- Isotopic analysis of sulfur as a function of size distribution provides clues of anthropogenic contribution to aerosol in the remote Amazon Basin as well as the degree of cloud processing and scavenging during its transport over the rainforest.
- Single particle analysis could provide useful information on the homogeneity of CCN-size aerosol and shed insight on cloud processing, condensational growth and interstitial scavenging.
- New particle formation has been observed near cloud perimeters, but more information is needed to estimate the rates of formation and growth processes that allow the interstitial aerosol to later serve as CCN.

Appendix A

Activation kinetics of a photometric static thermal-gradient cloud condensation nuclei counter

Abstract

The photodetector output of a photometric static thermal-gradient diffusion chamber was characterized by determining correlations between the detector output and monodisperse aerosol concentrations. A differential mobility analyzer (DMA) yielded monodisperse aerosol sizes selected to vary particle growth rates at different supersaturations between 0.15% to 1.50%. Köhler theory predicted the critical supersaturation well for inorganic salts (i.e., NaCl, K_2SO_4, $(NH_4)_2SO_4$), but adipic acid aerosol appears to exhibit different activation kinetics because of its slightly soluble nature and surface tension effects. Activation coefficients were found to be dependent on supersaturation and initial particle size. The particle size distribution influences the calculation of cloud condensation nuclei concentrations resulting in discrepancy in concentrations of ~ 20% between marine and urban aerosol types.

A.1. Introduction

Cloud condensation nuclei (CCN) have a fundamental role in determining the global climate. The size, concentration, and affinity to water vapor of CCN directly influence the size and concentration of cloud droplets, which determines the radiative properties of clouds [*Twomey*, 1977]. Measurements of CCN concentrations can be determined by direct activation in a chamber of controlled supersaturations or deduced in a continuous flow chamber from particle size information. The static chamber is perhaps the most widely used since its introduction by *Twomey* [1963]. A known supersaturation profile develops in the chamber between two wet parallel plates. Once activated, aerosol particles will grow and gravitationally settle out of the illuminated sample volume.

Two methods are commonly used to determine CCN concentrations in static thermal-gradient CCN instruments. Directly counting particles through photographic methods has the advantage of being size independent, but does not obtain continuous time information. The method also requires sophisticated image processing to yield viable results. The alternative approach of measuring the amount of light scattered in the chamber is appealing as it leads to simple automated method in determining CCN number concentrations. The calibration is obtained empirically and has been investigated by several groups [*Bartlett and Ayers*, 1981; *Lala and Jiusto*, 1977; *Oliveira and Vali*, 1995]. Previous calibrations rely on a comparison of direct and indirect counting procedures of an ambient aerosol to obtain the empirical calibration for the CCN counter.

This paper examines how the growth characteristics of monodisperse aerosol influence the empirically derived number concentrations. The results are not an absolute

calibration of the CCN counter, but underline the importance of size distribution information to obtain CCN number concentrations.

A.2. Experimental Methods

A.2.1. Description of the Apparatus

The measurements described were performed using a static thermal-gradient diffusion illustrated in Figure A.1. Its main component is a flat cylindrical chamber in which supersaturations are created by cooling the bottom plate and allowing the top plate to remain at ambient temperature. Whatman 4 filter paper is placed on both plates and kept soaked with water using an external capillary system. Activated particles are illuminated by a 50W Tungsten lamp, placed in a reflectance-coated housing to ensure a uniform intensity within the beam. Stray light is trapped in a 60 cm tube, which contains lenses and filters to image the sample volume into the chamber. A photodetector and lens arrangement is placed perpendicular to the illumination beam. Conical light traps are placed on opposite sides of the chamber to ensure a dark background and enhance the signal-to-noise ratio.

The CCN counter is controlled by a Hitachi 6303 Forth microprocessor, which provides control of the plate temperatures, a valve, lamp and pump. A RS-232 connection allows serial communication between the CCN counter and a personal computer for run-time commands and data acquisition. Photodetector signals are

recorded at 10 Hz and the reference light signal and plate temperatures are recorded at the beginning of each run.

The sample volume is determined by the size of the window used to image the beam into the cloud chamber. The illuminated volume detected by the photodetector is 0.116 cm^3. The photodetector used is an EG&G UV 444BQ photodiode which has a sensitivity of 10^{-14} W.

A.2.2. Experimental Procedure

The system used for characterizing activation kinetics within the CCN counter is illustrated in Figure A.2. Aerosol of a known composition was created by a nebulizer and passed through a diffusion dryer and neutralizer before being introduced into the differential mobility analyzer (DMA) (TSI 3071). NaCl, $(NH_4)_2SO_4$, K_2SO_4 and adipic acid aerosol were analyzed independently and the properties of the investigated compounds are shown in Table A.1. The flow rates through the DMA were controlled to 20 liters per minute (lpm) for sheath and excess air and 1.9 lpm for inlet and monodisperse aerosol flow. The voltage potential in the DMA was maintained constant throughout a sampling period to yield monodisperse aerosol. Particle diameters between 0.02 and 0.2 μm were chosen for each composition to observe various degrees of activation at different supersaturations. The monodisperse aerosol passed through another neutralizer before entering an initially aerosol free 19 liter vessel from which the particles were sampled. The glass jar allows the aerosol concentrations to vary without changing the system parameters during the sampling and the second neutralizer serves to

reduce electrostatic losses to the vessel's glass walls. Figure A.3 shows a typical variation in particle concentrations during a sample run. The aerosol was sampled from the glass vessel by the condensation particle counter (CPC) and CCN counters. To allow for continuous monitoring of particle concentrations during the batch sampling of the CCN counter, an aerosol free dilution air of 4 lpm was required so that outside aerosol did not contaminate the sample stream. The CCN chamber was purged 10 seconds before each sample to ensure a clean chamber and measurements were obtained by completing cycles of eleven supersaturations every ten minutes. Number concentrations were recorded every five seconds using a condensation particle counter (CPC) (TSI 3025) and ranged between zero and several thousand particles cm^{-3}. Data for the CCN and CPC counters were stored in a computer for subsequent analysis.

A.3. Results and Discussion

A.3.1. Time Delays and Variation of Peak Signal Maxima

The time of the maximum signal output after the chamber closes, τ_p, is determined for each supersaturation and aerosol composition for runs in which particles were activated. Particles were considered activated if the output signal was above a threshold defined as $6 \cdot \sigma_b$ where σ_b is the baseline variance. The mean values of the peak times $<\tau_p>$, their standard deviations σ_p, and number of runs n included in each average are shown in Table A.2 for ammonium sulfate. As expected, the trends show that higher supersaturations result in shorter peak times with less variation. Figure A.4 shows the

combined average of all activated runs for $(NH_4)_2SO_4$ particles. The measurement cycle begins (i.e., time equals zero) after purging the chamber and when it closes. Similar patterns are observed for the other investigated species. Note that peak times for the ensemble average (Figure A.4) are not the same as $<\tau_p>$ (Table A.2) due to the differences in averaging the data.

A.3.2. Activation Coefficients

The photodetector output signal was analyzed only if the particles in a given run were activated (i.e., signal > $6 \cdot \sigma_b$). For each particle size and supersaturation, a best-fit linear relationship restricted to pass through the origin was determined between the number concentration N and the CCN photodetector signal V_{area},

$$N = \frac{V_i}{\alpha_v} \tag{A.1}$$

where α_v is the activation coefficient dependent on supersaturation and particle size. The area under the signal that is above 75% of peak maximum is V_{area}. A value of zero for α_v indicates no activation occurred. The relationship between the photodetector signal and the number concentration was linear even for aerosol concentrations as high as 10^4 cm^{-3}. Number concentrations below 6000 cm^{-3} were used in these results.

In previous calibrations of static thermal-gradient chambers, the relationship between N and V_i was expressed in the form

$$N = V_i\left(\upsilon + \frac{\omega}{S}\right) \tag{A.2}$$

where S_v is the supersaturation (%) and ν and ϖ are calibration constants. Several different measures of the photodetector output V_i have been used for analyzing the observed CCN concentrations, including the maximum signal output, an average of the within a range of the peak, and the area under the signal. A comparison of the different techniques shows that activation coefficients using V_{area} yields better results; therefore, V_{area} is used in the rest of this paper. The constants of Equation A.2 are determined by first obtaining a linear best-fit relationship between N and V_i, restricting the fit to pass through the origin, and then obtaining a linear relationship between the constant of that proportionality and the inverse of the supersaturation [*Oliveira and Vali*, 1995]. However, in these experiments, it has been found that the activation coefficients are also dependent on particle size as shown in Figure A.5. The dashed line on the contour plot indicates the predicted critical supersaturation (S_c) from Köhler theory [*Seinfeld and Pandis*, 1998].

An alternative approach to characterizing the CCN counter will be described by establishing a new set of parameters, R' and S'. The relationship between α_v, R', and S' is shown in Figure A.6 and the axes are rotated by the expressions

$$\begin{aligned} R' &= \log_{10} 2R_p \cdot \cos(-\varphi) - \log_{10} S_c \cdot \sin(-\varphi) - x_o \\ S' &= \log_{10} 2R_p \cdot \sin(-\varphi) + \log_{10} S_c \cdot \cos(-\varphi) \end{aligned} \tag{A.3}$$

The $\log_{10}(S_c)$-$\log_{10}(R_p)$ plane is rotated by an angle ϕ, determined by a line representing the critical supersaturation calculated by Köhler theory for particles of an initial dry radius (R_{pi}). The origin of the rotated plane is adjusted such that the rotated $\log_{10}(S_c)$ axis, S', lies on the predicted critical supersaturation. R' is normal to S' and represents an adjusted particle size. $R' = 0$ is the particle size where activation occurs for all supersaturations and the calibration coefficient is on the axis perpendicular to the S'- R' plane. When $R' < 0$, the particles will not activate and $\alpha_v = 0$. When $R' > 0$, α_v increases until $R' = 0.5$. This increase illustrates the activation kinetics of cloud droplet formation. Figure A.7 shows the growth characteristics for the investigated compounds and the increase in α_v for particles between the critical size ($R' = 0$) and a threshold size R'_C. The CCN counter response appears to be independent of the initial dry particle size when $R' > R'_C$. For all inorganic salts in the calibration, the threshold size occurs when R' is ca. 0.5. This corresponds to droplet sizes that are nearly three times larger than the critical radius (R_{pc}).

As shown in Figure A.7, α_v begins to increase once the particles activate. The critical supersaturation (at $R' = 0$) is accurately predicted using Köhler theory for the inorganic soluble salts. The molecular weight, density, and van't Hoff factor, as shown in Equation A.3 and Table A.1, are well-defined properties of water-soluble inorganic salts. Water-soluble organic carbon compounds also influence CCN activity by decreasing the surface tension at the droplet's surface. Adipic acid aerosol exhibits slower growth trends as the inorganic salts probably because of its slightly soluble nature and relatively modest surface tension effects [*Shulman et al.*, 1996]. Important information regarding the growth kinetics of organic CCN may be obtained using this method.

A.4. Implications for Ambient Sampling

Ambient aerosol size distributions, however, are never monodisperse and will consequently effect the calculation of CCN number concentrations. Since α_v is smaller for particles sizes less than R'_C, estimations based on an activation coefficient independent of particle size will underestimate the actual CCN concentrations.

Idealized size distribution with prescribed number distributions and chemical composition are used to clearly sort out the physics involved. Size distributions are of the multiple mode lognormal form

$$\frac{\delta N}{\delta \log d_p} = \sum_{i=1}^{n_m} \frac{N}{\sqrt{2\pi}\ln\sigma_g} \exp\left[\frac{-\left(\ln d_p - \ln d_{pg}\right)^2}{2\ln^2\sigma_g}\right] \qquad \text{(A.4)}$$

where N_i is the aerosol number concentration, $R_{pg,i}$ is the geometric mean radius, and $\sigma_{g,i}$ is the geometric standard deviation for mode i, and n_m is the number of modes in the distribution. For a representation of different ambient aerosol distiributions, we have selected trimodel distributions described by *Whitby* [1978]; namely the marine, clean continental, average background and urban aerosol types. Values for N_i, $R_{pg,\,i}$ and $\sigma_{g,\,i}$ for these distributions are listed in Table A.3. The number distributions refer to dry size, while the chemical composition of the aerosol is assumed pure ammonium bisulfate.

Expected output signals from the CCN will be estimated by assessing the size dependence of α_v for different representations of ambient aerosol distributions. Using

Equation A.4 and assuming an unbiased response from all particles in the size distribution, $n(R_p)$, an integration over $n(R_p)$ will yield

$$\Psi_{area} = \int_{R_{pc}}^{\infty} \alpha_v(R_p) n(R_p) \cdot dR_p = \int_0^{\infty} \alpha_v(R') n(R') R_p(R') \cdot dR' \qquad (A.5)$$

where Ψ_{area} is the theoretical value of V_{area} to be measured by the instrument. Hence, the CCN number concentration of a polydisperse aerosol size distribution is calculated as shown in expression

$$N_{CCN} = V_{area} \Gamma(R') \qquad (A.6)$$

where V_{area} is the measured signal from the CCN counter and $\Gamma(R')$ is analogous to α_v^{-1}, which is determined as follows:

$$\Gamma(R') = \frac{N_{CCN}}{\Psi_{area}} = \frac{\int_0^{\infty} n(R') R_p(R') \cdot dR'}{\int_0^{\infty} \alpha_v(R') n(R') R_p(R') \cdot dR'} \qquad (A.7)$$

The dependence of $\Gamma(R')$ on the different aerosol distribution types is shown in Figure A.8. At lower supersaturations, the difference in $\Gamma(R')$ between the marine and land-based aerosol distributions originates from the higher concentration of smaller particles in the region between $R' = 0$ and R'_C in the land-based distributions.

For error estimation purposes, Figure A.9 represents the ratio of number concentrations (N_{const} / N_α) based on light-scattering growth calibrations (N_α) and a size independent calibration coefficient (N_{const}). For large changes in size distributions (i.e.,

marine to urban aerosol types), CCN number concentrations could vary by 50% at low supersaturations (ca. 0.15% S_v) for the thermal static-gradient CCN counter used in this experiment.

A.5. Conclusions

The photometric measurements of the CCN counter were performed using monodisperse aerosol of various soluble compounds and emphasize the dependence of the initial dry aerosol size on the light scattering calibration of a static thermal-gradient CCN counter. A different approach to characterizing the CCN counter was described by establishing a new set of parameters, R' and S' (Section 3.2). The results show that CCN number concentrations depend on aerosol size distributions because the calibration coefficient increases within a transitional growth regime, $0 < R' < 0.5$.

The inorganic soluble particles show similar growth characteristics and their critical supersaturations are accurately predicted by Köhler theory. Adipic acid exhibits slower growth trends than inorganic salts due to its slightly soluble nature and moderate surface tension effects. The results are not an absolute calibration of the CCN counter, but underline the importance of size distribution information to obtain accurate CCN number concentrations.

A.6. References

Bartlett, B.M., and G.P. Ayers, Static diffusion cloud chamber, *J. Rech. Atmos.*, *15*, 231-233, 1981.

Köhler, H., The nucleus in and the growth of hygroscopic droplets, *Trans. Faraday Soc.*, *32*, 1152-1161, 1936.

Lala, G.G., and J.E. Jiusto, An automatic light scattering CCN counter, *J. Appl. Meteor.*, *16* (4), 413-418, 1977.

Oliveira, J.C.P., and G. Vali, Calibration of a photoelectric cloud condensation nucleus chamber, *Atmos. Res.*, *38*, 237, 1995.

Seinfeld, J.H., and S.N. Pandis, *Atmospheric chemistry and physics: From air pollution to climate change*, 1326 pp., John Wiley, New York, 1998.

Shulman, M.L., M.C. Jacobson, R.J. Charlson, R.E. Synovec, and T.E. Young, Dissolution behavior and surface tension effects of organic compounds in nucleating cloud droplets, *Geophys. Res. Lett.*, *23*, 277-280, 1996.

Twomey, S., Measurements of natural cloud nuclei, *J. Rech. Atmos.*, *1*, 101-105, 1963.

Twomey, S., The influence of pollution on the short-wave albedo of clouds, *J. Atmos. Sci.*, *34*, 1149-1152, 1977.

Whitby, K., The physical characteristics of sulfur aerosols, *Atmos. Environ.*, *30*, 2335-2341, 1978.

Table A.1. The properties and theoretical activation diameters for investigated compounds.

	M_w (g mol^{-1})	ρ (g cm^{-3})	ν_H	D_{pc} (μm) S_c = 0.3%	D_{pc} (μm) S_c = 1.0%
Adipic acid	146.14	1.360	1	0.100	0.045
NaCl	58.44	2.165	2	0.050	0.022
K_2SO_4	174.26	2.662	3	0.058	0.026
$(NH_4)_2SO_4$	132.13	1.768	3	0.062	0.028

Note: The variables are defined as M_w, molecular weight; ρ, density; ν_H, number of dissociated ions (van't Hoff factor); D_{pc}, activation diameter. Calculations assume T = 293 K. ν_H for adipic acid was selected from *Cruz and Pandis* [1997].

Table A.2. Summary of time delays to peak maxima for ammonium sulfate.

$(NH_4)_2SO_4$			
S (%)	$<\tau_p>$ (s)	σ_p (s)	n
1.5	7.7	4.0	162
1.2	7.5	2.1	156
0.95	8.4	3.9	140
0.75	9.2	3.2	122
0.6	9.7	2.6	112
0.47	11.6	4.2	100
0.38	13.0	4.9	79
0.3	13.5	3.2	65
0.24	16.0	4.9	53
0.19	14.9	4.9	47
0.15	16.3	5.4	46

S is the supersaturation, $<\tau_p> \pm \sigma_p$ is the mean time delay from the chamber closing to the peak maximum and its variance. The total number of runs at the given supersaturation is n.

Table A.3. Aerosol number distribution parameters.

Aerosol type	Nuclei mode			Accumulation mode			Coarse mode		
	$r_{pg,1}$ (μm)	σ_1	N_1 (cm^{-3})	$r_{pg,2}$ (μm)	σ_2	N_2 (cm^{-3})	$r_{pg,3}$ (μm)	σ_3	N_3 (cm^{-3})
Marine	0.005	1.6	340	0.035	2.0	60	0.31	2.7	3.1
Clean continental	0.008	1.6	1000	0.034	2.1	800	0.46	2.2	0.72
Average background	0.008	1.7	6400	0.038	2.0	2300	0.51	2.16	3.2
Urban	0.007	1.8	10600	0.027	2.16	32000	0.43	2.21	5.4

These trimodel distributions described by *Whitby* [1978].

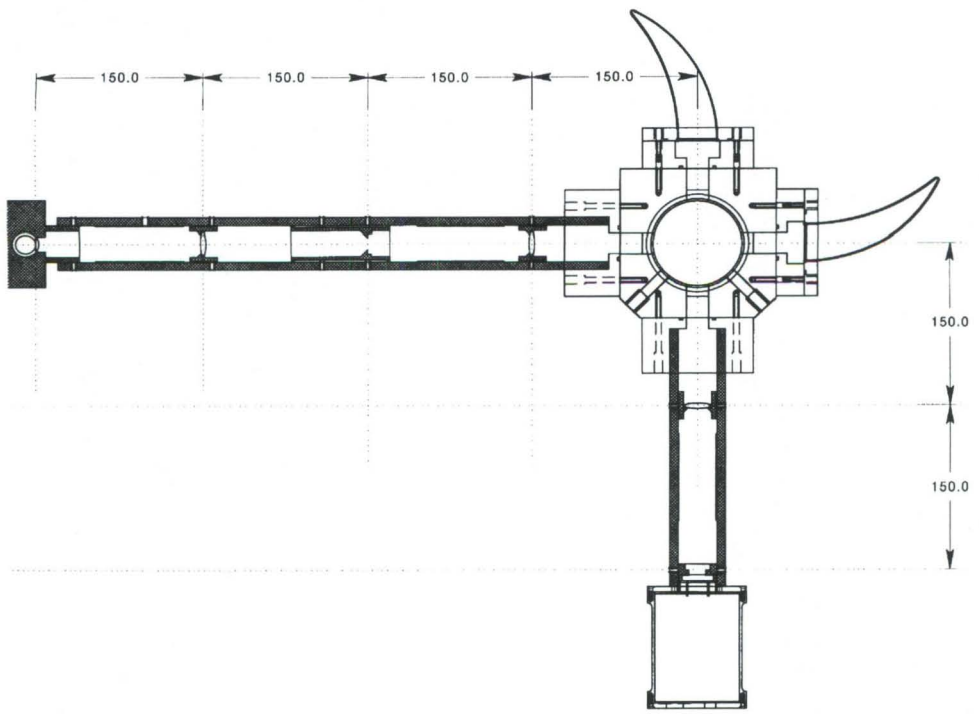

Figure A.1. Illustration of static thermal gradient CCN instrument. The tungsten lamp and photodiode detector are at the ends of the long and short tubes, respectively. The horns are light traps to enhance the signal-to-noise ratio.

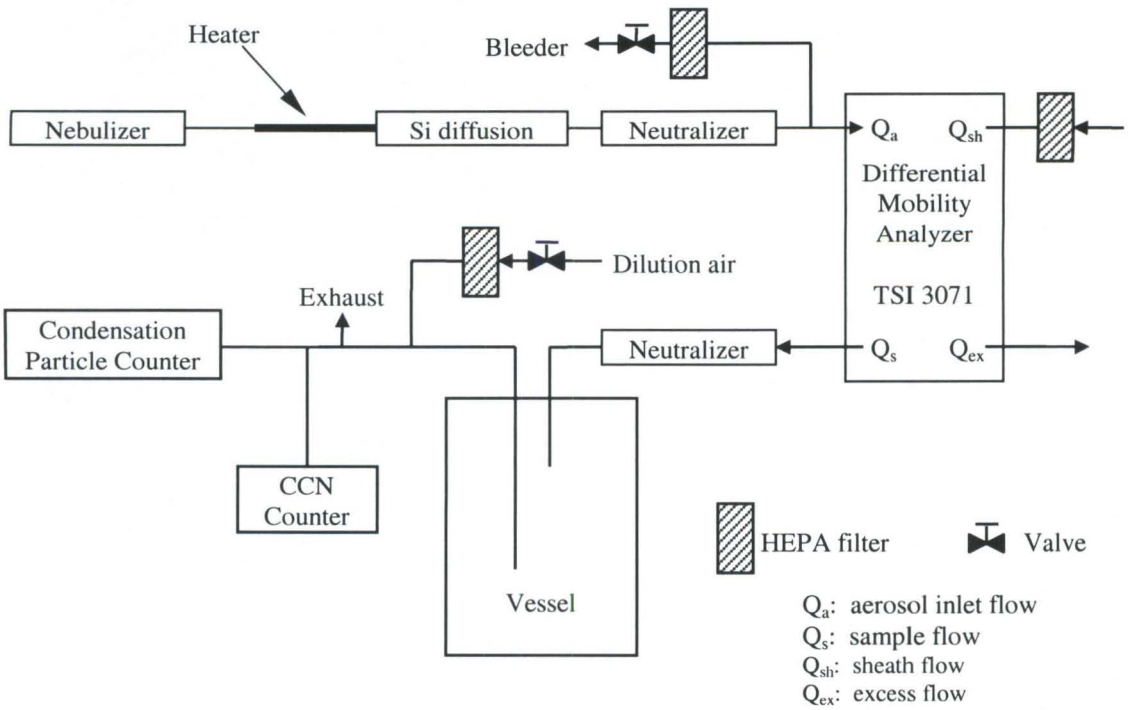

Figure A.2. The experimental setup for the photometric calibrations of the CCN chamber.

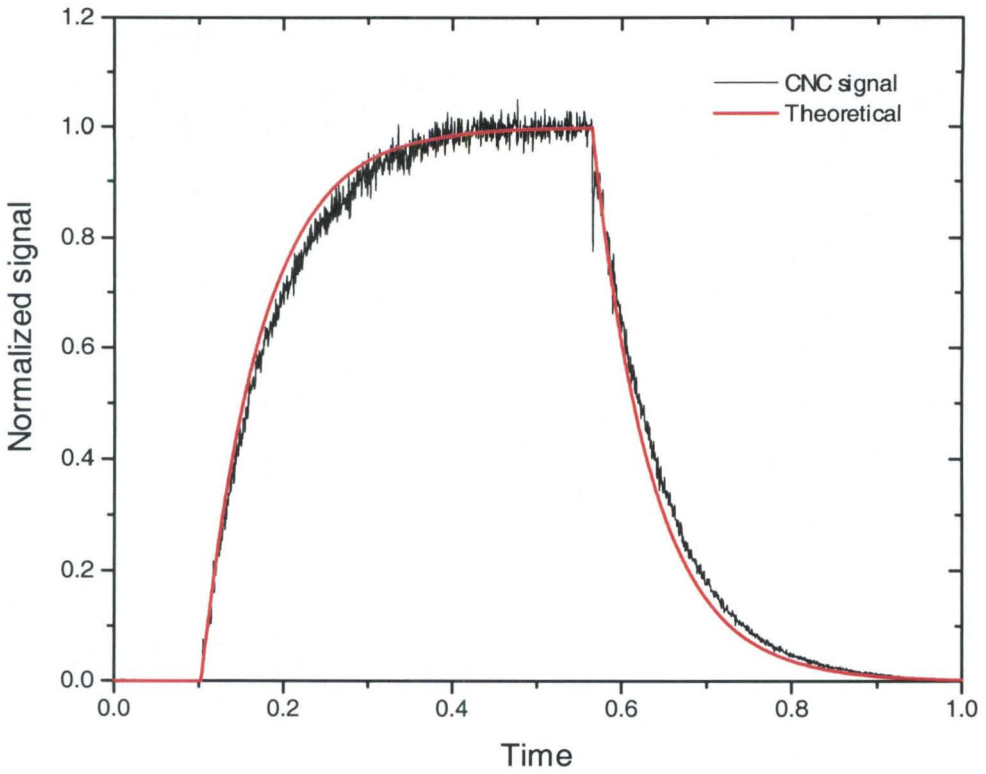

Figure A.3. Normalized particle concentration increase and decay in the glass jar. The red line represents the theoretical case for a well-mixed vessel. The slight deviation is a result of the slight over pressure in the vessel caused by the dilution line.

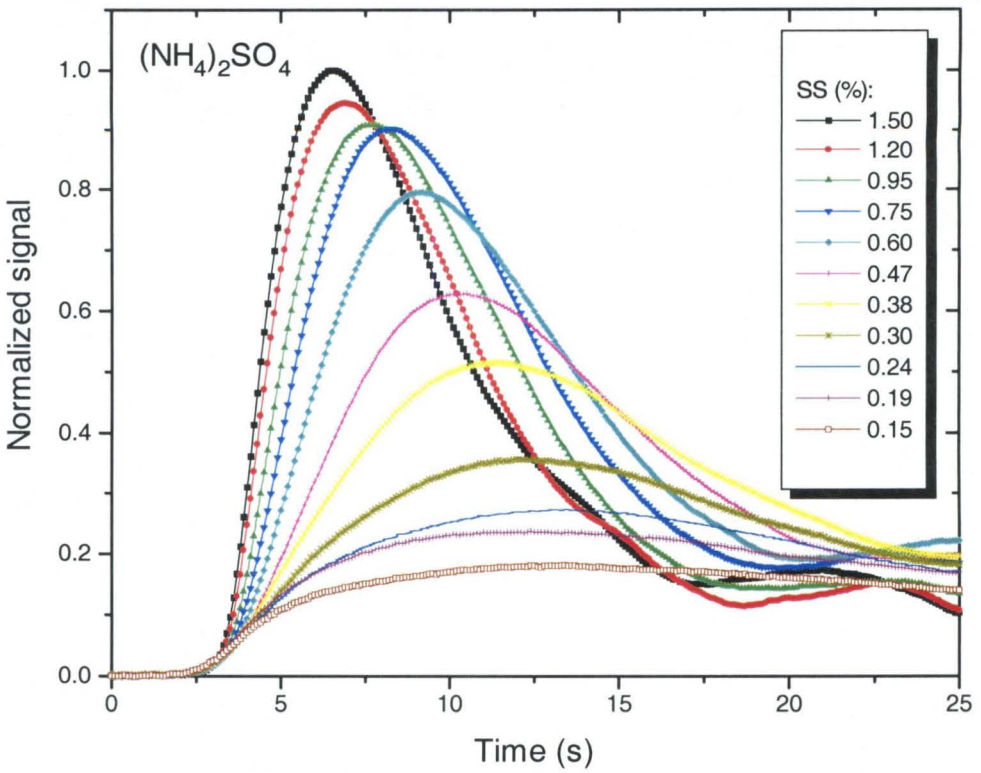

Figure A.4. Normalized ensemble average for all runs in which activation of $(NH_4)_2SO_4$ aerosol was observed.

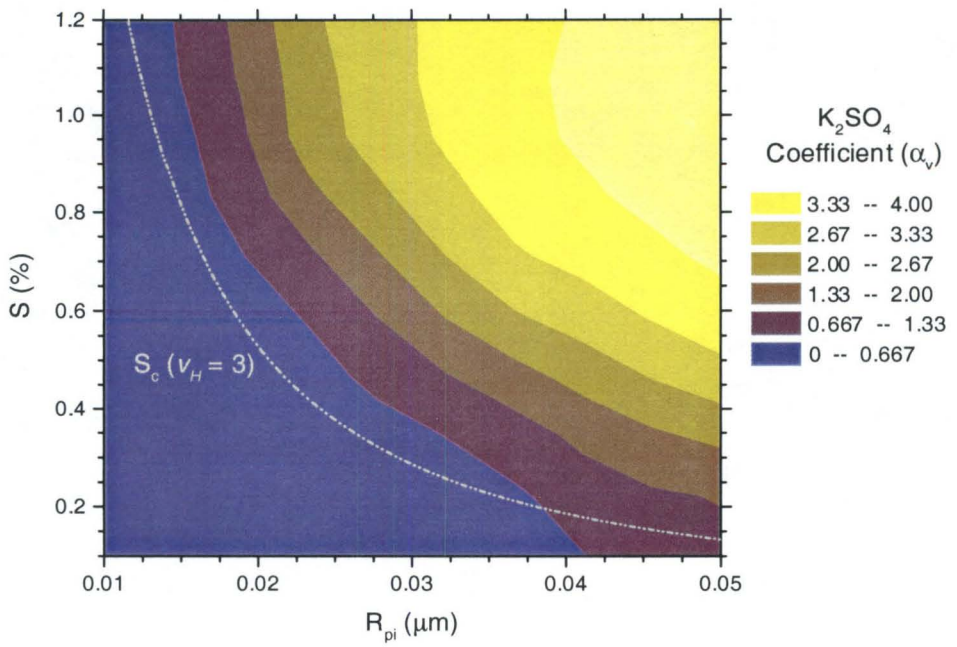

Figure A.5. The contour plot illustrates the dependence of α_a on R_p and S. The dashed line represents the critical supersaturation of the particles using Köhler theory.

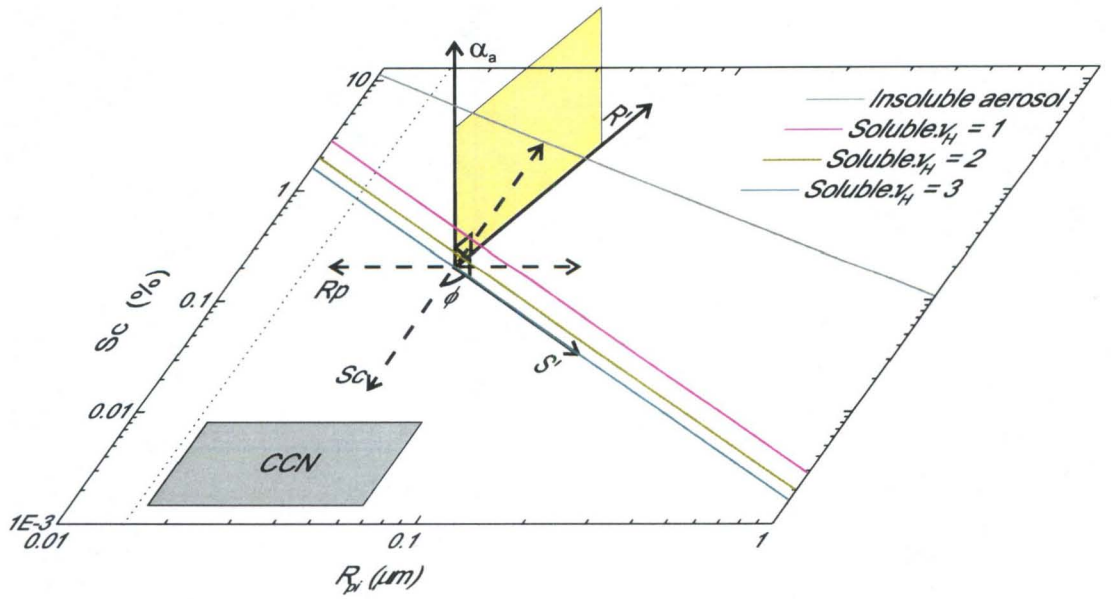

Figure A.6. Visualization of the axis rotation to obtain the S' and R' coordinate system. The underlying graph shows the relationship between the critical supersaturation S_c, dry particle radius R_p and the van't Hoff factor ν_H for $(NH_4)_2SO_4$ aerosol. The R' - α_v plane, perpendicular to the underlying graph, illustrates the activation kinetics (Figure A.7). The origin ($R' = 0$) is adjusted to lie on the critical supersaturation fit and only particles with $R' > 0$ will activate.

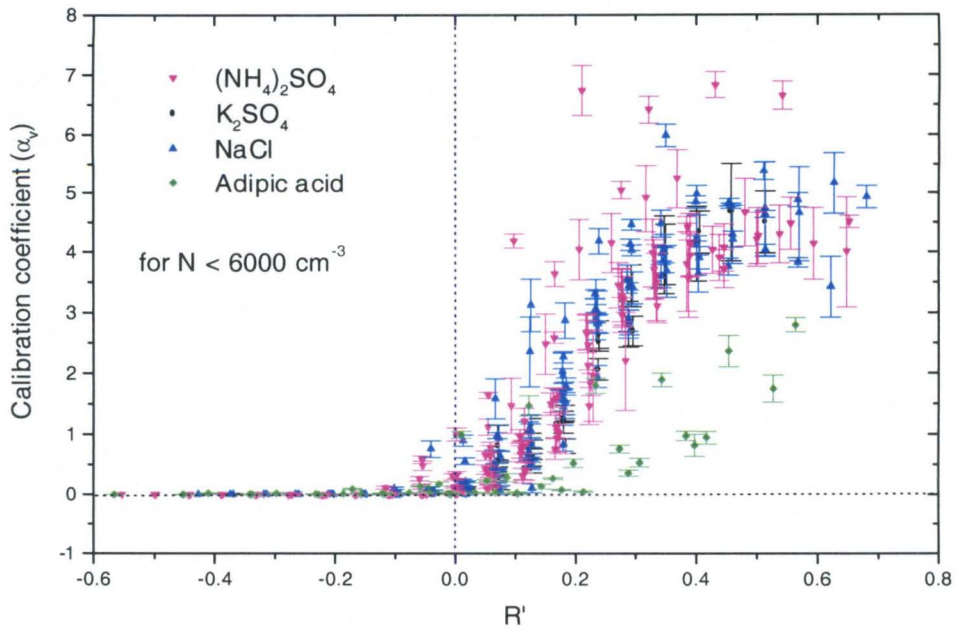

Figure A.7. The activation curve for all investigated species using parameters specified in Table A.1 and the axis rotation shown in Figure A.6. The vertical dotted line at $R' = 0$ indicates the critical supersaturation determined by Köhler theory.

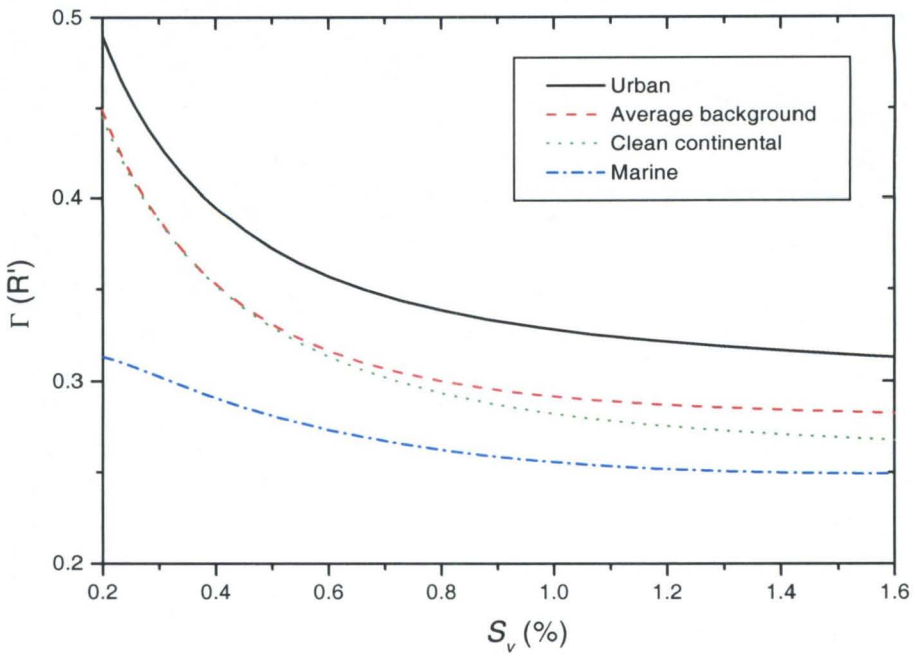

Figure A.8. Dependence of the calibration factor $\Gamma(R')$ on supersaturation for different representations of ambient aerosol distributions (Table A.4).

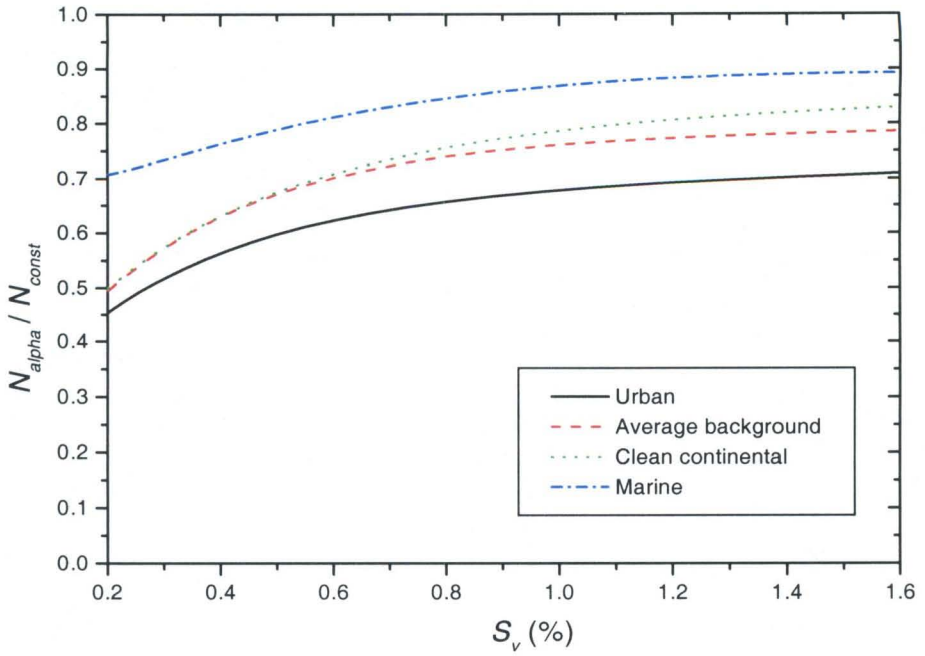

Figure A.9. Ratio of CCN coneentrations based on light-scattering growth calibrations (N_α) and a size independent calibration coefficient (N_{const}). Parameters of ambient aerosol distributions are listed in Table A.4.

Appendix A.A. Calculation of parameters and error analysis

Natural fluctuations of the voltage readings V_f on the flow controller are represented by

$$V_f \pm \sigma_V \tag{A.A.1}$$

The voltage readings are linearly proportional to the volume flow rate Q_i in a region near the desired flow rates. A linear relationship of slope m and y-intercept b relating V_f and Q_i is determined. Hence, the flow rates through the DMA and their standard deviations can be calculated by the following expressions:

$$Q_i = mV_f + b \tag{A.A.2}$$

$$\sigma_Q^2 = V_f^2\sigma_m^2 + m^2\sigma_V^2 + \sigma_n^2 \tag{A.A.3}$$

where Q_i is the sheath, excess, aerosol, and sample streams in the DMA, σ is the standard deviation for each variable.

The particle mobility Z which passes through the DMA can then be calculated to be

$$Z = \frac{(2Q_{sh} + Q_a - Q_s)}{2K} \tag{A.A.4}$$

$$\sigma_Z^2 = \left(\frac{1}{2K}\right)^2 \cdot \left(4\sigma_{sh}^2 + \sigma_a^2 + \sigma_s^2\right) \tag{A.A.5}$$

$$K = \frac{2\pi\, V_{DMA} L}{\ln\left(\frac{R_2}{R_1}\right)} \tag{A.A.6}$$

where V_{DMA} is the voltage potential, L is the axial length, and R_1 and R_2 are the inner and outer radii of the concentric cylinders in the DMA.

The particle mobility is related to the particle size by the following expressions:

$$D_p = \frac{eC_c}{6\pi\ \mu\ Z} \tag{A.A.7}$$

$$\sigma_{D_p}^2 = \left(\frac{1}{\frac{\partial Z}{\partial D_p}}\right)^2 \sigma_Z^2 \tag{A.A.8}$$

$$\frac{\partial Z}{\partial D_p} = \frac{e}{3\pi\ \mu}\left(\frac{1}{D_p}\frac{\partial C_c}{\partial D_p} - \frac{C_c}{D_p^2}\right) \tag{A.A.9}$$

where D_p is the particle radius, e is the charge of particle, C_c is the slip correction factor, μ is the viscosity of air.

Using the supersaturation expression derived by Köhler *et al.* [1936], one can determine the critical supersaturation for particles of a given size and composition

$$SS_c = \exp\left(\frac{\gamma}{R_P^{1.5}}\right) \tag{A.A.9}$$

$$\sigma_{SS_c}^2 = \frac{9}{4}\frac{\gamma^2}{R_p^5}\exp\left(\frac{2\gamma}{R_p^{1.5}}\right)\sigma_{R_p}^2 \tag{A.A.10}$$

$$\gamma = \left(\frac{32}{27}\frac{M_w}{v_H\rho}\right)^{\frac{1}{2}}\left(\frac{\sigma_t}{RT}\right)^{\frac{3}{2}} V_w \tag{A.A.11}$$

where M_w is the molecular weight, v_H is the Van't Hoff factor, ρ is the particle dry density, σ_t is the surface tension, R is the ideal gas constant, T is the temperature, and V_w

is the molar volume of water. The particle sizes and their critical supersaturations that were used during these experiments are shown in Table A.A.1.

Table A.A.1. Using expressions in Appendix A, errors in the particle sizes and their critical supersaturations are determined for these experiments.

	Particle Diameter		Critical Supersaturation	
	D_p (mm)	+/- error	S_c (%)	+/- error
$(NH_4)_2SO_4$	20.2	0.3	1.596	0.035
	21.0	0.3	1.506	0.033
	24.3	0.4	1.207	0.026
	28.5	0.4	0.950	0.021
	33.1	0.5	0.759	0.017
	38.8	0.6	0.598	0.013
	45.9	0.7	0.464	0.011
	52.1	0.8	0.383	0.009
	61.2	0.9	0.301	0.007
	70.2	1.1	0.245	0.006
	83.6	1.4	0.188	0.005
	97.6	1.6	0.149	0.004
	125.7	2.1	0.102	0.003
NaCl	24.3	0.4	0.882	0.020
	28.0	0.4	0.710	0.016
	32.8	0.5	0.562	0.013
	37.8	0.6	0.453	0.010
	44.0	0.7	0.361	0.008
	52.4	0.8	0.278	0.006
	59.7	0.9	0.228	0.005
	70.6	1.1	0.178	0.004
	81.8	1.3	0.142	0.003
	95.1	1.5	0.113	0.003
	112.1	1.9	0.089	0.002
	146.6	2.6	0.059	0.002
K_2SO_4	28.6	0.4	0.878	0.015
	38.7	0.6	0.558	0.010
	52.6	0.8	0.351	0.006
	71.5	1.1	0.221	0.004
	96.3	1.6	0.142	0.003

Appendix B

Composition and sources of aerosol in a central African rain forest during the dry season

Abstract

During the Experiment for Regional Sources and Sinks of Oxidants (EXPRESSO-96), size-fractionated aerosol samples were collected in November and December 1996 at a ground site in the tropical rain forest at the N'doki National Park (NNP) in the Republic of Congo. The samples were analyzed for up to 26 elements using particle-induced X-ray emission. Elements related to mineral dust and pyrogenic aerosol exhibited greater concentrations during the daytime, while aerosol produced by the rain forest exhibited higher concentrations at night. Samples were also collected at two levels on the tower, above and below the canopy, to characterize vegetation sources. Absolute principal component analysis (APCA) identified three major aerosol source types in each size fraction, which explained more than 90% of the data variance. The fine-size fraction contained mineral dust (Al, Si, Ca, Ti, and Fe), pyrogenic (black carbon, K, and Zn), and marine/anthropogenic sulfur components. The coarse-size fraction included a mineral dust (Al, Si, Ca, Ti, Mn, and Fe) and two primary biogenic components consisting of K, P, Zn, and S. Absolute principal component scores were calculated for the components of APCA, and temporal trends were compared to 7 day isopycnic backward trajectories. Consistent relationships between the temporal trends of the fine fraction aerosol components and meteorological patterns were observed. Trade wind air masses transported biomass burning and mineral dust aerosol to NNP during the first half of the experiment. The fine fraction sulfur component correlated well with the pyrogenic activity before the change in meteorological patterns halfway through the experiment. The fine and coarse sulfur concentrations nearly doubled in the latter part of the experiment as a monsoon circulation brought sulfur-enriched aerosol from the Atlantic

Ocean. Various industrial activities on the coast of Cameroon and Gabon probably contributed to the high sulfur concentrations as well.

B.1. Introduction

Biomass burning in the tropics is one of the oldest and most important anthropogenic activities. Although biomass burning is recognized as an important source of radiatively and chemically active trace gases and aerosols [*Crutzen and Andreae*, 1990; *Crutzen and Goldammer*, 1993; *Levine*, 1991; *Seiler and Crutzen*, 1980], its impact on the environment remains poorly quantified [*Scholes et al.*, 2001]. Nearly 80% of global biomass burning occurs in the tropics [*Hao and Liu*, 1994], particularly from the deforestation in the Amazon Basin, the savanna fires in Africa, and the domestic use of biomass fuels. Global assessments indicate that savanna fires are the single largest source of pyrogenic emissions [*Andreae*, 1993; *Andreae et al.*, 2000; *Hao and Liu*, 1994]. The rate of burning cultivated areas in the African savanna has increased due to increasing population and the use of controlled burning as a land management tool [*Hao et al.*, 1990; *Seiler and Crutzen*, 1980].

The emission of particulate matter from biomass burning results mainly in sub-micrometer aerosols [*Crutzen and Andreae*, 1990; *Reid and Hobbs*, 1998], which are efficient scatterers of solar radiation and affect the radiation budget [*Coakley et al.*, 1983; *Ross et al.*, 1998]. Biomass burning releases graphitic carbon, which can increase the absorption of solar radiation by the atmosphere [*Ackerman and Toon*, 1981] and by clouds [*Twomey et al.*, 1984]. *Penner et al.* [1992] and *Dickinson* [1993] estimated that a combined direct radiative effect from smoke particles and indirect effect through clouds are responsible for a change in planetary albedo that is comparable to that from sulfate aerosol [*Charlson et al.*, 1992; *Kiehl and Briegleb*, 1993; *Schneider*, 1994]. *Rogers et al.*

[1991], *Radke* [1989], and G. C. Roberts et al. (manuscript in preparation, 2001) (see Chapters 5 and 6) have shown that pyrogenic particles can serve as cloud condensation nuclei and potentially alter the radiative properties of clouds.

Since biomass burning aerosols are often enriched with K and Zn from vegetation and soil material, their transport to other ecosystems may result in a net nutrient loss from the burnt region. The alteration of the nutrient stocks and its potential effects are poorly documented and require further research [*Andreae*, 1991].

The Experiment for Regional Sources and Sinks of Oxidants (EXPRESSO) was organized to assess the role of biomass burning on atmospheric chemistry, climate, and ecology in equatorial regions of Africa. The fieldwork for EXPRESSO-96 took place during the dry season in November and December 1996. The purpose of the aerosol portion of this experiment was to quantify composition and concentration of aerosol particles in a tropical rain forest, to identify the major regional sources, and to evaluate the relative contribution from these sources, and in particular from biomass burning.

B.2. Experimental Methods

B.2.1. Sampling Site and Procedure

The sampling site was located in the tropical rain forest of northern Republic of Congo (Congo, Brazzaville) at the N'doki National Park (NNP) (2°12.39' N; 16°23.51' E; 360 m above sea level), which is 85 km northeast of Ouesso. A total of 37 size-fractionated aerosol samples was collected from November 27 to December 11, 1996, on

a meteorological tower at heights of 13.5 and 56 m to characterize the contribution from the mixed boundary layer and within the forest canopy. Twenty seven stacked filter unit (SFU) samples were collected above the canopy, and 10 sets were collected below the canopy level. The surrounding forest canopy is between 39 and 50 m. The EXPRESSO experiment took place in the dry season when savanna fires were extensive in central Africa. In November and December the Intertropical Convergence Zone (ITCZ) moves south over central Africa, enabling the dry northeast trade winds, also know as the Harmattan, to transport pyrogenic and mineral dust aerosol into the rain forest.

Aerosols were sampled using a two-stage SFU (Norwegian Institute for Air Research, Kjeller, Norway) consisting of two 47 mm diameter Nuclepore polycarbonate filters in series with pore sizes of 8 and 0.4 μm. The SFU sampler operates at an airflow rate of 15-16 L min^{-1}, which corresponds to a 50% cutoff of ~ 2 μm equivalent aerodynamic diameter (EAD) for the 8 μm EAD coarse filter [*John et al.*, 1983]. Upstream of the coarse filter is a preimpaction stage, which removes particles larger than 10 μm EAD. Consequently, the coarse Nuclepore filter collects the 2-10 μm EAD size fraction, and the fine filter collects particles less than 2 μm EAD. The flow rate was regulated using a rotameter, and the volume was measured using a calibrated dry gas meter. More details on the SFU sampler are provided by *Maenhaut et al.* [1994]. The SFU operated continuously for 12 hours and the filters were changed at 6:00 and 18:00 local time (GMT + 1) to collect separate diurnal and nocturnal samples. Samples were refrigerated until analysis.

B.2.2. Chemical Analysis

The fine and coarse filters of the SFU samples were analyzed for black carbon (BC) by a light reflectance technique [*Andreae*, 1983; *Andreae et al.*, 1984] and for up to 26 elements using particle-induced X-ray emission analysis (PIXE) at the University of Gent, Belgium. Precise experimental details of the PIXE analysis are given elsewhere [*Maenhaut and Raemdonck*, 1984; *Maenhaut et al.*, 1981; *Maenhaut and Vandenhaute*, 1986]. The following 16 elements were detected in the samples: Al, Si, P, S, Cl, K, Ca, Ti, Mn, Fe, Cu, Zn, Br, Rb, Sr, and Pb. The detection limit was typically 10 ng m^{-3} for elements with $Z \leq 20$ and around 1 ng m^{-3} for $21 \leq Z < 40$. The precision of the PIXE analysis varied from a few percent for the major elements to about 30% for elements with concentrations near the analytical detection limit.

B.2.3. Absolute Principal Component Analysis

The elemental concentration data were analyzed by absolute principal component analysis (APCA) to identify the various sources of aerosols sampled in the rain forest and extract the elemental source time trends. APCA is only able to resolve the aerosol components appropriately if there is sufficient variability in the data set, particularly in the relative impact of the various aerosol sources in the different samples [*Maenhaut et al.*, 1989]. The APCA method was derived from the procedures of *Thurston and Spengler* [1985] and *Maenhaut and Cafmeyer* [1987]. The basic criterion to retain an element for APCA was that it had to be present above the detection limit in at least 80%

of the samples. The most prominent eigenvectors (components) are retained for the Varimax rotation. The rotated component-loading matrix then represents the correlation between the trace elements and each component. Absolute principal component scores (APCS) are calculated and indicate the relative importance of each component in individual samples.

B.2.4 Backward Trajectory Calculations

To identify the sources of aerosol observed by APCS, 7 day, isopycnic backward trajectories for the N'doki National Park were determined for arrival times at 3 hour intervals during the sampling period for three levels (surface, 300 m, and 1000 m). The medium-range forecasting archive data (MRF) [*Stunder*, 1997] was used in conjunction with the Hybrid Single-Particle Langrangian Integrated Trajectory model (HYSPLIT 4) [*NOAA Air Resources Laboratory*, 1997] for these calculations. Because of the profound diel changes in the height of the boundary layer, only the backward trajectories during the daytime were used for analysis, when the boundary layer thickness is between 1 and 2 km. There were no measurements of the boundary layer thickness during the experiment.

B.3. Results and Discussion

B.3.1. Aerosol Composition

Biomass burning in the savannas of Central African Republic was widespread during the experiment, as shown by satellite and aircraft observations. Hence it is important to emphasize that sampled biosphere-related aerosol will consist of a heterogeneous mixture of natural release from vegetation and emissions from biomass burning. Table B.1 presents the average dry season atmospheric concentrations of the fine and coarse fraction for samples collected above the canopy in the NNP sampling site. Results cited throughout this paper refer to samples taken above the NNP forest canopy unless otherwise stated. For a comparison between a tropical rain forest and a savanna site during the dry season, Table B.1 also shows average elemental particulate concentrations collected in the Kruger National Park (KNP) at the Skukuza Airport sampling site (24°58.8'S, 31°35.9'E, Mpumalanga Province, South Africa) during the Southern African Fire-Atmosphere Research Initiative (SAFARI 1992) [*Maenhaut et al.*, 1996]. KNP is located at 260 m above sea level in the low-altitude savanna region in eastern South Africa.

A comparison of the total concentration of mineral dust elements (Al, Si, Ca, Ti, Mn, and Fe) suggests that the dust loading at the KNP savanna site is about 4 times higher than the NNP rain forest site, consistent with what one would expect for a more arid environment at KNP. NNP was much less influenced by marine aerosol than KNP and exhibits lower concentrations of coarse fraction Cl. When we only consider the fine

fraction, however, the dust element concentrations are slightly higher at NNP than at KNP. Mineral dust elements at NNP have a fine/coarse ratio of about 0.8, which is quite high compared to a value of 0.2 observed in South Africa (i.e., KNP) and the Amazon Basin [*Artaxo et al.*, 1988]. Since the absolute dust concentrations vary highly with time, a statistically reliable comparison of absolute levels would obviously require longer study periods than are available here. The difference in size distribution, however, may be a more robust aerosol property that reflects site-specific sources and sinks. Since soil dust below the forest canopy does not resuspend into the atmosphere, the higher fine/coarse ratio at NNP suggests that there is a large deposition of the coarse fraction of mineral dust into the rain forest. The distance to the source of the mineral dust does not appear to play a major role, as similar fine/coarse ratios have been reported for South Africa, where the sources are local to regional, and the Amazon Basin, where dust comes from over thousands of kilometers from Africa. We speculate that coarse fraction deposition may be related to transport processes. In contrast to the transatlantic transport of Sahara dust to Amazonia, which takes place in the free troposphere, the transport of aerosol over the central African rain forest is strongly coupled to the planetary boundary layer, which may facilitate coarse fraction deposition. The source of mineral dust at KNP, on the other hand, is a combination of locally suspended and long-range transported aerosol.

Figure B.1 shows the mean crustal enrichment factors (EFs), calculated relative to average crustal rock [*Mason*, 1966] with Al as the reference element. The EFs from KNP during SAFARI-92 are also shown in Figure B.1 for comparison. The elements in the fine and coarse fraction, which have crustal EFs close to unity, are attributed to soil dust dispersal. The highly enriched elements indicate vegetation or biomass burning sources.

Interestingly, Ca and Mn are not enriched even though biomass burning and natural biogenic emissions have been reported to contribute to their atmospheric concentrations [*Artaxo et al.*, 1988, 1993; *Maenhaut and Akilimali*, 1987]. The higher enrichment factors of coarse fraction P, S, Cu and Zn and fine fraction P and Cu at NNP suggest that rain forest vegetation is a probable source. The enrichment of coarse P, in particular, has been shown to be indicative of primary biogenic sources [*Artaxo et al.*, 1998]. As will be discussed below, this conclusion is further supported by the results of the APCA analysis (Section B.3.2).

The different aerosol components, mineral dust, pyrogenic (biomass burning) aerosol, and primary biogenic particles show different diurnal behavior. The first two components, which originate from sources external to the forest, are elevated during the daytime, while biogenic aerosol is enriched at night. The mineral dust (Al, Si, Ca, Ti, Mn, and Fe) and fine fraction pyrogenic elements (BC, K, and Zn) exhibit 54% and 14% higher daytime than nighttime levels, respectively (Figure B.2). During the daytime, the air at the canopy top level is coupled to a deep planetary boundary layer (PBL), enabling downward transport of aerosol over the forest. As a result, the aerosol concentrations at the canopy top reach levels comparable to those in the PBL during the daytime. At night, radiative cooling produces an inversion just above the canopy top, resulting in the formation of a shallow, decoupled layer, which is depleted of aerosols by dry deposition during the night, in a matter similar to that typical of ozone [*Cros et al.*, 1992]. Due to the larger particle size and therefore higher deposition velocity of the dust particles, they are removed more efficiently than the smaller pyrogenic particles. The elements representing primary biogenic particles (i.e., coarse-mode S, P, K, Cu, and Zn) showed

higher concentrations during the night when the nighttime inversion just above the forest canopy reduced atmospheric dispersion of aerosol produced in the rain forest. These particles originate from the forest vegetation and contain leaf debris, fungal material, and microbes [*Andreae and Crutzen*, 1997; *Simoneit et al.*, 1990]. *Artaxo and Maenhaut* [1990] observed similar results in the Amazon rain forest.

To characterize aerosol production within the rain forest, average elemental concentrations were calculated for concurrent above and below canopy samples. A comparison of the samples taken below the canopy (13.5 m) to those taken above the canopy (56 m) is shown in Figure B.3. Surprisingly, the mineral dust and biomass burning mass concentrations were nearly identical at both levels. Local dust sources below the canopy are improbable as high soil moisture and low wind velocity below the canopy render the resuspension of soil dust into the atmosphere difficult. Therefore sufficient downward mixing must transport mineral dust and biomass burning elements into the canopy. However, higher mass concentrations of the vegetation component, especially coarse P and K, were observed below the canopy and probably originate from pollen grains, plant debris, and fungal material.

The ratio between excess fine potassium (K_x) and black carbon is a useful tracer to study the long-range effects of biomass burning [*Andreae*, 1983]. K_x is calculated by subtracting soil potassium from particulate potassium concentration using Al as a soil tracer and crustal rock composition ratios [*Mason*, 1966]. The ratio of excess fine potassium and black carbon (K_x/BC) averaged 0.11. Values for biomass burning aerosol range between 0.033 and 0.340 [*Andreae et al.*, 1998; *Artaxo et al.*, 1988; *Crutzen and Andreae*, 1990].

It is evident from Table B.2 that fine-mode sulfur correlated strongly with the biomass burning elements before the influx of higher sulfur concentrations on December 6. The fine S/K mass ratio was 1.0 for the aged smoke aerosol, a result of several days of transport over the rain forest. Smoke particles evolve rapidly after emission, and their physical and chemical properties indicate their age. Previous experiments have shown that particulate S emissions are quite low in fresh plumes of savanna fires, with a fine S/K emission ratio between 0.05 and 0.2 in ground-based measurements and 0.4 in aircraft measurements [*Andreae et al.*, 1998; *Gaudichet et al.*, 1995; *Maenhaut et al.*, 1996]. S/K emission ratios increase as the smoke aerosol ages, and *Gaudichet et al.* [1995] and *Artaxo et al.* [1998] also found ratios near unity in regional haze over central Africa and the Amazon Basin, respectively. The Zn/K ratio of 0.01 at NNP is quite close to the emission ratio (0.007) reported by *Maenhaut et al.* [1996] and *Andreae et al.* [1998].

The lack of correlation of S with mineral dust elements (e.g., November 29 and 30) indicates that a significant amount of sulfur is acquired during its transport over the rain forest. This acquisition of S may occur on biomass burning aerosol as the fire plume ages, from the emission of sulfur species from vegetation and biomass burning, and from heterogeneous reactions in clouds. *Reid et al.* [1998] reported a 5-7% increase in the mass of combustion-generated aerosol in the Amazon Basin, most likely due to the addition of sulfate from the oxidation of sulfur-containing gases produced by biomass burning. They also observed that well-aged smoke, which had been subjected to convective cloud processes, exhibited a significant increase in the fraction of aerosol sulfate over the Amazon Basin. Since considerable convective activity occurred during

the experiment, the acquisition of sulfate may have been enhanced by heterogeneous reactions in cloud droplets.

Sulfur is produced by sources other than biomass burning, including biogenic emissions and industrial sources. Biogenic emissions from the rain forest also include a significant sulfur component comprising carbonyl sulfide (COS), dimethyl sulfide (DMS), hydrogen sulfide (H_2S), and sulfur dioxide (SO_2) [*Andreae et al.*, 1990]. The contribution from biogenic sources is, however, not likely to be large. Fine-mode particulate sulfur concentrations measured at NNP before December 6 are similar to those found by *Bingemer et al.* [1992] during the Dynamique et Chimie Atmosphérique en Forêt Equatoriale (DECAFE 88) experiment (Impfondo, Republic of Congo). These authors found a strong resemblance between the sulfur cycle over the Amazon Basin and the African rain forest, in particular with respect to the relatively low emissions of sulfur gases released by the rain forest. They concluded that biogenic sulfur emissions contributed little to the aerosol sulfur budget and suggested that gas-to-particle conversion of SO_2 from biomass burning and long-range transport of burning-derived sulfate are the most substantial contributors to fine-mode sulfur.

B.3.2. Absolute Principal Component Analysis

APCA was performed on the fine and coarse fraction element data sets from the SFU collections to investigate the different sources and their time trends during the experiment. Of the 17 particulate species detected, 9 were retained in the APCA calculations of the fine fraction and 10 were used in the coarse fraction analysis. Three

components were retained for each size fraction, which explained more than 90% of the data variance. Table B.3 presents the Varimax rotated component loading matrices. The standard deviation for the component loadings was calculated using the procedure suggested by *Heidam* [1982]. The mineral dust component accounts for 50-60% of the variance, while the remaining two components describe another 30%. Component 1 of the fine fraction exhibits high loadings for Al, Si, Ca, Ti, and Fe, which are all typical mineral dust elements. The second component has high loadings for BC, K, and Zn and clearly denotes biomass burning aerosol. Component 3 contains essentially only one species, S, and is attributed to biomass burning or marine/anthropogenic sources depending on the origin of the air mass. Back trajectories, which support evidence for the different sources of S, will be discussed in the next section. The principal elements in the mineral dust component (shown in brackets in Table B.3) exhibit a secondary correlation in the biomass burning component, and a similar observation applies to the main biomass burning elements in the mineral dust component. The secondary correlation between these components occurs because air masses originating over savanna and desert regions, where mineral dust elements are acquired, often pass over areas of pyrogenic activity as well. Furthermore, it has been found that savanna fires are efficient mobilizers of soil dust [*Gaudichet et al.*, 1995; *Maenhaut et al.*, 1996]. Hence during periods of intense savanna fires one would expect simultaneous large mass loadings of mineral dust and biomass burning aerosol. However, results shown in Section B.3.3 suggest that at NNP the Sahara Desert is the primary source for the mineral dust component.

Component 1 of the coarse fraction contains the same mineral dust elements as found in the fine fraction and in addition Mn. P and K are the elements with the highest loadings in component 2; they have a biogenic origin related to the emission of aerosols by plants. Sulfur and zinc are the primary elements in the third component. Observations, which have been discussed in the previous section (i.e., higher nighttime and below canopy concentrations for typical biogenic elements), indicate that coarse-mode sulfur can be attributed to a vegetation origin. However, time trends and backward trajectories show that biomass burning and marine/anthropogenic sources also affect its atmospheric concentration, probably through the acquisition of sulfur species on existing aerosol particles.

B.3.3. Temporal Trends and Backward Trajectories

Rather than dealing with the individual species, the time trends of the major aerosol components as identified by APCA will be discussed. Figure B.4 illustrates the time trends of the absolute principal component scores (APCS), and Figure B.5 shows the time trends of elemental concentrations grouped by their components. From inspection of the APCS time trends of the fine-particulate fraction, the experiment can be categorized into three distinct periods: a soil dust and biomass burning episode (November 29 and 30), biomass burning background (December 2 to 5), and high sulfur concentrations (after December 6 to the end of the experiment). The diel cycles, mentioned previously, are clearly seen for fine-mode mineral dust and the first coarse-mode biogenic component (P and K).

Further evidence for characterizing the observed time trends of APCA components was obtained from 7 day backward trajectories. The surface (i.e., 56 and 300 m) and 1000 m backward trajectories are shown in Figure B.6. The surface trajectories often exhibited different characteristics to those at 1000 m, as shown in Figure 3.6c, d, and f. The stratification occurred because the cooler monsoon circulation from the Atlantic Ocean pushed the lower levels of the ITCZ northward, bringing to NNP relatively clean surface air masses from the west. The upper levels of the ITCZ remained south of NNP, allowing the transport of biomass burning and mineral dust material over the rain forest. The ITCZ serves as an effective exchange zone and transport mechanism for aerosol in central Africa. A transition layer between the free troposphere and the boundary layer enables regional transport of aerosol particles, which could be reinjected into the boundary layer by entrainment [*Delon et al.*, 2000]. Since the average boundary layer height is ~ 1000 m, the upper trajectory (also at 1000 m) is a good indicator of regional sources of aerosol. The region between 8°E-28°E and 4°N-12°N was analyzed for savanna fires during EXPRESSO-96 by the Monitoring Tropical Vegetation Space Applications Institute / Joint Research Center (MTV/JRC), Ispra, Italy. The location and intensity of the fires within this region are shown in Figure B.6.

During November 29 and 30, Harmattan air masses transported soil dust and biomass burning aerosol into the NNP region. Surface and 1000 m trajectories, which originate (with a starting location 7 days before their arrival at NNP) over the desert in northern Sudan, accumulate mineral dust and pyrogenic material before reaching NNP. These trajectories are shown in Figures B.6a and b and correspond to the high mineral dust loadings in both size fractions shown by the APCS time trends in Figures 4 and 5.

The number of fires dramatically increases from November 26 (Figure B.6a) to November 28 (Figure B.6b); such an increase in the number of fires will clearly inject more pyrogenic material into the atmosphere. Hence a notable increase of the biomass burning component in Figure B.4a (i.e., fine fraction) is observed on November 30. Interestingly, the mineral dust component exhibits only a weak correlation to the pyrogenic activity and does not increase, which indicates that desert aerosol is the principal source of the mineral dust component. Similar meteorological patterns are also responsible for the rise in biomass burning and mineral dust elemental concentrations at the end of the experiment (December 9 and 10).

The period from December 2 to 5, predominantly influenced by the biomass burning component (shown in Figure B.4a), is characterized by a separation of the surface and 1000 m backward trajectories. This stratification is illustrated in Figures B.6c, d, and f as the surface air mass comes from the west, while the upper trajectory originates from the north. There was a notable increase in pyrogenic activity from December 1 to 2, which is not detected in the elemental concentrations because the trajectories bypass the regions of intense burning.

The time trends for the sulfur component in both size fractions show a pattern that is quite different from that of the pyrogenic compounds. Between December 6 and 10, the fluctuations of the daytime concentrations are salient features of the sulfur time trends in the fine-particulate fraction. The dramatic increase in S after December 6 occurs when the ITCZ shifted to the north, allowing marine aerosol to be transported from the Atlantic Ocean (e.g., Figure B.6e). It is likely that S also has anthropogenic origins, as coastal cities in Cameroon, Equatorial Guinea, and Gabon lie under the trajectory path. Figure

B.6f shows that on December 7, the upper trajectory shifted back to the north, resulting in lower daytime sulfur concentrations and higher mineral dust loadings. The same trends were observed on December 8 and 9 as the 1000 m backward trajectory shifted from a maritime to a continental origin. December 10 exhibits high sulfur concentrations, yet the trajectories show similar meteorological conditions as the mineral dust and biomass burning episode on November 29 and 30. The increase in sulfur after December 6 indicates that both size fractions have marine/anthropogenic origins even though diel trends are considerably different. The principal source for the coarse fraction sulfur is probably from the vegetation as supported by high nighttime and below canopy concentrations discussed in Section B.B.1. Since larger aerosol particles are likely to serve as cloud condensation nuclei, cloud droplets could take up sulfur gases through heterogeneous reactions. Hence high reduced-sulfur emissions from the Atlantic coast might have contributed to the increase of coarse fraction S at the end of the campaign.

B.4. Conclusions

Detailed measurements of the chemical properties of aerosol transported over the central African rain forest are described in this paper. Four characteristic types of aerosol sources, mineral dust from the Sahara Desert, pyrogenic aerosol from savanna fires, sulfur-enriched aerosol from the eastern coast of Africa, and biogenic aerosol from the forest vegetation, were identified using multivariate (APCA) analysis and backward trajectories (Table B.4). Biomass burning was prevalent in the savannas north of the sampling site as observed by satellite and aircraft during the EXPRESSO 1996 dry

season experiment. The back trajectory model (HYSPLIT 4) also supports the results found in this paper and was used to identify three distinct periods during the experiment: a soil dust and biomass burning episode, dry season burning background, and a monsoon circulation which brought in elevated sulfur concentrations.

An important result of this experiment is that the chemical properties of aged smoke aerosol in regional haze are different from those near the source of the burning. In particular, the sulfur content was relatively high and correlated well to the biomass burning elements before the onset of monsoon circulation on December 6. The smoke aerosol was transported for several days before reaching the forest site, which allowed for an increase of particulate sulfur through two likely processes. Biomass burning releases sulfur-containing gases whose oxidation products are taken up during aerosol transport, and biogenic emissions from the rain forest provide an additional sulfur component, which through oxidation and heterogeneous chemistry within cloud droplets also constitutes a probable source of particulate sulfur.

Filter sampling at two levels (above and below the forest canopy) suggests sufficient downward mixing into the rain forest, and the deposition of aerosol plays a vital role in nutrient cycles and forest ecology. The time trends indicate that the Sahara Desert and Sahel region offer a larger source of mineral dust elements than the savanna region. The contrast between the rain forests in Africa and Brazil may be a result of the differences in aerosol transport and deposition, which supplies the necessary nutrients to sustain an ecosystem. Yet the long-range transport of biomass burning species, such as K and Zn, represent a net loss of nutrients from savanna regions. The effects of the aerosol transport on regional ecosystems merits further exploration.

B.5. References

Ackerman, T.P., and O.B. Toon, Absorption of visible radiation in atmosphere containing mixtures of absorbing and nonabsorbing particles, *Appl. Opt.*, *20*, 3661-3667, 1981.

Andreae, M.O., Soot carbon and excess fine potassium: Long-range transport of combustion-derived aerosols, *Science*, *220*, 1148-1151, 1983.

Andreae, M.O., Biomass burning: Its history, use and distribution and its impact on environmental quality and global climate, in *Global Biomass Burning: Atmospheric, Climatic and Biospheric Implications*, edited by J.S. Levine, pp. 3-21, MIT Press, Cambridge, Mass., 1991.

Andreae, M.O., The influence of tropical biomass burning on climate and the atmospheric environment, in *Biogeochemistry of Global Change: Radiatively Active Trace Gases*, edited by R.S. Oremland, pp. 113-150, Chapman and Hall, New York, NY, 1993.

Andreae, M.O., T.W. Andreae, H. Annegarn, F. Beer, H. Cachier, P. Le Canut, W. Elbert, W. Maenhaut, I. Salma, F.G. Wienhold, and T. Zenker, Airborne studies of aerosol emissions from savanna fires in southern Africa, 2, Aerosol chemical composition, *J. Geophys. Res.*, *103*, 32,119-32,128, 1998.

Andreae, M.O., T.W. Andreae, R.J. Ferek, and H. Raemdonck, Long-range transport of soot carbon in the marine atmosphere, *Sci. Total Environ.*, *36*, 73-80, 1984.

Andreae, M.O., H. Berresheim, H. Bingemer, D.J. Jacob, B.L. Lewis, S.-M. Li, and R.W. Talbot, The atmospheric sulfur cycle over the Amazon Basin, 2, Wet season, *J. Geophys. Res.*, *95*, 16,813-16,824, 1990.

Andreae, M.O., and P.J. Crutzen, Atmospheric aerosols: Biogeochemical sources and role in atmospheric chemistry, *Science*, *276* (5315), 1052-1056, 1997.

Andreae, M.O., J.G. Goldammer, C.O. Justice, J.P. Lacaux, P. Merlet, M. Scholes, and B.J. Stocks, Biomass burning, in *IGAC Integration and Synthesis*, edited by G. Brasseur, 2000.

Artaxo, P., E.T. Fernandes, J.V. Martins, M.A. Yamasoe, P.V. Hobbs, W. Maenhaut, K.M. Longo, and A. Castanho, Large-scale aerosol source apportionment in Amazonia, *J. Geophys. Res.*, *103*, 31,837-31,847, 1998.

Artaxo, P., and W. Maenhaut, Trace element concentrations and size distributions of biogenic aerosols from the Amazon Basin during the wet season, *Nucl. Instrum. Methods Phys. Res.*, *49* (Sect. B), 366-371, 1990.

Artaxo, P., H. Storms, F. Bruynseels, R. Van Grieken, and W. Maenhaut, Composition and sources of aerosols from the Amazon basin, *J. Geophys. Res.*, *93*, 1605-1615, 1988.

Artaxo, P., M.A. Yamasoe, J.V. Martins, S. Kocinas, S. Carvalho, and W. Maenhaut, Case study of atmospheric aerosol measurements in Brazil: Aerosol emissions from Amazon Basin burning, in *Fire in the Environment: The Ecological, Atmospheric and Climatic Importance of Vegetation Fires*, edited by P.J. Crutzen, and J.G. Goldammer, pp. 139-158, John Wiley, New York, 1993.

Bingemer, H.G., M.O. Andreae, T.W. Andreae, P. Artaxo, G. Helas, D.J. Jacob, N. Mihalopoulos, and B.C. Nguyen, Sulfur gases and aerosols in and above the equatorial African rain forest, *J. Geophys. Res.*, *97*, 6207-6217, 1992.

Charlson, R.J., S.E. Schwartz, J.M. Hales, R.D. Cess, J.A. Coakley, J.E. Hansen, and D.J. Hofmann, Climate forcing by anthropogenic aerosols, *Science*, *255*, 423-430, 1992.

Coakley, J.A., R.D. Cess, and F.B. Yurevich, The effect of tropospheric aerosols on the earth's radiation budget: A parameterization for climate models, *J. Atmos. Sci.*, *40*, 116-138, 1983.

Cros, B., J. Fontan, A. Minga, G. Helas, D. Nganga, R. Delmas, A. Chapuis, B. Benech, and M.O. Andreae, Vertical profiles of ozone between 0 and 400 m in and above the African Equatorial Forest, *J. Geophys. Res.*, *97*, 12,877-12,887, 1992.

Crutzen, P.J., and M.O. Andreae, Biomass burning in the tropics: Impact on atmospheric chemistry and biogeochemical cycles, *Science*, *250*, 1669-1678, 1990.

Crutzen, P.J., and J.G. Goldammer, *Fire in the environment: The Ecological, Atmospheric, and Climatic Importance of Vegetation Fires*, 400 pp., John Wiley, New York, 1993.

Delon, C., A. Druilhet, R. Delmas, and P. Durand, Dynamic and thermodynamic structure of the lower troposphere above rain forest and wet savanna during the EXPRESSO campaign, *J. Geophys. Res.*, *105* (D11), 14,823-14,840, 2000.

Dickinson, R.E., Effect of fires on global radiation budget through aerosol and cloud properties, in *Fire in the Environment: The Ecological, Atmospheric, and Climatic Importance of Vegetation Fires*, edited by P.J. Crutzen, and J.G. Goldammer, pp. 107-122, John Wiley, New York, 1993.

Gaudichet, A., F. Echalar, B. Chatenet, J.P. Quisefit, G. Malingre, H. Cachier, P. Buat-Ménard, P. Artaxo, and W. Maenhaut, Trace elements in tropical African savanna biomass burning aerosols, *J. Atmos. Chem.*, *22*, 19-39, 1995.

Hao, W.-M., and M.-H. Liu, Spatial and temporal distribution of tropical biomass burning, *Global Biogeochem. Cycles*, *8* (4), 495-503, 1994.

Hao, W.-M., M.-H. Liu, and P.J. Crutzen, Estimates of annual and regional releases of CO_2 and other trace gases to the atmosphere from fires in the tropics, based on the FAO statistics for the period 1975-1980, in *Fire in the Tropical Biota: Ecosystem Processes and Global Challenges*, edited by J.G. Goldammer, pp. 440-462, Springer-Verlag, New York, 1990.

Heidam, N., Atmospheric aerosol factor models, mass and missing data, *Atmos. Environ.*, *16*, 1923-1931, 1982.

John, W., S. Hering, G. Reischl, G. Sasaki, and S. Goren, Characteristics of Nuclepore filters with large pore size, II, Filtration properties, *Atmos. Environ.*, *17*, 373-382, 1983.

Kiehl, J.T., and B.P. Briegleb, The relative role of sulfate aerosols and greenhouse gases in climate forcing, *Science*, *260*, 311-314, 1993.

Levine, J.S., *Global Biomass Burning: Atmospheric, Climatic, and Biospheric Implications*, 569 pp., MIT Press, Cambridge, Mass., 1991.

Maenhaut, W., and K. Akilimali, Study of atmospheric aerosol composition in equatorial Africa using PIXE as analytical technique, *Nucl. Instrum. Methods Phys. Res.*, *22* (Sect. B), 254-258, 1987.

Maenhaut, W., and J. Cafmeyer, Long-term atmospheric aerosol study at urban and rural sites in Belgium using multi-elemental analysis by particle-induced X-ray emission

spectrometry and short-irradiation instrumental neutron activation analysis, *X Ray Spectrom.*, *27* (4), 236-246, 1987.

Maenhaut, W., P. Cornille, J.M. Pacyna, and V. Vitols, Trace element composition and origin of the aerosol in the Norwegian Arctic, *Atmos. Environ.*, *23*, 2551-2569, 1989.

Maenhaut, W., F. François, and J. Cafmeyer, The "Gent" stacked filter unit (SFU) sampler for the collection of atmospheric aerosols in two size fractions: Description and instructions for installation and use, in *Applied Research on Air Pollution using Nuclear-Related Analytical Techniques. Report on the First Research Coordination Meeting*, pp. 249-263, NAHRES-19, Int. At. Energy Agency, Vienna, 1994.

Maenhaut, W., and H. Raemdonck, Accurate calibration of a Si(Li) detector for PIXE analysis., *Nucl. Instrum. Methods Phys. Res.*, *1* (Sect. B), 123-136, 1984.

Maenhaut, W., I. Salma, J. Cafmeyer, H.J. Annegarn, and M.O. Andreae, Regional atmospheric aerosol composition and sources in the Eastern Transvaal, South Africa, and impact of biomass burning, *J. Geophys. Res.*, *101*, 23,631-23,650, 1996.

Maenhaut, W., A. Selen, P.V. Espen, R.V. Grieken, and J.W. Winchester, PIXE analysis of aerosol samples collected over the Atlantic Ocean from a sailboat, *Nucl. Instrum. Methods*, *181*, 399-405, 1981.

Maenhaut, W., and J. Vandenhaute, Accurate analytic fitting of PIXE spectra, *Bull. Soc. Chim. Belg.*, *95*, 407-418, 1986.

Mason, B., *Principles of Geochemistry*, John Wiley, New York, 1966.

NOAA Air Resources Laboratory, HYSPLIT 4, Hybrid Single-Particle Lagrangian Integrated Trajectory Model, Silver Spring, Md., 1997.

Penner, J.E., R.E. Dickinson, and C.A. O'Neill, Effects of aerosol from biomass burning on the global radiation budget, *Science*, *256*, 1432-1434, 1992.

Radke, L.F., Airborne observations of cloud microphysics modified by anthropogenic forcing, in *Symposium on Atmospheric Chemistry and Global Climate, Jan. 29-Feb. 3, Anaheim, Calif.*, pp. 310-315, Am. Meteorol. Soc., Boston, Mass., 1989.

Reid, J.S., and P.V. Hobbs, Physical and optical properties of young smoke from individual biomass fires in Brazil, *J. Geophys. Res.*, *103*, 32,013-32,030, 1998.

Reid, J.S., P.V. Hobbs, R.J. Ferek, D.R. Blake, J.V. Martins, M.R. Dunlap, and C. Liousse, Physical, chemical, and optical properties of regional hazes dominated by smoke in Brazil, *J. Geophys. Res.*, *103*, 32,059-32,080, 1998.

Rogers, C.F., J.G. Hudson, B. Zielinska, R.L. Tanner, J. Hallett, and J.G. Watson, Cloud condensation nuclei from biomass burning, in *Global Biomass Burning: Atmospheric, Climatic and Biospheric Implications*, edited by J.S. Levine, pp. 431-438, MIT Press, Cambridge, Mass., 1991.

Ross, J.L., P.V. Hobbs, and B. Holben, Radiative characteristics of regional hazes dominated by smoke from biomass burning in Brazil: Closure tests and direct radiative forcing, *J. Geophys. Res.*, *103*, 31,925-31,941, 1998.

Schneider, S.H., Detecting the climatic change signals: Are there any "fingerprints"?, *Science*, *263*, 341-347, 1994.

Scholes, M.P., P. Matrai, K. Smith, M.O. Andreae, and A. Guenther, Biosphere-atmosphere interactions, in *Atmospheric Chemistry in a Changing World*, edited by G. Brasseur, R. Prinn, and A. Pszenny, pp. in press, Springer-Verlag, New York, 2001.

Seiler, W., and P.J. Crutzen, Estimates of gross and net fluxes of carbon between the biosphere and the atmosphere from biomass burning, *Clim. Change*, *2*, 207-247, 1980.

Simoneit, B.R.T., J.N. Cardoso, and N. Robinson, An assessment of the origin and composition of higher molecular weight organic matter in aerosols over Amazonia, *Chemosphere*, *21* (10-1), 1285-1301, 1990.

Stunder, B.J.B., NCEP model output - MRF archive data, NOAA Air Resour. Lab., Silver Spring, Md., 1997.

Thurston, G.D., and J.D. Spengler, A quantitative assessment of source contributions to inhalable particulate matter pollution in metropolitan Boston, *Atmos. Environ.*, *19*, 9-25, 1985.

Twomey, S.A., M. Piepgrass, and T.L. Wolfe, An assessment of the impact of pollution on global cloud albedo, *Tellus*, *36B*, 356-366, 1984.

Table B.1. Mean atmospheric concentrations for 17 elements in the fine and coarse fraction of the SFU samples from the N'doki National Park during EXPRESSO-96.

	EXPRESSO 1996 – dry season experiment Above Canopy				SAFARI 1992 Skukuza	
Species	Fine, ng m^{-3} ± s.d.	*n*	Coarse, ng m^{-3} ± s.d.	*n*	Fine, ng m^{-3}	Coarse, ng m^{-3}
Al	88.3 ± 51.3	(24)	108 ± 63	(25)	85.8	593
Si	386 ± 153	(27)	402 ± 211	(27)	177	1180
P	18.0 ± 5.4	(14)	36.7 ± 19.7	(27)	--	15.4
S	928 ± 625	(27)	127 ± 109	(27)	805	209
Cl	30.3 ± 14.5	(16)	111 ± 39	(13)	110	1542
K	503 ± 186	(27)	116 ± 38	(27)	215	172
Ca	23.9 ± 13.2	(26)	55.2 ± 35.4	(27)	33.5	174
Ti	6.49 ± 3.97	(22)	9.62 ± 5.80	(25)	6.93	40.7
Mn	1.36 ± 0.61	(16)	2.39 ± 1.02	(27)	1.56	9.22
Fe	51.3 ± 30.8	(27)	73.9 ± 45.3	(27)	55.0	360
Cu	2.71 ± 1.74	(12)	1.52 ± 0.86	(11)	1.27	3.12
Zn	4.67 ± 1.64	(26)	2.60 ± 1.36	(25)	2.28	2.07
Br	3.26 ± 0.31	(4)	---	(0)	8.39	3.73
Rb	1.96 ± 0.33	(8)	---	(0)	0.76	0.91
Sr	---	(0)	1.14 ± 0.05	(2)	0.87	2.44
Pb	2.13 ± 0.72	(9)	---	(0)	3.41	1.70
BC	4120 ± 1070	(26)	---	(0)	1090	300

Data from SAFARI-92 at the Skukuza sampling site are shown for comparison [*Maenhaut et al.*, 1996]. Variable *n* shows the number of samples in which the element was detected.

Table B.2. Pearson correlation table for fine fraction S compared to the biomass burning elements before and after the large change in sulfur concentrations on December 6.

EXPRESSO 1996 – Dry Season Experiment Fine-mode S Correlation				
S	K	Zn	BC	Al [a]
before Dec. 6	0.965 [b]	0.900 [b]	0.694 [b]	0.442
Dec. 6 to end	0.605 [c]	0.682 [c]	0.513	0.201

[a] Al is a reference for the mineral dust component.

[b] Correlation is significant at the 0.01 level.

[c] Correlation is significant at the 0.05 level.

Table B.3. Varimax rotated loadings for the 11 aerosol variables on the three retained components in the fine and coarse fraction.

EXPRESSO 1996 – Dry Season Experiment
Above Canopy Samples

Element	Fine Fraction				Coarse Fraction			
	Comp. 1, Mineral dust	Comp. 2, Pyrogenic	Comp. 3, Marine/ Anthrop.	Commu-nalities	Comp. 1, Mineral dust	Comp. 2, Biogenic I	Comp. 3, Biogenic II	Commu-nalities
Al	[0.94]	0.25	(0.09)	0.96	[0.97]	-0.12	(-0.08)	0.96
Si	[0.93]	(0.09)	-0.22	0.92	[0.98]	(-0.08)	(0.00)	0.96
P	--	--	--	--	-0.24	[0.92]	-0.21	0.95
S	(-0.04)	0.35	[0.93]	0.99	(-0.05)	(-0.01)	[0.91]	0.83
K	0.18	[0.93]	0.26	0.97	(0.05)	[0.95]	(0.20)	0.96
Ca	[0.77]	0.50	(0.16)	0.88	[0.95]	(-0.05)	(-0.04)	0.90
Ti	[0.96]	0.22	(0.05)	0.98	[0.97]	-0.14	(-0.09)	0.97
Mn	--	--	--	--	[0.93]	(0.12)	(-0.16)	0.91
Fe	[0.93]	0.35	(0.02)	0.98	[0.98]	(-0.10)	(-0.08)	0.97
Zn	0.27	[0.93]	(0.12)	0.96	(-0.14)	(0.03)	[0.88]	0.80
BC	0.40	[0.80]	(0.23)	0.84	--	--	--	--
Variance	4.40	2.99	1.09		5.64	1.83	1.74	
% variance	48.9	33.2	12.1		56.4	18.3	17.4	

Loadings, which were less than 3 times their associated standard deviation, are listed in parentheses in the table. "Comp." denominates the individual components from APCA. "Marine/Anthrop." stands for the marine/anthropogenic component. Communalities for each species are also shown.

Table B.4. Sources for each of the detected elements during EXPRESSO-96.

EXPRESSO 1996 – Dry Season Experiment Element Sources		
Source Type	Fine Fraction	Coarse Fraction
mineral dust	Al, Si, Ca, Ti, Mn, Fe	Al, Si, Ca, Ti, Mn, Fe
biomass burning	BC, S, Cl, K, Zn, Br, Pb, Ca	Sr
biogenic / forest	P, Cu	P, S, Cu, K, Zn
marine / anthropogenic	S	S

Diel cycles, above/below canopy concentrations, APCA, and backward trajectories provided information to assign sources to detected elements.

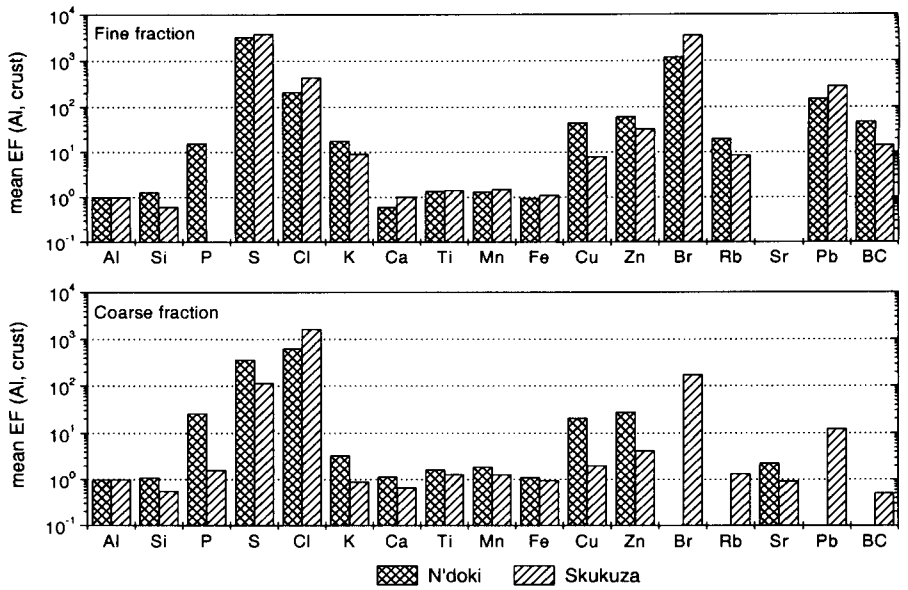

Figure B.1. Mean crustal enrichment factors (EFs), calculated relative to average crustal rock [*Mason*, 1966] with Al as the reference element, for 17 species for the coarse fraction (2 - 10 μm) and the fine fraction (< 2 μm). The data displayed for black carbon (BC) are concentration ratios to Al instead of EFs. Results from the EXPRESSO-96 and SAFARI-92 [*Maenhaut et al.*, 1996] experiments are shown.

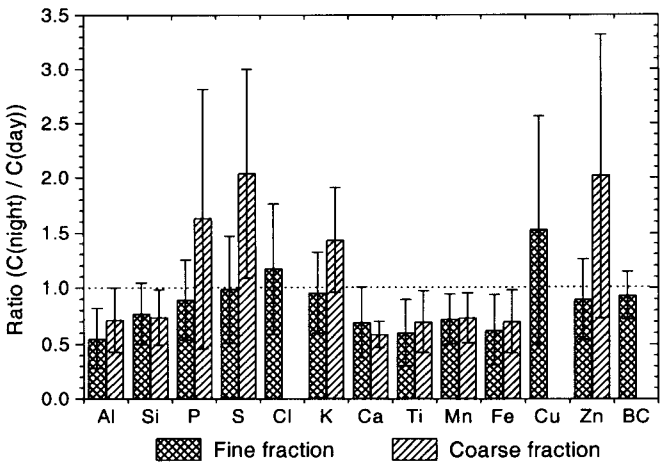

Figure B.2. Ratio of daytime and nighttime elemental concentrations at the EXPRESSO-96 site.

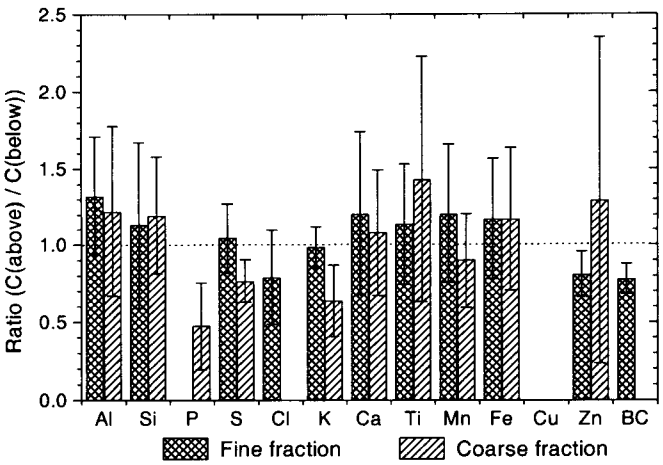

Figure B.3. Ratio of samples taken above and below the canopy at the EXPRESSO-96 site.

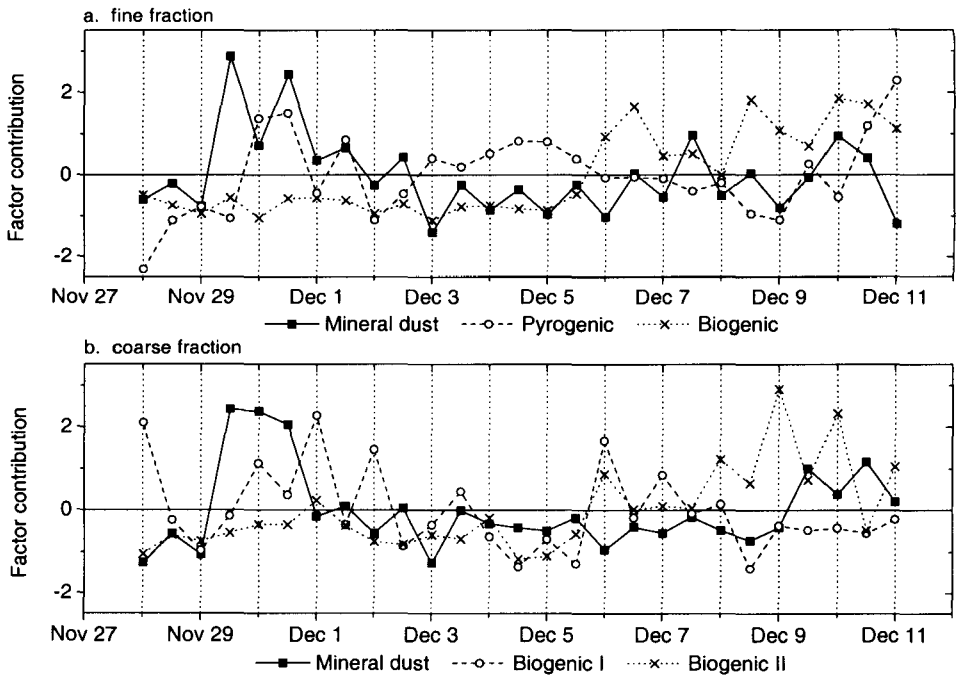

Figure B.4. Time trends for absolute principal component scores (APCS) for the three identified components of the (a) fine and (b) coarse fraction during the EXPRESSO-96 experiment. The vertical dotted lines indicate midnight of each day.

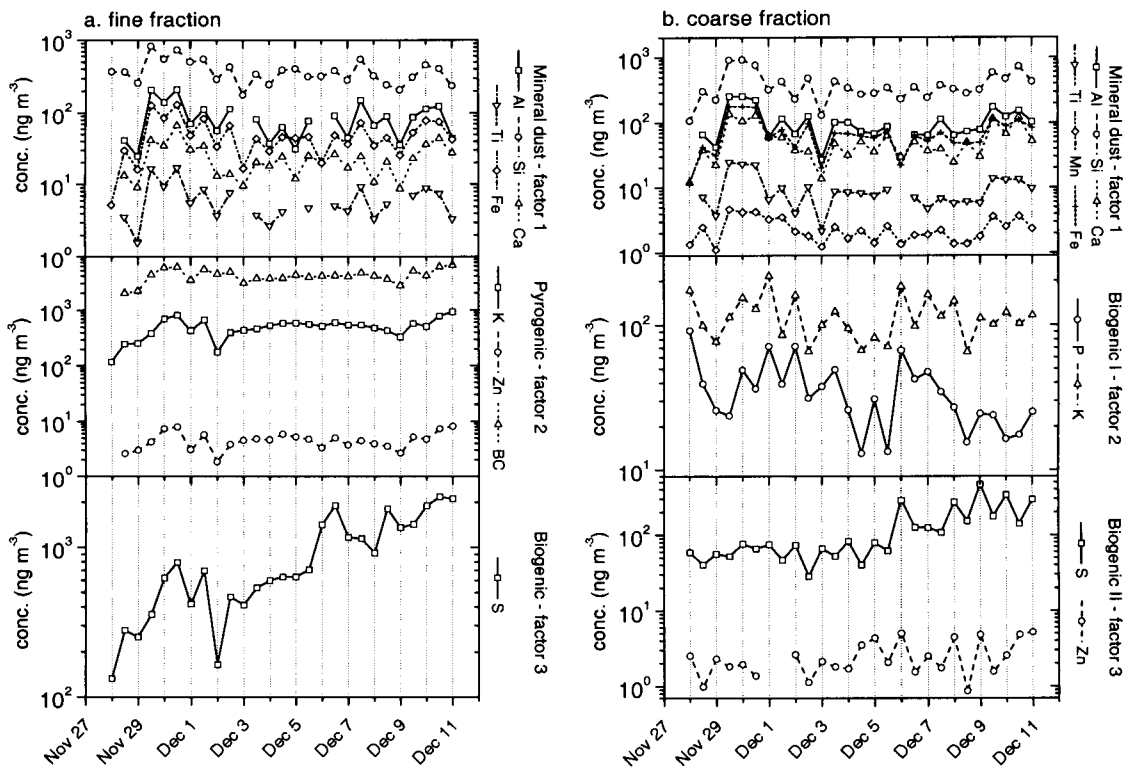

Figure B.5. Time trends of elemental concentrations for the three identified components of the (a) fine and (b) coarse fraction during the EXPRESSO-96 experiment. The vertical dotted lines indicate midnight of each day.

Figure B.6. Seven day, isopycnic back trajectories for November 29 to 30 and December 4 to 7, 1996 using medium range forecast (MRF) data [*Stunder*, 1997] and the HYSPLIT model [*NOAA Air Resources Laboratory*, 1997]. Five trajectories characterize each level; the beginning and end of the sampling period are shown by the darkest and lightest trajectory, respectively. The symbols (circles and crosses) represent trajectory positions every 24 hours. The circles are on the trajectory, which arrives at NNP at noon. The shaded gray region indicates the area analyzed for savanna fires; color squares within this region represent burning locations.

Figure B.6 (continued).

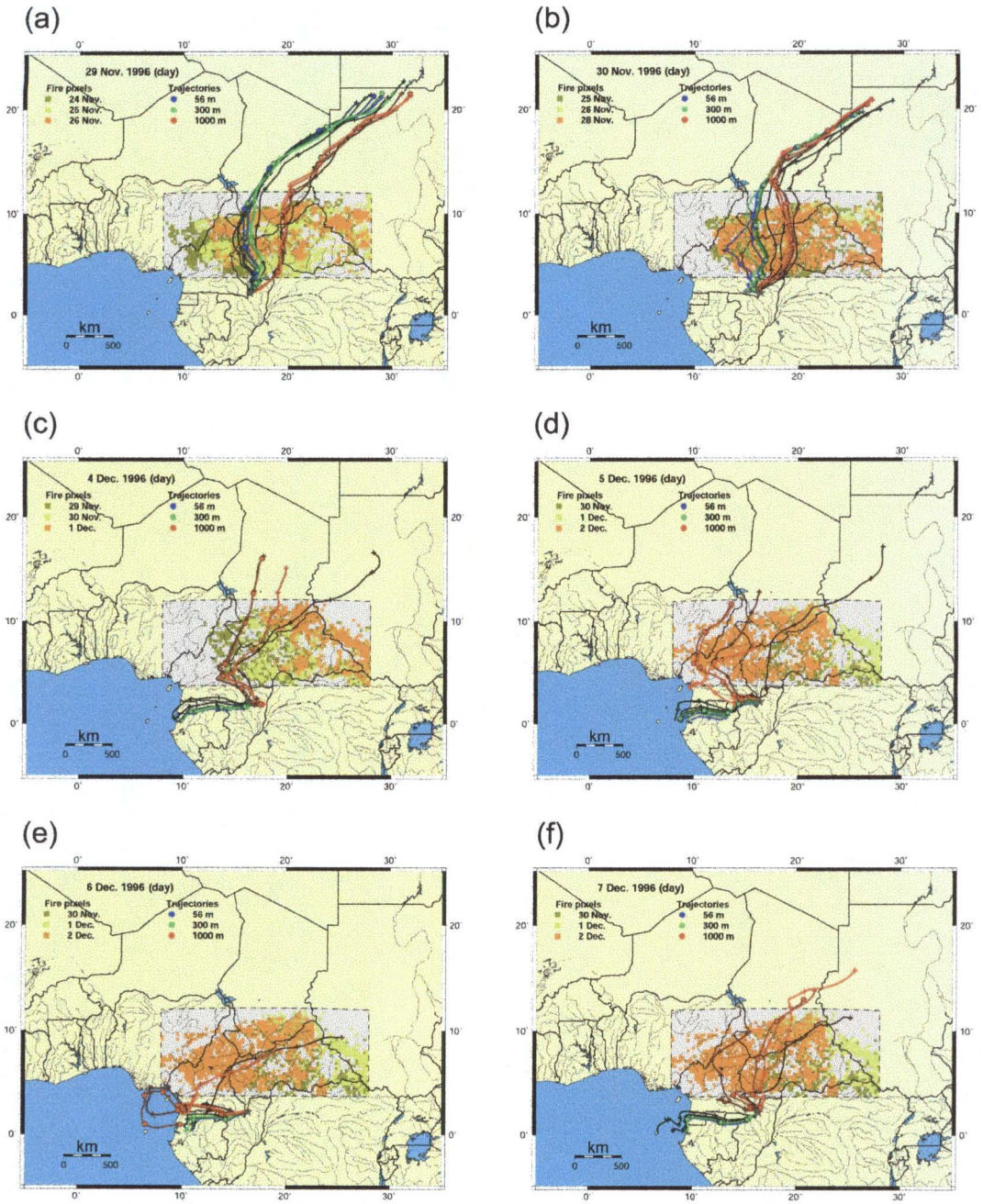

Appendix C

Biogenic gas (CH_4, N_2O, DMS) emission to the atmosphere from near-shore and shelf waters of the northwestern Black Sea

Abstract

The marine emissions of biogenic gases (CH_4, N_2O, DMS) were determined on the Northwest shelf of the Black Sea in July 1995. Methane (CH_4) saturation ratios (SR) averaged 930% (173 – 10,500%) and were inversely proportional to salinity. The mean nitrous oxide (N_2O) SR was 111% (96 - 149%), which is similar to other coastal water masses and did not present significant variability as a function of salinity. Dimethyl sulfide (DMS) concentrations were ranging between 2.96 and 11.9 nM and Chlorophyll *a* - normalized DMS concentrations were increasing exponentially with salinity, illustrating the influence of plankton speciation. Coastal and shelf waters affected by riverine inputs, which comprise 30% of the Black Sea surface area, contributed to 53% of the CH_4 flux during the summer period. Biogenic sulfur emissions, primarily as DMS, showed a strong gradient, increasing from open Black Sea waters to estuarine Danube waters. There was less variation in the flux densities of N_2O for the different water masses. Extrapolating values obtained during summer 1995, upper limits for the emissions from the Black Sea to the atmosphere were estimated to be 6.7-11.7 Gmol/yr of CH_4, 0.45-0.75 Gmol/yr of N_2O, and 0.30-0.80 Gmol/yr of DMS, using two different air-sea gas exchange models.

C.1. Introduction

For nearly three decades, Danube River inputs, rich in nutrients such as nitrogen and phosphorus, have been driving intense eutrophication processes on the northwestern (NW) shelf of the Black Sea. The effects from eutrophication usually peak during the summer season and have been found to modify both water column and sediment biogeochemistry [*Mee*, 1992]. In the Northwestern Black Sea, eutrophication induces both a shift in plankton speciation from diatoms to flagellate-dominated populations [*Mee*, 1992; *Lancelot et al.*, 1998] and anoxic conditions above the sediments [*Ivanov and Lein*, 1991]. Consequently, the eutrophication phenomena in Black Sea shelf waters may potentially affect the cycling of major elements involved in the production of biogenic gases. Previous investigations on the Black Sea have focused primarily on the biogeochemistry of CH_4 in the deep permanent anoxic basin [*Hunt*, 1974; *Scranton*, 1977; *Reeburgh et al.*, 1991]. Methane (CH_4) cycling in the main Black Sea basin has been investigated by *Reeburgh et al.* [1991] and is predominantly driven by gas seeps [*Ivanov et al.*, 1991] and microbial oxidation in the water column [*Reeburgh et al.*, 1991]. Reeburgh and co-authors estimated that the CH_4 flux to the atmosphere from the Black Sea is about 4.1 Gmol/yr. No published data, however, have quantified either the significance of nitrous oxide (N_2O) and volatile organic sulfur compounds (i.e., dimethyl sulfide, DMS) in the Black Sea or the importance of these biogenic gases on the NW Black Sea shelf.

CH_4 is an atmospheric trace gas that contributes 15% of the greenhouse effect and is undergoing atmospheric concentration increases that slowed down from 1 to about

0.5% yr^{-1} during the last two decades [*Steele et al.*, 1992; *Matthews*, 1994; *Houghton et al.*, 1996]. Coastal environments were found to account for 75% of the oceanic emissions to the atmosphere [*Bange et al.*, 1994], which contribute about 2% of the global atmospheric emission [*Matthews*, 1994; *Bates et al.*, 1996]. The Black Sea is also the largest surface water reservoir of methane (6000 Gmol), which is contained in the anoxic zone of the main basin [*Cicerone and Oremland*, 1988]. In the case of the NW Black Sea shelf, intense eutrophication may lead to the deposition of high amounts of organic matter to the sediment floor, which could provide labile organic carbon and generate favorable reducing conditions for the microbial production of methane [*Cicerone and Oremland*, 1988; *Scranton and McShane*, 1991; *Ivanov et al.*, 1991; *Bange et al.*, 1998]. The geochemistry of methane is therefore of primary importance in the Black Sea ecosystem, where both atmospheric evasion and methane oxidation represent the major sinks [*Reeburgh et al.*, 1991]. The present work will particularly emphasize the relative importance of coastal waters compared to open waters (above the deep basin) in the global emission budget of methane from the Black Sea.

N_2O is a gas responsible for 5-6% of the greenhouse effect [*Houghton et al.*, 1996]. N_2O also contributes to the destruction of the ozone layer and shows an annual growth rate of 0.3% yr^{-1} [*Khalil and Rasmussen*, 1992]. The oceans are considered to be significant sources for atmospheric N_2O, contributing to ca. 25% of the global emissions [*Nevison et al.*, 1995; *Bouwman et al.*, 1995]. Marine emissions need nevertheless to be reassessed, and coastal waters have been recently estimated to contribute 60% of the global oceanic flux when estuarine and upwelling coastal areas are included [*Bange et al.*, 1996a]. The eutrophication processes in coastal waters such as the Black Sea shelf

represent a potential source of atmospheric N_2O [*Seitzinger and Nixon*, 1985]. Similar to the case of CH_4, reducing conditions in bottom waters associated with sizeable loads of inorganic and organic nitrogen may lead to increased denitrification and nitrification rates, respectively, and thus to N_2O production [*Rönner*, 1983; *Seitzinger et al.*, 1983; *Seitzinger and Nixon*, 1985; *Hedmond and Duran*, 1989]. Both denitrification in coastal sediments [*Seitzinger et al.*, 1983] and nitrification in the stratified basin [*Rönner*, 1983] were consequently found to be efficient sinks of nitrogen to the ecosystem by the production and volatilization N_2O and other nitrogen gases. The present study will address the occurrence of N_2O in both open and coastal waters of the Black Sea and the significance of its atmospheric evasion for the nitrogen budget.

DMS represents 95% of the natural marine flux of sulfur gases into the atmosphere [*Andreae*, 1990] and has been proposed to counteract the greenhouse effect by subsequent oxidation to sulfate aerosols within the troposphere [Charlson *et al.*, 1987; *Ayers et al.*, 1991]. Sulfate aerosols readily form cloud condensation nuclei that may affect the reflectivity and stability of clouds. The global contribution of coastal waters to DMS emissions seems to be rather low compared to the activity of the large oligotrophic oceanic areas [*Andreae*, 1990; *Kettle et al.*, 1999]. However, significant bloom events observed in various shelf seas, such as the North Sea [*Turner et al.*, 1988] and the Baltic Sea [*Leck et al.*, 1990], involving mainly flagellate plankton organisms, have lead to the production of high DMS concentrations in surface seawaters. High fluxes to the atmosphere were consequently established in these temperate coastal and shelf areas during warmer seasons. Since coastal areas are submitted to large nutrient loads, the resulting eutrophication trend was postulated to enable an increase of the DMS emission

by the shift of plankton population to *Phaeocystis* species [*Lancelot et al.*, 1987]. In this work, the concentrations of DMS in open and coastal waters of the Black Sea will be presented and discussed for the first time and the related atmospheric emission will be estimated.

This paper intends to extend the global inventories of CH_4, N_2O and DMS fluxes to the atmosphere from marine environments and to indicate potential interactions between these fluxes and the biogeochemical changes on the northwestern shelf of the Black Sea. We investigated the distribution of CH_4, N_2O and DMS in surface waters of the northwestern Black Sea, mainly influenced by the Danube River inflow. CH_4 and N_2O mixing ratios in the atmosphere above the sea were also measured, in order to accurately determine the saturation of these gases in surface shelf waters. We finally estimated flux densities from the northwestern shelf and extrapolated the emission rates in the whole Black Sea basin during the summer period for the three biogenic gases.

C.2. Material and Methods

C.2.1. Field Sampling and Analysis

The first cruise of the European River – Ocean System 21 project (EROS 21) (Figure C.1) took place on the northwestern shelf of the Black Sea (18 July - 2 August 1995, R/V Professor Vodyanitskiy, Institute of Biology of the Southern Seas - IBSS, Sebastopol, Ukraine). The cruise track allowed us to sample different representative water masses of the Black Sea from estuarine to shelf waters along the Danube front, and from

shelf waters to open seawaters above the slope and the main deep basin (Figure C.1). The investigation of the near-shore waters was focused on the Danube estuarine plume along the delta output and on Constanza Bay (Romanian coast, West of the shelf). The study of shelf surface waters was conducted along two transects above the Crimean and the Bulgarian shelf break (south-east and south-west part of the shelf, respectively). Seawater temperature and salinity were monitored continuously using a towable Mark-III conductivity, temperature, depth (CTD) probe (Neil Brown, USA). The conductimeter was calibrated in order to obtain direct salinity values according to the Practical Salinity Scale (International System of Units). Meteorological parameters, such as wind speed, wind direction, temperature and relative humidity, were also continuously recorded using a portable, automated weather station (Campbell Scientifics, UK; Keithley Acquisition Systems, USA). For the measurements of the biogenic gases, two independent systems were used; a continuous sampling system measured the surface concentrations of CH_4 and N_2O throughout the entire cruise and a discrete sampling system was used to determine depth distributions of CH_4 and DMS at several stations on the shelf during the last part of the cruise (25-31 July). The discrete sampling system was also found useful to correct the surface concentrations of CH_4 measured by the continuous sampling system within highly stratified surface waters of the Danube front. In this part of the shelf area, the Danube plume behaves as an "outer" estuary with salinities below 15 in the first 2-3 meters depth. Thus surface layer samples (ca. 1 m depth) collected by discrete sampling were found to be enriched in methane by comparison with continuous measurements collected about 2 meters below. A good correlation was obtained for those surface waters between discrete and continuous measurements ($R^2 = 0.8$, n=20) with a slope of 2.3 (standard deviation of

35%), which was used as a correction factor for later saturation and flux calculations. For salinities above 15 (and up to 18), shelf surface waters were found to be well mixed in the first 5 to 10 meters, and no discrepancy was observed between the two CH_4 measurement techniques.

Continuous measurements of atmospheric and dissolved CH_4 and N_2O in the surface waters were obtained using a fully automated system involving gas chromatography (GC) (Dani 8500 GC with Alltech Molecular Sieve 5A packed column) with flame ionization and electron capture detection, respectively. Technical description and analytical performances of the automated manifold are described elsewhere [*Bange et al.*, 1996b]. Surface waters (3 m depth) were pumped continuously through an air-water equilibrator at 12-15 L/min and equilibrated air was subsequently sampled every two hours. The basic operational and physical principles of this equilibrator are described elsewhere [*Butler et al.*, 1988; *Weiss et al.*, 1992]. Under our operating conditions, the response time for full equilibration of both CH_4 and N_2O was estimated to range between 1 and 5 min. Atmospheric samples were pumped directly to the laboratory from the top of the main mast to collect clean air from the marine boundary layer. During discrete or CTD cast stations the ship was facing into the wind to avoid ship contamination.

For the discrete sampling measurements, water samples were taken using GO-FLO units (General Oceanics, Miami, USA) at various depths and subsequently analyzed for CH_4 and DMS (no N_2O measurement). Surface samples (1 m depth) were collected at most CTD cast stations, and two depth profiles were collected at station 17 and 22 (see *Figure C.1*). Station 17 is situated in front of the Danube Delta outflow from the St. George Branch (44°49'25'' N, 29°49'22'' E; 45 m depth) and is considered to represent

the Danube front between estuarine and shelf waters (surface salinity 12). Station 22 is positioned along Constanza Bay and downstream of the Danube estuarine plume (43°49'59'' N, 29°01'52'' E ; 50 m depth) and is considered to represent Northwestern shelf waters as influenced by Danube outflow (surface salinity 16). Before the cruise, the GO-FLO units were checked for gas leaks. Samples were filtered through pyrolyzed glass fiber filters (GF/F Whatman) directly into silanized glass loops (50 ml) using a helium (He) line (1.5 bars) and stored in the dark at ca. 10 °C. Samples were analyzed within a couple of hours after filtering. *Andreae and Barnard* [1983] have shown that storage of filtered samples for several hours in these conditions does not significantly change DMS concentrations. The DMS analytical system consisted of a purge and trap unit coupled to a gas chromatograph (Hewlett-Packard 5890 GC) fitted with a Carbopak A column (60/80 mesh in 3.2mm O.D. Teflon PFA tubing). The oven temperature program began at 50 °C for two minutes then steadily increased to 120 °C at a rate of 3.9 °C/min. The detection was performed with a monoblock flame ionization (FID) and photometric (FPD) detector using a hydrogen (H_2) flame (75 ml/min H_2 and 100 ml/min synthetic air). To minimize gas adsorption, glass surfaces were silanized with dimethyl-dichlorosilane and gas tight connections were made with Teflon tubing and connectors. The water samples were purged with cryo-cleaned He for 30 minutes (160 ml/min) and the volatile gases were collected in a cryogenic trap (3.2 mm I.D. x 20 cm U-shaped glass tubing packed with Chromosorb WHP, Supelco) immersed in liquid nitrogen. The sample was then injected into the GC using cryo-cleaned He carrier gas (60 ml/min). An intermediate glass U-trap, immersed in an acetone bath and maintained at –30 °C, was placed between the cryogenic trap and the purging vessel to remove water vapor. Two samples were

simultaneously processed by connecting two identical stripping and trapping apparatuses to the gas chromatograph via a ten-way gas stream selection valve (Valco, Supelco).

Calibrations were performed using standard gas mixtures for CH_4 and N_2O. Two gas mixtures calibrated against US NIST standards were used for CH_4 and N_2O. Certified concentrations for CH_4 and N_2O were, respectively, 3.4 part per million by volume (ppmv) and 460 part per billion by volume (ppbv) in the first gas mixture, and 5.07 ppmv and 618 ppbv in the second one (Deuste Steininger GmbH, Germany). DMS was calibrated using a thermostated (23 °C) permeation device (Vici Metronics, USA). Relative standard deviations on measurements obtained under field conditions were 1%, 2% and 10% for CH_4, N_2O and DMS, respectively. The FID/FPD detector was first optimized for DMS analysis using a H_2–rich flame for FPD sulfur detection (see conditions above). CH_4 detection with the FID for discrete samples was therefore less stable and sensitive and gave rise to a higher relative standard deviation of 25%.

C.2.2. Saturation Ratio and Flux Calculations

For CH_4 and N_2O, saturation ratios (SR) between surface waters and the overlying atmosphere were directly determined from the mixing ratios of both gases measured in the equilibrated air (X_w) and the ambient air (X_a), using the general relation:

$$SR(\%) = \frac{C_w}{C_a} \cdot 100 \qquad \text{(C.1)}$$

and

$$C_w = X_w \beta_w P_{atm}$$
$$C_a = X_a \beta_a P_{atm} \qquad \text{(C.2)}$$

where C_w and C_a (mol/l) are the concentrations of the dissolved gas observed in surface waters and theoretically in equilibrium with the ambient atmosphere, respectively. β_w and β_a (mol/l.atm) are the respective Bunsen solubility coefficients of the gas in the equilibrator and in surface waters (temperature and salinity dependent), and P_{atm} (atm) is the atmospheric pressure. Water temperature inside the equilibrator and atmospheric pressure were measured continuously using a thermistor probe and ship's pressure sensor. Gas solubility was corrected for the temperature difference between surface waters and the equilibrator (ca. 1 to 2 °C), and salinity was assumed to be identical. Bunsen solubility coefficients were obtained after *Weisenburg and Guinasso* [1979] and *Weiss and Price* [1980] for CH_4 and N_2O, respectively.

The air-sea gas flux densities (F_g, mol/m^2.s) were obtained using Fick's Law for diffusion. The sea-to-air fluxes for CH_4 and N_2O were calculated using the following relation:

$$F_g = k_W (C_w - C_a) \qquad \text{(C.3)}$$

where k_W (m/s) is the calculated transfer velocity of the gas from surface waters.

For DMS, assuming that marine coastal waters are highly supersaturated compared to the atmosphere ($C_w >> C_a$), the sea-to-air flux expression can be simplified to [*Andreae et al.*, 1994]:

$$F_g = k_W C_w \tag{C.4}$$

with C_w (DMS) directly measured after sample purge and trap – GC – FPD analysis.

The transfer velocity, k_W, was determined using the empirical formulas of Liss and *Merlivat* [1986] (hereafter referred to as LM86) and *Wanninkhof* [1992] (hereafter referred to as W92). These transfer velocity models are only dependent on wind speed, and surface water temperature and salinity. The transfer coefficient was adjusted by multiplying with $(Sc/600)^n$ for LM86 and $(Sc/660)^n$ for W92, where Sc is the Schmidt number. Sc was calculated according to *Jähne et al.* [1987], *Broecker and Peng* [1974] and *Saltzman et al.* [1993] for CH_4, N_2O and DMS, respectively. Continuously measured wind speed at about 12 m height, surface temperature and salinity at 1 m depth were used to calculate the various parameters. More details about the methods used here for CH_4, N_2O and DMS flux calculations are also given elsewhere [*Bange et al.*, 1996b, *Andreae et al.*, 1994].

C.3. Results and Discussion

C.3.1. Methane (CH_4)

Atmospheric CH_4 mixing ratios were fairly constant throughout the cruise averaging 1.85 ± 0.06 ppmv (Table C.1). The average mixing ratio is slightly higher than the results of the U.S. NOAA global sampling network, which reports values ranging from 1.73 to 1.80 ppmv from the monitoring sites at Borrow, Alaska and Mauna Loa, Hawaï, for the summer of 1995 (http://www.cmdl.noaa.gov/noah/). However, mixing ratios obtained above the main deep basin average 1.79 ppmv and are in good agreement with the US NOAA global sampling network. In near-shore areas, they increased significantly with maximum values up to 2.35 ppmv downwind (north/northwest) of the Danube Delta. These high values indicate that both Danube delta and estuary are important sources of atmospheric CH_4. In addition, it has been well established that delta and brackish water ecosystems are important sources of CH_4 to the atmosphere [*De Laune et al.*, 1983; *Heyer et al.*, 1990].

CH_4 concentrations measured in the NW Black Sea surface waters were mainly dependent on the water mass sampled, ranging from 4 nM above the main deep anoxic basin to 255 nM in front of the Danube Delta (Figure C.2). CH_4 concentrations in open Black Sea waters average 9.1 nM and are very similar to those obtained several years ago by *Reeburgh et al.* [1991] at ca. 10 nM (Table C.1). CH_4 concentrations along the estuarine salinity gradient show non-conservative behavior. Concentrations decrease rapidly seaward from salinity 8.5 to salinity 18.5 without following a linear mixing curve

(Figure C.2). The apparent CH_4 loss during the estuarine transfer is probably due to both ventilation and microbial methane oxidation. Such inverse relationships have also been found in various other estuarine and coastal environments [*De Angelis et al.*, 1987; *Butler et al.*, 1987; *Scranton and McShane*, 1991]. Further analysis would require more data for low salinity, but our data indicate that the Danube Delta is probably an important source of CH_4 to the NW Black Sea shelf and to the atmosphere.

To better understand CH_4 sources on the northwestern Black Sea shelf, two depth profiles have been performed within the Danube plume and on the southwestern part of the shelf. The depth profiles are presented in Figure C.3a (station 17) and Figure C.3b (station 22). At the Danube front area (station 17), temperature and salinity data show that a well developed and typical mixed layer was established at this time of the year with a strong thermocline situated at about 25 m depth (Figure C.3a). However, within the first 5 meters a slight increase of the salinity with depth demonstrates the occurrence of a surface layer corresponding to the Danube plume. Oxygen was not saturated but no anoxic condition was present in the whole water column (3-5 ml/l). CH_4 concentrations decreased sharply from 250 nM in the surface layer to 25-50 nM in the water column. These data clearly demonstrate the large input of CH_4 from the Danube Delta at the surface, which can then be easily ventilated to the atmosphere. Although concentrations were 10 times lower than at the surface, CH_4 was supersaturated in the whole water column. Production of CH_4 within the near-shore water column has been observed previously and may result from the presence of reducing microenvironments formed under intense primary productivity [*Scranton and McShane*, 1991]. *Bange et al.* [1998] showed that coastal sediments could also produce large amount of CH_4, but in this

specific area of the Danube front, *Ivanov and Lein* [1991] found that sulfate reduction is the dominant microbial activity and may prevent any methanogenesis to occur.

On the shelf, the water stratification was similar to that of the Danube front (Figure C.3b). In the first 3 meters the salinity signature of the Danube plume was still present (slight increase) and a well-marked thermocline was positioned at the same depth and within the same range of temperature (25 to 7 °C). Oxygen saturation was higher than in the Danube front, ca. 5-6 ml/l. CH_4 was found saturated in the whole water column, with homogeneous concentrations around 20-30 nM in the mixed layer, then increasing steadily with depth from 20 nM at the thermocline to 200 nM at the bottom. Surface waters are probably saturated from both the influence of the Danube plume, as indicated by the salinity signal at the surface, and the potential production of CH_4 within the water column [*Scranton and McShane*, 1991]. The sharp methane gradient shown in this profile also demonstrates that bottom sediments are probably a significant source of CH_4 for shelf waters [*Bange et al.*, 1998]. This statement is also in agreement with the observations of *Ivanov et al.* (manuscript in preparation) in the same area, which show that methane oxidation rates in the sediment and in the water column of the shelf could not counterbalance CH_4 production rates.

Surface waters in the NW Black Sea were all supersaturated with CH_4 (see Table C.1), and saturation ratios (SRs) ranged from 173% to 10,500%. SRs displayed in Figure C.4 were highly variable along the cruise track and inversely proportional to the salinity in surface waters, as shown previously for concentrations (see Figure C.2). Similar SR values and their relationship with salinity have been reported in several estuarine and coastal environments [*Bange et al.*, 1994]. As discussed above, for salinities around 12 or

less, surface waters were directly influenced by Danube estuarine waters and display high SRs, such as in the Danube Front or in Constanza Bay, averaging 5336%. Shelf sediments were also found to be a significant source of CH_4 to surface waters during the summer of 1995 (*Ivanov et al.*, manuscript in preparation), and could explain the high supersaturation in the whole shelf area investigated (average 567%). High SRs were observed in open surface waters of the NW Black Sea with an average of 401%. These values are in agreement with those obtained by *Reeburgh et al.* [1991] in surface waters of the central part of the Black Sea deep basin, which were ranging from 200 to 500%. They could result from both gas seep bubble input released by the shelf slope sediments and from vertical diffusion of methane produced in the permanent anoxic basin [*Ivanov et al.*, 1991; *Reeburgh et al.*, 1991]. SRs peaks at about 1100 and 1500% were additionally observed in both Crimean and Bulgarian shelf break transects, respectively (Figure C.4). They are probably a consequence of methane gas seeps, which were located in these areas by *Ivanov et al.* [1991] from systematic echo-sounding surveys. The two independent studies performed by *Ivanov et al.* [1991] and *Reeburgh et al.* [1991] have both outlined the role of the shelf slope sediments on the Black Sea CH_4 budget and estimated that these sediments release 685 μmol/m^2.d and 548 μmol/m^2.d of CH_4, respectively.

Air-sea flux densities are averaged for each of the three different water masses of the Black Sea (Table C.2). CH_4 fluxes in open waters, calculated with both air-sea exchange models, range from 28.9 to 50.5 μmol/m^2.d and are again in good agreement with values estimated previously [*Reeburgh et al.*, 1991] above the Black Sea deep basin, which were averaging 26.6 μmol/m^2.d. CH_4 emissions from riverfronts and shelf waters represent an important source contributing nearly 35% of the flux from the Black Sea

during summer. The CH_4 emission rate from the Black Sea, extrapolated from the flux densities values obtained during the summer period, is 6.7 to 11.7 Gmol/yr (Table C.2). These emission rates are about 1.5 to 3 times higher than those estimated by *Reeburgh et al.* [1991]. This difference cannot only be explained by seasonal trends or differences in air-sea exchange modeling, but also represent the important contribution of CH_4–enriched surface waters in the estuarine plume (i.e., Danube river front).

C.3.2. Nitrous Oxide (N_2O)

N_2O atmospheric mixing ratios were found to be fairly constant with an average of 315 ± 10 ppbv (Table C.1). The average mixing ratio value is also in good agreement with the results of the U.S. NOAA global sampling network, which reports values of ca. 313 ppbv from the monitoring sites at Barrow, Alaska, and Mauna Loa, Hawaii, for the summer of 1995 (http://www.cmdl.noaa.gov/noah/). However, our standard deviation appears to be rather high (ca. 3%) compared to previous studies in coastal environments [*Bange et al.*, 1996a]. Dominant winds throughout the cruise were from north/northwest and could lead to some mixing ratio spikes due to heterogeneous continental air mass inputs. Analytical error was, however, measured at about 2% and may explain most of the deviation from the average mixing ratio.

Our seawater N_2O measurements indicate that no significant variation in the N_2O concentrations on the shelf occurred between the different surface water masses, averaging 8.0 ± 0.6 nM (Table C.1). Higher concentrations between 8.0 and 10.0 nM were, however, observed in open waters above the main Black Sea basin and in near-

shore waters at the Danube riverfront. Lower concentrations, between 6.5 and 8.0 nM, appeared mainly in shelf surface waters. N_2O concentrations plotted versus salinity therefore do not present any significant trend (Figure C.2). The Danube River is supposed to bring considerable loads of inorganic nitrogen species into the NW Black Sea shelf, up to 340,000 tons per year [*Mee*, 1992]. One would expect that such an important stress on estuarine and coastal ecosystems leads to large production and release of N_2O in surface waters [*Seitzinger and Nixon*, 1985; *Butler et al.*, 1987; *Hedmond and Duran*, 1989; *Law et al.*, 1993]. However, potentially low denitrification rates in Danube Delta and near shore sediments may explain our observations [*Seitzinger et al.*, 1983, *Seitzinger and Nixon*, 1985]. This monotonous distribution of N_2O concentrations with salinity has also been observed by *Bange et al.* [1998] in estuarine and coastal waters of the southern Baltic Sea. They also obtained N_2O concentration maxima, exclusively during high nutrient loads coinciding with early spring flood events. For the northwestern Black Sea, more data are required in the upper estuary and delta and in shelf sediments to understand which processes are controlling N_2O formation and fate as influenced by Danube river inputs.

Unfortunately, no N_2O depth profile was performed during the cruise, which may have helped to provide an explanation for the rather low and constant levels of this gas in the surface waters of the northwestern shelf of the Black Sea. However, the oxidized nitrogen species concentrations within the water column from the two profiles shown in Figure C.3 may help to interpret our N_2O dataset. In the Danube front (Figure C.3a), the nitrate plus nitrite ($NO_3^- + NO_2^-$) concentrations display two maxima at the surface and at the bottom of the water column. The first one is associated with the Danube plume

outflow within the surface layer (0-5 m depth). The second corresponds to an increase of (NO_3^- + NO_2^-) concentrations with depth below the mixed layer and the maximum plankton biomass, as indicated by chlorophyll a concentrations. In the shelf waters (Figure C.3b), the influence of the Danube plume is not present and (NO_3^- + NO_2^-) concentrations are completely depleted in the surface waters down to the thermocline. Below the mixed layer, a sharp increase in (NO_3^- + NO_2^-) concentrations is observed down to the bottom. In both depth profiles, the phytoplankton biomass is large in the mixed layer (3-6 mg/m^3 Chl.a), but oxygen values indicate that no reducing conditions prevail in above-bottom waters. Consequently, bottom waters are likely to undergo significant nitrification activity, as indicated by the (NO_3^- + NO_2^-) maxima, and hydrological conditions do not seem to favor nitrogen reduction (denitrification). *Rönner* [1983] observed in the Baltic Sea that N_2O could be efficiently produced in bottom waters by nitrification, depleting most of the dissolved oxygen. Once anoxic conditions are present, N_2O can be simultaneously produced by denitrification in above-bottom waters. However, in the southern Baltic Sea, coastal sediments showed both consumption and release of N_2O, and nitrification/denitrification activity was apparently not correlated with N_2O concentrations [*Bange et al.*, 1998]. From the profiles obtained during our cruise, oxygen concentrations in bottom waters were not completely depleted in the northwest shelf of the Black Sea during summer 1995. High nitrification and denitrification rates are therefore not expected under these conditions and could explain the rather monotonous distribution of N_2O in surface coastal waters.

N_2O SRs averaged 111 ± 9%, and demonstrate that the majority of surface water types in the northwestern Black Sea were a source of atmospheric N_2O during the

summer period (Figure C.4). The SRs are comparable with those obtained in various estuarine and coastal environments, but higher values are generally found for low salinities [*Bange et al.*, 1996a]. Results indicate that SRs were rather high for open Black Sea waters (110%), but relatively low for the Danube estuarine waters (112%) when compared to literature data from similar coastal waters (Table C.1). The elevated SRs observed for open waters may originate from N_2O production and vertical diffusion due to high nitrification and denitrification rates at the oxic/anoxic interface, located between 150 m and 200 m depth, in the permanent anoxic Black Sea basin. *Rönner* [1983] has observed the same processes occurring above anoxic waters in the Bothnian basin of the Baltic Sea.

Extrapolated N_2O emission rates from our summer dataset range between 0.45 and 0.75 Gmol/yr and were found to be much lower than those of CH_4 for all type of surface waters in the northwestern Black Sea (Table C.2). Significant SRs during summer in both shelf and open Black Sea surface waters lead to a total emission rate equivalent to ca. 3% of the estimated inorganic nitrogen input from the Danube River [*Mee*, 1992]. Volatilization loss of denitrification gas products (N_2O, N_2) from surface waters could therefore be a significant sink for the nitrogen budget in the Black Sea basin [*Rönner*, 1983; *Seitzinger and Nixon*, 1985]. However, the unexpectedly low saturation ratio in the Danube estuarine waters could be due to a seasonal or peculiar event and could lead to an underestimate in our flux data. New data on the Danube River and delta may also help to understand the different biogeochemical processes involved in N_2O cycling in the northwestern Black Sea shelf.

C.3.3. Dimethyl Sulfide (DMS)

All DMS measurements were performed in the second half of the cruise located in the western part of the northwestern shelf (off the Romanian and Bulgarian coast). DMS concentrations measured by discrete sampling were found to be relatively high when compared to literature data (Table C.1), ranging from 2.69 nM in shelf surface waters to 11.9 nM in Danube estuarine waters. The ratio of DMS concentration (μg/l) to chlorophyll-a concentration (μg/l) was also investigated and shows a sharp increase from 0.05-0.2 μg/l in estuarine and shelf surface waters up to 0.90 in open Black Sea waters (Figure C.2). This trend has previously been reported by Iverson et al. [1989] in estuarine waters and was associated with changes in plankton speciation. The ratio obtained for the Danube front estuarine waters (salinity < 15) and shelf surface waters (15 < salinity < 18) is rather similar. This indicates that in these surface waters, DMS concentrations depend mainly on plankton biomass. On the other hand, the ratio is much higher for open waters (salinity > 18) above the Bulgarian shelf break. This may indicate plankton species with higher specific DMS production are occurring in more oligotrophic Black Sea waters. Preliminary data show that plankton species during the cruise were dominated by diatoms in shelf waters and by flagellates in the open waters (*S. Moncheva et al.*, manuscript in preparation). Diatoms are known to produce only small amounts of DMS [*Keller et al.*, 1989], which readily explains the low DMS/Chl ratios in the estuarine and shelf waters. High concentrations of DMS observed in the open waters, despite low phytoplankton biomass, may be due to the higher production of DMSP in flagellates than in diatoms, and

the further production of DMS from cell-released DMSP in surface waters [*Andreae*, 1990; *Leck et al.*, 1990].

Two depth profiles of DMS concentrations were also measured in the Danube front (Figure C.3a) and shelf waters (Figure C.3b). The first profile shows that DMS concentrations are following the temperature profile, with elevated concentrations in the warm mixed layer. Maximum values of 12 nM are observed in this layer, and no influence from the Danube plume outflow is discernable. On the second profile, a similar pattern can be found with maximum concentration up to 10 nM within the mixed layer decreasing sharply below the thermocline. In both depth profiles, DMS concentrations follow approximately the biomass distribution as indicated by the chlorophyll a contents. This type of distribution has been previously reported in near shore waters where concentrations of DMS were mostly related to the type of plankton species occurring within the water column [*Turner et al.*, 1988]. The results obtained by *Turner et al.* [1988] also indicate that a plankton population dominated by high specific DMS producers, such as flagellates or coccolithophores, would lead to much larger DMS concentrations in our samples, considering the high chlorophyll a concentrations observed. Again, this observation sustains that estuarine and shelf waters were mainly dominated by low DMS producer plankton species (e.g., diatoms).

From past observations, eutrophication stress, occurring mainly in summer in the northwestern Black Sea, is supposed to shift plankton species from diatoms to flagellates in near-shore and shelf waters [*Mee*, 1992; *Lancelot et al.*, 1998]. Given the high plankton biomass present, we would have expected higher DMS concentrations in the shelf and Danube estuarine areas than in the open waters during summer. In consequence,

conditions observed during our cruise were probably unusual, but more seasonal variation studies are certainly necessary to understand the real dynamics of plankton speciation and DMS production.

DMS flux densities and emission rates for the northwestern shelf waters were consistent with previous estimates from various coastal environments [*Andreae*, 1990]. Extrapolated DMS emission rates for whole Black Sea range between 0.3 and 0.8 Gmol/yr, and open waters account for about 60% during the summer season. Despite higher flux densities in the Danube front than in shelf or open waters, DMS emission to the atmosphere seems to be more dependent on plankton speciation than on plankton biomass [*Turner et al.*, 1988, *Andreae*, 1990, *Leck et al.*, 1990]. In a temperate climate, summer fluxes account for a large fraction of the annual emission [*Turner et al.*, 1988; *Kettle et al.*, 1999]. Flux estimation using our dataset is therefore indicative only of summer conditions, and cannot be used to predict seasonal and interannual DMS emission trends in the Black Sea.

C.4. Conclusions

In the present study, we have determined for the first time to our knowledge the concentrations and atmospheric fluxes of CH_4, N_2O and DMS in the northwestern Black Sea shelf. This study also addresses the potential importance of biogeochemical changes in the coastal environment of the Black Sea, due to anthropogenic disturbances such as *nutrient* load and chemical pollution, on the production of biogenic gases of atmospheric and climate interest. Atmospheric CH_4 fluxes from Black Sea waters are large compared

to other coastal ecosystems. Three different sources are releasing CH_4 in surface waters and subsequently to the atmosphere: CH_4 seeps in the slope of the main deep anoxic basin, methanogenesis in bottom shelf sediments, and CH_4 inflow from the Danube Delta and estuary. Atmospheric N_2O fluxes in Black Sea shelf waters were surprisingly low, probably because nitrification and denitrification activities were limited in this area at this time of the year. On the other hand, the oxic/anoxic interface above the main deep basin seems to generate significant amounts of N_2O, which can be ventilated to the atmosphere. DMS distribution and atmospheric fluxes were found to be rather similar to those reported in other temperate coastal environments and reflected diatom bloom event conditions. This suggests that expected changes in DMS budget due to eutrophication processes were not occurring at this time of the year. In order to assess the long-term effect of the biogeochemical changes in the northwestern Black Sea on the production of biogenic gases, further work focused on the seasonal and interannual variability is now necessary.

C.5. References

Andreae, M.O., Ocean-atmosphere interactions in the global biogeochemical sulfur cycle, *Marine Chemistry, 30*, 1-29, 1990.

Andreae, M.O., and W.R. Barnard, Determination of trace quantities of dimethylsulfide in aqueous solutions, *Analytical Chemistry, 55*, 608-612, 1983.

Andreae, T.W., M.O. Andreae, and G. Schebeske, Biogenic sulfur emissions and aerosols over the tropical South Atlantic, 1. DMS in seawater and in the atmospheric boundary layer, *J. Geophys. Res., 99*, 22,819-22,829, 1994.

Ayers, G.P., J.P. Ivey, and R.W. Gillett, Coherence between seasonal cycles of dimethyl sulphide, methanesulphonate and sulphate in marine air, *Nature, 349*, 404-406, 1991.

Bange, H.W., U.H. Bartell, S. Rapsomanikis, and M.O. Andreae, Methane in the Baltic and North Seas and a reassessment of the marine emissions of methane, *Glob. Biogeochem. Cycles, 8* (4), 465-480, 1994.

Bange, H.W., S. Dahlke, R. Ramesh, C. Wolff, L.-A. Meyer-Reil, S. Rapsomanikis, and M.O. Andreae, Seasonal study of methane and nitrous oxide in the coastal waters of the southern Baltic Sea, *Estuarine, Coastal and Shelf Science*, 1998.

Bange, H.W., S. Rapsomanikis, and M.O. Andreae, The Aegean Sea as a source of atmospheric nitrous oxide and methane, *Mar. Chem., 53*, 41-49, 1996a.

Bange, H.W., S. Rapsomanikis, and M.O. Andreae, Nitrous oxide in coastal waters, *Glob. Biogeochem. Cycles, 10*, 197-207, 1996b.

Bates, T.S., K.C. Kelly, J.E. Johnson, and R.H. Gammon, A reevaluation of the open ocean source of methane to the atmosphere, *J. Geophys. Res., 101*, 6953-6961, 1996.

Bouwman, A.F., K.W. Van der Hoek, and J.G.J. Olivier, Uncertainties in the global source distribution of nitrous oxide, *J. Geophys. Res., 100*, 2785-2800, 1995.

Broecker, W.S., and T.-H. Peng, Gas exchange rates between air and sea, *Tellus, 26*, 21-35, 1974.

Butler, J., J. Elkins, L. Bronson, T. Thomson, T. Conway, and D. Hall, Trace gases in and over the West Pacific and East Indian Oceans during the El Niño southern oscillation event of 1987, pp. *NOAA Data Report,*4-32, NOAA, Boulder, 1988.

Butler, J., R. Jones, J. Garber, and L. Gordon, Seasonal distributions and turnover of reduced trace gases and hydroxylamine in Yaquina Bay, *Geochim. Cosmochim. Acta*, 697-706, 1987.

Charlson, R.J., J.E. Lovelock, M.O. Andreae, and S.G. Warren, Oceanic phytoplankton, atmospheric sulphur, cloud albedo and climate, *Nature*, *326*, 655, 1987.

Cicerone, R.J., and R.S. Oremland, Biogeochemical aspects of atmospheric methane, *Glob. Biogeochem. Cycles*, *2*, 299-327, 1988.

De Angelis, M., and M. Lilley, Methane in surface waters of Oregon estuaries and rivers, *Limnol. Oceanogr.*, *32*, 716-722, 1987.

De Laune, R., C. Smith, and W. Patrick, Methane Release from Gulf coast wetlands, *Tellus*, *35*, 8-15, 1983.

Hedmond, H., and A. Duran, Fluxes of nitrous oxide at the sediment-water and water-atmosphere boundaries of a nitrogen-rich river, *Water Resour. Res.*, *25*, 839-846, 1989.

Heyer, J., U. Berger, and R. Suckow, Methanogenesis in different parts of a brackish water ecosystem, *Limnologica*, *20*, 135-139, 1990.

Houghton, J.T., L.G. Meira Filho, B.A. Callander, N. Harris, A. Kattenberg, and K. Maskell, Climate Change, 1995: The Science of Climate Change, pp. 572, Cambridge University Press, Cambridge, U.K., 1996.

Hunt, J., Hydrocarbon geochemistry of Black Sea, in *The Black Sea-geology, chemistry and biology*, edited by E. Degens, and D. Ross, pp. 499-504, American Association of Petroleum Geologist, 1974.

Ivanov, M., and A.Y. Lein, Causes of appearance of anaerobic conditions in pre-bottom waters of the north-western shelf of the Black Sea, in *COMAR Interregional Science Conference*, pp. 232-245, UNESCO, Paris, 1991.

Ivanov, M., G. Polikarpov, A.Y. Lein, V. Gal'chenko, V. Yegorov, S. Gulin, M. Gulin, I. Rusanov, Y. Miller, and V. Kuptsov, Biogeochemistry of the carbon cycle in an area of methane seeps in the Black Sea, *Transactions of the USSR Academy of Sciences: earth science sections*, *321*, 165-170, 1991.

Iverson, R.L., F.L. Nearhoof, and M.O. Andreae, Production of dimethylsulfonium propionate and dimethylsulfide by phytoplankton in estuarine and coastal waters, *Limnol. Oceanogr., 34*, 53-67, 1989.

Jähne, B., B. Heinz, and W. Dietrich, Measurements of the diffusion coefficients of sparingly soluble gases in water, *J. Geophys. Res., 92*, 10767-10776, 1987.

Keller, M.D., W.K. Bellows, and R.L. Guillard, Dimethyl sulfide production in marine phytoplankton, in *Biogenic Sulfur in the Environment. ACS Symposium Series 393*, edited by E.S. Saltzman, and W.J. Cooper, pp. 167-182, American Chemical Society, Washington, DC, 1989.

Kettle, A.J., M.O. Andreae, D. Amouroux, T.W. Andreae, T.S. Bates, H. Berresheim, H. Bingemer, R. Boniforti, M.A.J. Curran, G.R. DiTullio, G. Helas, G.B. Jones, M.D. Keller, R.P. Kiene, C. Leck, M. Levasseur, M. Maspero, P. Matrai, A.R. McTaggart, N. Mihalopoulos, B.C. Nguyen, A. Novo, J.P. Putaud, S. Rapsomanikis, G. Roberts, G. Schebeske, S. Sharma, R. Simó, R. Staubes, S. Turner, and G. Uher, A global database of sea surface dimethylsulfide (DMS) measurements and a simple model to predict sea surface DMS as a function of latitude, longitude and month, *Glob. Biogeochem. Cycles, 13* (2), 399-444, 1999.

Khalil, M.A.K., and R.A. Rasmussen, The global sources of nitrous oxide, *J. Geophys. Res., 97*, 14,651-14,660, 1992.

Lancelot, C., G. Billen, A. Sournia, T. Weisse, F. Colljn, M. Veldhuis, A. Davies, and P. Wassman, Phaeocystis blooms and nutrient enrichment in the continental coastal zones of the North Sea, *Ambio, 16*, 38-46, 1987.

Lancelot, C., N. Panin, and J. Martin, The northwestern Black Sea : a pilot site to understand the complex interaction between human activities and the coastal environment, in *3rd European Marine Science and Technology Conference*, edited by K.G. Barthel, pp. 703-713, European Commission, DG-XII Science, Research and Development, Lisbon, 1998.

Law, C.S., A.P. Rees, and N.J.P. Owens, Nitrous oxide: Estuarine sources and atmospheric flux, *Estuar. Coast. Shelf Sci., 35*, 301-314, 1992.

Leck, C., U. Larsson, L.E. Baagander, S. Johansson, and S. Hajdu, DMS in the Baltic Sea: Annual variability in relation to biological activity, *J. Geophys. Res.*, *95*, 3353-3363, 1990.

Liss, P.S., and L. Merlivat, Air-sea gas exchange rates: Introduction and synthesis, in *The Role of Air-Sea Exchange in Geochemical Cycling*, edited by P. Buat-Ménard, pp. 113-127, Reidel, Dordrecht, 1986.

Matthews, E., Assessment of methane sources and their uncertainties, *Pure and Applied Chemistry*, *66*, 154-162, 1994.

Mee, L., The Black Sea in crisis: A need for concerted international action, *Ambio*, *21*, 278- 286, 1922.

Nevison, C.D., R.F. Weiss, and E. D J, III, Global oceanic emissions of nitrous oxide, *J. Geophys. Res.*, *100*, 15,809-15,820, 1995.

Reeburgh, W.S., B.B. Ward, S.C. Whalen, K.A. Sandbeck, K.A. Kilpatrick, and L.J. Kerkof, Black Sea methane geochemistry, *Deep-Sea Research*, *38*, 1189-1210, 1991.

Rönner, U., Distribution, production and consumption of nitrous oxide in the Baltic Sea, *Geochimica et Cosmochimica Acta*, *47*, 2179-2188, 1983.

Saltzman, E.S., D.B. King, K. Holmen, and C. Leck, Experimental determination of the diffusion coefficient of dimethylsulfide in water, *J. Geophys. Res.*, *98*, 16,481-16,486, 1993.

Scranton, M., The marine geochemistry of methane, W.H.O.I/M.I.T. joint program, Woods Hole, 1977.

Scranton, M., and K. McShane, Methane fluxes in the southern North Sea: the role of European rivers, *Cont. Shelf Res.*, *11*, 37-52, 1991.

Seitzinger, S., and S. Nixon, Eutrophication and the rate of denitrification and N2O production in coastal marine sediments, *Limnol. Oceanogr.*, *30*, 1332-1339, 1985.

Seitzinger, S., M. Pilson, and S. Nixon, Nitrous oxide production in nearshore marine sediments, *Science*, *222*, 1244-1246, 1983.

Steele, L.P., E.J. Dlugokencky, P.M. Lang, P.P. Tans, R.C. Martin, and K.A. Masarie, Slowing down of the global accumulation of atmospheric methane during the 1980's, *Nature*, *358*, 313-316, 1992.

Turner, S.M., G. Malin, P.S. Liss, D.S. Harbour, and P.M. Holligan, The seasonal variation of dimethyl sulphide and dimethylsulphoniopropionate concentrations in nearshore waters., *Limnol. Oceanogr.*, *33*, 364-375, 1988.

Wanninkhof, R., Relationship between wind speed and gas exchange over the ocean, *J. Geophys. Res.*, *97* (C5), 7373-7382, 1992.

Weiss, R., and B. Price, Nitrous oxide solubility in water and seawater, *Marine Chemistry*, *8*, 347-359, 1980.

Weiss, R., F. Van Woy, and P. Salameh, Surface water and atmospheric carbon dioxide and nitrous oxide observations by shipboard automated gas chromatography: results from expeditions between 1977 and 1990, Carbon Dioxide Info. Anal. Cent., Oak Ridge Nat. Lab., Oak Ridge, TN, 1992.

Wiesenburg, D., and N. Guinasso, Equilibrium solubilities of methane, carbon monoxide and hydrogen in water and seawater, *J. Chem. Eng. Data*, *24*, 356-360, 1979.

Table C.1. Methane, nitrous oxide and dimethyl sulfide distributions in different surface water types of the northwestern Black Sea and comparison with average literature data compilations.

	Average Concentrations (nM)	Average Mixing Ratios (MR, ppmv)	Average Saturation Ratios (SR, %)	Literature SR (%) or Conc. (nM)	
CH_4:				(%)	
Open water (n=40) [a]	9.1 ± 5.7	1.79 ± 0.04	401	120 [c]	(1)
Reeburgh et al. [1991]	*10*	--	*200 - 500*		
Shelf water (n=80)	13.1 ± 10.6	1.85 ± 0.11	567	395 [c]	(2)
Danube plume (n=35)	131 ± 42 [b]	1.96 ± 0.15	5340 [b]	1230 [c]	(3)
N_2O:				(%)	
Open water (n=35)	8.0 ± 0.8	0.315 ± 0.010	110	103 [d]	(1)
Shelf water (n=55)	7.9 ± 0.8	0.315 ± 0.015	112	109 [d]	(2)
Danube plume (n=25)	8.0 ± 1.0	0.316 ± 0.018	112	608 [d]	(3)
DMS:				(nM)	
Open water (n=10)	8.2 ± 0.5	--	--	2.1 [e]	(1)
Shelf water (n=10)	6.7 ± 1.7	--	--	2.8 [e]	(2)
Danube plume (n=3)	10.1 ± 2.6	--	--	0.8 [f]	(3)

(1) open ocean, (2) coastal/shelf area, (3) estuaries.

[a] number of measurements.

[b] corrected continuous measurement values from discrete samples measurements in the Danube estuarine plume.

[c] *Bange et al.* [1994]

[d] *Bange et al.*[1996a]

[e] *Andreae* [1990]

[f] *Iverson et al.* [1989]

Table C.2. Sea-to-air flux densities from different surface water types of the northwestern Black Sea and extrapolated Black Sea summer emission rates for CH_4, N_2O and *DMS*.

	Flux Density (μmol/m^2/day)		Emission rate (Gmol/yr)	
	LM86 --	W92	LM86 --	W92
CH_4:				
Open waters [a]	29	50	3.1	5.5
Shelf waters [b]	32	53	1.2	2.0
River plumes [c]	260[d]	470[d]	2.3[d]	4.3[d]
N_2O:				
Open waters [a]	3.1	5.2	0.33	0.56
Shelf waters [b]	2.7	4.4	0.10	0.16
River plumes [c]	1.6	2.8	0.02	0.03
DMS:				
Open waters [a]	1.6	4.6	0.17	0.50
Shelf waters [b]	2.1	5.2	0.08	0.19
River plumes [c]	5.6	11.9	0.05	0.11

[a] Black Sea river plumes surface area = 0.25 x 10^5 km^2; derived from salinity measurements.

[b] Black Sea shelf waters surface area = 1.02 x 10^5 km^2; derived from salinity measurements.

[c] Black Sea open waters surface = 2.96 x 10^5 km^2 ; derived from *Mee* [1992].

[d] estimated using corrected values for CH_4 concentrations in the Danube plume.

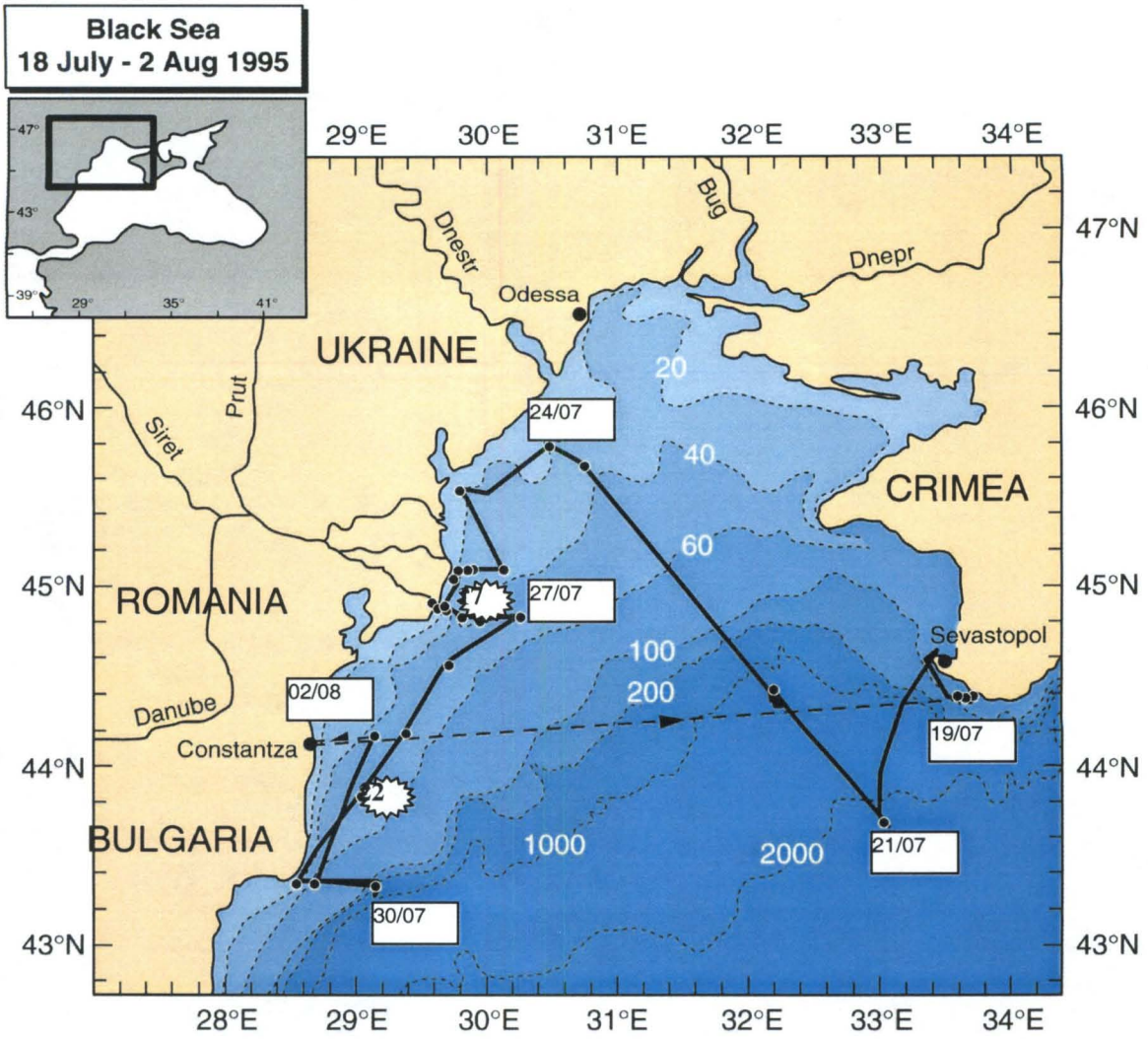

Figure C.1. Cruise track (solid line) of the research vessel Professor Vodianitskiy (IBSS, Sebastopol, Ukraine) during the EROS 21 experiment in the northwestern Black Sea shelf, from 18 July to 2 August 1995. Dots on the track represent the various hydro-cast stations performed during the cruise (stations 17 and 22 are highlighted by their respective number).

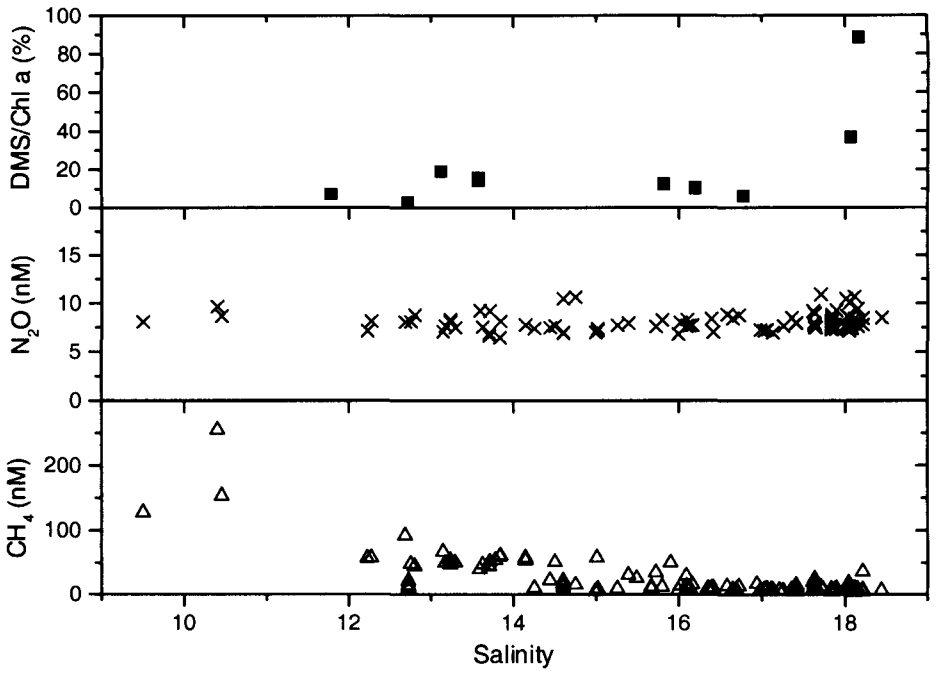

Figure C.2. Methane, nitrous oxide and chlorophyll a – normalized dimethyl sulfide concentrations in surface waters of the North-West Black Sea shelf as a function of water salinity. Methane and nitrous oxide concentrations were obtained from equilibrator mixing ratio measurements and Bunsen solubility coefficient calculations. Measured dimethyl sulfide concentrations (μg/L) were normalized to chlorophyll a contents (μg/L) in the same samples (weight ratio).

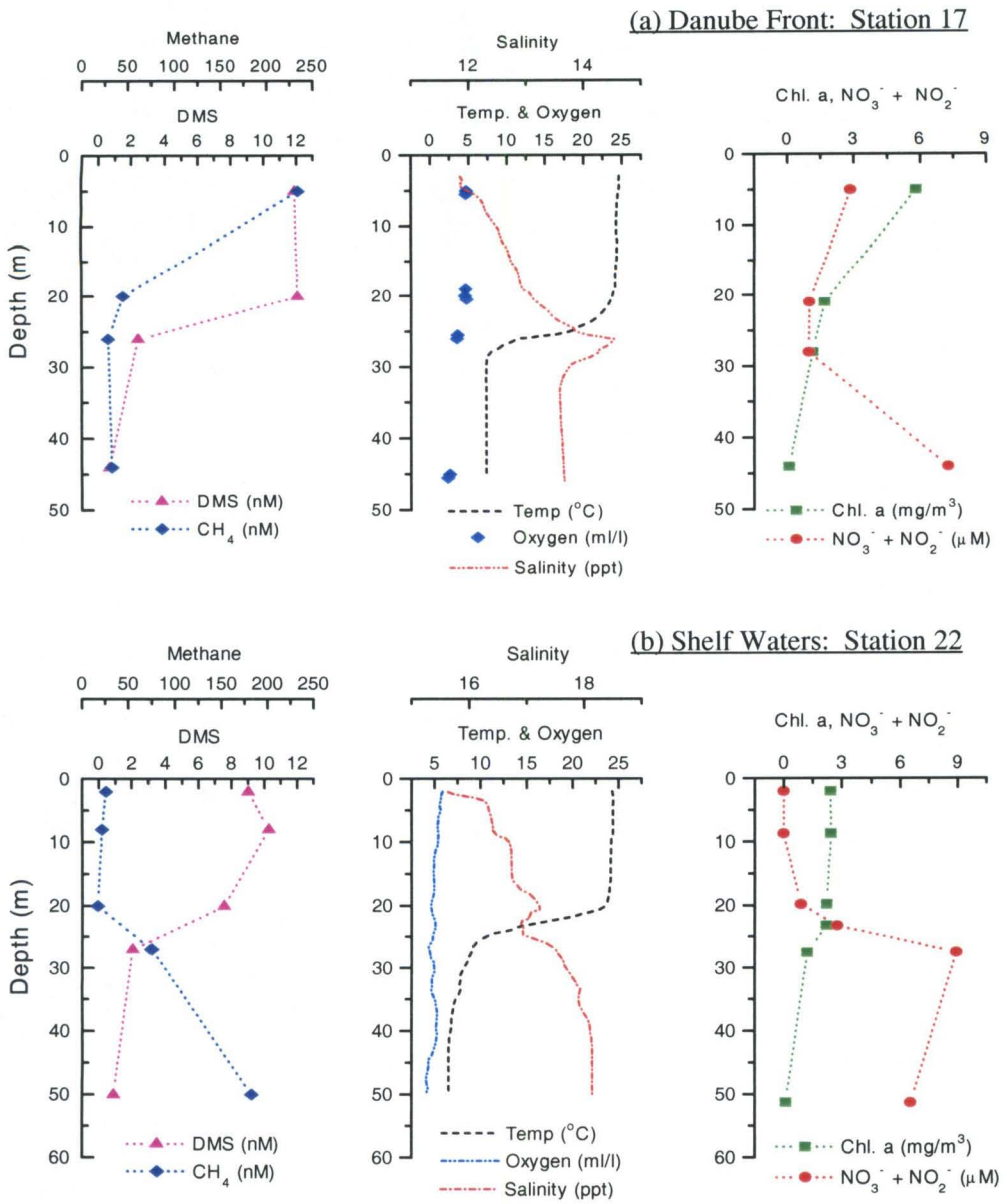

Figure C.3. Methane and Dimethylsulfide depth profiles in coastal waters of the Northwestern Black Sea shelf along with hydrological parameters (salinity, temperature, dissolved oxygen, oxidized nitrogen species, chlorophyll a). (a) Danube front, Latitude: 44°49'25'' N, Longitude: 29°49'22'' E. (b) Shelf waters, Latitude 43°49'59'' N, Longitude 29°01'52'' E.

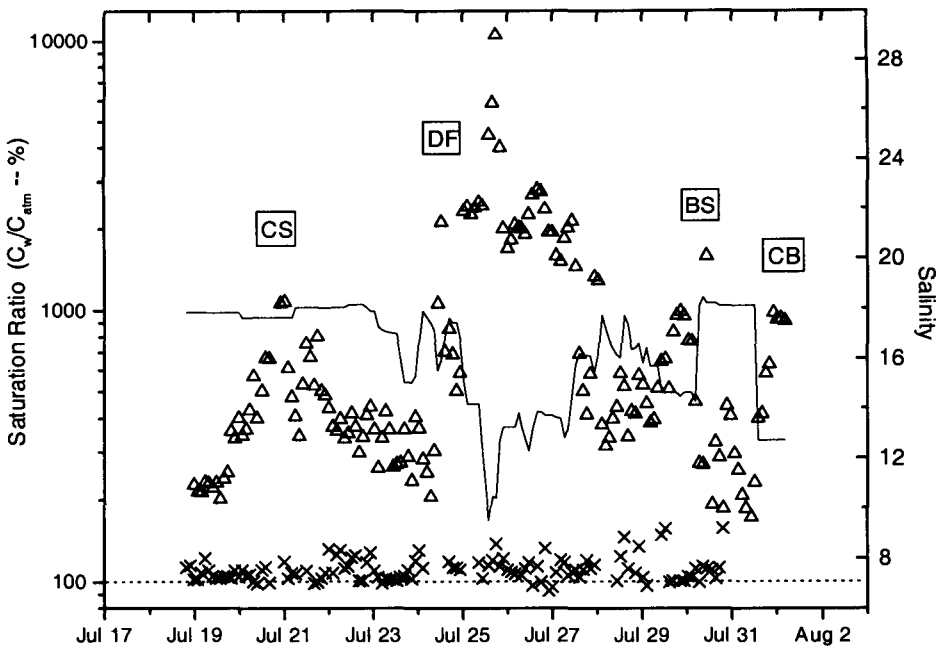

Figure C.4. Methane (Δ) and nitrous oxide (X) saturation ratios during the summer 1995 cruise on the northwestern Black Sea shelf. The air-sea equilibrium is shown by the dotted line. The different water masses are readily identified by the salinity (solid line): CS = Crimean Shelf break, DF = Danube Estuary front, BS = Bulgarian Shelf break, CB = Constanza Bay.